TAILORING OF Ni: 8YSZ CERMET VIA SOLUTION-BASED SYNTHESES

A THESIS SUBMITTED IN PARTIAL FULFILLMENT
OF THE REQUIREMENT FOR THE DEGREE OF

Doctor of Philosophy

in

Ceramic Engineering

by
SUBRAT KUMAR MOHANTY

under the guidance of
Dr. Bibhuti B. Nayak

Department of Ceramic Engineering
National Institute of Technology Rourkela
Odisha – 769 008, INDIA

Jan 2015

DEDICATED TO

My Parents

Shri Laksmidhar Mohanty
&
Smt. Manjubala Mohanty

Dr. Bibhuti Bhusan Nayak, Ph.D. (IIT Bombay)

Associate Professor
Department of Ceramic Engineering
National Institute of Technology
Rourkela, ODISHA – 769 008, INDIA
Tel: 91-661-246 2209; Fax: 91-661-247-2926
Email: bbnayak@nitrkl.ac.in (or) bibhutib@gmail.com   **Website: www.nitrkl.ac.in**

Date: 13-01-2015

CERTIFICATE

This is to certify that the thesis entitled *"Tailoring of Ni: 8YSZ cermet via solution-based syntheses"* submitted by Mr. Subrat Kumar Mohanty, for the award of the degree of Doctor of Philosophy, to the National Institute of Technology, Rourkela, is a record of bonafide research work carried out by him under my guidance and supervision at Department of Ceramic Engineering, NIT Rourkela.

In my opinion, the thesis has fulfilled all the requirements according to the regulations and has reached the standard necessary for submission. The results embodied in the thesis have not been submitted for the award of any other degree.

(Bibhuti B. Nayak)

DECLARATION

Date: 13-01-2015

I hereby declare that the work presented in the thesis entitled **"*Tailoring of Ni: 8YSZ cermet via solution-based syntheses*"** submitted for Ph. D. Degree to the National Institute of Technology, Rourkela has been carried out by me at Department of Ceramic Engineering, National Institute of Technology, Rourkela under the supervision of Dr. Bibhuti Bhusan Nayak. The work is original and has not been submitted in part or full by me for any degree or diploma to this or any other University/Institute.

Subrat Kumar Mohanty
Department of Ceramic Engineering
National Institute of Technology, Rourkela
ODISHA – 769008, INDIA

ACKNOWLEDGEMENTS

Subrat Kumar Mohanty

(Subrat Kumar Mohanty)

CONTENTS

ABSTRACT

Major challenges of Ni: 8YSZ cermet anode material in solid oxide fuel cell (SOFC) application are (i) the reduction of operating temperature, (ii) minimization of Ni concentration and (iii) optimization of porosity, without sacrificing electrical conductivity, thermal expansion compatibility and overall cell performance. Lowering of operating temperature is possible by increasing the density of triple phase boundary (TPB) by developing a suitable microstructure, containing fine grained Ni and 8YSZ. Decreasing grain size of Ni may minimize percolation threshold, and better Ni-Ni connectivity is possible via tailoring the microstructure of Ni: 8YSZ cermet. The porosity of cermet forms by the reduction of NiO to Ni and proper microstructure of NiO: 8YSZ composites may be developed by optimizing the fabrication parameters such as binder concentration, compaction pressure and sintering temperature. Above motivations led to work on tailoring the microstructural parameters such as size and distribution of NiO/Ni particles in NiO/Ni: 8YSZ composites, which strongly depends on the initial size and forms of Ni such as NiO, $Ni(OH)_2$ and Ni. These forms of Ni may evolve during different solution-based syntheses and varying synthesis conditions may develop different size and distribution of NiO in NiO: 8YSZ composites, which may result in different types of microstructure of Ni: 8YSZ cermet.

So, the main objective of this research work is to tailor Ni: 8YSZ cermet with fine Ni particles in 8YSZ matrix via solution-based syntheses, in order to achieve adequate electrical conductivity, compatible TEC and overall cell performance for IT-SOFC anode application.

Different conditions such as fuel lean, stoichiometric and rich in auto-combustion; direct, reverse and constant pH process in co-precipitation; and direct and reverse process in heterogeneous precipitation were adopted to prepare NiO/Ni: 8YSZ composites. Among these syntheses, fuel stoichiometric auto-combustion, constant pH co-precipitation and direct process heterogeneous precipitation are found to be most suitable for development of fine grained Ni: 8YSZ cermet. The porosity of anode lies in between 15 % to 39 %, depending on the synthesis / fabrication condition and volume fraction of Ni. Fine Ni particles (range in between ~200 nm to ~800 nm, depending on syntheses) are uniformly distributed in YSZ matrix at a sintering condition of 1200°C for all cermets. However, at 1300 °C, gradual chain formation of Ni (~ 600 to 900 nm) around YSZ (800 nm to 2µm) was observed in 30 and 40 vol % Ni containing cermet prepared at fuel stoichiometric condition and fine Ni particles are segregated on grain boundary as well as deposited on surface of YSZ (3 to 5µm) for 30 vol % Ni containing cermets, prepared by constant pH co-precipitation. On the other hand, fine Ni particles (~ 700 nm) are well-distributed in YSZ matrix for 20 vol % Ni containing cermet, prepared via direct process heterogeneous precipitation. Better conductivity was obtained in constant pH co-precipitation method and heterogeneous precipitation method at 40 and 20 vol % Ni, respectively. The electrical conductivity decreases either exponentially (in auto-combustion and co-precipitation) or linearly (heterogeneous precipitation) with temperature, depending on microstructure of cermet. The percolation threshold lies between 20 to 30 vol % Ni in fuel stoichiometric auto-combustion and constant pH co-precipitation derived cermet, whereas, 20 vol % Ni concentration provides adequate percolation in direct process heterogeneous precipitation method. The value of TEC of cermet is adequate and depends on the Ni concentration and synthesis conditions.

Impedance spectra of four different symmetrical cells were well fitted with different equivalent circuits. Charge transfer resistance, electrode conductivity, capacitance and exchange current density were determined from the circuit elements corresponding to high frequency arc. Major property such as charge transfer resistance is found to be lowest for CP CL N40 and the resistance of HP DP N20 is nearly comparable to CB FS N40. This specific property is comparable with some literature reported data. The coating thickness of the anode varies from 150 µm to 400 µm for different symmetrical cells and interface microstructure shows a strong adherence of the cermet layer to the electrolyte. The cell performance indicates the suitability of these materials for anode application.

The adopted solution-based syntheses are advantageous for the development of fine grained NiO/Ni: 8YSZ composites and are suitable for anode fabrication in terms of porosity, electrical conductivity, TEC and cell performance. The presence of $Ni(OH)_2$ in the as-synthesized powders prepared via constant pH co-precipitation method is more advantageous for developing finer grain size of Ni in the Ni: 8YSZ cermet and this particular cermet shows better anode properties for IT-SOFC application.

***Keywords**: SOFC; Ni: 8YSZ; cermet; Anode; electrical conductivity; TEC; Auto-combustion; Co-precipitation; Heterogeneous precipitation; Microstructure, Electrochemical performance.*

List of Figures

List of Tables

Nomenclature

a	Anode
A	Ampere
ASR	Area specific resistance
c	Cathode
C	Capacitance
e	electrolyte
F	Faraday's constant $= 9.648 \times 10^4$ C/mol
H	Enthalpy
Hz	Hertz
i	Current
i_0	Exchange current density
j	Imaginary unit
l_a	Anode thickness
l_c	Cathode thickness
l_e	Electrolyte thickness
L	Inductance
n	Frequency power
P	Pressure
p_{H2}	Partial pressure of hydrogen
p_{H2O}	Partial pressure of steam
p_{O2}	Partial pressure of oxygen
Q	Constant phase element
R	Resistance
$R_{contact}$	Contact resistance
R	Universal gas constant $= 8.314$ J/mol·K
S	Siemens
T	Absolute temperature
V	Volt
V_0	Reversible cell voltage at the standard state
V_r	Reversible cell voltage
W	Watt
Y	Pseudo-capacitance
z	Number of electrons
Z	Impedance
β	angular line width of half maximum intensity
$\Delta^r G$	Free or Gibb's enthalpy
$\Delta^r G^0$	Standard state free enthalpy
$\Delta^r H$	Reaction enthalpy of oxidation
$\Delta^r S$	Reaction entropy
ε_{EC}	Electrochemical efficiency
ε_J	Current efficiency
ε_T	Thermodynamic efficiency
ε_V	Voltage efficiency
η	Overpotential or polarization
η_{act}	Activation polarization
η_{conc}	Concentration polarization
η_{ohm}	Ohmic polarization
λ	Wavelength
μ	micron
Ω	Ohm
ω	Angular frequency
φ_e	Elemental stoichiometric co-efficient
ρ	Resistivity
ρ_a	Anode resistivity
ρ_c	Cathode resistivity
ρ_e	Electrolyte resistivity
σ	Conductivity
θ	Bragg's angle

Chapter 1

GENERAL INTRODUCTION

1.1: Introduction

Energy is one of the most vital inputs for the sustainable economic development of any country. The high standards of living in the developed countries are attributable to the high energy consumption levels. Almost 85% of the energy that we use comes from fossil fuels such as coal, oil and natural gas, which are on the verge of depletion as well as produce hazardous gases and substances like SO_2, NO_x, CO_2, and CO etc. With increasing demand for preserving a pollution free environment, several efforts are taken care by the governments, manufacturers, technology developers, and users worldwide to find alternate sources of energy and power supply. Analyzing the current energy scenario and associated problems, the fuel cells have come up as an excellent alternative for energy production. The direct electrochemical conversion of chemical energy of a fuel into electricity has made fuel cells beneficial [1, 2]. Fuel cells lend themselves to various applications in several sectors - large and small, portable and stationary and are likely to make an indelible mark on the future energy scenario.

The fuel cells are generally characterized by the type of electrolyte they use and the operation temperature. As of now, there are mainly five types of fuel cells such as polymer electrolyte membrane fuel cell (PEMFC), alkaline fuel cell (AFCs), phosphoric acid fuel cell (PAFC), molten carbonate fuel cell (MCFC) and solid oxide fuel cell (SOFC). Depending upon the operation temperature, the first three fuel cells are classified as low temperature fuel cells (80-250°C), whereas the remaining two types of fuel cells are intermediate to high temperature fuel cells (600-1000°C). Keeping in view the early market application, PEMFC and SOFC have greatly attracted attention [3], but PEMFC required expensive platinum catalysts, high purity H_2 for fuel, and the large fuel reformer. On the other hand, high efficiency ($\sim 60\%$) and multi fuel adaptability (it is possible to operate SOFC with a range of gaseous fuels e.g. hydrogen, natural gas, carbon monoxide, and various light hydrocarbons including bio-gas) are not the only advantages of SOFCs, they are attractive as energy sources because they are clean, reliable, and almost entirely nonpolluting. The SOFCs are of two types depending upon the conductivity of the electrolytes: one having proton conducting electrolyte and the other having oxide ion conducting electrolyte. Work on proton conductor SOFCs is limited because of material studies, clarification of conduction mechanisms and testing of small, laboratory scale cells [2]. Hence, almost all research work on fuel cells is focused on SOFCs having oxygen ion conducting electrolytes.

1.2: Components, materials and operating principle of SOFC
1.2.1: Components

A single cell SOFC has three major components, in which an electrolyte is sandwiched between two electrodes namely, anode and cathode. At anode, the fuel fed undergoes oxidation and

releases electron to the external circuit. The oxidant at cathode accepts electrons from the external circuit and suffers reduction forming oxide ions. The electron flow from anode to cathode through the external circuit produces a direct current with the solid electrolyte acting as the path for ion conduction. In SOFC, the most common fuel is hydrogen, which has high electrochemical reactivity and can be easily obtained from common fuels such as hydrocarbons, alcohols, or coal. Oxygen is the most widely used oxidant, which can be easily obtained from air. For reactions involving hydrogen and oxygen, oxides are the only electrolytes for use in fuel cells.

1.2.2: Materials

A single cell SOFC consists of two porous electrodes, anode and cathode, separated by a dense electrolyte and can be connected to other single cells by two interconnects at the two ends. Due to the high temperature operation, the choice of material for different components of fuel cell should fulfill four main criteria such as (i) The major cell components should have adequate electrical conductivity for proper cell functioning; (ii) The cell components should have chemical and structural stability during cell fabrication as well as operation; (iii) The cell materials should have necessary thermal expansion compatibility to avoid thermal stress and (iv) The materials should have minimum reactivity and inter-diffusion between them [2].

1.2.2.1: Cathode

The task of the cathode material is to allow the oxidant gas to be reduced by accepting electrons from the external circuit and transport the generated oxide ions to the cathode-electrolyte interface. The properties that the cathode material should have, are (i) high electronic conductivity, (ii) thermal and chemical compatibility with adjoining cell components, (iii) sufficient porosity to convey the oxidant gas and (iv) high catalytic activity [2]. Keeping in view the high operation temperature and low cost, doped (strontium, calcium and other lower valent cations) lanthanum manganite ($LaMnO_3$), having a perovskite structure, has been extensively studied as cathode material because of its high electrical conductivity in oxidizing atmosphere, acceptable thermal expansion match with other cell components and sufficient compatibility with YSZ electrolyte.

1.2.2.2: Electrolyte

The function of the electrolyte is to conduct the oxide ions generated at the cathode to the anode for electrochemical combination with the fuel. The electrolyte for SOFC should have high (i) ionic conductivity, (ii) high density, (iii) thermal and chemical compatibility and (iv) chemical as well as dimensional stability under both reducing and oxidizing environment [2]. Among the various types of oxide ion conductor used such as YSZ, doped ceria (CeO_2) and stabilized bismuth oxide (Bi_2O_3) etc., YSZ is the most suitable candidate because of its adequate oxygen ion conductivity and stability in both oxidizing and reducing atmosphere.

1.2.2.3: Anode

The function of anode is to oxidize the fuel gas and provide electrons to the external circuit for efficient operation of SOFC. So the requisite properties of the anode material are (i) high electronic conductivity; (ii) thermal expansion compatibility with the adjoining cell components; (iii) chemical, phase and microstructural stability in fuel environment; (iv) chemical compatibility with adjoining cell components; (v) sufficient porosity to transport fuel gas to the reaction sites and (vi) high catalytic activity for electrochemical oxidation of the fuel [2]. Due to the higher operation temperature and prevailing reducing atmosphere, only noble metals such as nickel (Ni), cobalt (Co), palladium (Pd) and platinum (Pt) etc. are suitable candidates for anode material in SOFC. Currently, the most widely used metal is Ni because of its low cost as compared to other metals. High thermal expansion co-efficient and sintering of Ni particles at high operation temperature does not permit Ni to be used alone and hence 8 mol% yttria (Y_2O_3) stabilized zirconia (ZrO_2) (YSZ) is incorporated as a support forming Ni-YSZ composite. The presence of YSZ inhibits coarsening of Ni, lowers the thermal mismatch and also provides ionic conductivity to the anode material.

1.2.2.4: Interconnect

The requirements of interconnect material are (i) high density, (ii) high electronic conductivity, (iii) thermal expansion and chemical compatibility with adjoining components as well as (iv) chemical, phase, morphological and dimensional stability in both oxidizing and reducing environments. Doped (substituting either La^{3+} or Cr^{3+} with lower valence ions such as Ca^{2+}, Ni^{2+}, Ti^{4+} etc.) lanthanum chromite ($LaCrO_3$) is generally used as interconnect material because of its high electronic conductivity, desired stability and compatibility in the fuel cell environment [2].

1.2.3: Operating principle

The most common fuel and oxidant that are used in SOFC are hydrogen and oxygen. Thus, during the operation of fuel cell oxidation of hydrogen and reduction of oxygen takes place at anode and cathode, respectively (see Fig. 1.1). For hydrogen and oxygen reaction [1],

1st reaction: $$H_{2(a)} \rightarrow 2H^+_{(a)} + 2e^- \qquad (1.1)$$

2nd reaction: $$\frac{1}{2}O_{2(c)} + 2e^- \rightarrow O^{2-}_{(c)} \qquad (1.2)$$

3rd reaction: $$2H^+_{(a)} + O^{2-}_{(a)} \rightarrow H_2O_{(a)} \qquad (1.3)$$

Overall reaction: $$H_{2(a)} + \frac{1}{2}O_{2(c)} \rightarrow H_2O_{(a)} \qquad (1.4)$$
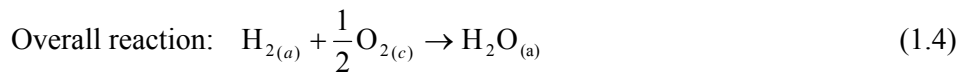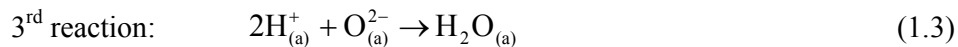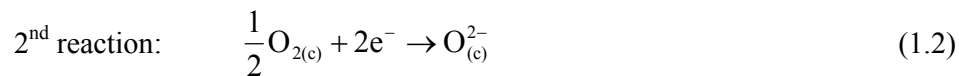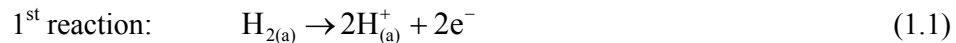
where the subscripts 'a' and 'c' stand for anode and cathode, respectively.

The reversible cell voltage (V_r) is given by

$$V_r = -\frac{\Delta^r G}{2F} = V_0 + \frac{RT}{4F}p_{O_2(c)} + \frac{RT}{2F}\ln\frac{p_{H_2(a)}}{p_{H_2O(a)}} \qquad (1.5)$$

where V_0 is the reversible voltage at the standard state and is given by

$$V_0 = -\frac{\Delta^r G^0}{2F}$$

(1.6)

$\Delta^r G$ = free or Gibb's enthalpy and is given by, $\Delta^r G = \Delta^r H - T \cdot \Delta^r S$

(1.7)

$\Delta^r H$ = reaction enthalpy of oxidation
$\Delta^r S$ = reaction entropy
$\Delta^r G^0$ = standard state free enthalpy,
R = universal gas constant = 8.314 J/mol·K,
T = absolute temperature,
F = Faraday's constant = 9.648×10^4 C/mol,
$p_{H_2O(a)}$, $p_{H_2(a)}$ and $p_{O_2(c)}$ are the partial pressures of H_2O, H_2 and O_2 respectively.
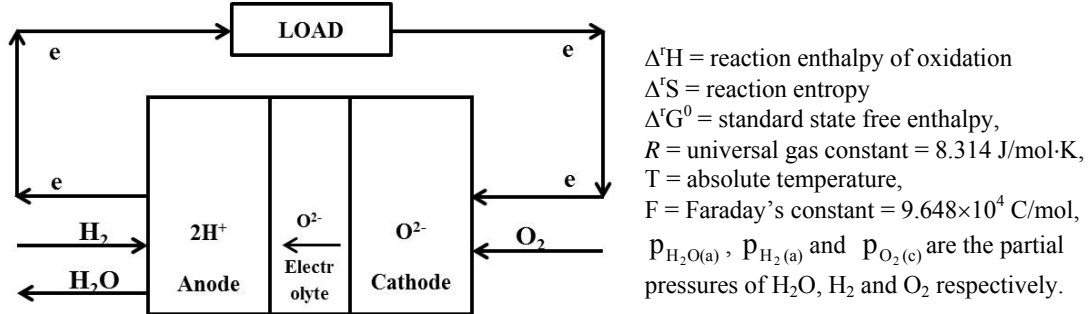
Fig. 1.1: Schematic diagram of SOFC operation

The effect of temperature and pressure on the reversible cell voltage can be analyzed in terms of the free energy change with temperature and pressure. This can be written as

$$(\partial V_r / \partial T)_P = \Delta^r S / 2F$$

(1.8)

$$(\partial V_r / \partial P)_T = -\Delta V / 2F$$

(1.9)

where ΔV is the volume change. For hydrogen/oxygen reaction, the entropy change and volume change are negative and positive, respectively. Thus, the reversible cell voltage is inversely and directly proportional to temperature and pressure, respectively, i.e. $V_r \propto 1/T$ and $V_r \propto P$.

Increase in temperature and pressure of operation improves the fuel cell performance due to enhanced mass transfer, reaction rate and low material resistance. At the same time, it imposes constraints on the material selection and hampers the integrity of the gas seal and cell structure.

The thermodynamic efficiency ε_T of a fuel cell is the ratio of the Gibb's enthalpy $\Delta^r G$ and the reaction enthalpy $\Delta^r H$ at the thermodynamic state of the fuel cell and is given by

$$\varepsilon_T = \frac{\Delta^r G}{\Delta^r H} = \frac{\Delta^r H - T \cdot \Delta^r S}{\Delta^r H}$$

(1.10)

The electrochemical efficiency of fuel cell includes the thermodynamic efficiency, voltage efficiency and current efficiency i.e. $\varepsilon_{EC} = \varepsilon_T \cdot \varepsilon_V \cdot \varepsilon_J$, where ε_{EC} is the electrochemical efficiency, ε_V is the voltage efficiency (the ratio of operating cell voltage under load to the equilibrium cell voltage) and ε_J is the current efficiency (ratio of actual current produced to the current available).

As current is drawn from fuel cell, the reversible cell voltage falls due to various kinds of losses (as described in following section), which are dependent on the current density, temperature, pressure, gas flow rate and composition as well as microstructure of the cell material.

1.3 Polarization

The difference between the operating cell voltage and theoretical thermodynamic voltage is referred to as polarization or overpotential, denoted by η. Depending upon various processes occurring in the cell, under a finite current, the polarization consists of a number of terms. The different terms are named as resistance or ohmic polarization, diffusion or concentration polarization and charge transfer or activation polarization.

(a) Ohmic polarization:

The resistance to the motion of charge, such as oxide ions in electrolyte and electrons in the electrodes, is called the resistance or ohmic polarization. The corresponding voltage loss, η_{ohm}, is given by

$$\eta_{ohm} = (\rho_e \, l_e + \rho_c \, l_c + \rho_a \, l_a + R_{contact}) \, i \tag{1.11}$$

where ρ_e, ρ_c and ρ_a are the electrolyte, cathode and anode resistivities, respectively, and l_e, l_c and l_a are respectively the electrolyte, cathode and anode thicknesses, and R is any possible contact resistance. In most SOFCs, the major contribution to η_{ohm} arises from the electrolyte, because its (e.g. YSZ) ionic resistivity is much higher than the resistivities of anode (e.g. Ni-YSZ) and cathode (e.g. LSM).

(b) Concentration polarization:

At a given current density, the physical resistance to the transport of gaseous species (e.g. H_2 at anode and O_2 at cathode) at electrodes appears as an electrical voltage loss, termed as the diffusion or concentration polarization, η_{conc}. This depends on the diffusivity and partial pressure of gases, microstructure and current density.

(c) Activation polarization:

Charge transfer is a major step in electrode reactions, wherein a neutral species is converted into an ion or vice versa. These reactions involve transfer of electrons from or to the reacting species, which needs to overcome an energy barrier. This energy barrier is termed as charge transfer or activation polarization, η_{act}, and depends upon the material properties, microstructure, temperature, atmosphere and current density.

All the above type of polarizations contributes to the total polarization of the cell and the total polarization can be written as

$$\eta = \eta_{ohm} + \eta_{conc} + \eta_{act} \tag{1.12}$$

Thus the actual cell voltage of fuel cell can be given by

$$V = V_r - \eta = V_r - (\eta_{ohm} + \eta_{conc} + \eta_{act}) \qquad\qquad (1.13)$$

Polarization cannot be eliminated, but can be minimized by modifying the microstructure of the materials and cell design.

1.4: Constraints of SOFC and challenges in IT-SOFC

The high temperature operation of SOFC has some specific advantages like internal reforming of light hydrocarbon fuels, rapid reaction kinetics, minimization of polarization loss and noise pollution. But, major problems associated with its commercialization are its cost in addition to stringency in materials requirements and processing. The high operating temperature of SOFC results in longer start-up times as well as mechanical and chemical compatibility issues. This also imposes restrictions on the choice of the materials. Therefore, significant effort has been made to reduce the operating temperature (600°C-800°C) of SOFC i.e., to develop intermediate temperature (IT) SOFC. The use of IT- SOFC facilitates the use of inexpensive materials, offers the potential for more rapid start up and shut down procedures, simplifies the design and material requirements and reduces corrosion rates. But, as the operating temperature of SOFC decreases, the conductivity of the electrolyte, catalytic activity of electrodes and power density of the cell decreases. Hence, to reduce the operating temperature, the above challenges need to be surmounted. There are several approaches to lower the operating temperature of SOFCs, which includes (i) decrease of YSZ electrolyte thickness; (ii) adoption of alternative electrolyte materials with higher ionic conductivity at low temperatures than conventional YSZ, such as doped ceria and doped lanthanum gallate; (iii) minimization of electrode polarization resistance. The electrode polarization could be minimized with the development of high catalytic activity electrode materials with a suitable microstructure.

1.5: Importance of anode material

Among the two electrodes, the anode plays a significant role in operation of SOFC, as it is responsible for the oxidation of fuel to generate electricity and removal of byproducts, and hence chosen in this research work for development. It is a challenge to design the anode with large number of active sites for the electrochemical oxidation of fuel, adequate electrical conductivity to transport the charge and appropriate porosity to allow the passage of fuel gas as well as removal of byproducts, at intermediate temperatures. The constraints imposed on anode by reducing the operating temperature are discussed in detail in the next section.

1.6: Constraints of anode material in SOFC

State-of-the art material for SOFC anode is Ni: YSZ cermet, as it possesses the requisite property requirements, discussed in section 1.2.2.3. One of the major drawbacks at higher operating

temperature is the deposition of carbon on the nickel surfaces on using hydrocarbon as a fuel that blocks the anode porosity and consequently disrupts the integrity of the cell. In anode material, Ni phase is responsible for electronic conduction and YSZ phase is responsible for ionic conduction. So, the electronic conductivity is also an important factor in SOFC anode. It also has the highest thermal expansion amongst all the components of SOFC, which causes stringent processing requirements for SOFC cell fabrication and application. As a consequence, scientists and researchers are working to reduce the thermal expansion of Ni: YSZ cermet anode without sacrificing its electrical conductivity. Also, at higher Ni concentration ($\geq$ 30 vol %), significant grain growth of Ni at higher operating temperatures lead to the degradation of electrical conductivity [4, 5]. Moreover, it decreases the overall cell performance. The solutions to all these problems are (i) to replace the nickel part by other metal or an alloy, (ii) to find an alternative anode material, (iii) to lower the operating temperature of SOFC and (iv) to reduce the nickel concentration. As far as the first and second solutions are concerned, several materials like Cu-YSZ, Ni/Cu-YSZ, perovskites like La doped $SrTiO_3$ doped with manganese or gallium and double perovskites like $Sr_2MgMoO_{6-\delta}$ have been studied [6-9]. But all these materials have their own limitations and none of these have been able to compete with the electrical conductivity and electro-catalytic activity of the anode. Hence, the reductions of operating temperature of SOFC into IT range as well as Ni concentrations are the essential requirements for better functionality of its components. During the last two decades, it has been a major challenge for the scientists hailing from different domains and working in the field of solid oxide fuel cell (SOFC), to reduce its operating temperature into the intermediate (IT) range for its commercialization. But, the major drawback that follows from decrease in operating temperature is the increase in anode over potential in IT-range.

1.7: Advantages of fine grained Ni: 8YSZ anode

The formation of fine grained Ni: YSZ anode material is beneficial in decreasing anode over potential and therefore, is the key for their operation in the IT-range. In general, the effective conductivity increases and anode over potential decreases with increase in triple phase boundary (TPB), as the Ni particle size in the Ni-YSZ cermet is reduced [10-13]. It is possible to achieve better percolation of Ni at lower concentration as well as better conductivity along with comparable thermal expansion coefficient (TEC) by modifying the microstructural parameters such as grain size, distribution of grains and porosity in NiO/Ni: 8YSZ composites [14, 15]. Although fine Ni particles sinter easily to form larger particles, but homogeneous mixing of the Ni-YSZ powders may lead to long term durability and adequate stability against thermal and redox cycling [16].

Further lower reduction temperatures also inhibit Ni coarsening [4]. In our study, grain size, phase distribution and density/porosity are modified in different amount of Ni containing Ni: 8YSZ cermet via solution-based syntheses. Further microstructural parameters can be analyzed through both qualitatively and quantitatively using different instrumental tools. Numerous techniques such as FIB-SEM, X-ray CT and modelling have been used for quantitative analysis of effect of microstructure on the properties of Ni: 8YSZ cermet with detailed three-dimensional (3D) understanding of the microstructure [17-24]. In addition to this, tortuosity, connectivity of phases, total TPB length cannot be estimated from 2D images and more importantly these factors can be estimated from 3D-images using highly sophisticated techniques such as FIB-SEM, X-ray CT and modelling. Due to limitations in our characterization techniques, the microstructural parameters such as porosity, grain size and Ni distribution are studied qualitatively from FESEM-images. Thus, this research work is based on tailoring of Ni: 8YSZ cermet with highly percolated fine Ni particles in 8YSZ matrix via solution-based syntheses.

1.8: Organization of thesis

General introduction to SOFC; components, materials and operation of SOFC; advantages and constraints of Intermediate temperature SOFC; Importance anode material and constraints of anode material in SOFC; advantages of fine grained Ni: 8YSZ anode, are discussed in Chapter 1. Chapter 2 provides a detailed discussion of literature on different ways of solution-based syntheses to prepare NiO: 8YSZ powders; microstructure and electrical conductivity of Ni: 8YSZ anode and electro-chemical performance of cell. Statement of the problem: proposed work, which is based on the literature survey, is presented towards the end of Chapter 2. In Chapter 3, details of syntheses to prepare NiO: 8YSZ powders and method of fabrication of Ni: 8YSZ cermet and symmetrical cell as well as different characterization techniques are described. Chapter 4 describes the properties of auto-combustion derived Ni: 8YSZ cermet. Different properties such as thermal, structure, powder morphology and shrinkage behavior of fuel lean, stoichiometric and rich derived NiO: 8YSZ powders are studied in Chapter 4.1. Effect of binder concentration and compaction pressure on density/porosity, microstructure and electrical conductivity of Ni: 8YSZ cermets have been studied in detail in Chapter 4.2. Effect of Ni concentration and sintering temperature on density/porosity, microstructure, electrical conductivity as well as TEC of fuel stoichiometric derived 20, 30 and 40 vol % Ni containing Ni: 8YSZ cermet was studied and analyzed in Chapter 4.3. In Chapter 5, Ni: 8YSZ cermet was fabricated using co-precipitation derived NiO: 8YSZ powders and properties are analyzed. Thermal, structure, powder morphology and shrinkage behavior of direct, reverse and constant pH derived Ni: 8YSZ cermet prepared using chloride and nitrate precursors are correlated

in Chapter 5.1. Density/porosity, microstructure and electrical conductivity of direct, reverse and constant pH derived Ni: 8YSZ cermet was studied and results are correlated in Chapter 5.2. Effect of Ni concentration and sintering temperature on density/porosity, microstructure, electrical conductivity and TEC of constant pH derived Ni: 8YSZ cermet was studied and analyzed in Chapter 5.3. Chapter 6 describes the properties of heterogeneous precipitation derived Ni: 8YSZ cermet. Chapter 6.1 describes the synthesis and characterization of 8YSZ nanopowders. Thermal, structure, morphology, shrinkage behavior of 20, 30 and 40 vol % Ni containing Ni: 8YSZ cermet via direct and reverse process is discussed in Chapter 6.2. Density/porosity, microstructure, electrical conductivity and TEC of 20, 30 and 40 vol % Ni containing Ni: 8YSZ cermet were compared and analyzed in Chapter 6.3. In Chapter 7, the polarization resistance of the anode materials, prepared through four different conditions, was studied from impedance measurement of symmetrical cells using YSZ as electrolyte. Finally, the results of Ph.D. work are correlated in conclusions section. Synthesis of Ni^{+2}-ion stabilized tetragonal zirconia nanopowders and Ni/NiO: ZrO_2 nanocomposites are discussed in appendices.

Chapter 2

LITERATURE REVIEW

2.1 Different syntheses to prepare NiO: 8YSZ powders and properties of Ni: 8YSZ cermet

2.1.1 Conventional method derived Ni: 8YSZ cermet

Mixing appropriate amount of commercially available NiO and YSZ powders and fabrication of Ni: 8YSZ anode using these powders is renowned and ubiquitous. This method of preparation is well established by many scientists. In general, these NiO and YSZ powders were mixed properly using either by ball mill or planetary mill and then pressed into pellets. These NiO: 8YSZ pellets were sintered at higher temperature in air atmosphere and then reduced under the flow of H_2 gas atmosphere to form Ni: 8YSZ cermet. The major properties such as electrical conductivity, porosity and TEC of Ni: 8YSZ cermet strongly depends on the microstructure, distribution of Ni in YSZ matrix and Ni concentration. These properties are strongly dependent on type or size of NiO or YSZ particles.

Matsushima et al. [25] have developed 30 to 60 wt% Ni containing Ni: 8YSZ cermet using two different types of YSZ powders such as pre-calcined (1200 °C/2h) and commercial. Two different types of YSZ strongly affect the shrinkage behavior and sinterability is lower for pre-calcined YSZ powder. The shrinkage is largely governed by the NiO content during firing process and is decreased with the increase in NiO content. The porosity was higher in the samples, prepared using pre-calcined YSZ powder, even though the firing temperature was 200 °C higher. After sintering at 1400 °C/2h and reduction, the conductivity of cermet was found to be 1000 S/cm in case of pre-calcined YSZ powder and remained almost constant for different NiO content. However, the conductivity was 800 S/cm in case of commercial YSZ powder and decreased with decrease in NiO content.

Use of different grain size and surface area of commercial NiO powder also affect the properties of Ni: 8YSZ cermet. Tietz et al. [26] have used eight different commercial NiO powders, having different grain size and surface area, to fabricate anode substrates with 55 wt % NiO. The substrates prepared using fine NiO powders showed high density, low gas permeability and high electrical conductivity as compared to other samples. It was deduced that the prediction of the properties of the components from powder properties is possible only if the powders for component fabrication remain largely unchanged during the processing steps. In other way, same particle size of NiO and YSZ powders (~ 2 μm) were ball milled for 24 h to prepare NiO-YSZ composites and then sintered at 1400 °C/3h followed by reduction at 1000 °C/12h in H_2 atmosphere [27]. Density of Ni-YSZ cermet decreased with increase in NiO content, due to more oxygen extraction during reduction. The average particle size of Ni and YSZ was larger for higher Ni and YSZ fractional composition, respectively, due to the higher contact probability. The grain growth of YSZ occurred during sintering, while additional Ni coarsening occurred during reduction. The contiguity between

same phases depended upon the content of that phase, whereas the contiguity between different phases additionally depended upon the microstructural evolution. The coarsening rate and growing direction of Ni mainly controlled the overall microstructural evolution. In this cermet, the electrical conductivity increased with increase in Ni concentration and the suitable range was found to be 40-50 vol% for use as anode in SOFC.

Use of fine size of NiO / YSZ also strongly affects the properties of Ni: 8YSZ cermet. Fukui et al. [28] have prepared 65.2 wt % Ni containing NiO-YSZ composite by an advanced mechano-fusion method. It was found that submicron NiO particles were covered around finer YSZ particles. The particle sizes of the NiO and YSZ were found to be 600 nm and 100 nm, respectively. During cell fabrication using YSZ as electrolyte, the NiO-YSZ anode layer and LSM-YSZ cathode layer were sintered at 1350°C and 1200°C, respectively. The anode polarization was measured and found to be comparable with other anodes. This is due to the drastic increase in TPB, which was attributed to the nanoscale structure of Ni and YSZ. Similarly Lee et al. [29] have also prepared NiO-YSZ composites using fine (0.25 μm) and coarse (1.8 μm) YSZ powders and NiO (0.8 μm) powders. Two different granulation methods such as spray drying method (SDM) and liquid condensation process (LCP) were used in order to get different microstructural parameters in anode substrates and anode supported SOFC. Anisotropy and directionality in microstructure was observed in SDM samples, whereas uniform distribution of NiO, YSZ and pore phases were observed in LCP samples. In spite of larger porosity and pore diameter in SDM samples, the gas permeability was found to be more in LCP samples, due to higher effective porosity. Hence, for better gas permeability, uniform distribution and proper connection between appropriately sized pores are more important factors than total apparent porosity itself. Similarly, higher electrical conductivity and higher power density was obtained in case of the Ni-YSZ substrate and unit cell SOFC, respectively, prepared by LCP.

The above literature analysis points out the fact that the type or size of commercially available NiO or YSZ strongly affects the properties of Ni: 8YSZ cermet. Lower the particle size of NiO/YSZ, better the physical properties of Ni: 8YSZ cermet. So, the particle size of NiO/YSZ in NiO: 8YSZ powders could further be reduced via solution-based syntheses. Solution-based syntheses can be beneficial in getting finer starting powders for SOFC application [30-33]. So, researchers were motivated to work on synthesis of finer NiO/YSZ powders via solution-based synthesis methods. The major properties such as electrical conductivity, TEC, porosity and electrochemical performance of Ni: 8YSZ are expected to be influenced by the use of finer sized NiO: 8YSZ powders. So, in the next section, the physical properties of Ni: 8YSZ cermet, prepared via auto-combustion, co-precipitation and coating methods are discussed as follows.

2.1.2 Auto-combustion derived Ni: 8YSZ cermet

Fine NiO: 8YSZ powders can be prepared through auto-combustion method by controlling the oxidizer to fuel ratio and also using different fuels such as carbohydrazide , glycine, urea, citric acid and succinic acid [34-38]. Lots of work has been performed by many researchers through auto-combustion process to synthesize fine grained NiO: 8YSZ powders. The properties of Ni: 8YSZ cermet strongly depends on the initial size of NiO: 8YSZ powders. The initial size of NiO and YSZ strongly depends on the auto-combustion synthesis conditions as well as synthesis parameters such as pH, temperature and type of fuels. The grain size and distribution of Ni and YSZ in cermet can be optimized using smaller size of NiO and YSZ during fabrication of NiO: 8YSZ pellets and also by varying sintering temperatures. Effect of different conditions as well as different parameters on the physical properties of auto-combustion derived Ni: 8YSZ cermets are described.

Ni: 9YSZ nanopowders, containing 15, 30 and 50 vol% Ni containing powders were prepared through auto-combustion method using carbohydrazide as fuel [34] at fuel lean and fuel rich condition. The as-synthesized powders are weakly crystalline at fuel lean and crystalline at fuel rich condition. The compacted NiO-9YSZ were sintered at 1350°C for 4 h and then reduced at 800°C for 2h. The density was found to be more than 70% for 15 and 30 vol% Ni containing cermet and low density was obtained for 50 vol% Ni containing samples. The electrical conductivity was found to be 0.103 S/cm, 40 S/cm and 989 °C at 900°C for cermet containing 15, 30 and 50 vol% Ni, respectively. However, the as synthesized powders were found to be amorphous even after calcination at 650°C for 0.5 h, when synthesized at fuel lean condition using glycine as a fuel [39]. On the other hand, the powders were found to be crystalline for fuel stoichiometric and fuel rich conditions. Upon sintering at 1500°C for 2 h and reduction at 1000°C for 1.5 h, fine Ni particles of 3 to 5 μm were found to be distributed uniformly and increase the triple phase boundary.

The effect of citrate to nitrate (c / n) ratio on the combustion kinetics, particle morphology, phase evolution, shrinkage and sintering behavior of the composites were extensively studied by Marinšek et al. [36], in order to evaluate the suitability of the method for manufacturing SOFC anode of 40 vol % Ni content. The samples were sintered at 1380°C for 2 h and the density of NiO-YSZ pellets was found to be decreased with increase in c/n ratio. After reduction at 950°C in 4 vol % H_2 + 96 vol% Ar, fine Ni particles (micro- or sub-micrometer) were found to be randomly distributed in YSZ matrix in the cermet. The electrical conductivity value was found to be 1.58 S/cm at 900°C. The same group [12] have also studied the sintering behavior of fine NiO-YSZ powders (containing 50 vol% Ni in the final Ni-YSZ cermet) synthesized by microwave assisted citrate-nitrate combustion method. Two different sintering temperatures such as 1420 °C and 1200

°C are used for un-milled samples and attrition milled samples, respectively. A relative density of 91.4% with maximum connectivity between Ni grains was found for the samples sintered at a temperature as low as 1200°C. This temperature was also suggested as the optimum temperature for getting smallest Ni grains (diameter ~ 0.27 μm) in the final Ni-YSZ cermet.

Porosity is yet another significant factor in monitoring the electrical conductivity and electrochemical performance of Ni: 8YSZ cermet. Glycine-nitrate gel-combustion synthesis was followed by Kakade et al. [37] to prepare NiO-YSZ powders containing 50 vol% Ni. The samples were sintered at 1450°C for different soaking times (0.5, 1, 2 and 5h) in order to obtain a porosity variation in the final Ni-YSZ cermet. The electrical conductivity was found to depend upon the porosity and decreased with increased porosity. Also uniformly distributed fine grains and pores sufficiently enhanced the density of the triple phase boundary. Due to the presence of desired amount of porosity and interconnected grain structure, it was found that Ni-YSZ cermets having 41% porosity are suitable as anode material for SOFC. NiO-YSZ composite powders, containing 45 vol% of Ni, were also synthesized by Priyatham et al. [40] using stoichiometric amount of urea as fuel without any intermediate calcination step. The powders were nanocrystalline in nature having crystallite sizes of 29 and 22 nm for NiO and YSZ, respectively. The sample was sintered at 1300°C for 3h in air and reduced at 800°C for 90 min. The reduced Ni-YSZ pellet possessed a porosity of 27% with interconnected network of pores. The electrical conductivity exhibited electronic behavior due to improved Ni-to-Ni contact.

Nano-sized NiO powder on submicron-sized YSZ particles, containing 50 wt% NiO, were synthesized by Liang et al. [38] in homogeneous precipitation followed by combustion process using urea. In this work, the pre-sintered NiO-YSZ porous support layer along with the hydrogen electrode and electrolyte layer were co-sintered at 1400°C for 4h followed by the sintering of LSM-YSZ oxygen electrode at 1180°C for 2h. Finest microstructure NiO-YSZ was observed, when the molar ratio of $CO(NH_2)_2$ to $Ni(NO_3)_2$ was kept at 2:1. The cell prepared with this composition showed lowest and stable electrolytic voltage of 0.98 V after 90 minutes of electrolysis with no degradation. The impedance measured at 900°C also confirmed lowest polarization resistance of 0.865 Ω cm^2, caused by H_2O adsorption, O_2 desorption or a surface diffusion process, for this composition.

In order to study the effect of pH of the precursor solution on the combustion behavior and powder characteristics, Mohebbi et al. [41] have prepared nano-crystalline Ni/NiO-YSZ powders by microwave-assisted combustion synthesis using glycine as fuel. As glycine formed monodentate ligand with the metal cations at lower pH, the rate of combustion was more as compared to higher pH, at which the formation of bidentate ligand was observed. With increase in

pH value, there was decrease in crystallite size and increase in surface area of the powders. Mohebbi et al. [42] have also observed very homogeneous dispersion of Ni and NiO in the NiO/Ni: YSZ nanocomposites.

Ringuedé et al. [43] have used urea as fuel to synthesize homogeneous (NiO+Ni)/YSZ nanocrystalline powders in combustion technique. The symmetrical cells were prepared using these powders and electrochemical behavior of the cell was performed. The electrochemical impedance spectra consisted of polarization arcs of peak frequency 20 Hz and 39 Hz at temperatures 681°C and 761°C, respectively and are strongly dependent on temperature. It was further suggested that the improvements can be brought about by optimizing the microstructure of cermet such as lowering its thickness or sintering temperature.

Other than auto-combustion method, co-precipitation method has also been adopted by many researchers to prepare NiO: 8YSZ powders and the physical properties of cermet are discussed.

2.1.3 Co-precipitation derived Ni: 8YSZ cermet

In general, co-precipitation reaction takes place between chloride/ nitrate precursors and suitable precipitating agents at room temperature or at higher synthesis temperature. Aqueous/ methanol based solutions have been used by Marinšek et al. [44] to prepare NiO-YSZ composite powders using gel-precipitation method at different temperatures (RT, 75°C and 95°C) varying the concentration of Ni. The densities of the samples were found to increase with increase in NiO content after sintering at 1300°C, assuring good contact between YSZ particles and NiO particles, respectively. The conductivity in the samples containing more than 31 vol% of Ni shows electronic type behavior and below that concentration of Ni, the conductivity is similar to that of the pure YSZ matrix. Same group [45] has also used chlorides salts of aqueous/methanol solutions to prepare Ni-YSZ powder mixtures in gel-precipitation method. The ball milled samples are sintered at 1300°C/2h and maximum sintered densities of ~97% and ~96% were found in case of pure NiO and samples rich in NiO, respectively. In reducing atmosphere, the samples containing 42 wt% or more Ni showed an electronic conductivity of ~0.4 S/cm at 1000°C and it shows ionic type behavior at below 26 wt% Ni.

As a modification to the co-precipitation technique, Li et al. [46] have used a buffer solution of $NH_3·H_2O-NH_4HCO_3$ to prepare NiO-YSZ composite powders with varying Ni content (17, 28 and 43 wt%). For comparison purpose, NiO-YSZ powder containing 43 wt% Ni has also prepared by mechanical mixing method. After calcination at 800°C/2h, the mean particle size of all the powders was observed to be 30 nm. The samples were sintered at 1400°C/2h and reduced at 1200°C in a reducing gas mixture of CO and CO_2. The electrical conductivity was found to be 0.08,

88.94, 709.73 S/cm for the samples containing 17, 28 and 43 wt% Ni, respectively at 1000°C. On the other hand, the sample prepared by mechanical mixing method had a conductivity of 376.10 S/cm at 1000°C. The samples prepared by buffer solution showed good distribution of Ni particles in YSZ matrix as compared to that prepared by mechanical mixing method. In order to control the composition accuracy, which is an essential requirement for anode supported configuration of SOFC, Li et al. [47] have also synthesized NiO-YSZ anode powder by three different precipitating agents namely $NH_3 \cdot H_2O$, $NH_3 \cdot H_2O$-NH_4HCO_3 buffer solution and NaOH solution. The powder composition was greatly affected by the type of precipitating agents. The loss of Ni^{2+} led to low yield of NiO, when $NH_3 \cdot H_2O$ was used. By using $NH_3 \cdot H_2O$-NH_4HCO_3 buffer solution the yield increased and accurate composition was obtained while using NaOH.

Effect of NH_3, NH_3+NaOH and NaOH as precipitating agents on the crystallization mechanism, powder properties and sintering behavior of 50 wt% NiO containing NiO-YSZ anode materials have also been studied by Grgicak et al. [48] through co-precipitation method. The formation of nickel-ammonia complex resulted in low yield of NiO in the final NiO-YSZ composite. On the other hand, the use of NH_3+NaOH and NaOH yielded 80% of NiO. Nickel hydroxide [$Ni(OH)_2$] was present in crystalline form in the as synthesized powders when NH_3+NaOH was used. However, amorphous powder was obtained by using only NaOH. After calcination, the crystallite size of YSZ in both prepared powders was almost same, whereas that of NiO was doubled by use of NaOH. Homogeneous distribution of fine NiO-YSZ particles was observed in the sample prepared by NH_3+NaOH. The electrical conductivity of the samples prepared by NH_3+NaOH was found to be lower as compared to NaOH precipitated powders due to higher dispersion of YSZ. In addition to Ni-YSZ system, same group have [49] also reported the precipitation mechanism, powder morphology, sinteractivity and electrochemical performance of Cu-YSZ and Co-YSZ systems using the same precipitating agents. Lowest polarization resistance was obtained for Co-YSZ system synthesized using NaOH as precipitating agent. The characteristic of the anode precursor powder, sintering and performance was found to be strongly affected by the initial synthesis conditions.

In order to get finer microstructure with homogeneous distribution of Ni, YSZ and pore phases, Sato et al. [50] have synthesized NiO/YSZ composites, containing 50 vol% Ni, by co-precipitation method using NaOH as precipitating agent at pH 10 and 13. The NiO/YSZ layer in the electrolyte supported cell was sintered at 1300°C for 2h followed by reduction at 800°C in wet hydrogen. After sintering, fine and uniform microstructure with narrow size distribution was observed in the anode layer, prepared from the particles synthesized at pH 13. The area specific resistance was also found to be lower for these particles (0.36 Ω cm^2) as compared to that

synthesized at pH 10 (0.57 Ωcm^2). Same group has also [51] used aqueous suspension of YSZ nanoparticles (~3 nm) and nucleated non crystalline nickel carbonate hydroxides onto the surface of dispersed YSZ particles. After calcination at 600°C, the crystallite size of NiO and YSZ phases was found to be 6 and 4 nm, respectively. The anode fabricated at 1300°C consisted of fine grains in the range of 200-300 nm. The area specific resistance (ASR) of these anodes was found to be 2.29, 0.43 and 0.15 Ω cm^2 at 600, 700 and 800°C, respectively.

Homogeneous co-precipitation and hydrothermal treatment can be used simultaneously to synthesize NiO-YSZ composite powders using different precipitators such as ammonium bicarbonate (NH_4HCO_3), urea (($NH_2)_2CO$), ammonia (NH_3) and sodium hydroxide (NaOH) [52]. The yield of $Zr(OH)_4$ was 100% irrespective of the type of precipitator, whereas the yield of $Ni(OH)_2$ was above 90% and 99% for NH_3 and NaOH, respectively and was strongly dependent on the pH and concentration of the solution. Higher pH value led to finer hydroxide phases with uniform distribution, when NaOH was used as precipitator. The power density of the cell fabricated using these powders was 0.87 W/cm^2 at 750°C, which was higher as compared to that prepared using conventional method.

The interaction of anionic Zr carbonate complex with cationic Ni and Y ions was explored by Xi et al. [53], using tetramethylammonium hydrogen carbonate (TMAC)-tetramethyl ammonium hydroxide (TMAH) system, with an aim to synthesize NiO-YSZ nanocomposite particles (50 vol% Ni). The as prepared powder was amorphous in nature with yield more than 94 wt%. The powders calcined at 1000°C were crystalline with NiO and YSZ crystallite sizes of 71 nm and 36 nm, respectively. The anode fabricated, from these powders, on the electrolyte supported cell was sintered at 1350°C for 2h and reduced at 800°C under wet hydrogen containing 3 vol% H_2O. Fine grains in the range of 200 to 400 nm were observed in the Ni/YSZ anode. The ASR values obtained from the EIS spectra were found to be 0.62, 0.34 and 0.23 Ω cm^2 at 700, 750 and 800°C, respectively.

Mosch et al. [54] have studied the electrochemical activity and long term stability of the Ni-YSZ anodes synthesized by co-precipitation method using NaOH as precipitator. The performance of the cell was tested using both 8YSZ and 10Sc1CeSZ as electrolyte and LSM-YSZ as cathode. The maximum power density of these cells was found to be twice by using 10Sc1CeSZ as electrolyte as compared to that by using 8YSZ as electolyte, in the temperature range of 850 °C to 960 °C.. At 350 mA/cm^2 and 850°C, the anode polarization resistance was about 0.31 Ω cm^2 and 0.18 Ω cm^2 for the cells prepared using 8YSZ and 10Sc1CeSZ as electrolyte, respectively. The cell resistance was increased from 0.42 Ωcm^2 to 0.51 Ωcm^2 whereas the anode polarization resistance

increased from 0.2 to 0.22 Ωcm^2, after 1200 h of operation at 850° C, at a current density of 430-450 mA/cm^2 @ 0.7 V.

Mosch et al. [55] have also observed a decrease in cell polarization resistance with increase in pH_2O and varied in the range 0.35-0.40 Ωcm^2 for 10Sc1CeSZ supported cell, from the impedance spectra at 850°C. Further, no significant difference in cell resistance was noticed by comparing the impedance spectra under open circuit voltage and current load.

Haberko et al. [56] have prepared NiO: 8YSZ powders, containing 50 wt% Ni, by co-precipitation method using nickel, yttrium and zirconium nitrate solutions as precursors and ammonia solution as precipitant. The powders were calcined at 700 °C, compacted into pellets at 200 kPa, sintered at 1300 °C/3h and reduced in 5%H_2/Ar, at 800 °C for 6 h. The porosity and TEC of the cermet were found to be 50.8 % and 15.1 × 10^{-6} K^{-1}, respectively. Both Ni and YSZ are uniformly distributed and the electrical conductivity was found to show electronic behavior.

Depending on the various parameters, fine size of NiO and YSZ formed via auto-combustion and co-precipitation method modifies the microstructure of cermet and affects the properties of cermet. In order to enhance the properties of Ni: YSZ cermet specifically, electrical conductivity, various coating techniques based on the principle of heterogeneous nucleation could be utilized and are discussed as follows.

2.1.4 Coating technique derived Ni: 8YSZ cermet

Thermal hydrolysis of $ZrO(NO_3)_2 \cdot H_2O$ in a mixed solvent of 4 molar ratio of iso-PrOH/water on NiO (0.3-0.6 μm) powder was used by Moon et al. [57] to prepare ZrO_2 (15 vol%)-coated NiO powder by a new surface induced coating method. Due to heterogeneous nucleation, a 20 nm layer of amorphous zirconium hydroxide was deposited on the NiO powder. After calcination at 900°C, a porous coating of tetragonal ZrO_2, with particle size 40-60 nm was obtained. The presence of nanometer sized ZrO_2 particle on the NiO surface restrained the sintering of Ni particles after reduction in H_2 atmosphere at 900 °C/2h.

Wen et al. [58] have produced porous Ni/ZrO_2 structural forms by using electroless Ni coated fine YSZ powders and studied the effect of processing parameters on the microstructure of Ni coatings. After sensitizing and activating the YSZ powder (~60 μm), the plating was conducted in an electroless bath, at different temperatures (70-95°C) for different times (5-60 minutes). The bath temperature significantly affected the coating morphology. Spherical Ni particles with dense coating were obtained at 75°C, whereas porous coating having needle-like Ni particles was observed at 95°C.

Wang et al. [10] have synthesized NiO-YSZ powders by coating precipitation method, in which NiO powders were obtained by precipitation of 1.5M Ni(NO$_3$)$_2$·6H$_2$O using 3M NH$_3$·H$_2$O as

precipitant. These NiO powders were dispersed in a solution (1M) of $ZrOCl_2 \cdot 8H_2O$ and Y_2O_3 (9 mol %) followed by precipitation, using 3M $NH_3 \cdot H_2O$ at pH between 8.5 and 9.0, so as to obtain a Ni content of 55% in the final Ni-YSZ cermet. After calcination at 600°C and 800°C, the particle size of the NiO-YSZ powders was found to be 20 nm. The NiO-YSZ pellets were sintered at 1400°C/2h and reduced at 800°C/4h in hydrogen atmosphere. Interestingly, the conductivity of Ni-YSZ cermets showed electronic behavior with the existence of certain amount of ionic conductance, as confirmed from the non-linear behavior of temperature dependent conductivity graph, shown in Fig. 2.1. The value of conductivity reached around 900 S/cm between 600-800°C.
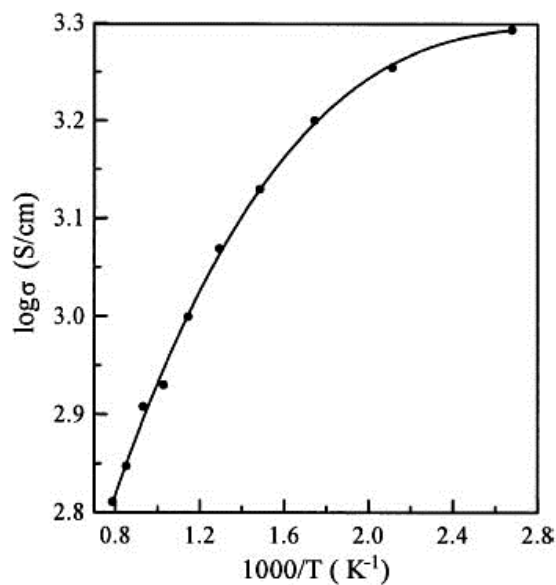
Fig.2.1: The relation between temperature and conductivity of Ni/YSZ cermet. Adapted from ref. [10]

A simpler electroless coating technique was employed by Pratihar et al. [59] to synthesize Ni coated YSZ powder, varying Ni content from 5-60 vol%. This method was optimized by different process parameters such as $PdCl_2$ concentration, YSZ concentration and deposition behavior with time. In this condition, conductivity percolation occurred at much lower Ni concentration of 20 vol% and the value was 200 S/cm, due to the continuous ring formation of Ni particles around YSZ particles. The conductivity of these anodes were compared with that prepared by solid state and liquid dispersion techniques [60]. Due to better microstructural properties, these anodes had the highest electrical conductivity, whereas the conductivity was intermediate and lowest for liquid dispersion and solid state techniques, respectively. Effect of initial YSZ particle size, matrix porosity and Ni content on the temperature dependent electrical conductivity of these Ni-YSZ cermets have also been studied by same group [61]. The conductivity increased with increase in initial YSZ particle size for a particular Ni content and porosity, whereas it decreased

with increase in porosity for a particular YSZ particle size and Ni content. Due to the lower thermal expansion coefficient and higher electrical conductivity [62] of the Ni-YSZ cermets, this method and material have been suggested for potential SOFC anode application.

Kim et al. [16] have adopted a Pechini method, by using fine and coarse YSZ powders, to obtain nano-sized NiO coated YSZ powders (40 vol% Ni) by the calcination (600°C) and milling of polymeric intermediates. The anode powders were die-pressed and sintered at 1400°C for 3h, followed by reduction at 850°C. The optimized fraction of coarse YSZ powder was found to be 0.8 in order to achieve a porosity of 40% and mechanical strength of 27 MPa for the Ni-YSZ cermets. The thermal cycling test (10 times) at 800°C revealed a very little change in anode microstructure and after 20 cycling tests, there was 10% decrease in electrical conductivity. For the fabrication of anode supported single cell, the anode substrates were pre-sintered at 1300°C for 3h, followed by coating and sintering of YSZ electrolyte and LSM-YSZ cathode at 1400°C and 1150°C for 3h, respectively. The power density of the cell was found to be 0.32 W/cm^2 and 0.56 W/cm^2 at 700 and 800°C, respectively. The polarization resistance at OCV at 800°C was found to be 0.17 Ω cm^2. The performance of these cells were compared with a commercial anode supported fuel cell [63] having similar thickness of electrolyte and cathode. The ASR value of this cell was found to be half (0.42 Ω cm^2 at 800°C) than the commercial one. The maximum power density of the cell was found to be more than twice of the commercial cell at 800°C. The performance and durability test conducted for more than 500 h under subsequent air and hydrogen interruption suggested increased system reliability.

Ni coated nano 8YSZ powders, containing 36, 41, 47 and 51 wt% Ni, were successfully prepared by Rahman   et al. [64] using sodium hypophosphite monohydrate (NaH$_2$PO$_2$·H$_2$O), sodium acetate trihydrate (C$_2$H$_3$O$_2$Na·3H$_2$O) and nickel sulphate hexahydrate (NiSO$_4$·6H$_2$O) as reducing agent, complexing agent and the source of Ni^{2+} ions, respectively. The powders calcined at 600°C in Ar atmosphere were found to contain Ni$_3$P phase, which after sintering at 1300°C/2 h converted into Ni$_3$(PO$_4$)$_2$ and caused dissociation of cubic zirconia into monoclinic zirconia. The room temperature conductivity of the porous Ni-YSZ cermets increased with Ni content. The temperature dependent electrical conductivity showed electronic behavior and the sample containing 41 wt% Ni was suggested to be used as anode material in the intermediate range.

Lin et al. [65] have followed urea hydrolysis method to synthesize YSZ powders and calcined at 800°C for 1.5 h, followed by deposition of NiO on to these powders by the same method, varying the concentration of NiO (10, 30 and 50 wt%). The resulting powders were calcined at 500-800°C for different times and the yield of NiO was found to be 56-76%. For comparison, they have also prepared NiO-YSZ powders using different YSZ (Tosoh 8YSZ)

powders. The resulting powders were compacted and sintered at 1350°C for 3 h followed by reduction at 1000°C for 3 h in 5% H_2-95% N_2 atmosphere. The density of the sintered pellets was found to be 80 % of theoretical density and was not affected by NiO content. The electrical conductivity values were measured to be 5.79×10^{-7}, 37.3 and 61.3 S/cm at 700°C for 10, 30 and 50 wt% NiO, respectively.

In electroless coating technique, the major step includes the sensitization and activation of YSZ powders, which is usually performed by mixing these powders in a solution of $PdCl_2$ and $SnCl_2$ followed by ultrasonication. Because of the limitations to handle large volume of precursors powders in a single run, Mukhopadhyay et al. [66] have replaced the ultrasonication by ball milling. The rpm and time of the ball milling process was optimized to be 45 rpm and 2000 min, respectively, for optimum Pd^0 adsorption on to the surface of the YSZ powders. These Ni coated YSZ powders were compacted at a pressure of 170MPa and sintered at 1400°C for 6 h, followed by reduction at 1000°C. The density, conductivity and microstructure of these anodes were compared with conventionally prepared anodes. Though these anodes were more porous than the conventionally prepared anodes, yet their electrical conductivity was found to be higher than the conventional ones. The conductivity was found to be 500 S/cm at 800°C at a Ni concentration of ~33 vol%, which is 40 vol% for the anodes prepared by solid state technique.

Li et al. [67] have electrolessly coated Ni on to presintered (1000°C/3 h) fibrous YSZ powders to prepare 30 wt % Ni containing Ni-YSZ nanofibres. These fibres were slurry coated onto a commercial single electrode SOFC cell having electrolyte (thickness ~130 μm) and cathode (thickness ~24 μm) and were sintered at 1300°C for 1 h. The cell performance was tested between 650°C to 800°C and was compared with another cell prepared using Ni-YSZ powder. The peak power density was found to be 40 mW/cm^2 and 20 mW/cm^2 for fibre-derived and powder-derived anode, respectively, at 800°C.

Bauri [68] synthesized Ni coated YSZ cermet anode materials by electroless coating technique, varying the amount of Ni as 5, 10, 30 and 40 vol%, without using hypophosphite. Two types of reducing agents, such as hydrazine and formaldehyde, were used in order to study their effect on the bath stability. Beyond 30 vol% of Ni concentration, the use of more amount of hydrazine caused destabilization of the electroless bath due the formation of hydrogenized Ni species and hence was replaced by formaldehyde. The as coated powder was found to contain Ni phase, in addition to YSZ, which upon oxidation at 1000°C converted into NiO. After compaction of powders, the pellets were sintered at 1300°C for 3 h and subsequently reduced at 800°C in H_2 atmosphere. The presence of Ni network around YSZ particles, along with 25% porosity, was observed in the reduced samples containing 40 vol% Ni.

2.1.5 Other synthesis method derived Ni: 8YSZ cermet

Zirconium tetrachloride, yttrium nitrate hexahydrate and nickel nitrate hexahydrate were used as precursors to prepare NiO-YSZ powders (50 and 60 wt % Ni) in sol-gel method using sucrose: pectin mixture as complexation/polymerization agents [69]. The specific surface area was found to vary from 5 m^2/g to 169 m^2/g, depending upon the composition and calcination temperature. The crystallite size of NiO and ZrO$_2$ was found to lie within 37-60 nm and 11-32 nm, respectively, whereas the mean particle size was 28-60 nm.

Haberko et al. [56] have prepared NiO: 8YSZ powders by impregnation method in which yttrium and zirconium nitrate solutions were first co-precipitated with ammonia solution. The powders were calcined at 700 °C, compacted into pellets at 200 kPa and sintered at 1300 °C/3h. Then the pellets were impregnated with nickel nitrate to obtain 30 and 48 wt % Ni and reduced in 5%H$_2$/Ar, at 800 °C for 6 h. The porosity of YSZ before impregnation was 49.2%. The TEC of the cermets were found to be 11.3 and 13.2 × 10^{-6}K^{-1} for 30 and 48 wt % Ni, respectively. The symmetrical Wagner method was used to determine the partial conductivities of Ni: 8YSZ cermets. The electrical conductivity was found to show electronic behavior with increase in temperature.

2.2 Effect of microstructural and other parameters on the electrical conductivity of Ni: 8YSZ cermet

Electrical conductivity of Ni-YSZ cermet is significantly affected by the following factors.

1. Volume fraction of Ni
2. Size, shape and distribution of Ni and YSZ particles
3. Porosity
4. Reduction temperature

2.2.1 Volume fraction of Ni

The volume fraction of Ni in Ni-YSZ cermet has a significant effect on its electrical conductivity. The percolation limit for electrical conductivity of two phase metal-insulator composites was studied by both computational as well as experimental methods. A percolation model was established considering the characteristics of metal powders such as particle diameter, aspect ratio of metal particles, relative particle penetration, angle between the average particle orientation, percolation direction and maximal angular deviation of individual particles from average particle orientation [21]. The percolation threshold increased from 21 to 38 vol% with decrease in aspect ratio from 10 to 1, whereas it decreased from 39 to 19 vol% with increase in relative particle penetration from 0.075 to 0.25. On the other hand, high threshold values were obtained for metal particles having average orientation perpendicular to the percolation direction.

Both Monte Carlo simulations based on percolation theory and experiment were conducted by Kawashima et al. [22] to study the composition dependence of the conductivity of Ni-YSZ cermet. In this case, ionic conductivity was observed up to a Ni-volume fraction of 0.32. Between Ni-volume fractions of 0.22 to 0.32, there was a sharp transition in conduction mechanism because of the conduction through the Ni phase. The effective medium percolation theory (EMPT) adopted using a resistor network model [23]. It has also predicted the composition dependence of electrical conductivity in dense and porous metal-ceramic composites. According to this model, for dense composites, ambipolar conductivity may be obtained for volume fraction of metal in between 1/3 to 2/3. The continuity of metal phase occurs when its volume fraction is greater than 1/3 and for metal volume fraction greater than 2/3, the ceramic phase becomes discontinuous. For porous metal-ceramic composites, volume fraction of metal needed to form a continuous phase increases to about 2/3 with increase in porosity, as pores interrupt the continuity of metal phase. The range of metal content in which ambipolar conductivity occurs also narrows down with increase in porosity. Finally it was suggested that the porosity should be kept within 30% for optimized transport of both ionic and electronic species. Monte Carlo simulations performed using three dimensional resistor network approach [24] predicted a sharp transition from low to high conductivity at approximately 30 vol% Ni. The prediction is valid for cubic lattices randomly occupied by electrode or electrolyte particles and for random packings with uniform particle radii. The Ni concentration dependent electrical conductivity follows an S-shaped curve as shown in Fig. 2.2 [70].
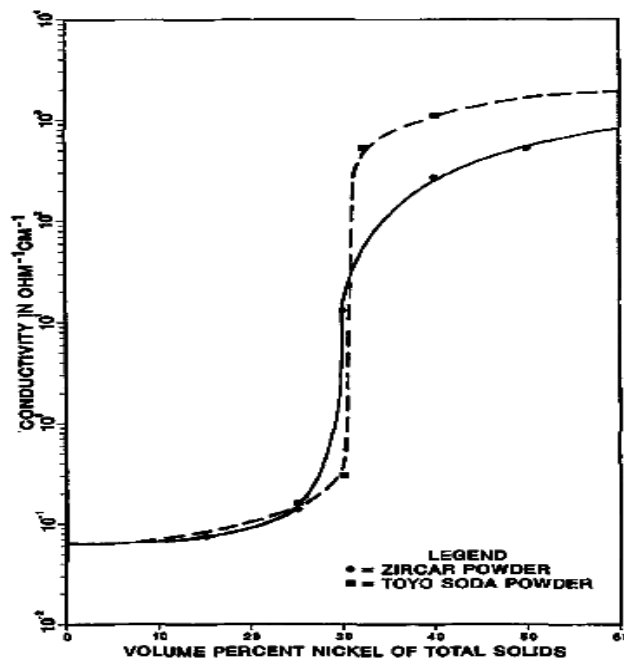
Fig. 2.2: Conductivity of cermets at 1000 °C vs. vol% Ni of total solids fabricated with Toyo Soda and Zircar zirconia powders. Adapted from ref. [70].

The electrical conductivity of NiO: YSZ composites were also studied as a function of NiO content [71, 72]. The variation of grain and grain boundary conductivity with temperature and composition was found to depend upon microstructure and activation energy. The NiO: YSZ composites having NiO concentration below 40 mol% was found to show ionic behavior whereas that above 80 mol% of NiO showed electronic behavior. Mixed ionic and electronic conductivity was observed in between 40 – 80 mol% of NiO concentration as shown in Fig.2.3.
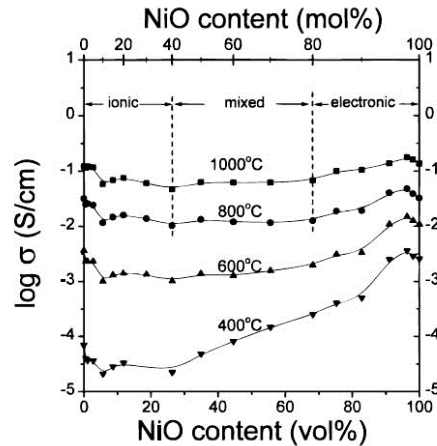
Fig. 2.3: Total electrical conductivity of the YSZ-NiO composites measured by the four-probe method as a function of NiO concentration. The ionic, mixed, and electronic region are indicated as determined from the transference number measurement. Adapted from ref. [72].

2.2.2 Size, shape and distribution of Ni and YSZ particles

The percolation behavior and hence the conductivity of a metal containing biphasic composite material depends up on the size and shape of the metal particles [73]. As the size of the metal particle increases, there is a tendency for it to be percolated at a higher concentration [74]. In case of Ni: 8YSZ, it has been observed that finer metal particles have a greater tendency to be percolated at lower Ni concentration [75]. Higher electrical conductivity in Ni: 8YSZ can be obtained by using finer initial NiO powders. The electrical conductivity can be as high as 657 S/cm, 702 S/cm and 3990 S/cm for NiO particles having initial particle size 0.8, 0.5 and 0.6 μm, respectively [26]. The electrical conductivity Ni: 8YSZ was found to be above 1000 S/cm by using starting NiO particles of size 0.839 μm-0.878 μm, whether fine (0.762 μm) or coarse (7.798 μm) YSZ particles are used [15] as shown in Fig. 4. By using a combination of both fine and coarse YSZ powders in Ni: 8YSZ cermet, the conductivity value can also be enhanced [76-78]. Keeping the concentration of YSZ fixed at 60 vol%, the electrical conductivity was found to be greatly improved with increase in coarse YSZ content, as shown in Fig. 5. Using 45 wt % of NiO, the electrical conductivity of 430 S/cm was observed, at 800 – 1000 °C, when the particle size of NiO and YSZ varied from 0.4 – 0.7 μm [79]. Further, the electrical conductivity was also found to

increase with increase in size ratio of YSZ to NiO, i.e. d_{YSZ}/d_{NiO} [80]. The gradual degradation of electrical conductivity in Ni: 8YSZ is also attributed to the growth and agglomeration of Ni particles at higher operating temperatures and redox cycling [4, 81, 82]. Recently, Davarpanah et al. [83] have also studied the effect of Ni particle size on the electrical conductivity of 30 vol% Ni containing Ni: 8YSZ cermets. For Ni particles of size 0.35 – 0.55 μm, the conductivity was found to be ~467 S/cm and ~398 S/cm at 800 °C and 1000 °C, respectively. The conductivity decreased to ~275 S/cm and ~ 240 S/cm at 800 °C and 1000 °C, respectively, when the Ni: 8YSZ cermet contained small (≤0.6 μm) and large agglomerated (1.1 – 1.4 μm) Ni particles.

.
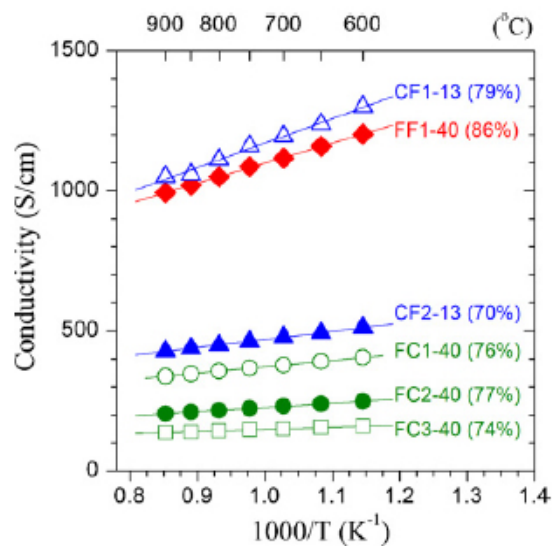
Fig. 2.4: Electrical conductivity of Ni–YSZ cermets as a function of temperature. Their relative sintered densities of NiO–YSZ composites are also presented in the brackets. Adapted from ref.[15].
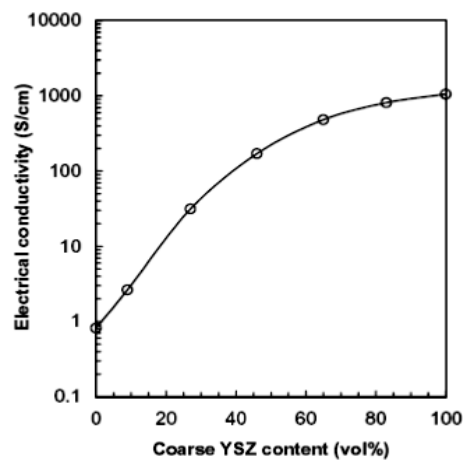
Fig. 2.5: Electrical conductivity measured at 1000 °C of Ni/YSZ cermet containing both coarse and fine YSZ particles as a function of coarse YSZ content of total YSZ. Adapted from ref.[76].

The shape of the metal particle also plays a vital role in determining the percolation behavior and conductivity. It has been observed that as the metal particle aspect ratio increases (>1), the percolation threshold decreases [21]. Theoretically, 33 vol% of metal content is required to attain percolation. But it may also go up to 38 vol%, as the aspect ratio approaches unity.

The uniform distribution of Ni particles in YSZ matrix is also an essential requirement to achieve better electrical properties along with stability of the Ni: 8YSZ anode. These factors can be carefully controlled by different preparation techniques, either by monitoring the particle size distribution of Ni and YSZ [84] or sintering temperature [85]. Two-step sintering process was also found to be suitable for manipulation of porosity and conductivity of Ni: 8YSZ cermets. Electrical conductivity in the range of 170 – 420 S/cm was observed for cermets having 26 – 35 % porosity, at 600 – 900 °C [83].

2.2.3 Porosity

The porosity and pore size are also accountable factors for determining the electrical conductivity of the Ni: 8YSZ cermets [77, 86, 87], which in turn depend upon the sintering temperature. With increase in porosity, the electrical conductivity was found to decrease. The porosity and pore structure can be modified by adding different types of pore formers [88].For example, by adding 5 wt% of starch as pore former, the conductivity in Ni: 8YSZ cermet was found to be 1380 – 1710 S/cm, whereas 1 wt % of starch addition gives rise to a conductivity of 1850 – 2200 S/cm [89]. The incorporation of carbon microspheres of different sizes (0.27 – 11.5 μm) and varying amounts (1 – 15 wt %) was also found to have profound impact on the pore shape and size distribution of pores [90]. The electrical conductivity was found to be 352 – 480 S/cm, 302 – 511 S/cm and 253 – 453 S/cm for porosity in the range of 33 – 37 %, 32 – 40 % and 31 – 39 %, respectively, using different size and amount of carbon microspheres. Using the phase inversion technique and sintering, finger and sponge like pores were produced in NiO: YSZ hollow fibres [91]. The effect of sintering temperature on the electrical conductivity of the Ni: YSZ anode substrates was also studied. The electrical conductivity was found to increase with increase in sintering temperature from 1250 °C to 1400 °C and the room temperature conductivity was 1.25 – 2.25×10^3 S/cm at a sintering temperature of 1400 °C, for 47.2 wt % Ni content. Using the same phase-in-version sintering technique and varying the amount of ethanol, the porosity of the Ni: YSZ hollow fibres was controlled between 28 – 67 % and the corresponding shrinkage, mechanical strength and electrical conductivity was also studied [92]. The conductivity was found to vary in between ~1200 – ~700 S/cm, from 600 – 800 °C, depending on the ethanol concentration. The electrical conductivity of Ni: YSZ anode, containing 50 vol% Ni, was found to be ~ 4 S/cm and ~800 S/cm for sintering temperature of 1400 ° and 1500 °C, respectively, measured at 1000 °C

[93]. The porosity of NiO: YSZ can also be tailored by using precalcined YSZ powders. The resistivity of Ni: YSZ has been observed to increase with increase in pre-calcination temperature of YSZ powders from 900 - 1200 °C, due to the formation of more pores [94]. The conductivity of a porous Ni: YSZ cermet containing 50 vol% of Ni, coated on YSZ, was found to be ~254 S/cm as compared to dense YSZ cermet having same Ni content [95]. Pore anisotropy also plays an important role in determining the electrical conductivity of Ni: YSZ cermet. Lee et al. [29] have studied the electrical conductivity of Ni: YSZ cermet prepared by two different techniques such as spray drying method (SDM) and liquid condensation process (LCP). Electrical conductivity was found to be higher and varied from 1900-1400 S/cm for LCP technique, in between 600 – 1000 °C, due to isotropic distribution of pores. On the other hand, due to pore anisotropy, the conductivity was found to be ~100 S/cm in a direction parallel to the current flow and varied from 600 – 500 S/cm in a direction perpendicular to the direction of current flow, in between 600 – 1000 °C.

2.2.4 Reduction temperature of the Ni: 8YSZ cermet

The electrical conductivity is also affected by the initial reduction temperature [96]. Grahl - Madsen et al. [97] have obtained an electrical conductivity of 1000 S/cm, in 40 vol% Ni containing Ni: YSZ cermets, at a reduction temperature of 1000 °C. The conductivity decreased by 6 times when the samples were reduced at 650 °C. But the observation was opposite in case of Pihlatie et al. [98]. After initial reduction at 600 °C, the Ni: YSZ cermets containing 50 – 55 wt % of NiO showed a stable conductivity of ~1100 S/cm [98]. The conductivity was increased to ~ 2000 S/cm after reoxidation and following reduction at the same temperature. However, the cermets reduced at 850 °C possessed initial conductivity loss. But after reoxidation and subsequent reduction at the same temperature, the conductivity and loss remained the same.

2. 3. Electrochemical performance of the cell

2.3.1 Effect of composition of Ni-YSZ anode

The polarization behavior of the Ni: YSZ cermet anode material depends on several factors including its preparation conditions, characteristic of starting powders, volume percent of Ni, microstructural parameters such as grain size, distribution of grains, porosity and pore size. Adequate contact between nickel particles is required in order to decrease the polarization resistance. This was found to depend upon nickel content, pre-calcination temperature and baking temperature [99, 100]. It was observed that below 30 vol% Ni, the exchange current density decreases and the electrode polarization increases. The ohmic resistance was found to decrease drastically, when more than 40 vol% of Ni was used, as confirmed from Fig. 2.6.
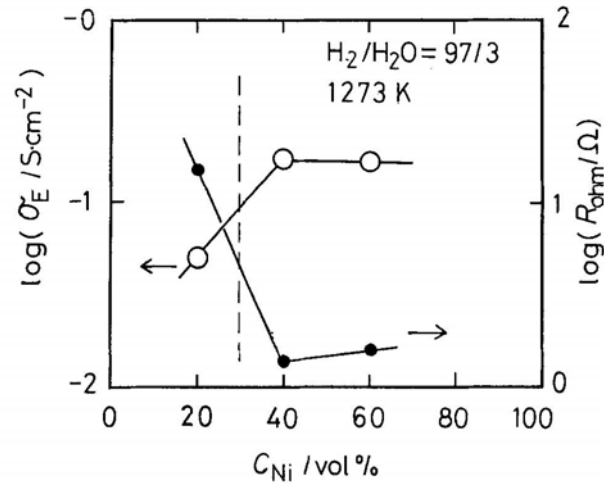
Fig. 2.6: Effect of Ni content on electrode/electrolyte interface conductivity (σ_E) and on ohmic resistance (R_{ohm}) between the working and the reference electrodes at 1273 K. Electrodes were prepared using the same NiO and YSZ powders and treated at the same temperature: Precalcination temperature (T_{pc}) = 1673 K, Sintering/baking temperature ($T_{b)}$) = 1773 K. Adapted from ref. [100].

Jiang et al. have observed a decrease in anode interfacial resistance and overpotential with decrease in Ni content [101]. The anode overpotential was found to decrease from ~75 mV to ~28 mV, at 250 mA/cm^2, when the Ni content is decreased from 70 vol% to 40 vol%. Similarly, the anode interfacial resistance was also decreased from 0.43 Ωcm^2 to 0.18 Ωcm^2 for the same decrease in Ni content. This was attributed to the better coverage of Ni particles byYSZ particles and decrease in anode porosity at 40 vol% Ni content as compared to 70 vol% Ni.

Koide et al. [102] have also studied the effect of anode composition on the IR resistance, overpotential and cell performance. The IR resistance was found to decrease with increase in Ni concentration from 40 to 87 vol%. The power output increased from 1.10 W to 1.97 W with increase in Ni content from 31 to 87 vol%. However, the polarization resistance decreased from 340 mΩcm^2 to 235 mΩcm^2, when the Ni concentration is decreased from 87 to 40 vol%. This was attributed to the enhancement of triple phase boundary which can be modified by different fabrication techniques [103].

In a similar study, the anode overpotentials were found to be 220 mV and 200 mV for 40 and 45 vol% Ni containing anodes, respectively, at 1000 mA/cm^2. When the Ni concentration was increased to 50 and 55 vol%, the over potentials increased to 280 mV and 370 mV, respectively [93].

In order to enhance the performance of cells, the impact of double layer anode has also been studied by Koide et al. [102]. The double layer consisted of a 40 μm thick cermet containing 61 vol% Ni, coated on to the electrolyte and another layer (thickness 160 μm), containing 40 vol% Ni,

was coated on it. This cell exhibited highest power output of 2.10 W, IR resistance comparable to 87 vol% Ni containing anode and polarization resistance comparable to 40 vol% Ni containing anode. This configuration was also studied by other authors [104, 105]. Kong et al. [106] have also studied the effect of thickness, composition and particle size of anode functional layer on the power density of single cell using Ni: YSZ as anode and platinum (Pt) as cathode. The anode substrate, anode functional layer I (AFL I) and anode functional layer II (AFL II) consisted of 70, 50 and 60 wt % of NiO, respectively. Maximum power density of 374.77 mW/cm^2 was obtained for 20 μm thick anode functional layers. By manipulating the particle size of NiO and YSZ, the power density was increased to 467.14 mW/cm^2. Similarly, the use cathode functional layer was also found to increase the electrical performance of SOFC [107].

Recently, Xi et al. [108] have obtained lower polarization resistance of 0.18 Ωcm^2 using 40 vol% Ni, at 800 °C, as compared to 0.34 Ωcm^2 and 0.23 Ωcm^2 using 30 vol% and 50 vol% Ni, respectively.

2.3.2 Effect of pre-calcination

Kawada et al. have studied the effect of pre-calcination temperature on the polarization resistance of Ni: YSZ anode [99, 100]. The powders without pre-calcination resulted in low current density and high over voltage was observed, when the baking temperature is less than the pre-calcination temperature. With increase in pre-calcination temperature from 1200 °C to 1400 °C, the polarization resistance decreased from ~0.6 Ωcm^2 to ~0.3 Ωcm^2.

The influence of pre-calcination temperature on the anode overpotential was investigated by Huebner et al. [93]. Pre-calcined (1400 °C) NiO and YSZ powder, containing 50 vol% Ni, deposited on to the YSZ electrolyte showed more stable and lower over potential of 240 mV as compared to 380 mV for conventionally prepared powder, at 1000 mA/cm^2, after 24 h of operation. This was attributed to the more rigid structure of YSZ formed by higher temperature calcination of NiO and YSZ.

Effect of coarsening temperature on the anode overpotential was studied by Jiang et al. [101] in which NiO powders were coarsened at 900 °C and 1000 °C. It was observed that the particles in the smaller size (1 μm) range exhibited lower anode overpotential by coarsening at lower temperature (900 °C) whereas the particles in the larger size range (5 μm and 10 μm) require higher coarsening temperature (1000 °C) for better performance.

The effect of precalcination temperature on the overpotential of 50 vol% Ni containing Ni-SDC anodes was also studied by Chen et al. [109]. The lowest polarization resistance of 0.11 Ωcm^2 was obtained, when the powders were precalcined at 1000 °C as compared to other temperatures.

2.3.3 Effect of sintering/reduction temperature

Kawada et al. [100] have studied the effect of sintering temperature on the polarization resistance of Ni: YSZ anodes. Keeping the pre-calcination temperature constant at 1400 °C, the polarization resistance decreased from 12.5 Ωcm^2 to 0.3 Ωcm^2 as the sintering temperature is increased from 1200 °C to 1500 °C At high frequencies; the effect of grain boundary resistance was confirmed.

It was also observed that after 24 h of operation the pre-calcined (1400 °C) powders, containing 50 vol% Ni, showed overpotential of ~400 mV at 400 mA/cm^2, when sintered at 1300 °C. On the other hand, the same powders exhibited overpotentials of 240 mV and 220 mV, at 1000 mA/cm^2, when sintered at 1400 °C and 1500 °C, respectively. Jiang et al. [101] have also observed increase in anode performance with increase in firing temperature. However, the increase in anode performance with decrease in sintering temperature was also reported by some authors [110, 111], may be due to the properties of starting powders.

The effect of sintering temperature on the electrochemical performance of symmetrical cells prepared using Ni: YSZ anode (53 wt % NiO) was studied by Primdahl et al. [112]. Lower polarization resistance of 0.09 Ωcm^2 was observed at sintering temperatures of 1300 °C and 1400 °C, as compared to 1100 °C, 1200 °C and 1500 °C (see Fig. 6).
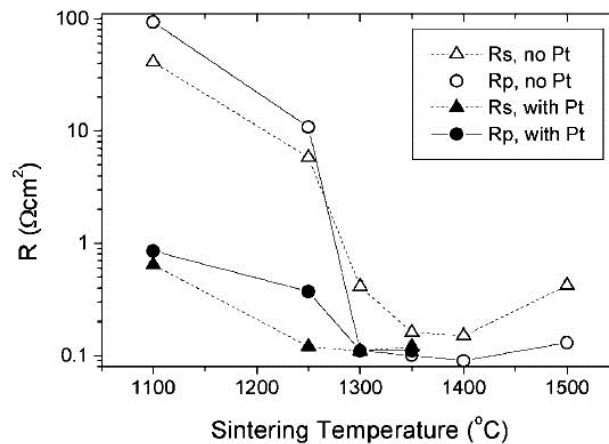
Fig. 2.7: Area-specific series resistance, RS, with (▲) and without (Δ) a platinum current collector, and polarization resistance, RP, with (●) and without (○) a platinum current collector, as functions of sintering temperature (all cells measured by impedance spectroscopy, in 97% H_2 + 3% H_2O with no polarization at 1000°C). Adapted from ref. [112].

The reduction temperature was also found to affect the electrochemical performance of SOFC. Li et al. [113] have studied the effect of three different reduction temperatures such as 550 °C, 650 °C and 750 °C on the performance of a Ni: 8YSZ anode supported single cell. The area specific resistance and polarization resistance were found to be lowest, 0.5 Ωcm^2 and 0.72 Ωcm^2,

respectively, at a reduction temperature of 650 °C, measured at 850 °C. At the same condition, the power density was also found to be maximum (0.56 W/cm^2).

2.3.4 Effect of particle size of starting powders

The polarization resistance of anode is a strong function of particle size of Ni and the ratio of YSZ to Ni particle, d_{YSZ}/d_{Ni}. van Berkel et al. have studied the effect of YSZ to Ni particle size on the electrolyte resistance and anode loss [114]. With increase in d_{YSZ}/d_{Ni} from 0.4 to 8.7, the electrolyte resistance was found to decrease from 0.662 Ω to 0.1233 Ω. Similarly, the anode loss also decreased from 570 mV to 240 mV, at 100 mA/cm^2 and 920 °C.

In order to study the effect of initial NiO particle size on the anode overpotential, Huebner et al. [93] have taken NiO powders synthesized by glycine-nitrate process (calcined at 900 °C), a commercial NiO powders of size < 45 μm in 325 mesh and spray dried powder of size < 10 μm. After 24 hr of operation, the glycine-nitrate powder, 325 mesh powder and spray dried powder, containing 45 vol% of Ni, showed overpotential of ~250 mV, ~370 mV and ~450 mV, respectively, at 600 mA/cm^2. The lower overpotential of glycine-nitrate synthesized powders was attributed to the lower particle size, which resulted in enhancement of reaction sites.

Three different NiO powders having particle sizes 1 μm (NiO-1), 5 μm (NiO-2) and 10 μm (NiO-3) were selected for investigating the effect on the anode overpotential, ohmic and electrode interfacial resistance of 70 vol % Ni containing Ni: YSZ cermet as shown in Fig. 6[101]. The anode over potential was found to be the lowest for NiO-1, due to its finer size as compared to NiO-2 and NiO-3. Similarly, the anode overpotential was also found to be lower for finer YSZ particles.
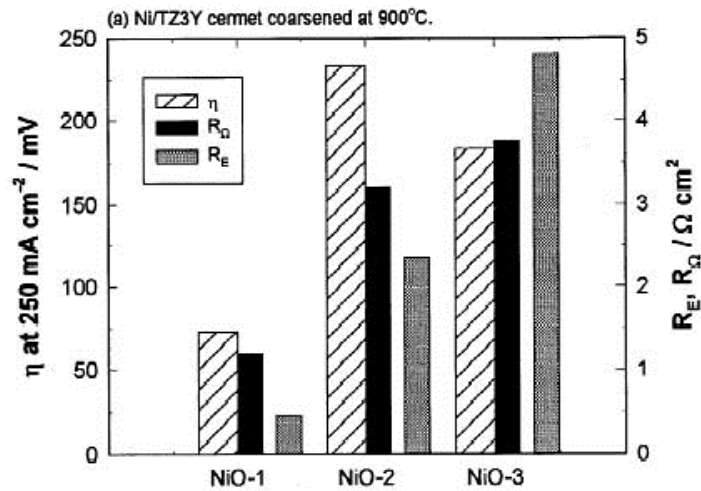
Fig. 2.8: A comparison of electrode performance of Ni (70 vol%) / TZ3Y (30 vol%) cermet anodes (10008C) prepared from various commercial NiO powders. Anodes were prepared from Ni/TZ3Y cermet powders coarsened at 900 °C. Adapted from ref. [101]

2.3.5 Effect of current/voltage

The decrease in anode resistance has been observed during the passage of anodic current through anode. Substantial decrease in anode resistance from 2.4 to 0.1 Ω was found, while the anode current was increased from 0 to 567 mA [111]. With increase in anode overpotential, significant decrease in anode interfacial resistance was also investigated [115, 116] .

2.3.6 Effect of atmosphere

The influence of dry and moist hydrogen on the polarization resistance of Ni: YSZ was studied by Jiang et al. [116]. As compared to dry hydrogen, both the high and low frequency contribution to the polarization resistance decreased by using moist (98 % H_2 + 2% H_2O). Keeping the concentration of H_2O constant, a decrease in H_2 concentration resulted in an increase in partial pressure of oxygen (P_{O2}). By decreasing the H_2 concentration, the size of the low frequency arc increased and the size of the high frequency arc decreased. The high frequency arc corresponds to the charge transfer resistance and the low frequency arc is characterized by the adsorption or diffusion of H_2 on the Ni surface.

Primdahl et al. [115] have observed three arcs in the impedance spectra corresponding to the high (1 – 50 kHz), mid (10 Hz – 1 kHz) and low frequency (0.1 – 10 Hz) regions. The high frequency contribution was found to be insensitive to the atmospheric composition. The polarization resistance corresponding to high frequency arc was related to the microstructure of the cermet. On the other hand, the mid and low frequency arcs were found to be most sensitive to the partial pressures of H_2 and H_2O.

Either by changing the partial pressure of H_2 at constant water partial pressure or by replacing pure H_2 by 80 % Ar, the anode polarization does not change significantly [103, 117, 118].

2.3.7 Effect of pores

Porosity, pore size and pore morphology also influence the transport of gaseous species through the electrodes and thus resulting in concentration polarization [119]. Zhao et al. [120] have studied the effect of porosity of Ni: YSZ anode support, containing 70 wt% NiO, on the electrochemical performance of a single cell. The porosity of the anode support was varied from 32 to 76 % by adding requisite amount of carbon. The maximum power density of a cell with anode support porosity of 32%, 57% and 76% was found to be ~0.72 W/cm^2, ~1.55 W/cm^2 and ~1.5 W/cm^2, respectively. The lower open circuit voltage and leakage through the electrolyte were supposed to be the main reason of lower performance of 76 % porous anode supported cell, despite higher porosity. The area specific resistance (ASR) was also found to decrease from 0.156 Ωcm^2 to 0.074 Ωcm^2 with increase in porosity from 32 % to 76 %.

Suzuki et al. [121] have fabricated micro-tubular SOFC by using NiO-Sc-stabilized zirconia (ScSZ) and Ce-doped zirconia (10Sc1CeSZ) as anode, 10Sc1CeSZ as electrolyte and (La, Sr)(Fe, Co)O_3 (LSCF)-Gd-doped ceria (GDC) as cathode. After co-sintering with the electrolyte at 1250 °C, 1300 °C and 1400 °C, the porosities of the anodes in three cells were 54 %, 47 % and 37 %, respectively. For cell having 54 % anode porosity, the maximum power densities of 1.1 and 0.5 W/cm^2 were obtained at 600 °C and 550 °C, respectively. At 600 °C, the maximum power densities were decreased to 0.36 and 0.2 W/cm^2 for anode porosities of 47 % and 37 %, respectively. Though the ohmic resistance was same (~0.1 Ωcm^2) for all cells, the size of the semicircles increased with decrease in porosity indicating increase in polarization resistance with decrease in porosity.

An et al. [122] have studied the effect of porosity gradient in Ni: YSZ anode on the performance of porous anode supported SOFC. The porosity of the anode support layer was 35 %. Four different cells having non active layer (only support layer), one active layer (20 % porosity), two active layers (20 and 24 % porosity) and three active layers (20, 24 and 36 % porosity) were tested. The maximum power density was found to be 76 (for non-active layer), 86 (for 1-active layer), 97 (for 2-active layers) and 101 mW/cm^2, at 600 °C. The polarization resistances were also found to be 1.92, 1.86, 1.8 and 1.2 Ωcm^2 for non-, 1-, 2-, 3- active layer systems, respectively, at 600 °C.

2.4 Summary of literature

From the above literature survey, the following points can be summarized.

- The electrical conductivity and electrochemical performance of Ni: 8YSZ anode depends solely on the concentration of Ni in the cermet and microstructural parameters such as porosity, size and distribution of Ni particles in 8YSZ matrix.

- The pretreatment of the starting powders, addition of pore formers as well as sintering temperature have a profound effect on these factors.

- The properties of the starting NiO: YSZ powders can be controlled by using different synthesis methods.

- In combustion method, the pH and ratio of oxidizer to fuel can have a significant effect on the properties of starting NiO: YSZ powders.

- In precipitation method, the type of precipitant and pH plays an important role in controlling the composition and microstructure of NiO: YSZ powders.

- The starting materials, synthesized by different methods, may contain different forms of Ni such as NiO, Ni(OH)$_2$ or Ni.

- There is hardly any study, which describe the microstructure of Ni: 8YSZ cermet, based on the different forms of Ni.

- The effect of oxidizer to fuel ratio, in auto-combustion method, on the starting NiO: YSZ powders and on the properties of Ni: YSZ cermet has not been studied in detail.
- Detailed study on the effect of fabrication parameters such as binder concentration and compaction pressure on the density/porosity, microstructure of NiO/Ni: YSZ composites has not been reported.
- The characteristic of NiO: YSZ powders and hence NiO/Ni: YSZ composites, based on the order of addition of precipitants in precipitation method, have not been investigated.

So it will be interesting to evaluate the microstructural and electrical properties of the Ni: 8YSZ cermet, based on the different forms of Ni, in the as-synthesized powder. The effect of fuel to oxidizer ratio in auto-combustion method and the order of addition of precipitants in precipitation method on the various properties of NiO/Ni: YSZ composites may also be studied. Further an investigation on the effect of binder concentration and compaction pressure may also give some insight on the density/porosity, microstructure and electrical properties of NiO/Ni: YSZ composites.

2.5 Statement of the problem

Generally, Ni: 8YSZ cermet anode material with more than 30 vol % Ni concentration is mostly investigated for SOFC application due to its better mechanical integrity, chemical stability under reducing atmosphere, suitable electrical and electrochemical properties at higher temperature (800-1000°C) [1, 2]. The grain growth of Ni becomes more prominent at higher Ni concentration as well as higher operating temperature, which degrades the electrical conductivity and overall cell performance [4]. Hence, the reduction of operating temperature to IT range as well as Ni concentration and its distribution are the essential requirements for better anode performance [10-12, 16, 61, 123, 124]. It is possible to achieve better electrical conductivity at lower Ni concentration, comparable TEC and cell performance of Ni: 8YSZ anode by modifying the microstructural parameters such as size and distribution of NiO/Ni particles as well as porosity [29, 63, 125, 126]. It is important to focus on the following major points for tailoring the microstructure of Ni: 8YSZ anode.

2.5.1   Activation polarization

The minimization of operating temperature has put some barriers, the most significant being the increase in electrode over potential, which needs to be surmounted. In this perspective, the anode of the SOFC, which frequently undergoes reduction and oxidation during the operation, requires special attention. The electrochemical oxidation of fuel takes place at the electrode, electrolyte and gas triple phase boundary (TPB) and enhancement of TPB will be advantageous for reducing the operating temperature of SOFC. By comparing Fig. 2.1 (a) and (b), it is well understood that smaller size particles of Ni enhance the density of TPB. So, fine grain size of NiO/Ni and 8YSZ may enhance the TPB and decrease its activation polarization.
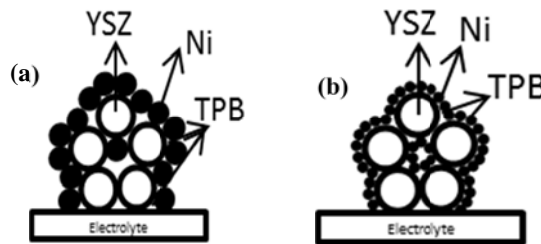
Fig. 2.9: Effect of finer NiO/Ni particles on TPB

2.5.2   Concentration of Ni in anode

Concentration of Ni plays a major role in controlling TEC and electrical conductivity of the Ni: 8YSZ cermet. The TEC of Ni: 8YSZ should be compatible with that of the other adjoining components, specifically 8YSZ electrolyte. Higher concentration of Ni increases TEC, resulting in thermal mismatch between the cell components and hence degrades the mechanical stability.

Further, lower concentration of Ni may not be suitable for providing better connectivity between the Ni particles and hence may decrease the electrical conductivity. In order to find out the relation between volume fraction of Ni and size (radius) of Ni particles, a simple theoretical calculation was done assuming uniform distribution of spherical Ni particles around the spherical YSZ particles for a particular porosity.

Let 'R' and 'r' be the radius of YSZ and Ni particles, respectively. The volume fraction of Ni in cermet is given by $[V_{Ni} / (V_{Ni} + V_{YSZ})]$, where V_{Ni} is the volume of Ni particles and V_{YSZ} is the volume of YSZ particles. Based on this formula, the volume fraction of Ni is calculated and found to be $[1-(R/r)^3]$. As 'r' decreases, the volume fraction of Ni decreases. Thus, smaller size of NiO/Ni reduces the volume fraction of Ni in NiO/Ni: 8YSZ cermet and the concentration of Ni can be minimized by tailoring the microstructure of cermet.

2.5.3 Porosity in the Ni:8YSZ cermet

The porosity of the Ni-YSZ is yet another important factor which is responsible for the concentration polarization. The presence of open pores (around 30 to 40 vol %) in the cermet conveys the fuel gas to the TPB. The porosity in Ni-YSZ is generally formed by the reduction of NiO to Ni. Hence, the shape and size of pores depend upon the shape and size of NiO grains, which if appropriately designed may help in reducing the concentration polarization.

2.5.4 Electrical conductivity

The electrical conductivity of the Ni: 8YSZ cermet is significantly affected by volume fraction of Ni, size and distribution of Ni as well as porosity. These factors can be controlled by developing a suitable microstructure by optimizing the fabrication parameters such as binder concentration, compaction pressure and sintering temperature of NiO: 8YSZ pellets.

2.6 Objectives

From above factors, it may be concluded that the size and distribution of Ni in Ni: 8YSZ cermet is very much important from anode properties point of view and the particle size of Ni should be as small as possible. Particle size of Ni in anode directly depends on the particle size of NiO in NiO: 8YSZ composites. Again, the size and distribution of NiO in NiO: 8YSZ composites is strongly dependent on the initial size and forms of Ni such as NiO, $Ni(OH)_2$ and Ni, which may evolve during solution-based syntheses.

From literature review, it was confirmed that NiO and $Ni(OH)_2$ may form in auto-combustion and co-precipitation method, respectively, by optimizing different synthesis parameters. However, Ni may form if the precipitation method is carried out within 70 °C to 95 °C,

using suitable precipitating agents. In auto-combustion process, the initial size of NiO and YSZ may vary depending on the oxidizer to fuel ratio. Similarly, different ways of synthesis such as direct strike / reverse strike / constant pH method in precipitation may alter the size of NiO and YSZ. Variation of synthesis conditions in different solution-based syntheses may develop different size and distribution of NiO in NiO: 8YSZ composites, which may result in different types of microstructure of Ni: 8YSZ cermet. In this Ph.D. work, three different solution-based syntheses such as auto-combustion, co-precipitation and heterogeneous precipitation were adopted on the basis of different forms of Ni, as stated above, to tailor the microstructure of Ni: 8YSZ anode.

So, the main objective of this research work is to tailor Ni: 8YSZ cermet with fine Ni particles in 8YSZ matrix via different solution-based syntheses, in order to achieve adequate electrical conductivity, compatible TEC and overall cell performance for IT-SOFC anode application.

Chapter 3

EXPERIMENTAL WORK

Nanopowders of NiO: 8YSZ have been prepared using different ways of solution-based syntheses such as auto-combustion, co-precipitation and heterogeneous precipitation. Ni: 8YSZ cermets have been fabricated using these NiO: 8YSZ powders and different characterization techniques have been used to study the properties of these materials. In this chapter, the synthesis and characterization techniques are described in detail.

3.1 Introduction

Three different solution-based syntheses such as auto-combustion, co-precipitation and heterogeneous precipitation were adopted to synthesize NiO: 8YSZ powders. 20, 30 and 40 vol % Ni containing Ni: 8YSZ cermet was fabricated using different solution-based synthesized NiO: 8YSZ powders. The estimation of the stock solution, powder synthesis methods and characterization techniques are discussed in this chapter.

3.2: Raw Materials

Raw materials (purity 99.5%) used in this research work are nickel chloride hexahydrate ($NiCl_2 \cdot 6H_2O$) (Lobachemie, India) / nickel nitrate hexahydrate ($Ni(NO_3)_2 \cdot 6H_2O$) (Lobachemie, India), zirconium oxychloride octahydrate ($ZrOCl_2 \cdot 8H_2O$) (Lobachemie, India) / zirconium oxynitrate monohydrate ($ZrO(NO_3)_2 \cdot H_2O$) (Lobachemie, India) and yttrium oxide (Y_2O_3) (Lobachemie, India) [Y_2O_3 was dissolved in HCl / HNO_3 with required amount of distilled water].

3.3 Estimation of the stock solutions

Separate stock solutions of individual precursors such as $NiCl_2 \cdot 6H_2O / Ni(NO_3)_2 \cdot 6H_2O$, $ZrOCl_2 \cdot 8H_2O / ZrO(NO_3)_2 \cdot H_2O$, having 0.75 M concentration, were prepared by dissolving them in distilled water. The quantitative estimation of these precursor solutions was necessary, before proceeding with the powder preparation. The estimation of the above precursors was carried out by taking 5 ml of each of the stock solution separately in 250 ml beakers. To precipitates Ni-salts, 2M sodium hydroxide (NaOH) was used, whereas, 20 vol% hydrazine hydrate (N_2H_5OH) (denoted as HH) was used to precipitates Zr-salts. The final pH of the precipitates was 13 and 10 for $NiCl_2 \cdot 6H_2O / Ni(NO_3)_2 \cdot 6H_2O$ and $ZrOCl_2 \cdot 8H_2O / ZrO(NO_3)_2 \cdot H_2O$, respectively. The possible reactions that took place can be summarized as follows [49].

$$NiCl_2 \cdot 6H_2O + 2NaOH \rightarrow Ni(OH)_2 + 2NaCl + 6H_2O$$

$$Ni(NO_3)_2 \cdot 6H_2O + 2NaOH \rightarrow Ni(OH)_2 + 2NaNO_3 + 6H_2O$$

$$ZrOCl_2 \cdot 8H_2O + 2N_2H_5OH \rightarrow ZrO(OH)_2 + 2NH_4Cl + N_2 + H_2 + 8H_2O$$

$$ZrO(NO_3)_2 \cdot H_2O + 2N_2H_5OH \rightarrow ZrO(OH)_2 + 2NH_4NO_3 + N_2 + H_2 + H_2O$$

$$ZrO(OH)_2 + 2N_2H_5OH \rightarrow Zr(OH)_4 + 2N_2 + 4H_2 + H_2O$$
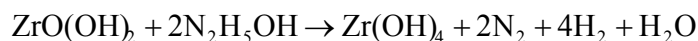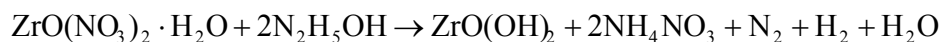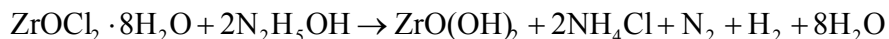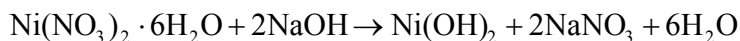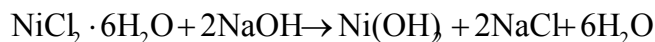
The precipitates obtained in each case were transferred into funnels fitted with Whatman (40/42) filter papers, after removing the supernatant. Then the precipitates were washed several times with warm water to remove chlorides / nitrates / other inorganic substances until pH becomes ~7. After washing, the precipitates were dried overnight along with the filter paper at 100 °C in an oven. The filter paper containing the dried precipitates were transferred to pre-weighed platinum crucibles and fired at 1000 °C for 1 h. The difference between the weights of the crucibles before

and after firing is equal to the weight of the calcined precipitates, which corresponds to the weight of the oxides (hydroxides of Ni / Zr converted to oxides of Ni/ Zr during calcination) per 5 ml of stock solution.

3.4 Powder synthesis

3.4.1 Auto-combustion

Three different conditions such as fuel lean, fuel stoichiometric and fuel rich were followed to synthesize NiO: 8YSZ powders in auto-combustion method using glycine ($C_2H_5NO_2$) as fuel. The experimental details of auto-combustion synthesized NiO: 8YSZ powders are discussed in experimental section of chapter 4.1.2. However, the amount of glycine ($C_2H_5NO_2$) to be added, was calculated using the following formula for elemental stoichiometric coefficient (φ_e) [127].

$$\varphi_e = \frac{\sum(Coefficient\ of\ oxidizing\ elements\ in\ specific\ formula\ \times Valency)}{(-1)\sum(Coefficient\ of\ reducing\ elements\ in\ specific\ formula\ \times Valency)}$$

φ_e is found to be 1.59, 1 and 0.59 for fuel lean, fuel stoichiometric and fuel rich condition, respectively. The experimental details of auto-combustion synthesized NiO: 8YSZ powders are discussed in experimental section of chapter 4.1.2. Fig. 3 (a) indicates the viscous green gel during heating of the green precursor solution at 70-80 °C. After some time, the green gel combusted to give fine powders and Fig. 3 (b), (c) and (d) shows the combustion of fuel lean, fuel stoichiometric and fuel rich condition. Inset of Fig. 3 (b), (c) and (d) shows the as-synthesized powders obtained after combustion process.
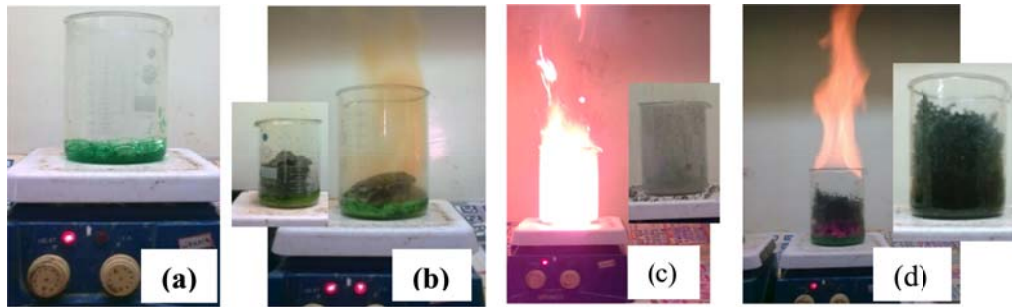
Fig. 3.1: Photographs of green gel (a), fuel lean combustion (b), fuel stoichiometric combustion (c) and fuel rich combustion (d). Inset of (b), (c) and (d) corresponds to as-synthesized powders obtained after auto-combustion.

During auto-combustion, the possible reaction of metal nitrates with glycine can be described as follows based on reported literature [41].

$$9Ni(NO_3)_2 + 10C_2H_5NO_2 \rightarrow 9NiO + 14N_2 + 20CO_2 + 25H_2O$$
$$9ZrO(NO_3)_2 + 10C_2H_5NO_2 \rightarrow 9ZrO_2 + 14N_2 + 20CO_2 + 25H_2O$$
$$6Y(NO_3)_3 + 10C_2H_5NO_2 \rightarrow 3Y_2O_3 + 14N_2 + 20CO_2 + 25H_2O$$
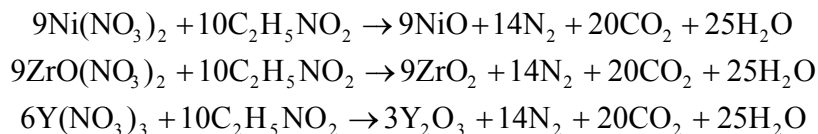
As auto-combustion is a single step process, both the particles of NiO and YSZ may form at the same time. At this condition, both the particles are expected to be of similar size, depending on the exothermicity of the combustion. During sintering of auto-combustion derived samples, the particles of NiO and YSZ may be of same size and particularly Ni particles may found to be smaller in Ni: 8YSZ cermet after reduction in H_2 atmosphere, due to change in volume of NiO.

3.4.2 Co-precipitation

Three different ways such as direct, reverse and constant pH process was followed to prepare NiO: 8YSZ powders through co-precipitation method using chloride and nitrate precursors of the corresponding Ni and Zr salts, separately. N_2H_5OH (denoted as HH) and sodium hydroxide (NaOH) were used as precipitating agents. The experimental details of co-precipitation synthesized NiO: 8YSZ powders are discussed in experimental section of chapter 5.1.2. However, during this synthesis, the possible reaction of metal chlorides/nitrates with HH and NaOH can be described as follows based on reported literatures [126, 128, 129].

$$NiCl_2 \cdot 6H_2O_{(aq)} \xrightarrow{N_2H_5OH(excess)} [Ni(N_2H_4)_3]Cl_{2(aq)} \xrightarrow{2NaOH} Ni(OH)_{2(s)} + 3N_2H_{4(l)} + 2NaCl_{(l)}$$

$$NiCl_2 \cdot 6H_2O_{(aq)} \xrightarrow{N_2H_5OH} [Ni(N_2H_4)_2]Cl_{2(aq)} \xrightarrow{2NaOH} Ni(OH)_{2(s)} + 2N_2H_{4(l)} + 2NaCl_{(l)}$$

$$Ni(NO_3)_2 \cdot 6H_2O_{(aq)} \xrightarrow{N_2H_5OH(excess)} [Ni(N_2H_4)_3](NO_3)_{2(aq)} \xrightarrow{2NaOH} Ni(OH)_{2(s)} + 3N_2H_{4(l)} + 2NaNO_{3(l)}$$

$$Ni(NO_3)_2 \cdot 6H_2O_{(aq)} \xrightarrow{N_2H_5OH} [Ni(N_2H_4)_3](NO_3)_{2(aq)} \xrightarrow{2NaOH} Ni(OH)_{2(s)} + 2N_2H_{4(l)} + 2NaNO_{3(l)}$$

$$ZrOCl_2 \cdot 8H_2O_{(l)} + 2N_2H_5OH_{(l)} \rightarrow ZrO(OH)_{2(s)} + 2NH_4Cl_{(l)} + N_{2(g)} + H_{2(g)} + 8H_2O_{(l)}$$

$$ZrO(NO_3)_2 \cdot 8H_2O_{(l)} + 2N_2H_5OH_{(l)} \rightarrow ZrO(OH)_{2(s)} + 2NH_4NO_{3(l)} + N_{2(g)} + H_{2(g)} + 8H_2O_{(l)}$$

$$ZrO(OH)_{2(s)} + 2N_2H_5OH_{(l)} \rightarrow Zr(OH)_4 + 2N_{2(g)} + 4H_{2(g)} + H_2O_{(l)}$$

In this study, HH was used as precipitating agent up to a pH of ~10. At this pH, complete precipitation of all Ni ions cannot be expected, due to formation of Ni-complexes as per the above reaction. However, partial precipitation of Ni ions cannot be overestimated and primary particles of Ni may form at this stage. But this pH is sufficient to precipitate Zr ions and complete precipitation of Zr ions can be expected. After addition of NaOH, the Ni particles, which are in the form of complexes, have probability to nucleate either on the primary particles of Ni or the particles of Zr. At this condition, the particles of Ni may be same as or different from Zr particles and hence this different type of microstructure can be expected after sintering/reduction.

3.4.3 Heterogeneous precipitation

20, 30 and 40 vol % Ni containing NiO: 8YSZ powders were prepared via direct and reverse process through heterogeneous precipitation method using calcined YSZ as one of the starting materials. However, the constant pH method was not adopted in heterogeneous

precipitation method, as one of the starting materials is calcined YSZ powders. Generally, in constant pH process, reverse process is followed along with an extra amount of HH to be added from second burette. So, there is no need to follow constant pH process, as reverse process is used in this heterogeneous precipitation method. The synthesis of YSZ powders and NiO: 8YSZ powders are discussed in experimental section of chapter 6.1.2 and chapter 6.2.2, respectively. During this synthesis, the possible reaction of Ni-salt with HH and NaOH can be described as follows, based on reported literatures [130].

$$NiCl_2 \cdot 6H_2O_{(aq)} \xrightarrow{N_2H_5OH+2NaOH} [Ni(N_2H_4)_n]Cl_{2(aq)} + 2NaOH \xrightarrow{2NaOH} Ni(OH)_{2(s)} + nN_2H_{4(l)} + 2NaCl_{(l)}$$
$$2Ni(OH)_{2(s)} + N_2H_{4(l)} \rightarrow 2Ni + N_{2(g)} + 4H_2O_{(l)}$$
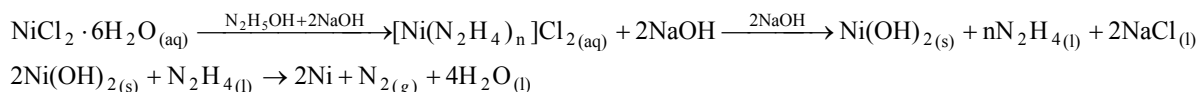
In case of heterogeneous precipitation, a mixture of HH and NaOH was used as precipitating agent and the reaction was carried out at around 80 °C. As per above reaction, the Ni ions may directly precipitate as metallic Ni or in the form of $Ni(OH)_2$, depending on the concentration of Ni and HH. Hence both Ni and $Ni(OH)_2$ may be observed in the as-synthesized powders, depending on the Ni concentration. These two different forms may help in tailoring the microstructure of Ni: 8YSZ cermet.

3.5 Powder compaction, sintering and reduction

Powder compaction constitutes an essential step in fabrication of Ni: 8YSZ cermet. The density/porosity of composite materials can be controlled by optimization of binder concentration and compaction pressure [131]. The calcined NiO-8YSZ powders prepared via solution-based syntheses were properly mixed with an organic binder such as polyvinyl alcohol (PVA) using mortar and pestle and dried. The dried powders were compacted into pellets using circular (diameter 12.5 mm and 15 mm) as well as rectangular (20 mm×5mm) die punch, in a hydraulic press (Model 3887, Carver Inc. USA). Stearic acid dissolved in isopropyl alcohol (IPA) was used as lubricant to facilitate the removal of pellets after withdrawal of compaction pressure. The NiO-8YSZ pellets were sintered in air atmosphere in the temperature range of 1200 – 1300°C for 4 h at a heating rate of 3°C/min and holding at 650°C for 1 h for binder burn out. The sintered pellets were reduced in hydrogen (H_2) atmosphere at 900°C for 1h at a heating rate of 5°C/min, to obtain Ni-8YSZ pellets.

3.6 Fabrication of symmetrical SOFC

A dense YSZ discs having a thickness of ~ 0.55 mm and diameter ~ 13 mm, were fabricated, using YSZ powders prepared in constant pH process, as discussed in Chapter 6.1. The

photographs of the YSZ discs are shown in Figure 3.2 (a). This dense YSZ disc is used as an electrolyte. The procedure for preparing anode ink is discussed in experimental section of chapter 7. Anode layers were formed by coating (manually) the YSZ discs 6 times on each side. The symmetrical cell was sintered at 1350°C for 4 h, at a heating rate of 2°C/min up to 400°C and then 3°C/min up to final temperature and the sintering process was followed on each coating. The symmetrical cells were reduced under hydrogen atmosphere at 900°C for 1h. Figure 3.2 (b) and (c) shows the photograph of typical symmetrical cells before and after reduction in H_2 atmosphere, respectively.

Fig. 3.2: Photograph of dense YSZ (a), symmetrical cells before (b) and after (c) reduction.

For determining impedance spectra, silver paste was used as current collector and applied on both the working electrode (anode) and counter electrode (anode) surfaces and then dried. For better electrochemical performance, uniform coating of current collector is required [132]. Due to limitation in our experimental, silver paste was coated manually on both the surfaces. The symmetrical cells were placed within an alumina tube fitted to a sample holder (designed by us) as shown in Figure 3.3 (a). The working and counter electrodes (after drying the silver paste) were contacted with several mm Ni wire (thickness 0.5 mm) pressed against the center. The samples were hold tightly in the sample holder by a spring load arrangement. The Ni wires were drawn outside the sample holder and connected to an LCR meter supplied by HIOKI 3532-50 HiTESTER. The alumina tube of the sample holder, containing the sample, was introduced into a horizontal tube furnace (as shown in Fig. 3.3 b) and heated up to 900 °C in H_2 atmosphere at a heating rate of 10 °C/min. The H_2 gas was supplied to the furnace from a cylinder through a pipe fitted to the sample holder. Further, with proper care, the impedance spectra measurement was performed.
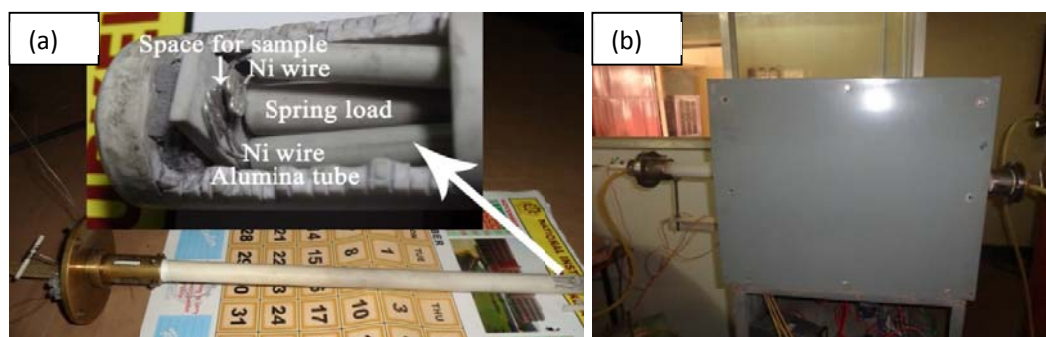
Fig. 3.3: Typical photograph of the sample holder (a) and tube furnace (b).

3.7 General characterization:
3.7.1 Differential scanning calorimetry (DSC) and thermogravimetry (TG)

The thermal behavior of the as-synthesized powders were analyzed by DSC-TG (NEFTZSCH STA 409C) in nitrogen (N_2) atmosphere at a heating rate of 10°C/min using α-alumina as reference material. This gives information about the crystallization and weight loss/gain behavior of the as synthesized powders.

3.7.2 X-ray diffraction

Phase formation in different systems was studied using the room temperature powder X-ray diffraction (Cu-Kα radiation) performed with Phillips PW 1830, Holland and Rigaku Ultima-IV, Japan. Samples are scanned in a continuous mode from 20° – 90° using a step size of 0.02.

3.7.3 Dilatometer

(i) Shrinkage behavior

The shrinkage behavior of the compact pellets was studied by dilatometer (NETZSCH DL 402C) from room temperature to 1200°C at a heating rate of 10°C/min. This gives information regarding the sinterability of the green compacts.

(ii) Thermal expansion co-efficient

Thermal expansion co-efficient of material was also determined from Dilatometer. Calcined pellets in the form of rectangular bar of dimension 10 mm x 3 mm x 2 mm was used to determine TEC from dilatometer under the flow of inert (Ar) gas atmosphere.

3.7.4 Scanning electron microscope (SEM)/field emission SEM (FE-SEM)

The morphology the powders, surface as well as fracture microstructure of sintered pellets were studied using SEM (model: JEOL-JSM-6480LV) or FESEM (model: NOVA Nano SEM/FEI 450). The powders, sintered/reduced pellets are coated with Au. These samples are used for microscopy.

3.7.5 Transmission Electron Microscope (TEM)

The particle morphology was studied in TEM (model: CM 200, Phillips). For preparation of TEM sample, the powders are dispersed in isopropyl alcohol and sonicated for half an hour. One drop of the well-dispersed sample solution is deposited on to a carbon coated copper grid (400 mesh). The dried grid was used for microscopy.

3.7.6 Density and porosity

The density and porosity of the sintered as well as reduced specimens were measured by Archimedes principle using kerosene as immersion media using ASTM standard C20. The value density/porosity reported in this work was calculated with an error of ± 1 %. The formula for the calculation of bulk density and apparent porosity were as follows.

$$Bulk\,density = \frac{W_D}{W_S - W_{Su}} \times Density\,of\,Kerosene$$

where W_D, W_S and W_{Su} are the dry weight, soaked weight and suspended weight of the specimens, respectively. The theoretical density (TD) of a biphasic composite material can be calculated as follows [53].

$$TD\ of\ composite\ = \sum (Volume\ fraction\ of\ the\ phase \times Theoretica\,l\ density\ of\ the\ phase)$$

The relative density can be calculated according to the following formula.

$$Relative\,density = \frac{Bulk\,density}{Theoretica\,l\,density} \times 100$$

Apparent porosity is determined from 100-relative density, which includes only open pores.

3.7.7 Particle size measurement

There are number of particle sizes that arise depending on the measuring technique discussed below.

Physical size (D_P): This refers to the true size of the particles or grain and is usually obtained with scanning electron microscopy / field emission electron microscopy / transmission electron microscopy (TEM).

Crystallite size (D_X): The size corresponds to the mean value of the crystalline domain size of the particles is determined from the X-ray line broadening using Scherrer formula with correction factor as given below [133],

$$D_x = \frac{0.9\lambda}{\beta\cos\theta}$$

Where D_X is average crystalline size, λ is the X-ray wavelength used, β the angular line width of half maximum intensity and θ the Bragg's angle in degree.

3.7.8 Electrical conductivity

For the measurement electrical conductivity, four grooves were made at four different portions on the rectangular bar shaped samples (after reduction). Then, the samples were cleaned with acetone in an ultrasonic bath for 12 min. and dried in a vacuum oven at 100°C. Four electrodes were painted on the grooves using a conducting silver paste followed by drying at 100°C for 1 h. For complete curing of the silver paste the samples were heated at 550°C for 1 h in H_2 atmosphere in order to avoid surface oxidation. The electrical resistance of the samples was measured by dc four-probe method using a 6-digit multi-meter (Agilent 34970A) up to 900°C under H_2 atmosphere with an error of ± 1 %.

3.7.9 Impedance spectroscopy

　　　The impedance response of the symmetrical cells was studied using an LCR meter supplied by HIOKI. The impedance spectra were collected within a frequency range of 42 Hz to 5 M Hz at 1 V, in H_2 atmosphere from 600 °C to 900 °C, during cooling. The spectra were extrapolated to low frequency region using Kramers-Kroning relations and were fitted with respective equivalent circuits, using ZSimpWin software. The polarization resistance, electrode conductivity, capacitance and exchange current density were determined.

RESULTS AND DISCUSSION

CHAPTER 4

Microstructure, electrical conductivity and TEC of Ni: 8YSZ cermet fabricated using auto-combustion synthesized NiO: 8YSZ powders

This chapter contains three sub-chapters. In Chapter 4.1, 30 vol % Ni containing NiO: 8YSZ powders have been synthesized via fuel lean, fuel stoichiometric and fuel rich auto-combustion method. Different physical properties of these powders are correlated.

In Chapter 4.2, effect of binder concentration and compaction pressure on density/porosity, microstructure and electrical conductivity of NiO/Ni: 8YSZ composites (fabricated from NiO: 8YSZ powders discussed in Chapter 4.1) have been studied and properties are correlated.

In Chapter 4.3, effect of Ni concentration (20, 30 and 40 vol %) and sintering temperature (1200 °C and 1300 °C) on density/porosity, microstructure and electrical conductivity of fuel stoichiometric auto-combustion derived Ni: 8YSZ cermet have been studied and TEC was measured as a function of Ni concentration.

CHAPTER 4.1

Synthesis and characterization of auto-combustion derived NiO: 8YSZ powders

4.1.1: Introduction

To tailor the microstructure of Ni: 8YSZ cermet for use as anode in IT-SOFC application, auto-combustion synthesis was adopted in this research work. 30 vol % Ni containing NiO: 8YSZ powders were synthesized by varying the elemental stoichiometric coefficient, so as to get fuel lean (ϕ_e= 1.59), fuel stoichiometric (ϕ_e= 1) and fuel rich (ϕ_e= 0.59) combustion. Thermal behavior, structure, powder morphology and shrinkage behavior of NiO: 8YSZ were studied and analyzed.

4.1.2: Experimental

The raw materials for preparing NiO: 8YSZ powders, using auto-combustion method, were nickel nitrate hexahydrate [$Ni(NO_3)_2 \cdot 6H_2O$], zirconium oxynitrate monohydrate [$ZrO(NO_3)_2 \cdot H_2O$], yttria [Y_2O_3, which was dissolved in HNO_3 and distilled water] and glycine [$C_2H_5NO_2$]. Three different solutions based on fuel lean, fuel stoichiometric and fuel rich condition have been prepared using appropriate amount of raw materials. Individual solutions were heated on hot plate (at 70 °C - 80 °C) and stirred using a magnetic needle. The gradual evaporation of solvent slowly converted the green solution in to a viscous green gel and finally combusted to produce fine powders. The powders were collected, pulverized in mortar pestle and then calcined at different temperatures. Thermal behavior, structure, powder morphology and shrinkage behavior of the prepared samples were studied and analyzed.

4.1.3: Results and discussion

4.1.3.1: Thermal behavior

DSC-TG analysis was performed to understand the thermal behavior of fuel lean, fuel stoichiometric and fuel rich combustion derived as-synthesized powders and is shown in Fig. 4.1 (a), (b) and (c), respectively. DSC and TG behavior of fuel lean and fuel rich combustion derived as-synthesized powder looks similar in nature. In both conditions, the sample undergoes a continuous weight loss from room temperature to ~ 800 °C and then slightly gains weight up to 1000°C. The total weight loss was found to be ~13 % and ~ 9 % at fuel lean and fuel rich condition, respectively. However, the fuel stoichiometric combustion derived sample undergoes a continuous weight gain (total weight gain is ~ 4 %) up to 1000°C. The broad exothermic peak centered at ~ 800 °C, for fuel lean combustion, corresponds to crystallization of nickel oxide and / or zirconia [134], which is absent for both fuel stoichiometric and fuel rich combustion. These thermal behaviors can be correlated with the XRD patterns of the calcined powders.
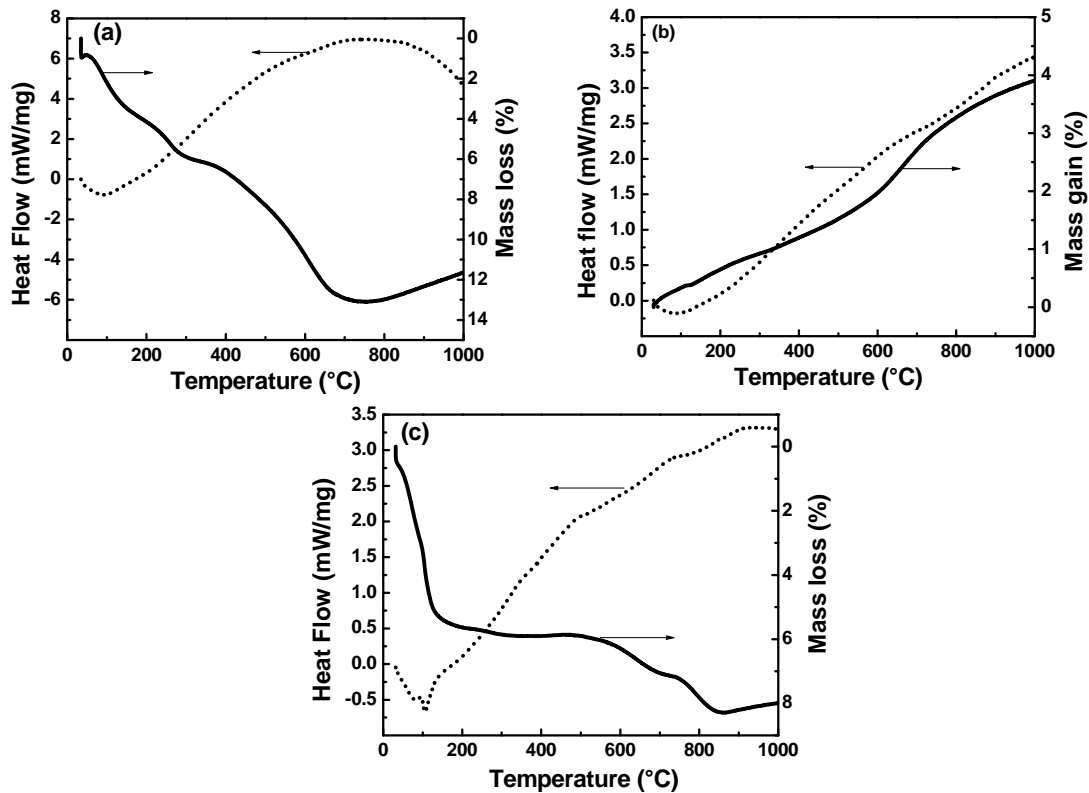
Fig. 4.1: DSC-TG curves of the as-synthesized powders prepared at (a) fuel lean, (b) fuel stoichiometric and (c) fuel rich condition.

4.1.3.2: Structure

Figure 4.2 (a), (b) and (c) show XRD patterns of fuel lean, fuel stoichiometric and fuel rich combustion derived as-synthesized powders, respectively.
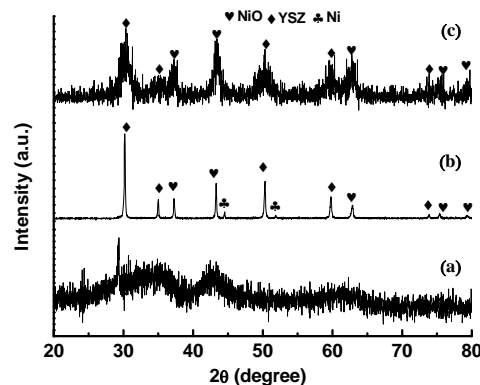
Fig. 4.2: XRD patterns of as synthesized powders prepared at (a) fuel lean, (b) fuel stoichiometric and (c) fuel rich condition.

XRD patterns of fuel lean and fuel rich combustion derived as-synthesized powders show amorphous and semi-crystalline nature. The amorphous nature is due to insufficient fuel that ignites the mixture resulting in lean misfire and semi-crystalline nature is due to incomplete combustion

because of excess of fuel used and limiting oxygen. All the peaks of fuel rich derived as-synthesized sample are identified with either NiO or YSZ, as per JCPDS file number 01-078-0423 and 01-081-1551, respectively. The corresponding crystallite size of NiO and YSZ was found to be ~ 8 nm each, as per Scherrer's formula [133]. However, the fuel stoichiometric derived as-synthesized powder is purely crystalline in nature. All the peaks are identified with either NiO or YSZ with minute amount of Ni phase (JCPDS file number 01-087-0712). The sharp nature of peaks indicate that the crystallite size of both NiO (71 nm) and YSZ (53 nm) is quite larger as compared to fuel rich derived as-synthesized powders. Crystalline nature indicates that the exothermicity of the combustion attains its maximum at fuel stoichiometric condition.

Comparing Fig. 4.1 and Fig. 4.2, the observed weight loss in both fuel lean and fuel rich combustion derived powders may be attributed to the presence of some nitrogen and carbon containing compounds in the as-synthesized powders, respectively. Further, the weight gain in fuel stoichiometric combustion derived samples may be due to the adsorption of N_2 on surface of Ni [135]. The presence of broad exothermic peak in DSC for fuel lean combustion is due to amorphous nature of this powder and absence of this peak in fuel stoichiometric and fuel rich combustion is due to crystalline nature of these powders.

To understand the phase evolution and variation of crystallite size, the as-synthesized powders were calcined at different temperatures. Fig. 4.3 (a), (b) and (c) show the XRD patterns of the calcined powders, prepared at fuel lean, fuel stoichiometric and fuel rich condition, respectively. Phase pure NiO and YSZ were developed in all conditions at 650 °C.
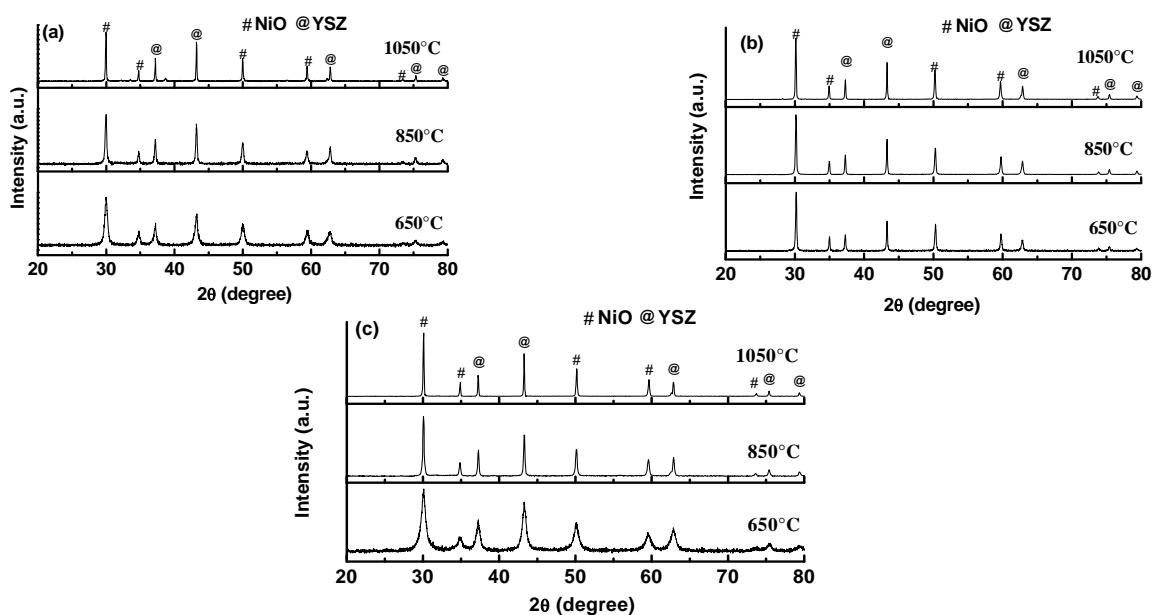
Fig. 4.3: XRD patterns of (a) fuel lean, (b) fuel stoichiometric and (c) fuel rich combustion derived powders calcined at different temperatures.

The crystallite size of NiO and YSZ were calculated for powders calcined at different temperatures (650 °C, 850 °C and 1050 °C) and are mentioned in Table 4.1. The crystallite size of both NiO and YSZ for fuel lean and fuel rich combustion samples increases with the increase in calcination temperature. However, the crystallite size of NiO and YSZ for fuel stoichiometric combustion derived as-synthesized as well as calcined (650 °C and 850 °C) samples remains nearly unchanged. These results further confirmed that the self-generated heat was maximum and reaches about 850 °C, when the powders are synthesized at fuel stoichiometric condition. The growth rate of NiO and YSZ is slower in fuel stoichiometric condition as compared to fuel lean and fuel rich condition up to 1050 °C.

Table 4.1: Crystallite size of NiO and YSZ at different calcination temperatures and synthesized at different conditions

Synthesis condition	Calcination temperature (°C)	Crystallite size of NiO (nm)	Crystallite size of YSZ (nm)
Fuel lean	As-synthesized	--	--
	650 °C	15	19
	850 °C	47	33
	1050 °C	225	88
Fuel stoichiometric	As-synthesized	71	53
	650 °C	71	53
	850 °C	81	54
	1050 °C	125	67
Fuel rich	As-synthesized	--	--
	650 °C	22	19
	850 °C	55	41
	1050 °C	237	68

In order to study the phase formation of Ni and YSZ, the NiO: 8YSZ powders were calcined at 1200 °C and then reduced in H_2 atmosphere at 900 °C. The typical XRD pattern of Ni: 8YSZ is shown in Fig. 4.4. All the peaks are assigned to Ni and YSZ and it was confirmed that NiO successfully converted to Ni after reduction.
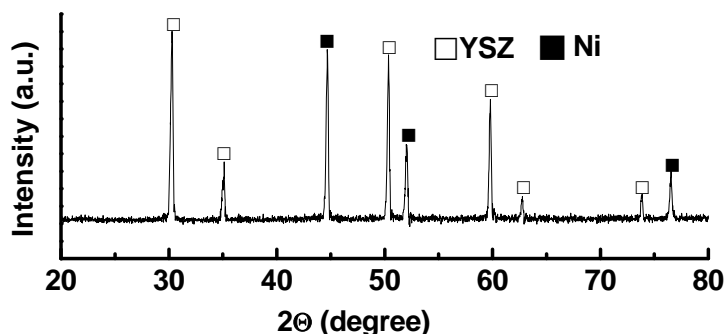
Fig. 4.4: XRD patterns of Ni: 8YSZ pellet after reduction of NiO: 8YSZ.

4.1.3.3: Powder morphology

Morphology of calcined (650°C) NiO: 8YSZ powders prepared at fuel lean, fuel stoichiometric and fuel rich condition was observed using FE-SEM and are shown in Fig. 4.5 (a), (b) and (c), respectively. The particles are found to be agglomerated and irregular in shape at all synthesis conditions. The size of particles was found to be nearly same at fuel lean and fuel rich condition. However, the size is larger at fuel stoichiometric condition.
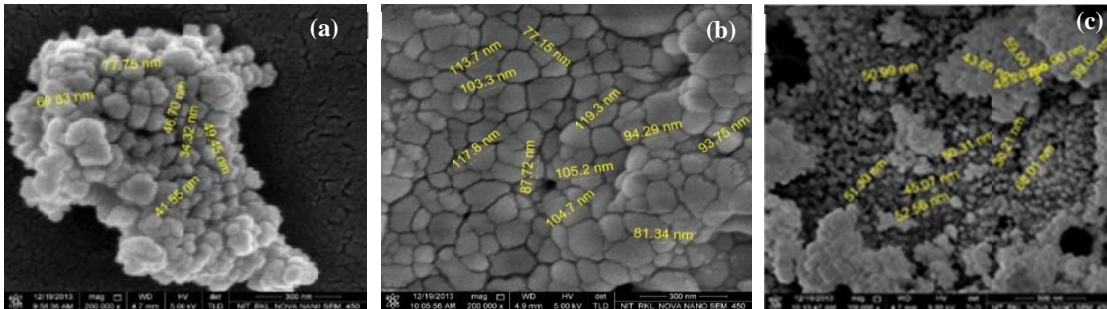
Fig. 4.5: Morphology of (a) fuel lean, (b) fuel stoichiometric and (c) fuel rich combustion derived calcined powders.

4.1.3.4: Shrinkage behavior

Shrinkage behavior of green NiO: 8YSZ compact pellet was studied using dilatometer and is shown in Fig. 4.6. Shrinkage of nearly 2%, 4 % and 9 % was observed in NiO: 8YSZ pellets, prepared at fuel lean, fuel stochiometric and fuel rich condition, respectively, up to 1200 °C. The variation of shrinkage may be attributed to the amount of fuel used in three different synthesis conditions and may result in difference of sinterability for NiO: 8YSZ composites.
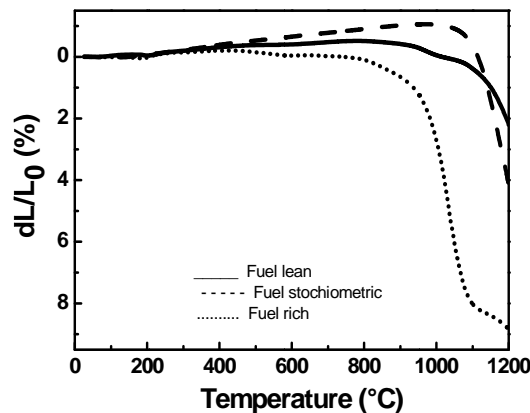
Fig. 4.6: Shrinkage behavior of auto-combustion derived green NiO: 8YSZ pellets.

4.1.4: Summary

NiO: 8YSZ powders have successfully been prepared through auto-combustion method at three different conditions such as fuel lean, fuel stoichiometric and fuel rich. The powders were found to be amorphous, crystalline and semi-crystalline for fuel lean, fuel stoichiometric and fuel rich combustion, respectively. With increase in calcination temperature, the growth rate of crystallites was found to be slower for fuel stoichiometric combustion as compared to fuel lean and fuel rich combustion up to 1050 °C. However, the particle size was larger in the sample prepared at fuel stoichiometric condition due to higher exothermicity of combustion. The NiO: 8YSZ pellets may be sintered at or above 1200 °C, as observed from shrinkage behavior.

It is highly pivotal and significant to optimize the binder concentration and compaction pressure during the fabrication of NiO: 8YSZ composites in order to achieve adequate density/porosity in Ni: 8YSZ cermet. These factors are considered in the next chapter. The investigation of microstructure and electrical conductivity of Ni: 8YSZ cermets under the basis of porosity have been carried out to deduce the best sample for further analysis.

CHAPTER 4.2

Effect of binder concentration and compaction pressure on density/porosity of NiO/Ni: 8YSZ composites and effect of porosity on electrical conductivity of Ni: 8YSZ cermet

4.2.1: Introduction

Porosity is one of the dominating factors in determining the electrical conductivity of Ni: 8YSZ cermet, which can be optimized during fabrication of NiO: 8YSZ pellets, using appropriate amount of binder and compaction pressure. So, in this chapter, the effect of binder concentration and compaction pressure on density/porosity of 30 vol % Ni containing NiO/Ni: 8YSZ composites were studied. The porosity dependent electrical conductivity of 30 vol % Ni containing Ni: 8YSZ with temperature have been analyzed.

4.2.2: Experimental

Fuel lean combustion derived NiO: 8YSZ powders were initially chosen for optimizing the density/porosity of NiO/Ni: 8YSZ pellets and the optimized fabrication parameters were applied to both fuel stoichiometric and fuel rich combustion derived powders. The calcined (650 °C) powders were thoroughly mixed with different concentration (1, 2, 3, and 5 wt %) of binder, poly vinyl alcohol (PVA). These powders were compacted to rectangular pellets at different compaction pressure using hydraulic press. The compaction pressure was varied from 98 MPa to 1372 MPa, depending upon the binder concentration. The NiO: 8YSZ pellets were sintered at 1200°C in air atmosphere and then reduced at 900 °C in H_2 atmosphere to obtain Ni: 8YSZ cermet. Density and porosity of all samples before and after reduction was measured. Microstructure and electrical conductivity of Ni: 8YSZ cermet was studied and analyzed.

4.2.3: Results and discussion

4.2.3.1: Effect of binder concentration and compaction pressure on density / porosity of NiO/Ni: 8YSZ composites and porosity dependent electrical conductivity of Ni: 8YSZ cermet

Starting with the optimization of density/porosity, fuel lean combustion derived calcined NiO: 8YSZ powders were mixed with different concentration of binder and compacted in to pellets at a suitable range of compaction pressure. Above certain compaction pressure, NiO: 8YSZ pellet could not be fabricated due to crack formation in the green body. This was due to the fact that the pellets undergo elastic compression, which increases with the increase in compaction pressure and the release of stored elastic energy during removal of applied pressure leads to expansion of pellets

causing crack on the green body. The density/porosity of sintered (1200 °C) NiO: 8YSZ pellets were measured and are shown in Fig. 4.7.
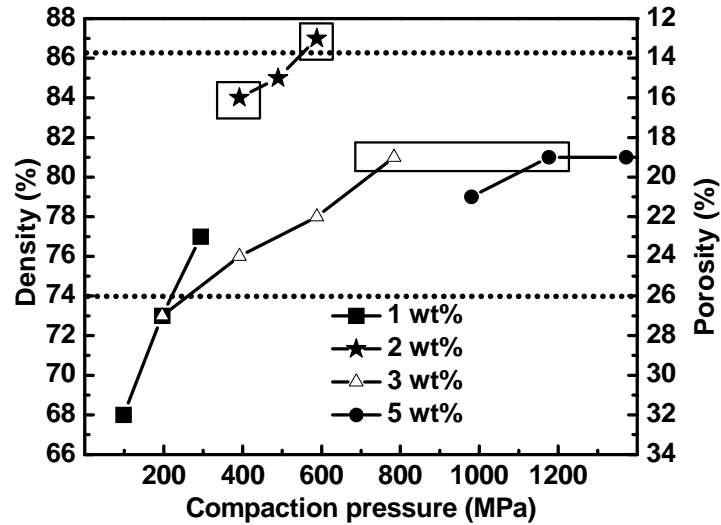
Fig.4.7: Effect of binder concentration and compaction pressure on the density or porosity of 30 vol % Ni containing NiO: 8YSZ sintered (1200 °C) pellets.

At different wt % of binder, the density of sintered NiO: 8YSZ composites increase with increase in compaction pressure. The 1 wt % PVA added NiO: 8YSZ composites show lowest density (varies from 68 % to 77 %, when compaction pressure used in between 98 MPa to 294 MPa), whereas, addition of 2 wt % binder led to highest density. Three different compaction pressures (392 MPa, 490 MPa and 588 MPa) have been used to fabricate NiO: 8YSZ composites using 2 wt % PVA. The highest and lowest density of NiO: 8YSZ composites was found to be ~ 87 % and 84 %, when compacted at a pressure of 588 MPa and 392 MPa, respectively. Similarly, for 3 wt % binder addition, the density of NiO: 8YSZ composites lie in between 73 % to 81 %, when compaction pressure used lies in between 196 MPa to 784 MPa. The highest compaction pressures have been used in between 980 MPa to 1372 MPa to fabricate 5 wt % PVA added NiO: 8YSZ composites and the density lies in between 79 % to 81 %. With further increase in binder concentration, the density was not improved even on increasing compaction pressure, due to the fact that more amount of binder hinders the thermal debinding process. It was also observed that the composites prepared at 784 MPa using 3 wt % PVA and 1176 MPa using 5 wt % PVA show same density of ~ 81 %.

The two dotted horizontal lines in Fig. 4.7 demonstrate the optimum range of density or porosity in NiO: 8YSZ sintered pellets, in order to achieve a porosity of 30% to 40% in Ni: 8YSZ cermet, which is generally considered for SOFC anode application. These lines were drawn on the

basis of the observed porosity in NiO: 8YSZ composite before and after reduction, as shown in Fig. 4.8. The trend of air-fired porosity (NiO: 8YSZ) against hydrogen-fired porosity (Ni: 8YSZ) was found to be linear and agrees quite well with the reported data [24].
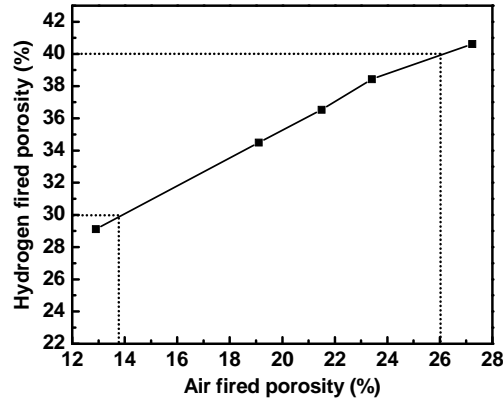
Fig.4.8: Air-fired vs hydrogen fired porosity of NiO/Ni-8YSZ composites

The above results suggest that the desirable porosity of Ni: 8YSZ cermet lies in between the dotted horizontal lines in Fig. 4.7. So it is interesting to study the electrical conductivity of some specific samples, as marked in square and rectangular box in Fig. 4.7. The porosity of Ni: 8YSZ cermet, prepared at a compaction pressure of 392 MPa and 588 MPa using 2 wt % PVA [as marked as two square solid box in Fig. 4.7], was found to be 32 % and 29 %, respectively [determined from Fig. 4.8]. In contrast to this, the porosity of Ni: 8YSZ cermet, prepared at compaction pressure of 784 MPa (using 3 wt % PVA) and 1176 MPa (using 5 wt % PVA) [as marked as rectangular solid box in Fig. 4.7], was found to be 35 % [determined from Fig. 4.8]. The temperature dependent electrical conductivity of Ni: 8YSZ cermet having porosity of 35%, but prepared using 3 wt % and 5 wt % PVA is shown in Fig. 4.9 (a). Similarly, the electrical conductivity variation with temperature of Ni: 8YSZ cermet prepared using 2 wt % PVA, but having porosity of 32 % and 29 % is shown in Fig. 4.9 (b). The electrical conductivity of Ni: 8YSZ cermet having 35 % porosity shows ionic type behavior, in which conductivity increases with increase in temperature. However, Ni: 8YSZ cermet having porosity of 32 % and 29 % show electronic type behavior, in which conductivity decreases with increase in temperature. The conductivity value of Ni: 8YSZ cermet having 29 % porosity was found to be higher (~ 5.5 S/cm at 300 °C and decreases to ~ 2.5 S/cm at 900 °C) than the cermet having 32 % porosity. The value of conductivity of Ni: 8YSZ cermet having 32 % porosity is 0.225 S/cm at 300 °C and decreases to ~ 0.08 S/cm at 900 °C. This observation concluded that the transition from ionic to electronic conductivity took place in Ni: 8YSZ cermet at a porosity of either 34 % or 33%.
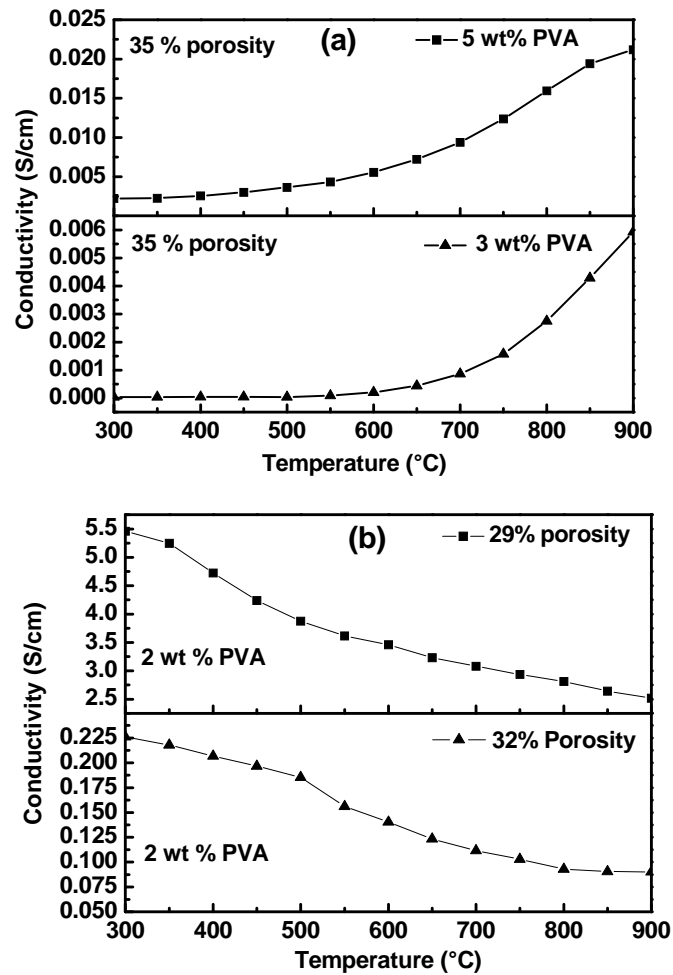
Fig. 4.9: Electrical conductivity as a function of temperature for Ni: 8YSZ cermet having (a) same porosity (35 %), but prepared using different PVA concentration and (b) different porosity (29%, 32 %), but prepared at 2 wt % PVA.

Similarly, the fuel stoichiometric and fuel rich combustion derived NiO: 8YSZ composites were fabricated using the optimized parameters (2 wt % PVA and compaction pressure of 392 MPa, 490 MPa and 588 MPa) and sintered at 1200 °C. Densities of these composites were determined and are shown in Fig. 4.10. For comparison purpose, density data of fuel lean combustion derived sintered NiO: 8YSZ composites have also been incorporated. In all cases, the density of sintered NiO: 8YSZ composites increases with compaction pressure. The two dotted horizontal lines in Fig. 4.10 demonstrate the optimum range of density [determined from Fig. 4.8] in NiO: 8YSZ composites in order to achieve a porosity of 30% to 40% in Ni: 8YSZ cermet. From Fig. 4.10, it was observed that the density of fuel stoichiometric combustion derived sintered NiO: 8YSZ composites, fabricated at compaction pressure of 588 MPa using 2 wt % PVA, was higher (88 %). At this compaction pressure and binder concentration, the density of fuel lean and fuel rich

combustion derived sintered NiO: 8YSZ composites was found to be 87 % and 76 %, respectively. The corresponding porosity of fuel lean, fuel stoichiometric and fuel rich combustion derived Ni: 8YSZ cermet was determined from Fig. 4.8 and found to be ~ 29 %, ~28 %, and ~39 %, respectively. So, it is interesting to study the microstructure, distribution of Ni, YSZ and electrical conductivity of the Ni: 8YSZ cermet, corresponding to the specified box in Fig. 4.10.
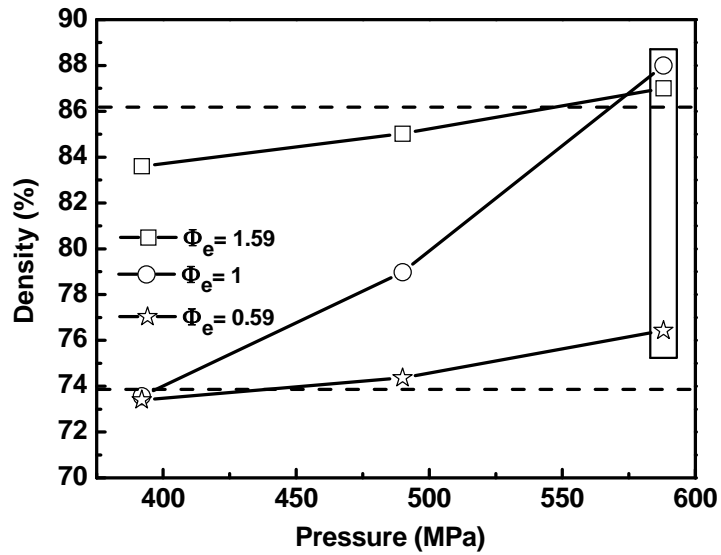
Fig. 4.10: Density variation with compaction pressure of fuel lean, fuel stoichiometric and fuel rich combustion derived sintered NiO: 8YSZ composites fabricated using 2 wt % PVA.

4.2.3.2: Microstructure

Microstructure of fuel lean, fuel stoichiometric and fuel rich combustion derived sintered NiO: 8YSZ composites were studied using SEM and are shown in Fig. 4.11 (a), (b) and (c), respectively. In all samples, the shape of NiO/YSZ particles is nearly spherical in nature. The porosity seems to be higher at fuel rich condition and dense microstructure was observed at fuel stoichiometric condition. The particle size is found to be in the range of ~500 nm to ~2μm at all preparation conditions. After reduction of three specific samples, microstructure of Ni: 8YSZ cermet was studied using FE-SEM. Fig. 4.12 (a), (b) and (c) show FE-SEM micrographs of Ni: 8YSZ cermet, prepared at fuel lean, fuel stoichiometric and fuel rich condition, respectively. The porosity of fuel rich combustion derived Ni: 8YSZ cermet seems to be higher as compared to fuel lean and fuel stoichiometric combustion derived cermet. The particle size of Ni/YSZ was uniform and nearly spherical in nature. The particle size of Ni/YSZ is found to be in the range of ~300 nm to ~2μm at all preparation conditions. To further understand the distribution of Ni and YSZ in Ni: 8YSZ cermet, EDS mapping was performed.
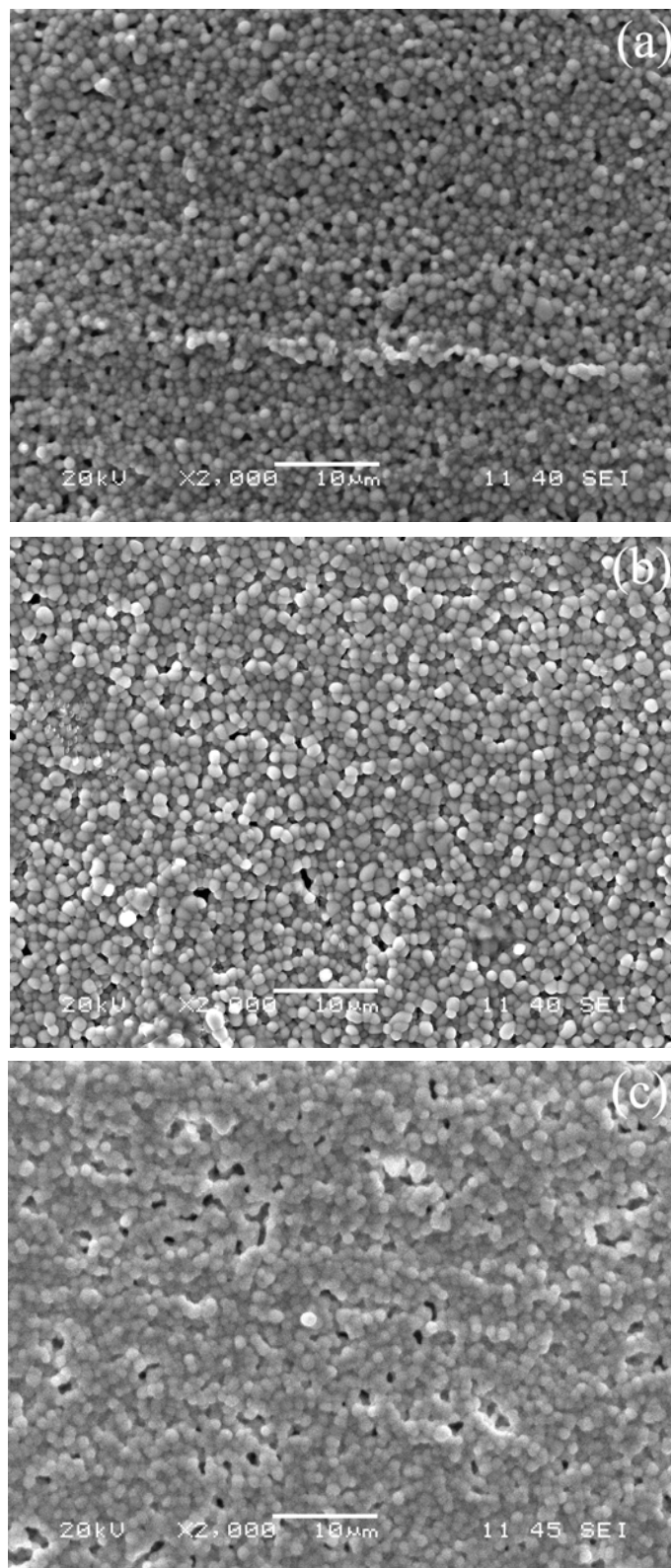
Fig. 4.11: SEM micrographs of sintered NiO: 8YSZ composites, prepared at (a) fuel lean, (b) fuel stoichiometric and (c) fuel rich condition.
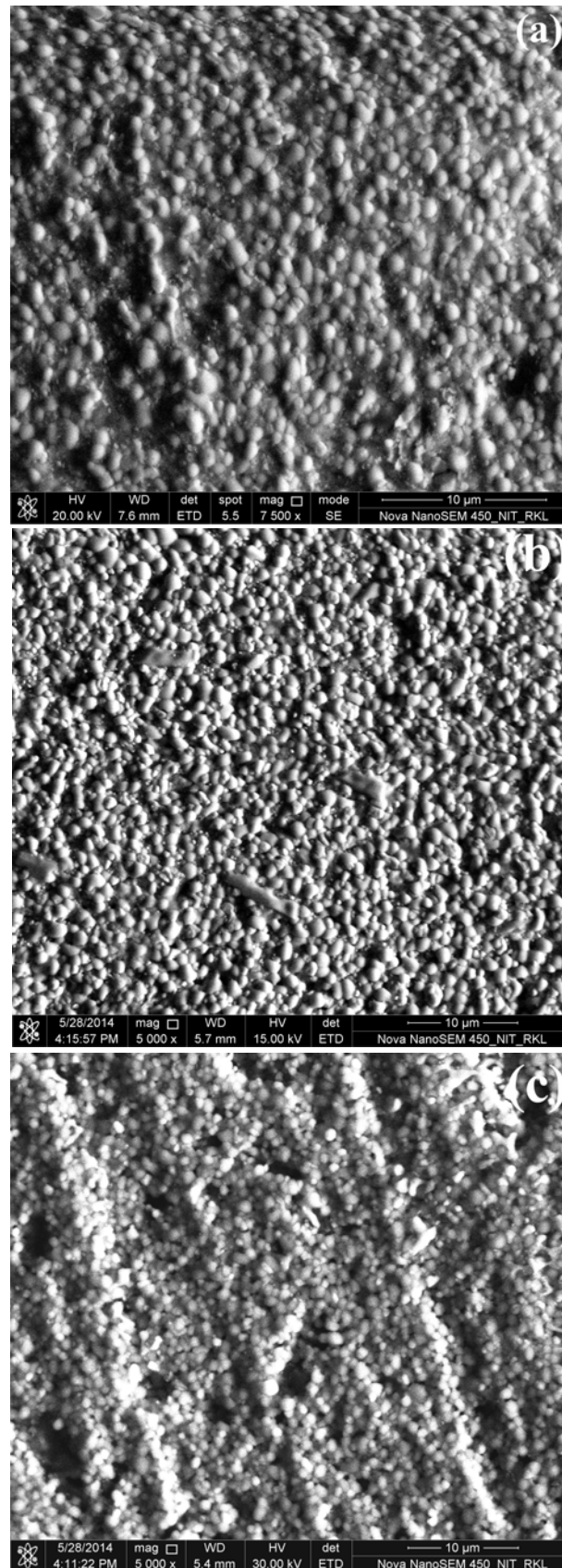
Fig. 4.12: FE-SEM micrographs of Ni: 8YSZ cermet, prepared at (a) fuel lean, (b) fuel stoichiometric and (c) fuel rich condition.

Figure 4.13 (a), (b) and (c) show EDS mapping of Ni: 8YSZ cermet, prepared at fuel lean, fuel stoichiometric and fuel rich condition, respectively. Elemental mapping of Ni and Zr are marked as red and blue color, respectively in Fig. 4.13. Ni particles are well distributed in 8YSZ matrix for all samples. To further confirm the distribution of Ni and YSZ, secondary image with elemental mapping of corresponding Ni: 8YSZ cermets are also presented in Fig. 4.14. It was confirmed that the fine Ni particles are well connected for fuel lean and fuel stoichiometric condition, whereas, this Ni-Ni connection is poor at fuel rich condition, due to higher porosity. The connectivity of Ni particles can also be confirmed from the measurement of electrical conductivity of these samples.
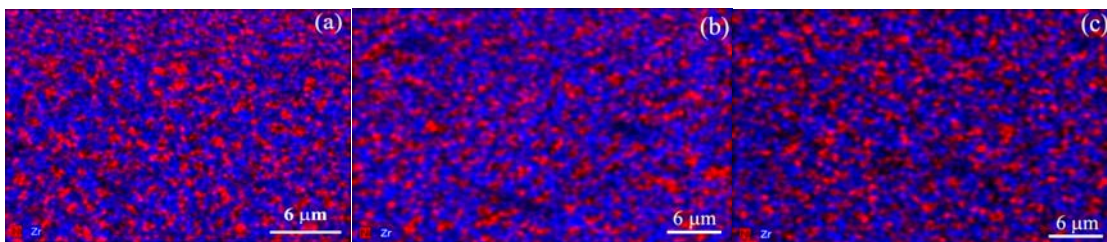
Fig. 4.13: Distribution of Ni (red) and Zr (blue) in Ni: 8YSZ cermet, prepared at (a) fuel lean, (b) fuel stoichiometric and (c) fuel rich condition.
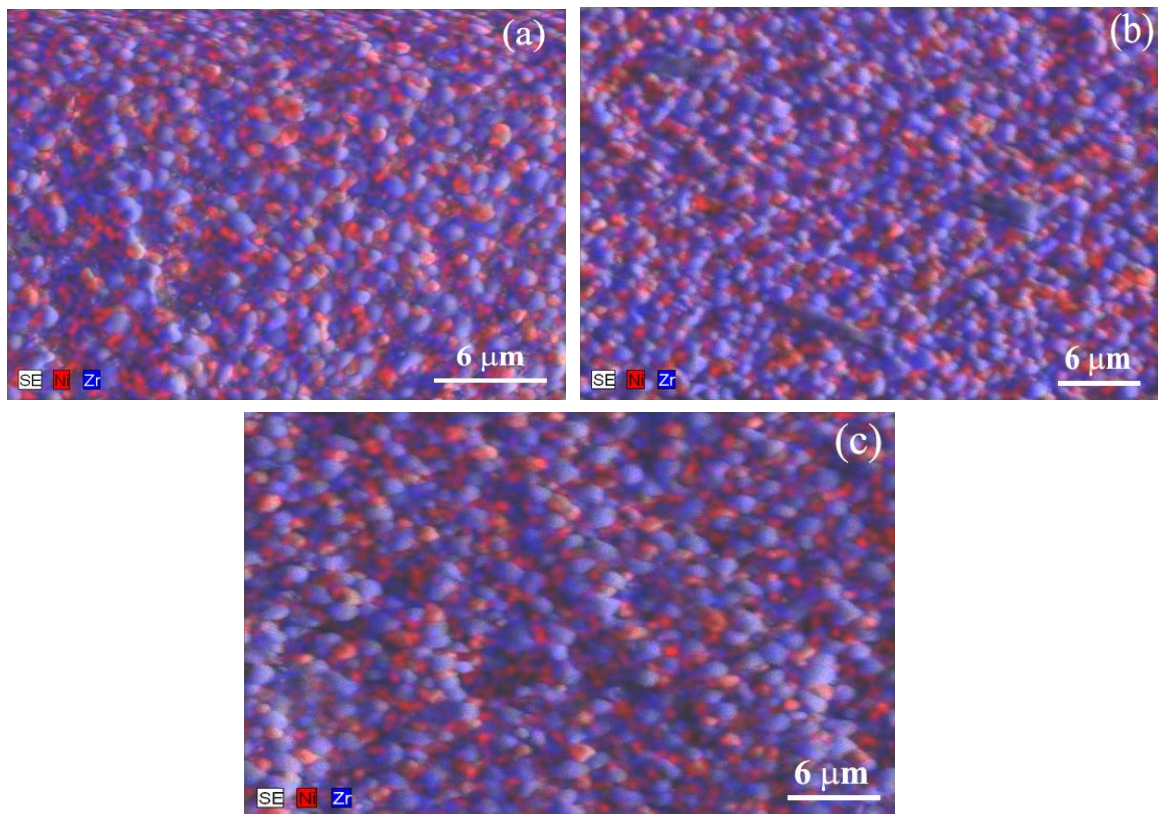
Fig. 4.14: Secondary image with elemental mapping of Ni: 8YSZ cermet, prepared at (a) fuel lean, (b) fuel stoichiometric and (c) fuel rich condition.

4.2.3.3: Electrical conductivity

The temperature dependent electrical conductivity behavior of fuel lean, fuel stoichiometric and fuel rich combustion derived Ni: 8YSZ cermet is shown in Fig. 4.15 (a), (b) and (c), respectively.

Both fuel lean and fuel stoichiometric combustion derived Ni: 8YSZ cermet show electronic type behavior, whereas fuel rich combustion derived cermet shows ionic type behavior. The electronic and ionic type behavior strongly depends on the Ni-Ni and YSZ-YSZ contact, respectively, in the cermet and also depends on the porosity. Higher porosity (~ 39%) with dominating YSZ-YSZ contact led to ionic type conductivity and better Ni-Ni contact with lower porosity (~ 28 to 29%) led to electronic type conductivity. The conductivity of fuel lean derived Ni: 8YSZ cermet was found to be ~5.5 S/cm at 300 °C and decreases to ~ 2.5 S/cm at 900 °C. However, the conductivity of fuel stoichiometric combustion derived cermet shows a highest value of ~ 16 S/cm at 300 °C and decreases to ~ 5 S/cm at 900 °C. The higher conductivity for fuel stoichiometric combustion derived cermet was mainly due to well distribution of Ni and better connection between Ni-Ni particles in YSZ matrix.
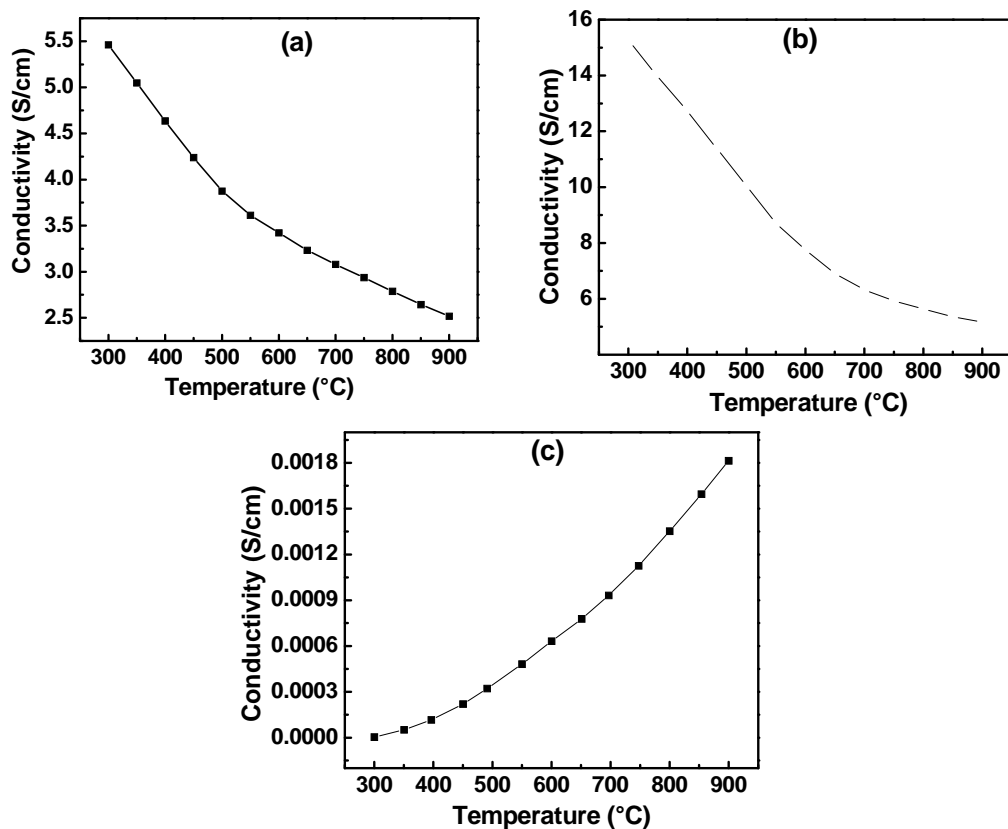
Fig. 4.15: Electrical conductivity as a function of temperature of Ni: 8YSZ cermet, prepared at (a) fuel lean, (b) fuel stoichiometric and (c) fuel rich condition.

4.2.4: Summary

To obtain a suitable density/porosity of Ni: 8YSZ cermet, binder concentration and compaction pressure was optimized for fuel lean derived NiO: 8YSZ composites. It was found that 2 wt % addition of binder (PVA) and employing a compaction pressure of 588 MPa, led to higher density (87%) in sintered NiO: 8YSZ composites. Using the optimized binder concentration and compaction pressure, NiO: 8YSZ composite shows highest density (88 %) for fuel stoichiometric condition, whereas lowest density (76 %) was observed for fuel rich condition. EDS mapping confirmed that the Ni-Ni particles are not well-connected in fuel rich combustion derived cermet, whereas, better connection of Ni-Ni particles are observed in fuel lean as well as fuel stoichiometric combustion derived cermet. From the electrical conductivity point of view, the Ni: 8YSZ cermet having porosity in between 28 % to 32 % shows a electronic type behavior and the cermet having more than 33 % porosity behaves as an ionic conductor. The electronic and ionic behavior was mainly due to the connectivity between Ni-Ni particles and YSZ-YSZ particles, respectively, in the cermet. The conductivity of fuel stoichiometric combustion derived cermet shows a highest value of ~ 16 S/cm at 300 °C and it decreases to ~ 5 S/cm at 900 °C.

The fuel stoichiometric combustion derived Ni: 8YSZ cermet shows better electrical conductivity with suitable microstructure and porosity as compared to fuel lean and fuel rich combustion derived cermet. So, fuel stoichiometric combustion was found to be suitable for development of Ni: 8YSZ cermet. In the next chapter, effect of Ni concentration and sintering temperature on density/porosity, microstructure, electrical conductivity and TEC of fuel stoichiometric combustion derived Ni: 8YSZ cermet is studied.

CHAPTER 4.3

Effect on Ni concentration and sintering temperature on density/porosity, microstructure and electrical conductivity of fuel stoichiometric combustion derived Ni: 8YSZ cermet

4.3.1: Introduction

Based on the results and discussion of Chapter 4.1 and Chapter 4.2, it was confirmed that the fuel stoichiometric combustion derived 30 vol % Ni containing Ni: 8YSZ cermet show suitable microstructure with adequate porosity and electrical conductivity. The density/porosity, microstructure, electrical conductivity and TEC are strongly dependent on the concentration of Ni in Ni: 8YSZ cermet. So, different volume percentages (20, 30 and 40) of Ni have been used to fabricate Ni: 8YSZ cermet using fuel stoichiometric combustion derived calcined NiO: 8YSZ powders. Sintering temperature of NiO: 8YSZ may also affect the microstructure and electrical conductivity. So, the effect of Ni concentration and sintering temperature on the density/porosity, microstructure and electrical conductivity of Ni: 8YSZ cermets were studied and also TEC was measured as a function of Ni concentration.

4.3.2: Experimental

The experimental procedure for preparing 30 vol % Ni containing NiO: 8YSZ powders via auto-combustion method were discussed in section 4.1.2. Same procedure was followed for preparing 20, 30 and 40 vol % Ni containing NiO: 8YSZ powders at fuel stoichiometric condition. After combustion, the obtained as-synthesized powders were calcined at 650 °C and compacted to pellets using the optimized binder concentration (2 wt % PVA) and compaction pressure (588 MPa). The compacted NiO: 8YSZ composites were sintered at 1200°C and 1300 °C in air atmosphere. The sintered NiO-8YSZ pellets were further reduced at 900°C in H_2 atmosphere to develop Ni-8YSZ cermet. The composite/cermet prepared at different Ni concentration and sintering temperature are designated as FS N*X0* S12/13 R, where FS represents fuel stoichiometric combustion; N*X0* represents vol % of Ni; S12/13 represents sintering temperature (1200 °C/1300 °C) and R represents reduced sample.

4.3.3: Results and discussion

4.3.3.1: Density and porosity

The effect of Ni concentration on density/porosity of NiO/Ni: 8YSZ, prepared at two different sintering conditions of 1200 °C and 1300 °C are shown in Fig. 4.16 (a) and (b), respectively. At sintering condition of 1200 °C/1300 °C, the density of NiO: 8YSZ (before reduction) was higher than Ni: 8YSZ (after reduction) due to change in volume by the reduction of

NiO to Ni. At sintering condition of 1200 °C, the density of Ni: 8YSZ decreases from 77 % to 71 % with the increase in Ni concentration. The corresponding porosity of Ni: 8YSZ cermet increases from 23 % to 29 %. However, at sintering condition of 1300 °C, the density of Ni: 8YSZ decreases from 80 % to 72 % with increase in Ni concentration. The corresponding porosity of Ni: 8YSZ cermet increases from 20 % to 28 %.
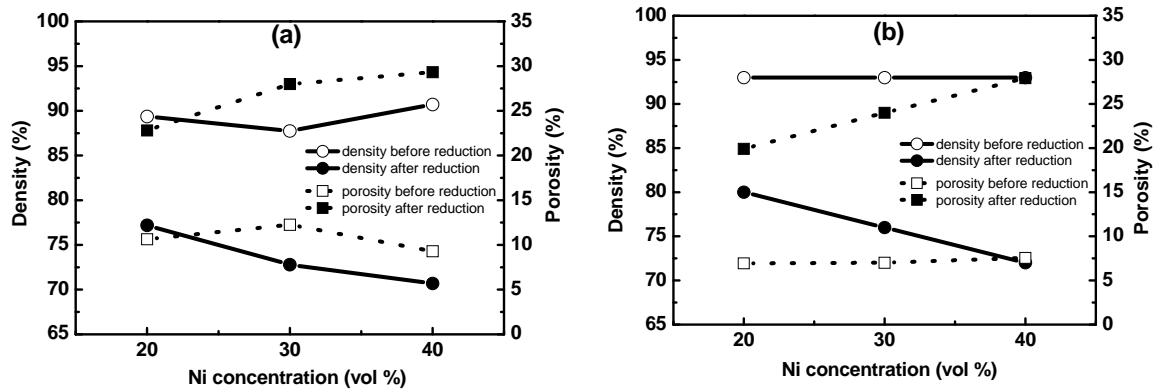
Fig. 4.16: Effect of Ni concentration on density and porosity of NiO: 8YSZ and Ni: 8YSZ prepared at two different sintering conditions, (a) 1200 °C and (b) 1300 °C.

4.3.3.2: Microstructure

Microstructure of NiO: 8YSZ composites (30 vol % Ni) at sintering condition of 1200 °C and 1300 °C are shown in Fig. 4.17 (a) and (b), respectively. The particles are found to be nearly spherical in shape and size of the particles increase with the sintering temperature. However, the particle size varies from 500 nm to 2.5 µm, depending on the sintering condition.
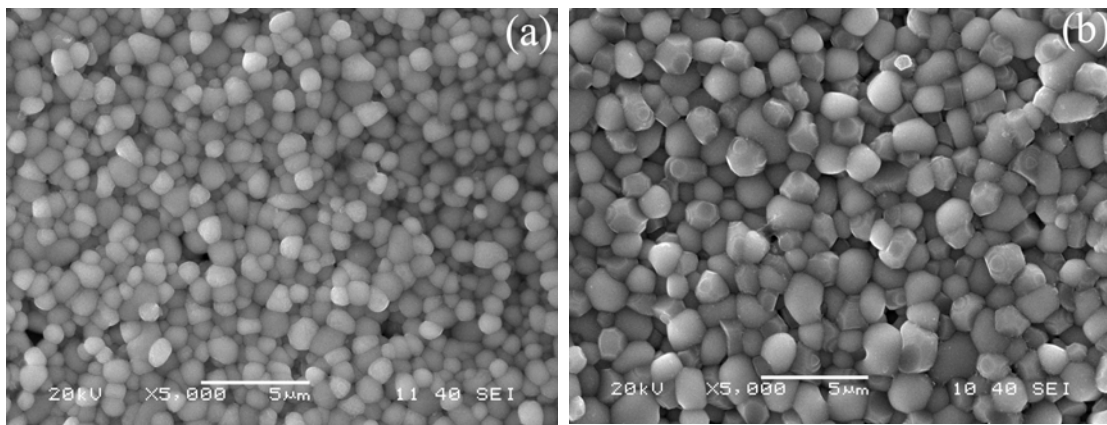
Fig. 4.17: SEM micrographs of NiO: 8YSZ prepared under the sintering condition of (a) 1200 °C and (b) 1300 °C.

To further understand the effect of Ni concentration on microstructure of Ni: 8YSZ cermet for two different sintering conditions, FE-SEM was performed. Fig. 4.18 (a), (b), and (c) show FE-SEM micrographs of FSN20S12 R, FSN30S12 R and FSN40S12 R, respectively.
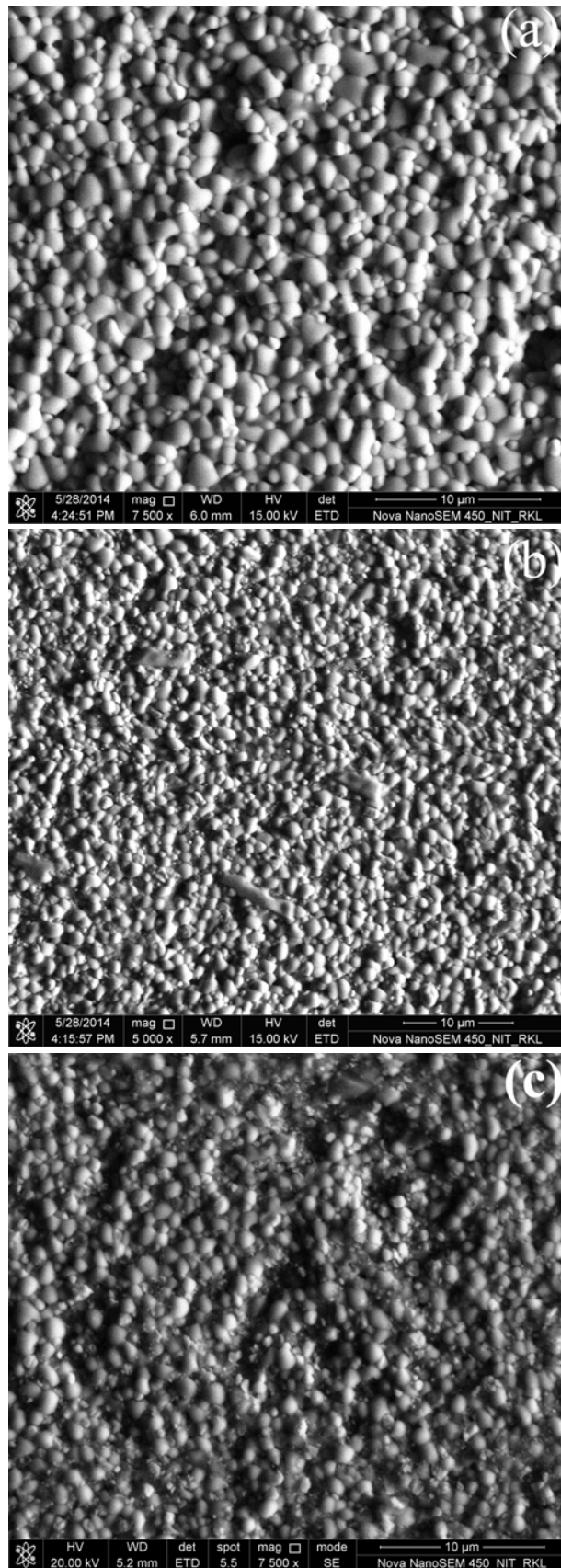
Fig. 4.18: FE-SEM micrographs of (a) Ni20S12 R, (b) N30S12 R and (c) N40S12 R.

The particles are nearly spherical in shape for all cases. The particle size was found to be in the range of ~ 500 nm to ~ 2 μm. But, the particles of FSN30S12 R and FSN40S12 R are found to be smaller in size than FSN20S12 R. However, the particles of Ni and YSZ cannot be distinguished from these micrographs. Hence, to further understand the distribution of Ni and YSZ, elemental mapping of Ni and Zr are performed on these samples and are shown in Fig. 4.19 [red color for Ni and blue color for Zr]. The corresponding secondary image along with mapping is also shown in Fig. 4.20. It was confirmed that the particles of Ni are well distributed in 8YSZ matrix in the cermet. However, Ni connectivity in 8YSZ matrix was more prominent in FSN30S12 R and FSN40S12 R composites. The particle size of YSZ was found to be larger for FSN20S12 R cermet due to dominating YSZ concentration, which suppresses the grain growth of Ni. With the increase in Ni concentration, the particle size of Ni and YSZ are comparable due to gradual increase in dominating effect of Ni in YSZ matrix. The average grain size of Ni was found to be 400 nm to 800 nm and average grain size of YSZ was found to be ~ 700 nm to ~ 1.5 μm.
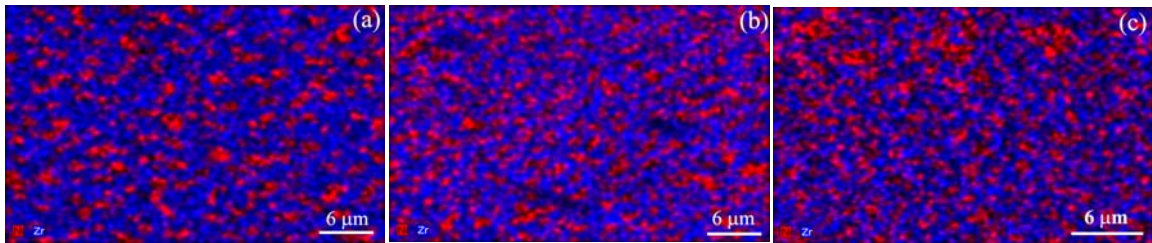
Fig. 4.19: Elemental mapping of (a) FSN20S12 R, (b) FSN30S12 R and (c) FSN40S12 R.
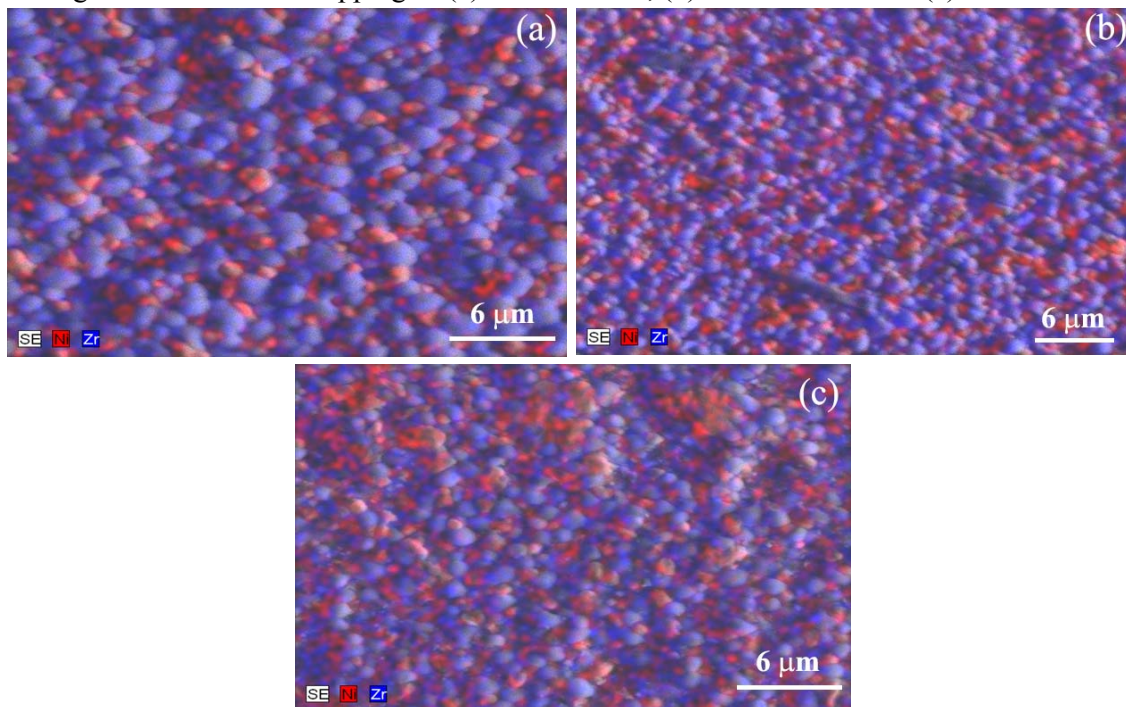
Fig. 4.20: Secondary image with mapping of (a) FSN20S12 R, (b) FSN30S12 R and (c) FSN40S12 R

To further understand the microstructure of 20, 30 and 40 vol % Ni containing Ni: 8YSZ cermet, prepared at the sintering condition of 1300 °C, FE-SEM was performed. Fig. 4.21 (a), (b), and (c) show FE-SEM micrographs of FSN20S13 R, FSN30S13 R and FSN40S13 R, respectively.
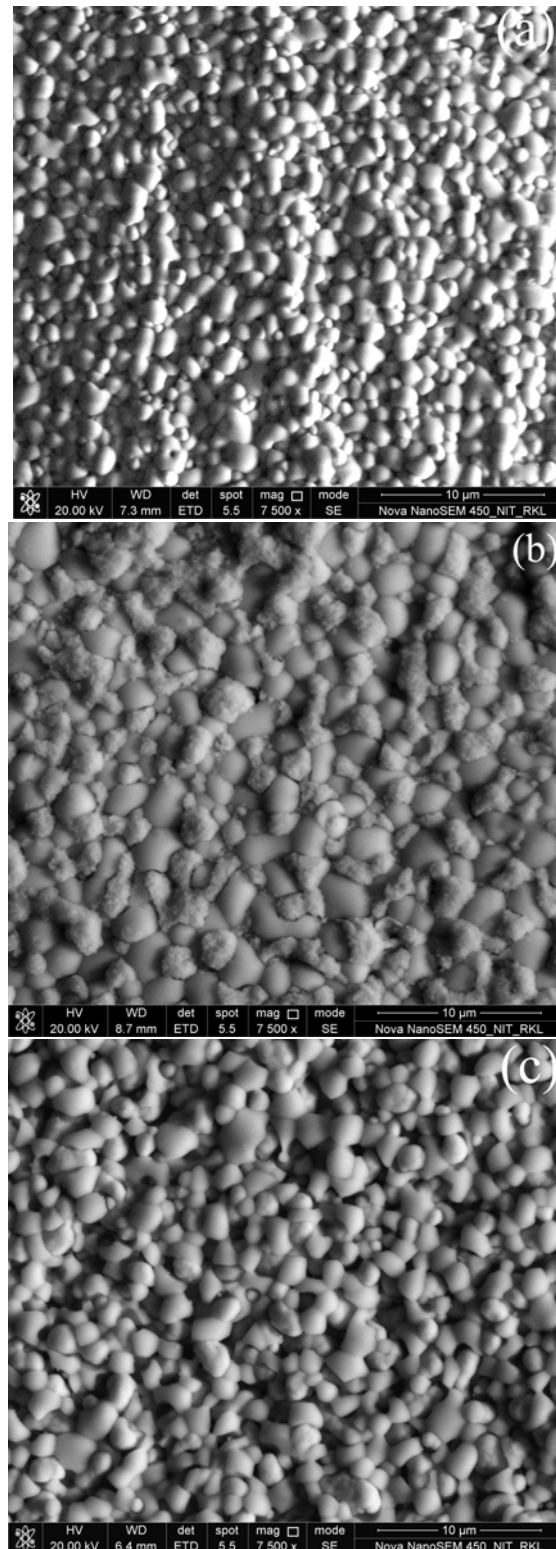
Fig. 4.21: FE-SEM micrographs of (a) FSN20S13 R, (b) FSN30S13 R and (c) FSN40S13 R.

It was well understood that the particle size increases with sintering temperature. So, the particle size of Ni: 8YSZ cermet prepared at the sintering condition of 1300 °C was larger than the cermet prepared at the sintering condition of 1200 °C. At the sintering condition of 1300 °C, the shape of particles deviates from spherical nature and show irregular shape. The particle size of FSN20S13 R was found to be smaller than FSN30S13 R and FSN40S13 R. The particle size was found to be in the range of ~ 800 nm to ~ 2.5 µm. The clear picture of the distribution of Ni and YSZ in these cermets can be visualized from EDS mapping. Elemental mapping of Ni and Zr in these cermets are shown in Fig. 4.22 and corresponding secondary image with elemental mapping are shown in Fig. 4.23. Due to higher sintering temperature of 1300 °C, the agglomeration of Ni takes place, which increases with increase in Ni concentration. These agglomerated Ni particles seem to form a continuous chain around each YSZ particles for sample FSN30S13 R and FSN40S13 R, as observed from Fig. 4.22 and 4.23. The average particle size of Ni was found to be ~ 600 nm to ~ 900 nm and that for YSZ particle was found to be ~ 800 nm to ~ 2 µm.
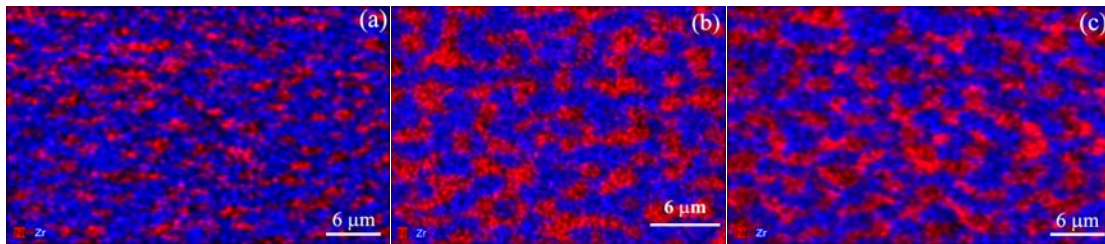
Fig. 4.22: Elemental mapping of (a) FSN20S13 R, (b) FSN30S13 R and (c) FSN40S13 R.
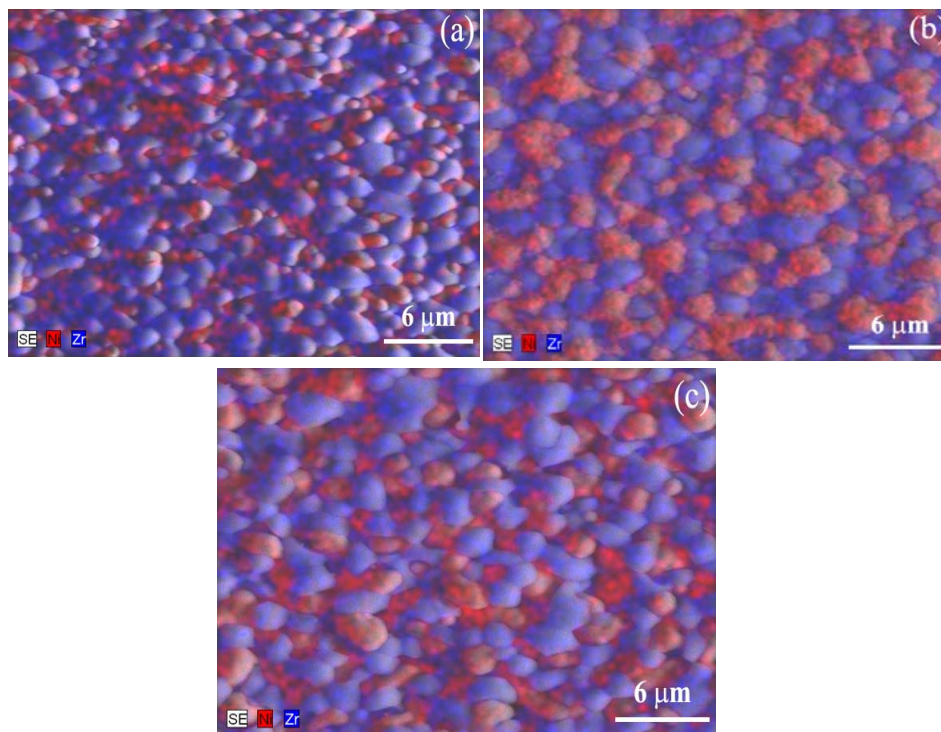
Fig. 4.23: Secondary image with mapping of (a) FSN20S13 R, (b) FSN30S13 R and (c) FSN40S13 R

4.3.3.3 Electrical conductivity

The temperature dependent electrical conductivity of Ni: 8YSZ cermet such as FSN20S12 R, FSN30S12 R and FSN40S12 R, prepared at sintering condition of 1200 °C are shown in Fig. 4.24 (a), (b) and (c), respectively. Also, the temperature dependent electrical conductivity of Ni: 8YSZ cermet such as FSN20S13 R, FSN30S13 R and FSN40S13 R, prepared at sintering condition of 1300 °C are shown in Fig. 4.25 (a), (b) and (c), respectively.
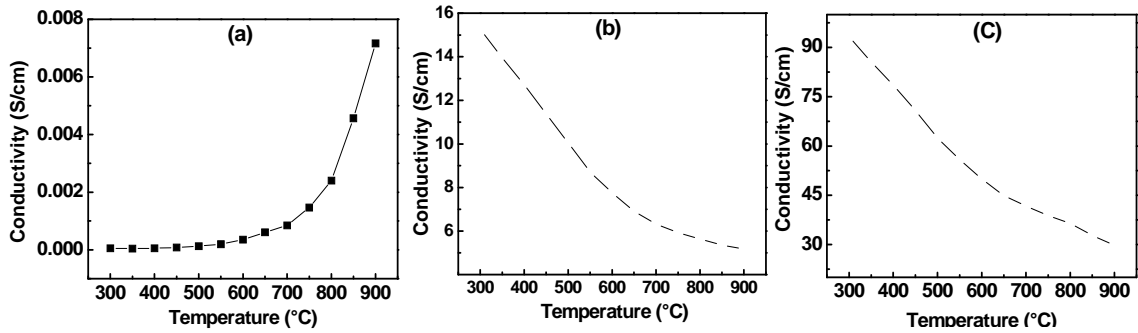
Fig. 4.24: Temperature dependent electrical conductivity of (a) FSN20S12 R, (b) FSN30S12 R and (c) FSN40S12 R.
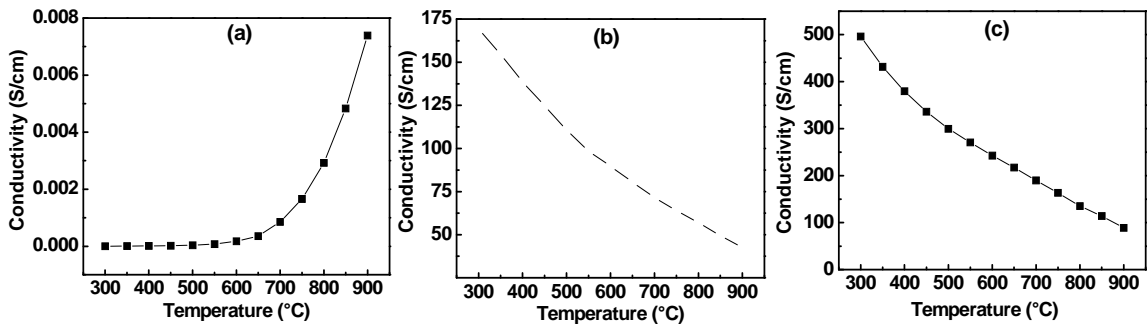
Fig. 4.25: Temperature dependent electrical conductivity of (a) FSN20S13 R, (b) FSN30S13 R and (c) FSN40S13 R.

The fabricated cermet containing 20 vol % Ni such as FSN20S12 R and FSN20S13 R show ionic type behavior, whereas, cermet containing 30 and 40 vol % Ni such as FSN30S12 R, FSN30S13 R, FSN40S12 R and FSN40S13 R show electronic type behavior. The ionic and electronic type behavior of Ni: 8YSZ cermet was mainly due to dominating YSZ-YSZ contact and better Ni-Ni connectivity, which was also confirmed from EDS mapping. The electrical conductivity value of Ni: 8YSZ cermet (30 and 40 vol % Ni) increases with increase in Ni concentration and sintering temperature. Highest value of conductivity (~ 500 S/cm at 300 °C and decreases to 89 S/cm at 900 °C) was observed for FSN40S13 R cermet.

The conductivity of the Ni: 8YSZ cermet material was determined by the path of conduction such as YSZ-to-YSZ or Ni-to-Ni. In the cermet containing 20 vol% Ni such as FSN20S12 R or FSN20S13 R, the YSZ-to-YSZ contact provides the conduction path, whereas for the cermet containing $\geq$ 30 vol% Ni such as FSN30S12 R, FSN30S13 R, FSN40S12 R and FSN40S13 R, the Ni-to-Ni contact acts as the dominating path for conduction. As the conductivity of Ni is several orders of magnitude higher than that of YSZ, the cermet containing 20 vol% Ni shows low conductivity with ionic type behavior and those containing 30 vol% or more Ni show electronic type behavior, indicating a conductivity percolation in between 20 vol % to 30 vol% Ni. To further understand the percolation behavior, the temperature dependent electrical conductivity of FSN20S12 R, FSN20S13 R, FSN30S12 R and FSN30S13 R cermets was re-plotted and is shown in Fig. 4.26. These results also indicate that the conductivity percolation was in between 20 to 30 vol % Ni. It was also observed that the electrical conductivity of the cermet having $\geq$ 30 vol% Ni decreases exponentially with increase in temperature. But, theoretically, it should decrease linearly with temperature. This non-linear nature of conductivity may be due to some ionic contribution in these cermets[10].
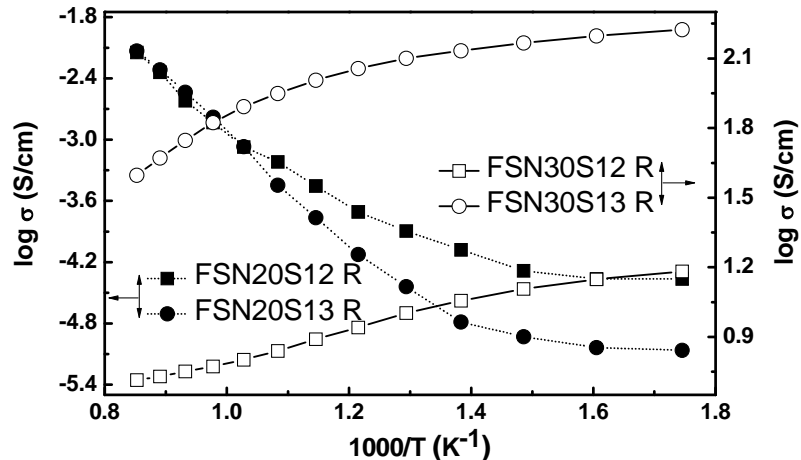
Fig. 4.26: Electrical conductivity as a function of temperature for sample FSN20S12 R, FSN20S13 R, FSN30S12 R and FSN30S13 R.

The value of electrical conductivity in Ni: 8YSZ cermet is strongly dependent on the concentration of Ni. The electrical conductivity value obtained at different temperatures (400 °C to 800 °C) for all Ni: 8YSZ cermet, prepared at sintering condition of 1200 °C and 1300 °C are shown in Fig. 4.27 (a) and (b), respectively. In both cases, electrical conductivity of Ni: 8YSZ increases with Ni content. Below 30 vol% Ni, the conductivity of the Ni: 8YSZ was very low due to absence of electronic conduction and dominating ionic conduction. This can also observed from the increase in conductivity with temperature (400 °C to 800 °C) for 20 vol % Ni containing cermet. Above 30

vol% Ni, the conductivity sharply increases by nearly four/five orders of magnitude due to increased electronic conduction through the Ni phase. This was supported by the electronic conduction behavior and consequently the decrease in conductivity with temperature (400 °C to 800 °C) for the cermet containing 30 or 40 vol % Ni. This also confirms that the percolation threshold lies in between 20 to 30 vol % Ni.
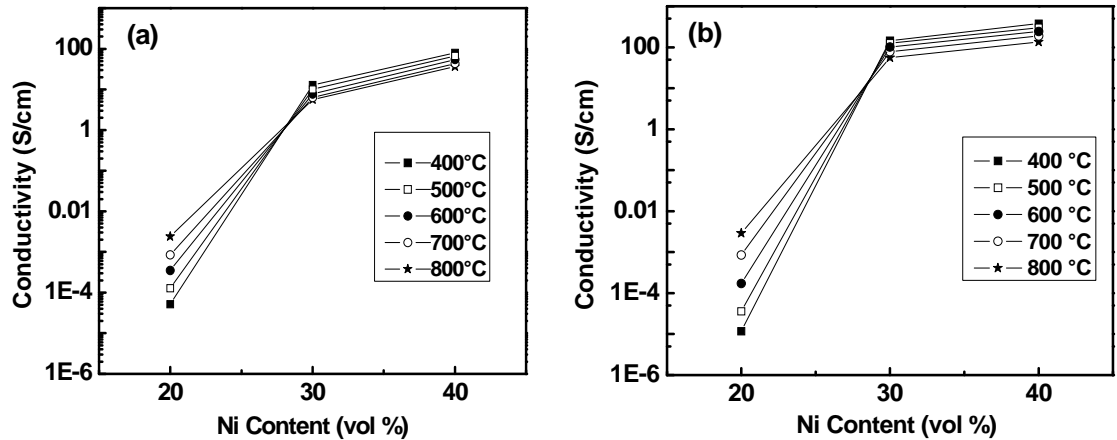
Fig. 4.27: Electrical conductivity as a function of Ni content at different temperatures for Ni: 8YSZ cermet prepared at sintering condition of (a) 1200 °C and (b) 1300 °C.

4.3.3.4: Thermal expansion coefficient

Thermal expansion behavior of 20, 30 and 40 vol % Ni containing cermet prepared at the sintering condition of 1300 °C is shown in Fig. 4.28 (a). The thermal expansion was found to increase linearly with temperature. As expected, the slope of the expansion curve also increases with Ni concentration. Thermal expansion co-efficient (TEC) of these cermets was calculated and is shown in Fig. 4.28 (b). The TEC of 20 and 30 vol % Ni containing cermet was nearly same and found to be 12.8×10^{-6} /°C to 12.9×10^{-6} /°C, respectively and it may be due to change in microstructure. However, the TEC of 40 vol % Ni containing cermet increases to 13.8×10^{-6} /°C.
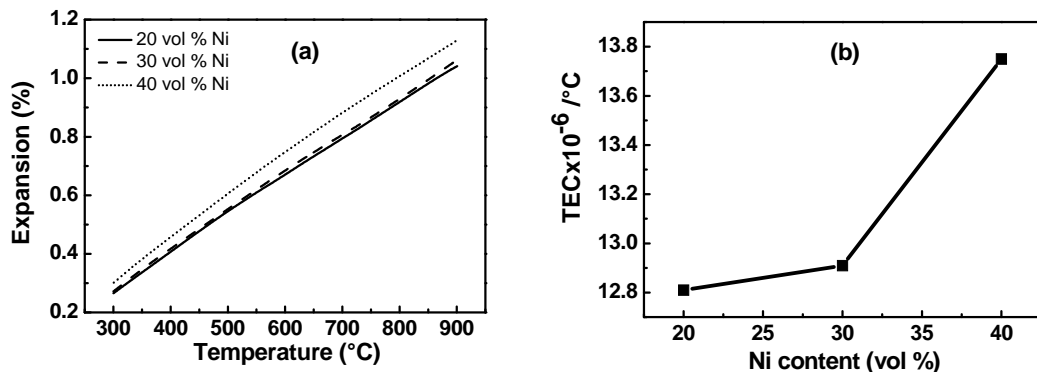
Fig. 4.28: Thermal expansion behavior of Ni: 8YSZ cermet (a), TEC as a function of Ni content (b)

The results obtained for porosity, conductivity and TEC of fuel stoichiometric combustion derived cermets are correlated with some of the reported literatures based on auto-combustion synthesis method. The correlation of Ni content, sintering/reduction temperature, porosity, conductivity and TEC of some reported data with the present study are given in Table 4.1. In this study, specifically the electrical conductivity data of fuel stoichiometric combustion derived cermets are quite comparable with some of the reported data [1-4]. However, Marinšek et.al. [5] have obtained lower conductivity value using 40 vol % Ni. It seems that the synthesis method adopted in this present study is highly effective for development of Ni: 8YSZ cermet.

Table 4.2: Comparison of porosity, electrical conductivity and TEC of Ni: 8YSZ with literatures.

Concentration of Ni (vol%)	Sintering/reduction temperature (°C)	Porosity (%)	Electrical conductivity (S/cm) /measuring temperature (°C)	TEC ($\times 10^{-6}$/°C)	[Ref]
15	1350/800	30	0.103/900	10.40	[34]
30	1350/800	30	40/900	11.64	
50	1350/800	39	989/900	13.20	
50	1400/900	36	100-200 / 900		[136]
45	1300/800	27	12.5/555,7.94/1000		[40]
20	---	---	3.162/1000	---	[137]
30	---	---	31.62/1000	---	
40	---	---	125/1000	---	
40	1380/---	--	1.58/900	--	[36]
50	1450/1000	23,34,41	1072,906,817/950	11.46, 11.58,11.6	[37]
50 *	1250	--	--	--	[138]
	1300	55,62,66	--	--	
	1350	42,49,57,60	1706,392,6,-- /25	--	
	1400	35,41,50,54	5521,2517,833,464 /25	--	
	1450	32,39,46,42	5816, 3314,2132,1823 /25	--	
20	1300/900	20	--	12.8	[in this
30	1300/900	24	169/300,42/900	12.9	study]
40	1300/900	28	496/300, 88/900	13.8	

Note: * wt % Ni

4.3.4: Summary

The required porosity of Ni: 8YSZ cermet is one of the crucial factors for use as anode in IT-SOFC and depends on the concentration of Ni and sintering temperature of NiO: 8YSZ. At sintering condition of 1200 °C, the porosity of Ni: 8YSZ cermet increases from 23 % to 29 % with increase in Ni concentration. Similarly, at 1300 °C, the porosity of Ni: 8YSZ cermet increases from 20 % to 28 % with increase in Ni concentration.

The electrical conductivity of Ni: 8YSZ cermet strongly depends on the microstructure of the cermet, concentration of Ni and sintering temperature. The 20 vol % Ni containing cermet such as FSN20S12 R and FSN20S13 R show ionic type behavior. In these two samples, Ni particles are smaller in size as compared to YSZ and these Ni particles are not in contact with each other in YSZ matrix. However, $\geq$ 30 vol % Ni containing cermet (FSN30S12 R, FSN40S12 R, FSN30S13 R and FSN40S13 R) shows electronic type behavior due to better Ni-Ni contact. For FSN30S12 R and FSN40S12 R cermets, both Ni and YSZ particles are nearly uniform in size and are well distributed in the cermet. However, for FSN30S13 R and FSN40S13 R cermets, agglomerated fine Ni particles are forming a continuous chain around each YSZ particles. In these samples, the average grain size of Ni was found to be 600 nm to 900 nm and average grain size of YSZ was found to be ~ 800 nm to ~ 2 μm. The conductivity percolation in Ni: 8YSZ cermet prepared via fuel stoichiometric condition was found to be in between 20 and 30 vol % Ni. The non-linear nature of the conductivity of $\geq$ 30 vol % Ni containing cermet may be due to some ionic contribution to the conductivity. The TEC of 20, 30 and 40 vol % Ni containing cermet was found to be 12.8×10^{-6} /°C, 12.9×10^{-6} /°C and 13.8×10^{-6} /°C, respectively.

From porosity, microstructure, electrical conductivity and TEC point of view, it was concluded that the fuel stoichiometric combustion derived Ni: 8YSZ cermet may be used as anode in IT-SOFC. Further, to confirm the applicability of fuel stoichiometric combustion derived powders in IT-SOFC, the electrochemical performance of symmetrical cell was studied and discussed in chapter 7.

CHAPTER 5

Microstructure, electrical conductivity and TEC of Ni: 8YSZ cermet fabricated using co-precipitation synthesized NiO: 8YSZ powders

This chapter contains three sub-chapters. In Chapter 5.1, 30 vol % Ni containing NiO: 8YSZ powders have been synthesized at three different processes of co-precipitation method, such as direct, reverse and constant pH, using both chloride and nitrate precursors. Different properties such as thermal behavior, structure, powder morphology and shrinkage behavior NiO: 8YSZ powders were studied.

In Chapter 5.2, different properties such as density/porosity, microstructure, and electrical conductivity of direct, reverse and constant pH process derived 30 vol % Ni containing NiO/Ni: 8YSZ composites were correlated and analyzed.

In Chapter 5.3, effect of Ni concentration and sintering temperature on density/porosity, microstructure and electrical conductivity of constant pH process derived Ni: 8YSZ cermet was studied and TEC was measured as a function of Ni concentration.

CHAPTER 5.1

Thermal behavior, structure, powder morphology and shrinkage behavior of direct, reverse and constant pH co-precipitation derived NiO: 8YSZ powders

5.1.1: Introduction

The presence of well-connected fine Ni particles in YSZ matrix along with adequate conductivity, porosity and compatible TEC are the essential requirements of Ni: 8YSZ cermet for use as anode in SOFC. All the above criteria can be fulfilled by controlling the characteristic of starting NiO: 8YSZ powders, which strongly depend on the initial precursors and way of synthesis. So, chloride and nitrate precursors have been used to develop 30 vol% Ni containing fine NiO: 8YSZ powders by three different ways of co-precipitation such as direct, reverse and constant pH process. The thermal behavior, structure, powder morphology and shrinkage behavior of these powders are discussed in this Chapter.

5.1.2: Experimental

NiO: 8YSZ powders, containing 30 vol% Ni, were synthesized by co-precipitation method using chloride and nitrate precursors. Three different ways of co-precipitation synthesis such as direct (D), reverse (R) and constant pH (C) process were followed using 20 vol% HH and 2 M NaOH solutions as precipitating agents. In 'D' process, appropriate amount of HH solution was added drop wise to the requisite amount of chloride / nitrate precursors of Ni, Zr and Y salts, until the pH reaches ~10. The pH of this chloride / nitrate precursor solution was further increased to ~ 13 by the addition of NaOH solution. In 'R' process, same amount of chloride / nitrate precursors of Ni, Zr and Y salts were added drop wise to HH solution (same amount used as in direct process). After completion of reaction, appropriate amount of NaOH was added to the precursor up to pH 13. However, in 'C' process, both HH and chloride / nitrate precursors of Ni, Zr and Y salts were added drop wise to HH solution to maintain a pH ~ 10. After reaction, appropriate amount of NaOH was added to increase the pH of the precursor up to 13. The precipitates obtained in all these three ways of synthesis, using either chloride or nitrate precursors, were collected, washed and dried in an oven to form as-synthesized powder. Then these powders were mixed with iso-propyl alcohol and ground in planetary mill at 350 rpm for 1h, using zirconia balls. The powders were dried after ball milling and were calcined at 650 °C. The prepared samples are designated as D/R/C N30 CL/NT AS/650, where D/R/C represent direct/reverse/constant pH process, N30 represent 30 vol% nickel, CL/NT represents precursor containing chloride/nitrate salts of metal ions, AS/650 represents as-synthesized/calcined at 650 °C. Thermal behavior, structure, morphology and shrinkage behavior of different process derived NiO: 8YSZ powders were analyzed.

5.1.3: Results and discussion

5.1.3.1: Thermal

DSC-TG curves of D N30 CL AS, R N30 CL AS and C N30 CL AS are shown in Fig. 5.1 (a), (b) and (c), respectively and Fig. 5.2 (a), (b) and (c) show DSC-TG curves of D N30 NT AS, R N30 NT AS and C N30 NT AS, respectively.
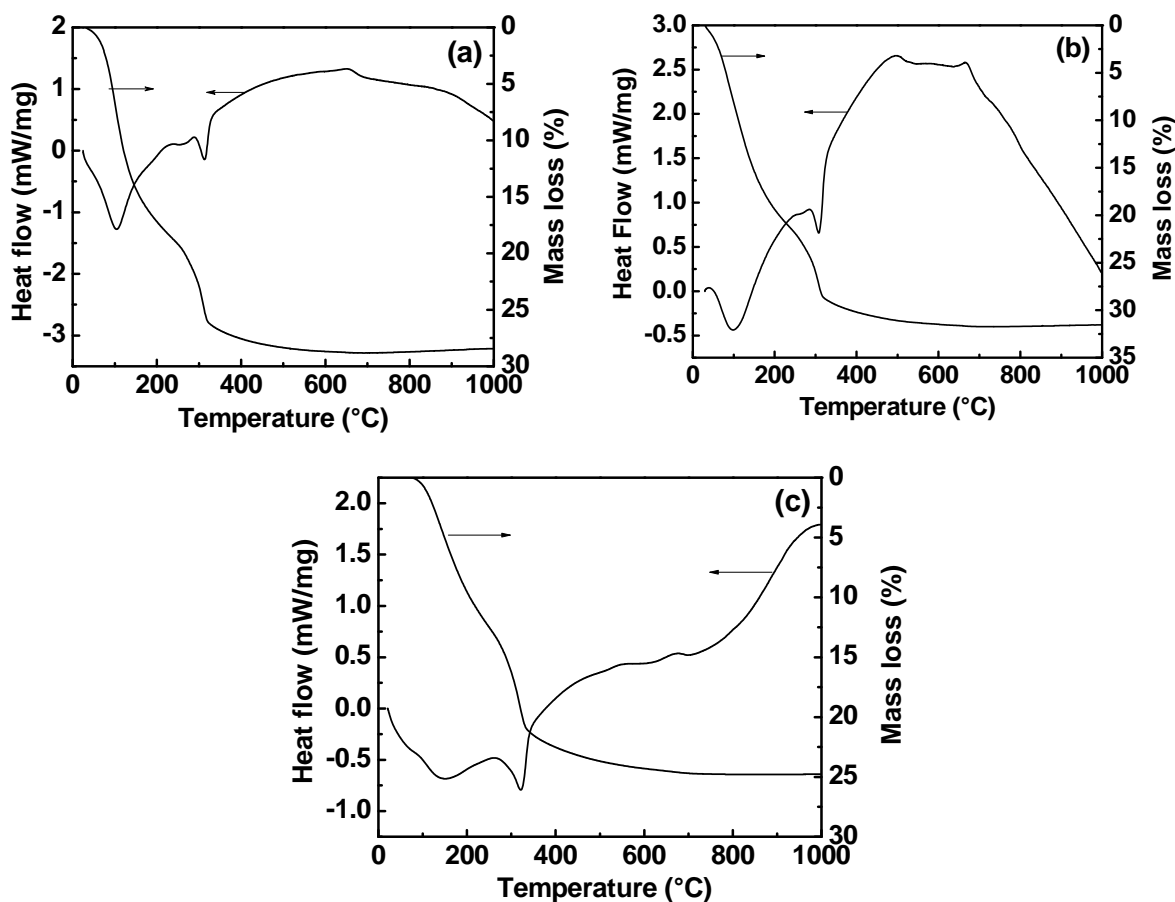
Fig. 5.1: DSC-TG curves of (a) D N30 CL AS, (b) R N30 CL AS and (c) C N30 CL AS.

DSC-TG curves of the as-synthesized powders prepared via either direct, reverse or constant pH process, using either chloride or nitrate precursors, look similar in nature. A major weight loss of around 30 % was observed in all samples from room temperature to 400 °C accompanied with two endothermic peaks at around 100 °C and 325°C. The first endothermic peak was due to the evaporation of physically adsorbed water or moisture present in the sample and the second peak may be due to evaporation of chemically bonded water or decomposition of nickel hydroxides (which may present in the as-synthesized condition). The broad exothermic peak starting from 400°C to 800°C along with a weak exothermic peak centered at around 650°C was

due to crystallization of NiO and/or zirconia. To further understand the phase formation behavior, the as-synthesized powders were calcined at 650 °C and XRD was performed on both the as-synthesized and calcined powders.
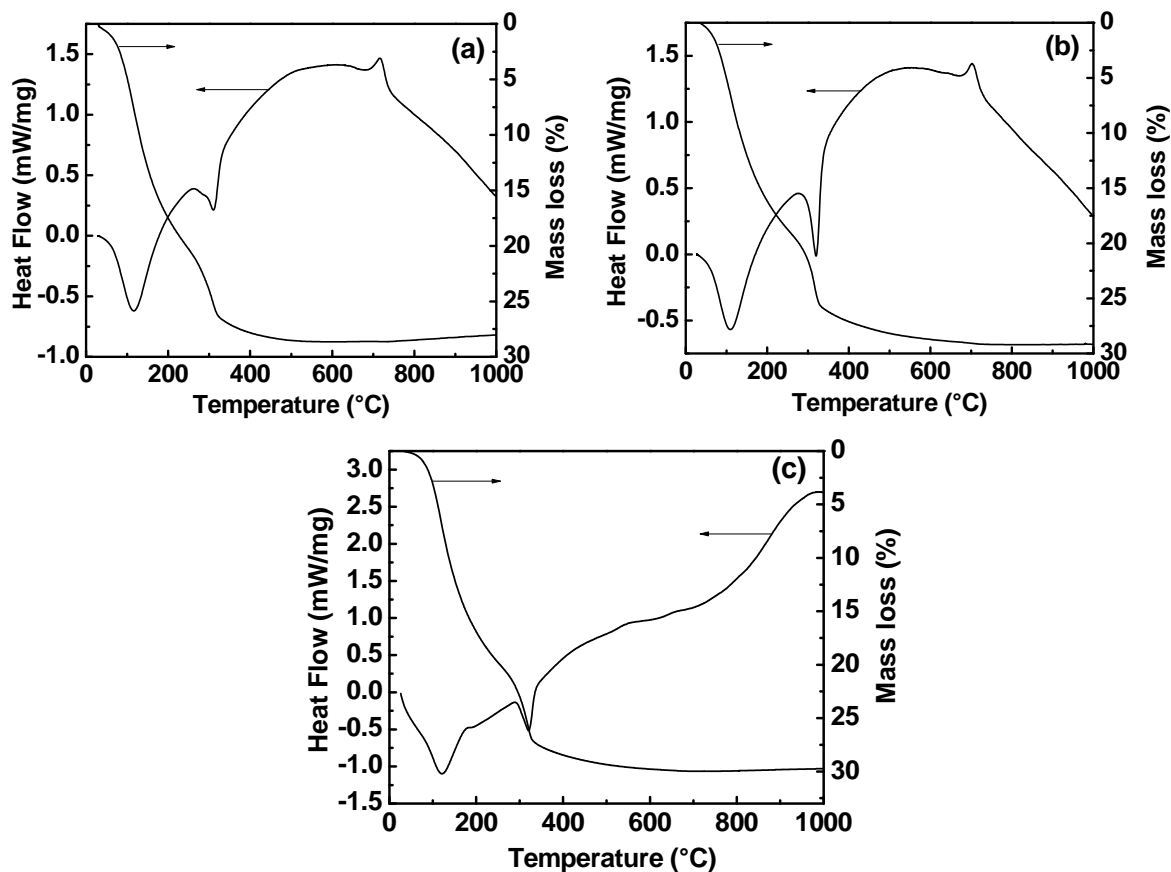
Fig. 5.2: DSC-TG curves of (a) D N30 NT AS, (b) R N30 NT AS and (c) C N30 NT AS.

5.1.3.2: Structure

XRD patterns of as-synthesized and calcined (650 °C) powders prepared in various processes of co-precipitation synthesis are shown in Fig. 5.3 and Fig. 5.4, respectively. The direct, reverse and constant pH process derived as-synthesized powders were found to contain crystalline $Ni(OH)_2$ [as per JCPDS number 00-014-0117] and amorphous zirconium hydroxide. After calcination at 650 °C, all the peaks in Fig. 5.4 are identified with either cubic NiO or cubic YSZ as per the JCPDS number 01-078-0423or 00-049-1642, respectively. The crystallite size of $Ni(OH)_2$ (as-synthesized) and NiO, YSZ (calcined at 650 °C), prepared in different processes are given in Table 5.1. The crystallite size of $Ni(OH)_2$, NiO and YSZ were found to be the lowest for the samples prepared in constant pH process, using either chloride or nitrate precursors.
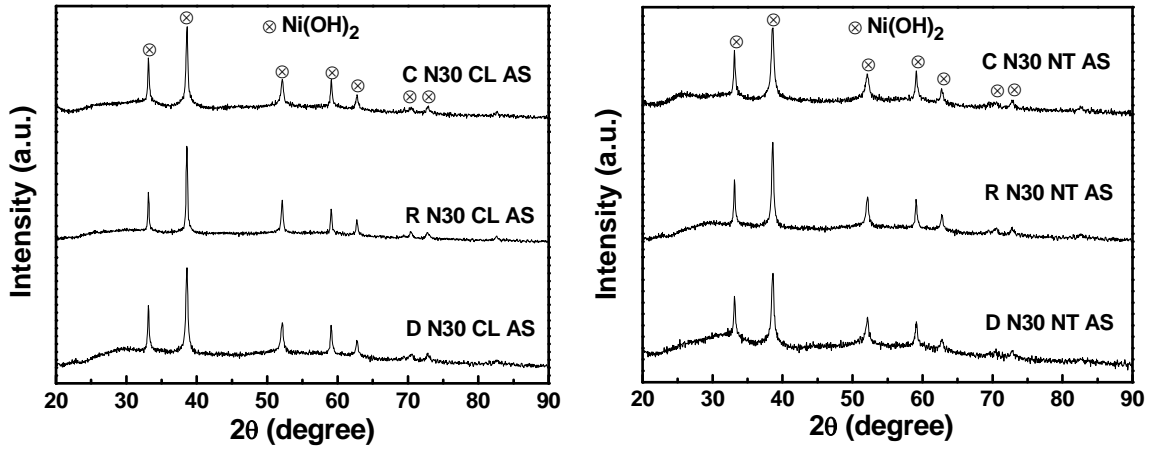
Fig. 5.3: XRD patterns of as-synthesized powders prepared in various conditions.
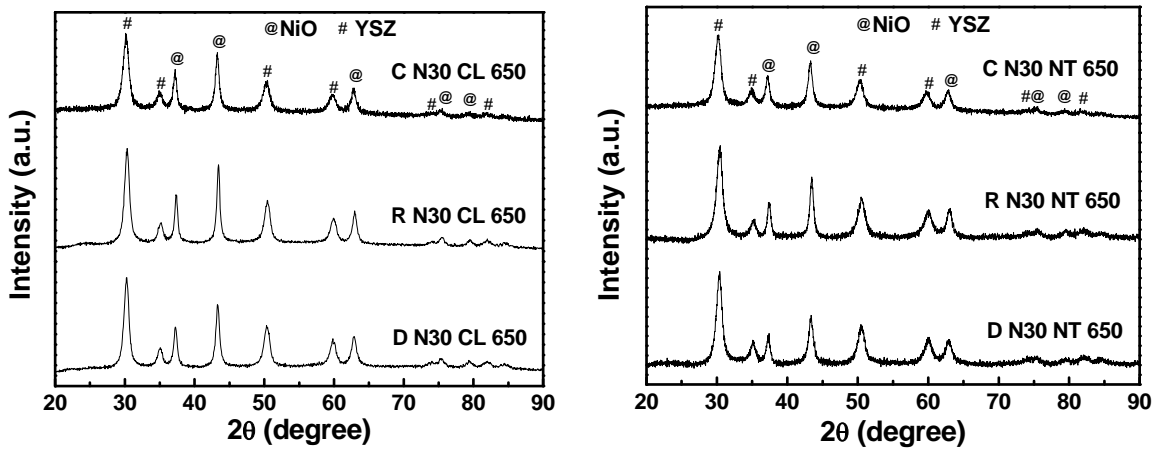
Fig. 5.4: XRD patterns of calcined powders prepared in various ways of synthesis condition.

Table 5.1: Crystallite size of $Ni(OH)_2$, NiO and YSZ for different samples

Sample	Crystallite size of $Ni(OH)_2$ (nm)	Sample	Crystallite size of NiO (nm)	Crystallite size of YSZ (nm)
D N30 CL AS	26	D N30 CL 650	14	10
R N30 CL AS	36	R N30 CL 650	17	10
C N30 CL AS	25	C N30 CL 650	14	8
D N30 NT AS	21	D N30 NT 650	12	10
R N30 NT AS	25	R N30 NT 650	15	9
C N30 NT AS	18	C N30 NT 650	12	8

To confirm the phase before and after reduction, the as-synthesized powders were calcined at 1200 °C and then reduced in H_2 atmosphere at 900 °C. Typical XRD patterns of constant pH process derived powders before and after reduction are shown in Fig. 5.5 (a) and (b), respectively. The calcined powders were found to contain cubic NiO and YSZ, whereas, after reduction, successful conversion of NiO to Ni was confirmed along with YSZ.
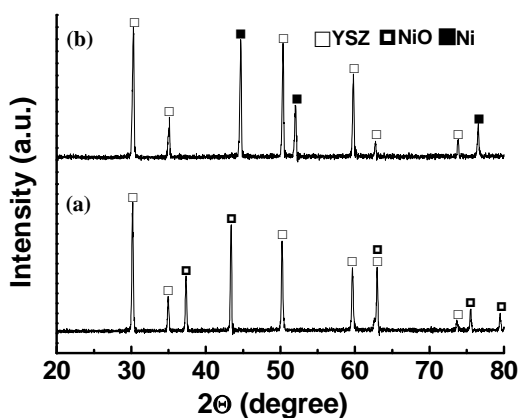
Fig. 5.5: XRD patterns of (a) NiO: 8YSZ and (b) Ni: 8YSZ

5.1.3.3: Morphology

Powder morphology of two specific samples such as C N30 CL 650 and C N30 NT 650 was observed using FE-SEM and these are shown in Fig. 5.6 (a) and (b), respectively. The shape of the particles are nearly spherical in nature. The particle size was found to be ~ 40 nm in both cases.
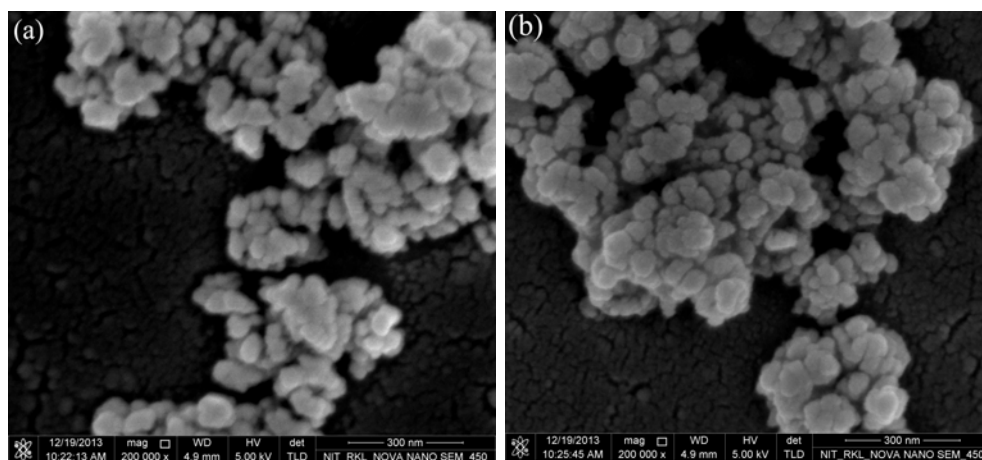
Fig. 5.6: Powder morphology of (a) CN30CLS650 (b) CN30NT650.

5.1.3.4: Shrinkage

Shrinkage behavior of NiO: 8YSZ pellets, fabricated using chloride and nitrate precursor based calcined powders, were studied using dilatometer and are shown in Fig. 5.7 (a) and (b), respectively. In all cases, shrinkage was found to be 14 to 18 % up to 1200 °C. From this study, it seems that NiO: 8YSZ pellets may be sintered near or above 1200 °C.
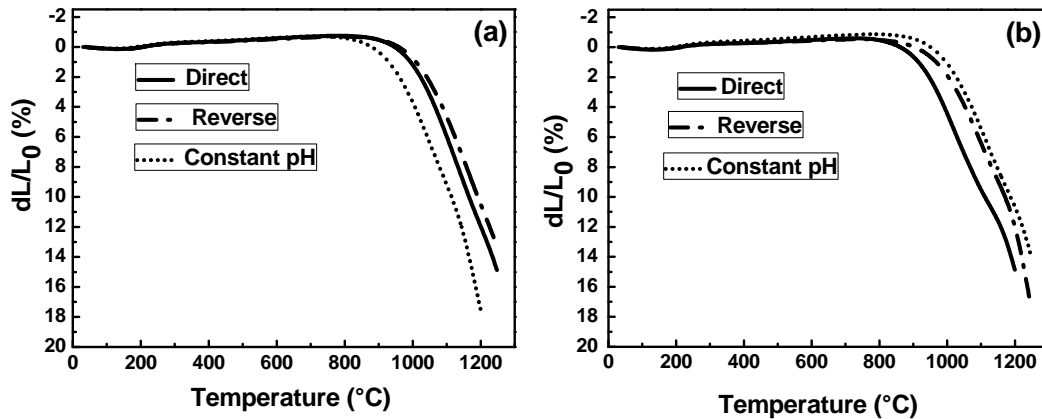
Fig. 5.7: Shrinkage behavior of NiO: 8YSZ pellets, prepared using (a) chloride and (b) nitrate precursor based processes.

5.1.4: Summary

30 vol % Ni containing NiO: 8YSZ powders have been successfully prepared through co-precipitation method via direct, reverse and constant pH process using both chloride and nitrate precursors. The as-synthesized powders contain crystalline $Ni(OH)_2$ and amorphous zirconium hydroxide. All powders show cubic NiO and YSZ phases after calcination at 650 °C and the crystallite size of NiO and YSZ was found to be the lowest for constant pH process based powders. The powders were nearly spherical in shape with particle size of ~ 40 nm. The NiO: 8YSZ pellets prepared in all processes may be sintered at or above 1200 °C.

Density/porosity and microstructure of NiO/Ni: 8YSZ composites as well as electrical conductivity of Ni: 8YSZ cermet, fabricated using the above prepared fine powders is motivating and hence have been studied and discussed in the next Chapter.

CHAPTER 5.2

Density/porosity and microstructure of direct, reverse and constant pH derived NiO/Ni: 8YSZ composites as well as electrical conductivity of Ni: 8YSZ cermet

5.2.1: Introduction

In the previous Chapter, 30 vol % Ni containing NiO: 8YSZ powders were successfully synthesized via direct, reverse and constant pH process of co-precipitation method, using both chloride and nitrate precursors. Density/porosity and microstructure 30 vol % Ni containing NiO/Ni: 8YSZ composites as well as electrical conductivity of Ni: 8YSZ cermet, fabricated using these powders were studied and results are correlated in this Chapter.

5.2.2: Experimental

Synthesis of NiO: 8YSZ powders via direct, reverse and constant pH process through co-precipitation method using either chloride or nitrate precursors were discussed in section 5.1.2 in chapter 5.1. After calcination at 650 °C, the NiO: 8YSZ powders were mixed thoroughly with the optimized amount of binder (2 wt % PVA) and then compacted into rectangular pellets at optimized compaction pressure (588 MPa) [the optimization of binder concentration and compaction pressure was discussed in Chapter 4.2]. The green NiO: 8YSZ pellets were sintered at 1200 °C in air atmosphere to obtain dense NiO: 8YSZ composites. These composites were reduced in H_2 atmosphere at 900 °C to form Ni: 8YSZ cermet. The composites and cermets, fabricated from powders synthesized in different processes are designated as D/R/C N30 CL/NT S12 UR/R, where D/R/C represent direct/reverse/constant pH process, N30 represent 30 vol% nickel, CL/NT represents chloride/nitrate precursor, S12 represents sintered at 1200°C, UR/R represents unreduced / reduced samples. The properties such as density/porosity, microstructure and electrical conductivity of these composites or cermets were studied and the results are compared.

5.2.3: Results and discussion

5.2.3.1: Density and porosity

The variation of density/porosity of NiO/Ni: 8YSZ fabricated using calcined powders prepared in different processes using chloride and nitrate precursors are shown in Fig. 5.8 (a) and (b), respectively. Density of NiO: 8YSZ (before reduction) composites prepared using chloride and nitrate precursors was found to be in between 85 % and 95 %, depending on synthesis processes. The corresponding density of Ni: 8YSZ (after reduction) cermets was found to be in between 70 % and 80 %, depending on synthesis processes. However, constant pH derived samples show better density before as well as after reduction. The porosity of NiO: 8YSZ composite was lower than the

porosity of Ni: 8YSZ cermet, because of the volume change associated with the reduction of NiO to Ni after heat-treatment in H_2 atmosphere. The porosity of Ni: 8YSZ cermet, fabricated from powders prepared in different processes using chloride and nitrate precursors, was found to be in between 20 % and 30 %.
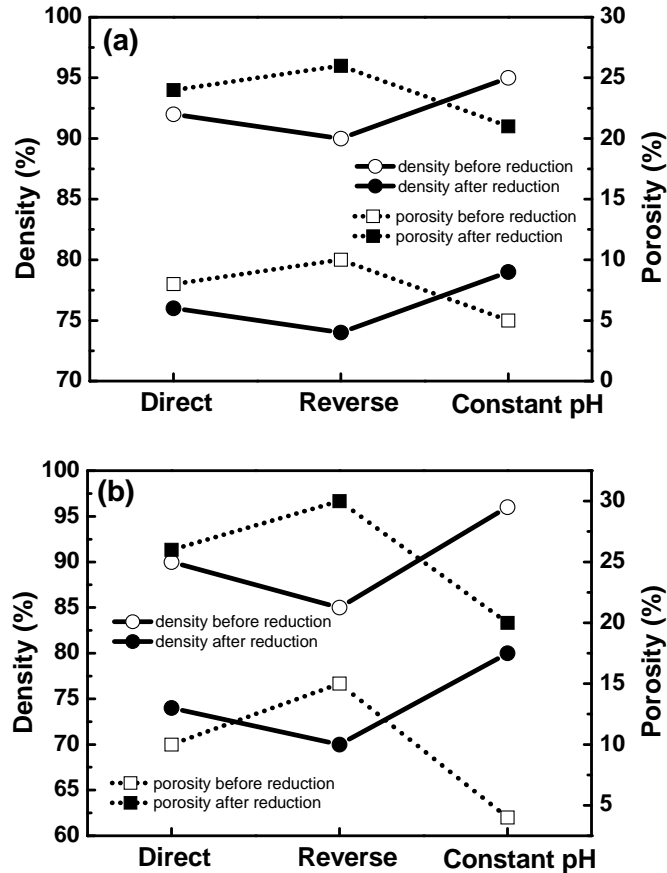
Fig. 5.8: Density/porosity variation for direct, reverse and constant pH process derived NiO: 8YSZ composite (before reduction) and Ni: 8YSZ (after reduction) cermet prepared using (a) chloride and (b) nitrate precursors.

5.2.3.2: Microstructure

Microstructure of sintered NiO: 8YSZ composites prepared in different processes using chloride precursors is shown in Fig. 5.9. In these composites, smaller and uniform particles are observed. Higher density with less porosity was observed in CN30CLS12 UR composites. The particle size in CN30CLS12 UR composite was found to be in the range of 300 nm to 600 nm. Microstructure of sintered NiO: 8YSZ composites prepared in different processes using nitrate precursors is shown in Fig. 5.10. Dense microstructure with non-uniform particles is observed in CN30NTS12 UR composite. The particle size was found to be in the range of 500 nm to 1.5 µm. However, direct and reverse process derived composites are more porous in nature.
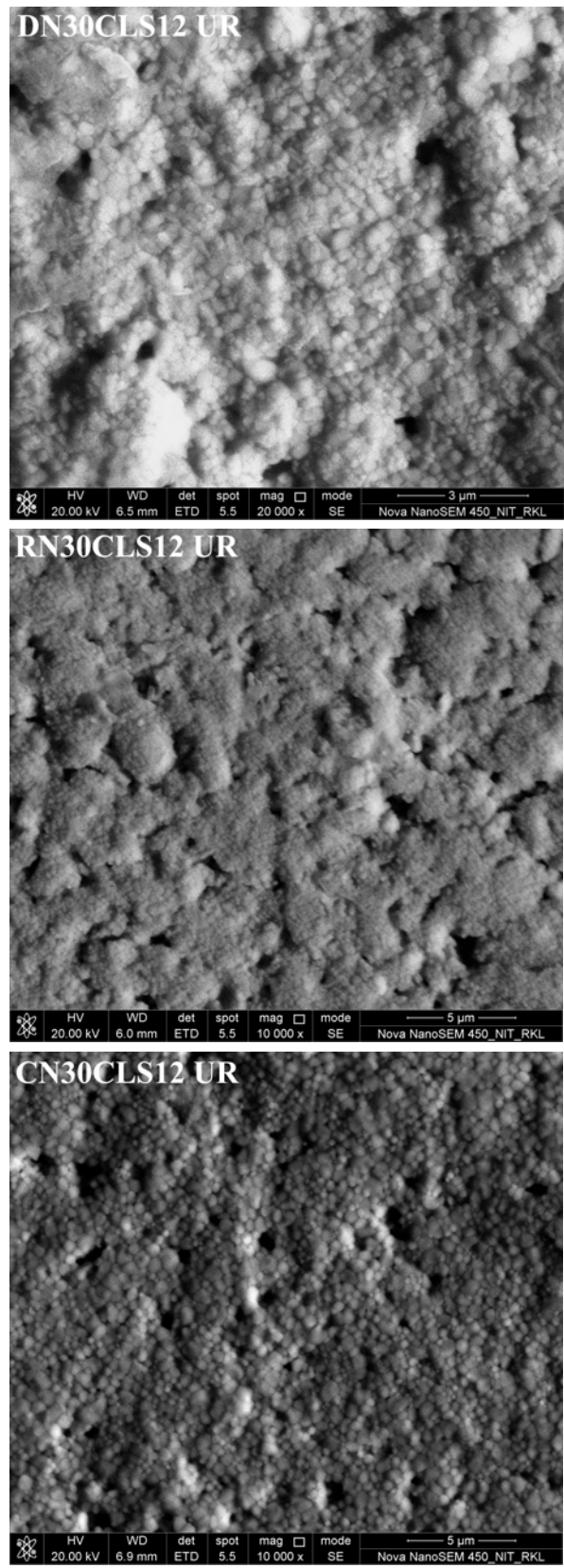
Fig. 5.9: FE-SEM micrographs of sintered NiO: 8YSZ pellets prepared using chloride salts.
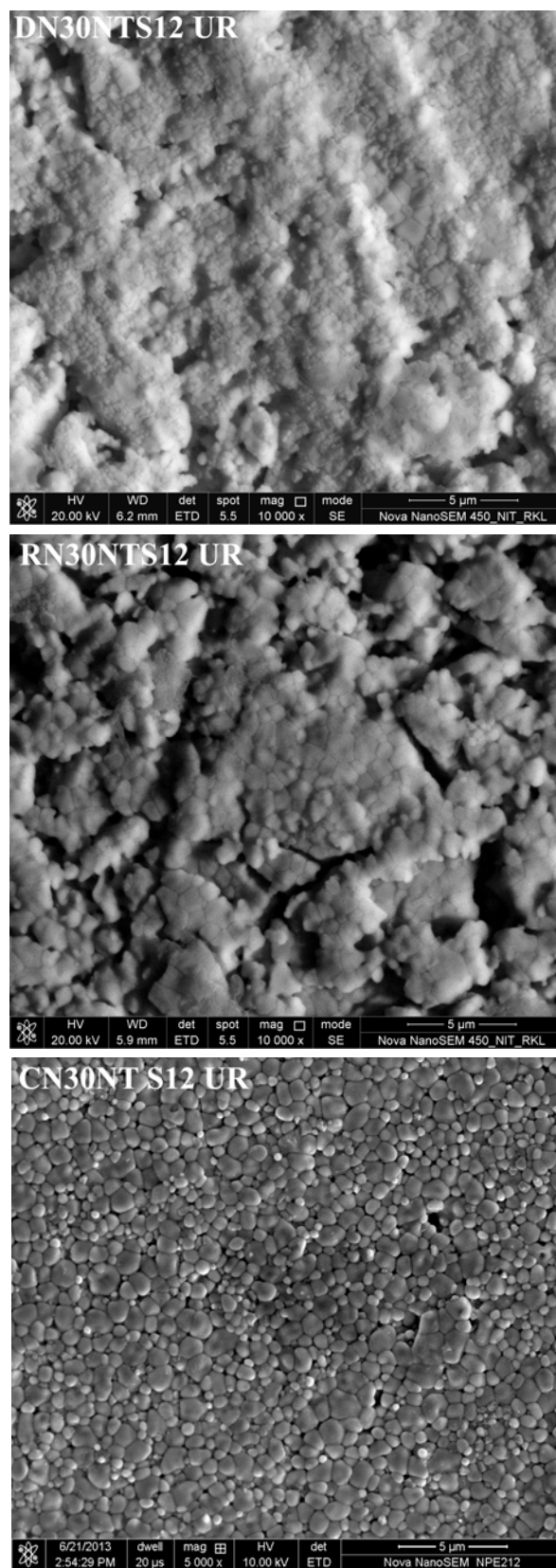
Fig. 5.10: FE-SEM micrographs of sintered NiO: 8YSZ pellets prepared using nitrate salts.

From the microstructure point of view, the sintered NiO: 8YSZ composites prepared via constant pH process using chloride and nitrate precursor are more suitable than direct and reverse processes. To further understand the particle size and the microstructure at higher sintering temperature, the constant pH process derived NiO: 8YSZ composites were sintered at 1300 °C. Fig. 5.11 shows FE-SEM micrographs of constant pH process derived sintered (1300 °C) NiO: 8YSZ composites prepared using chloride and nitrate precursors. Both composites CN30CLS13 UR and CN30 NTS13 UR show dense microstructure having particle size in the range of 500 nm to 2 μm. It was also observed that there is no significant increase in the particle size with increase in sintering temperature.
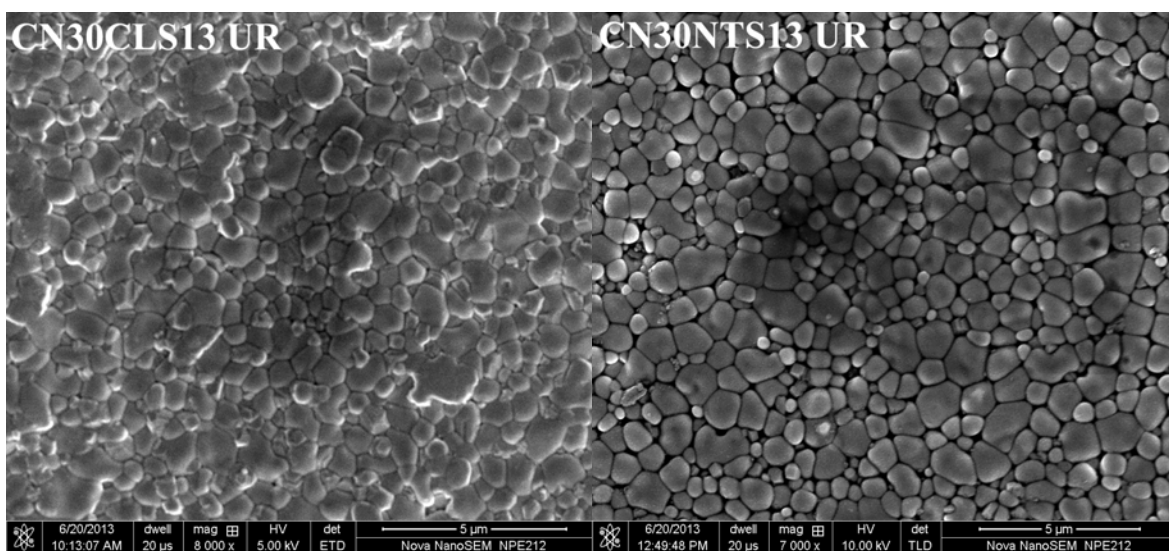
Fig. 5.11: FE-SEM micrographs of sintered (1300 °C) NiO: 8YSZ pellets.

To compare the microstructure of Ni: 8YSZ cermets prepared in different processes, the sintered (1200 °C) NiO: 8YSZ composites are heat-treated in H_2 atmosphere. Fig. 5.12 shows FE-SEM micrographs of DN30CLS12 R, RN30CLS12 R and CN30CLS12 R cermet. In all three samples, particle size is found to be uniform with the presence of fine pores. The particle size was found to be in the range of 300 nm to 600 nm. To visualize the different phases present and understand the distribution of Ni in YSZ, elemental mapping of Ni and Zr was performed and is shown in Fig. 5.13. It was observed that Ni particles (red) are uniformly distributed in YSZ (blue) matrix in all samples. However, ultra-fine Ni particles are present in DN30CLS12 R cermet, as observed from both micrograph and elemental mapping.

Fig. 5.12: FE-SEM micrographs of DN30CLS12 R, RN30CLS12 R and CN30CLS12 R.

.
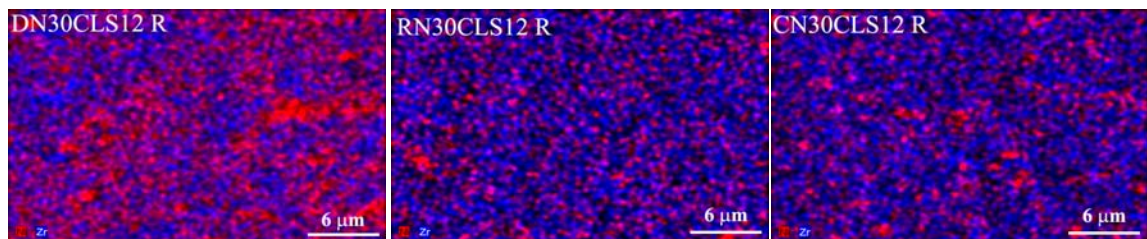
Fig. 5.13: EDS mapping of DN30CLS12 R, RN30CLS12 R and CN30CLS12 R.

Fig. 5.14 shows FE-SEM micrographs of DN30NTS12 R, RN30NTS12 R and CN30NTS12 R cermet and corresponding EDS mapping are shown in Fig. 5.15.
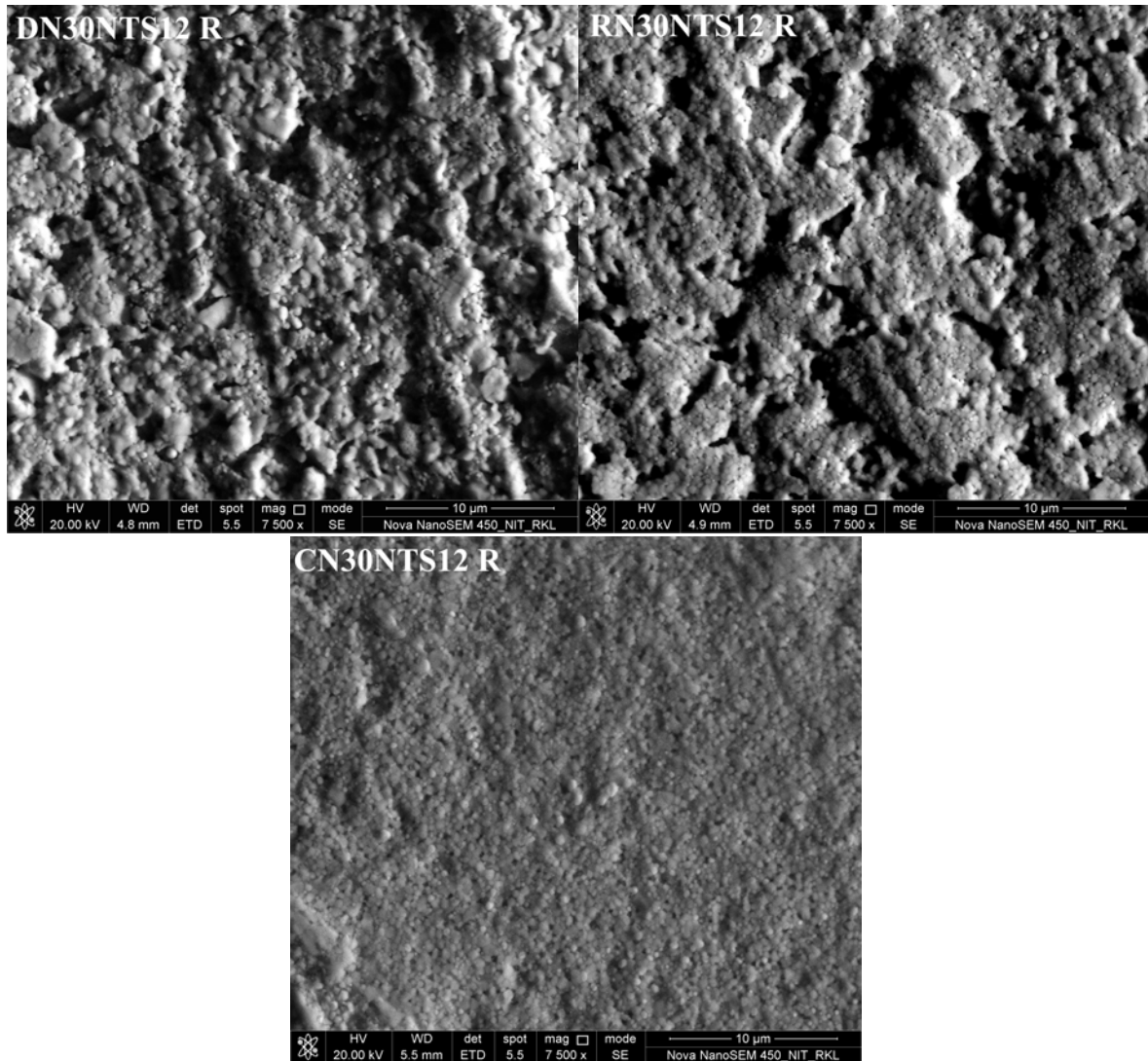
Fig. 5.14: FE-SEM micrographs of DN30NTS12 R, RN30NTS12 R and CN30NTS12 R.
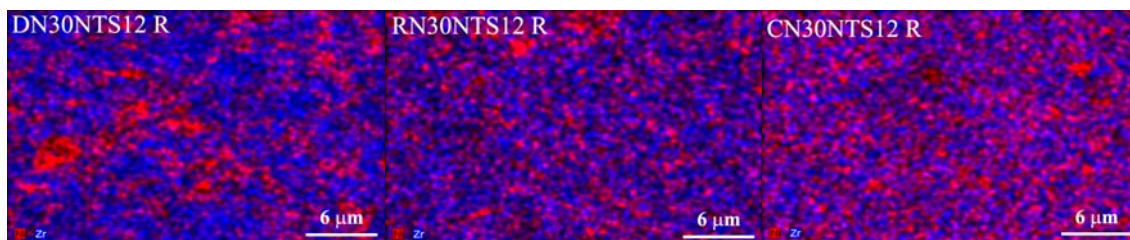
Fig. 5.15: EDS mapping of DN30NTS12 R, RN30NTS12 R and CN30NTS12 R.

Ni: 8YSZ cermet prepared via direct and reverse process such as DN30NTS12 R and RN30NTS12 R are found to be more porous than CN30NTS12 R cermet. The particles in CN30NTS12 R cermet were nearly spherical in shape and particle size ranges in between 400 nm to 600 nm. From EDS mapping it was confirmed that Ni particles are more connected in CN30NTS12 R cermet than in other samples. From analysis of microstructure and EDS mapping of Ni: 8YSZ, it was further interesting to study the electrical conductivity of these cermets for suitability in SOFC application.

5.2.3.3: Electrical conductivity

Fig. 5.16 shows temperature dependent conductivity of DN30CLS12 R, RN30CLS12 R and CN30CLS12 R cermet.
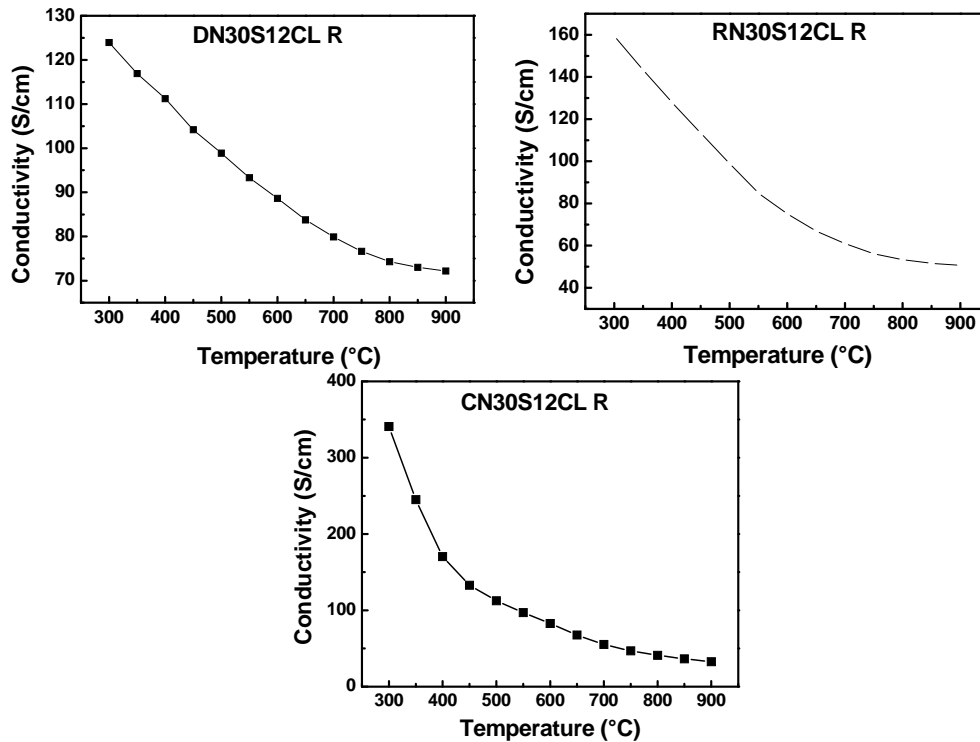
Fig. 5.16: Temperature dependent electrical conductivity of DN30CLS12 R, RN30CLS12 R and CN30CLS12 R.

All the cermets show electronic type behavior and CN30NTS12 R cermet shows higher conductivity than DN30NTS12 R and RN30NTS12 R. Fig. 5.17 show temperature dependent electrical conductivity of DN30NTS12 R, RN30NTS12 R and CN30NTS12 R cermets. All the cermets show electronic type behavior. The highest conductivity was also observed for CN30NTS12 R cermet. The value of conductivity of CN30CLS12 R and CN30NTS12 R was found to be nearly same (~ 350 S/ cm at 300 °C and ~ 30 S/cm at 900 °C). The higher conductivity for

constant pH process derived cermets may be attributed to the highly dense microstructure and better Ni-Ni connectivity.
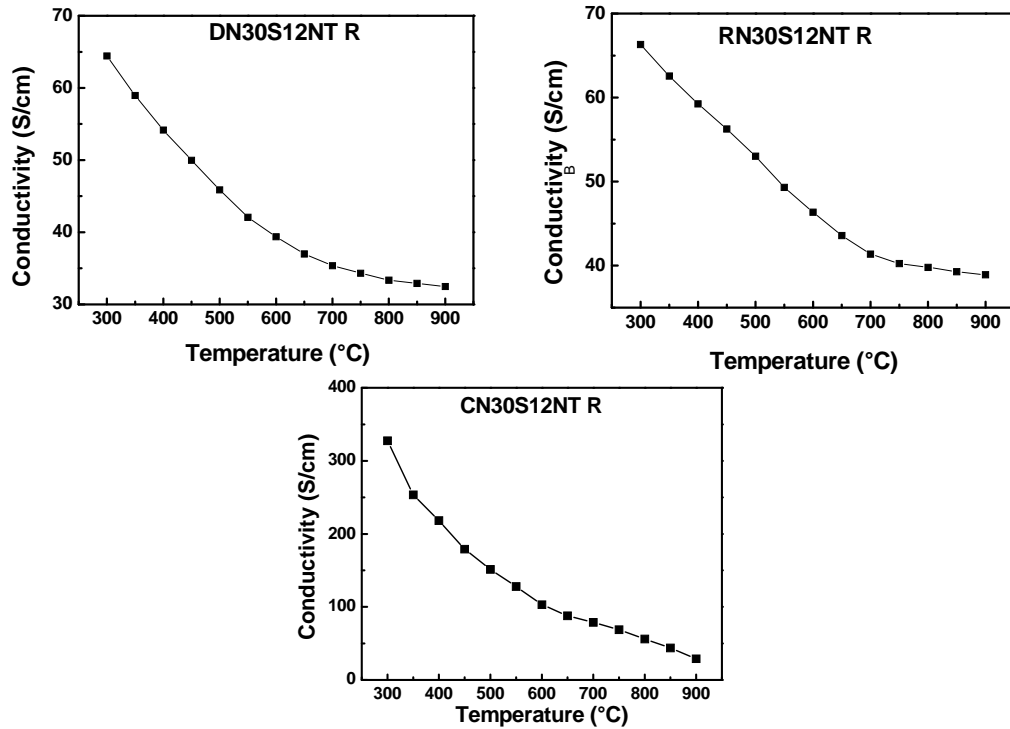
Fig. 5.17: Temperature dependent electrical conductivity of DN30NTS12 R, RN30NTS12 R and CN30NTS12

5.2.4: Summary

The density of NiO/Ni: 8YSZ composites fabricated from constant pH process derived powders using chloride and nitrate precursors was found to be higher as compared to other processes. The particle size of these composites was in the range of 300 nm to 1.5 μm, depending on the precursors used. The chloride and nitrate precursor based constant pH process derived Ni: 8YSZ cermet shows better electrical conductivity with suitable microstructure as compared to the cermets prepared via either direct or reverse process. So, it will be interesting to study the effect of Ni concentration and sintering temperature on microstructure and electrical conductivity of constant pH process derived Ni: 8YSZ cermet.

CHAPTER 5.3

Microstructure, electrical conductivity and TEC of constant pH co-precipitation derived 20, 30 and 40 vol % Ni containing Ni: 8YSZ cermets

5.3.1: Introduction

From Chapter 5.2, it was confirmed that the constant pH process is most suitable to develop Ni: 8YSZ cermet for SOFC application in terms of density/porosity, microstructure and electrical conductivity. It would be conducive to analyze the effect of Ni concentration and sintering temperature on the microstructure and electrical conductivity, along with the determination of TEC which would give a better insight for further development of Ni: 8SYZ cermet. Hence, in this Chapter, effect of Ni concentration and sintering temperature on the microstructure and electrical conductivity of constant pH co-precipitation derived Ni: 8YSZ cermets, prepared using chloride and nitrate precursors, are investigated and the TEC value is reported.

5.3.2: Experimental

The procedure for synthesis of NiO: 8YSZ powders by constant pH co-precipitation process using chloride and nitrate precursors, is discussed in Chapter 5.1.2. NiO: 8YSZ powders containing 20, 30 and 40 vol% Ni were synthesized by constant pH process using both chloride and nitrate precursors. After calcination (650 °C), the powders were compacted into pellets using optimized binder concentration (2 wt% PVA) and compaction pressure (588 MPa). The compacted pellets were sintered at 1200 °C and 1300 °C in air atmosphere to obtain NiO: 8YSZ composites and then reduced in H_2 atmosphere at 900 °C to obtain Ni: 8YSZ cermet. The prepared composites are designated as CN*X0*CL/NT S12/13 R, where C represent constant pH process, N*X0* represent vol% nickel, CL/NT represents chloride/nitrate precursors, R represents reduced sample. Different characterization such as density/porosity, microstructure, elemental mapping, electrical conductivity and TEC of Ni: 8YSZ ceremts have been studied and analyzed.

5.3.3: Results and discussion

5.3.3.1: Density and porosity

The effect of Ni concentration on density/porosity of chloride and nitrate precursor based constant pH process derived NiO/Ni: 8YSZ composites, developed at sintering condition of 1200 °C are shown in Fig. 5.18 (a) and (b), respectively. The density of NiO: 8YSZ and Ni: 8YSZ was found to be comparatively higher, while using nitrate precursors. The porosity of both chloride and nitrate precursors based Ni: 8YSZ cermets lie in between 20 % to 27 %, depending on the Ni concentration. Figure 5.19 (a) and (b) show density/porosity of NiO/Ni: 8YSZ composites,

prepared using chloride and nitrate precursors based powders, respectively, at sintering condition of 1300 °C. The density of NiO: 8YSZ composite was comparatively same while using either chloride or nitrate precursor based powders. However, the density of NiO: 8YSZ lies between 90 % to 96 % and the porosity of Ni: 8YSZ cermet varies from 20 % to 27 %, depending on the Ni concentration.
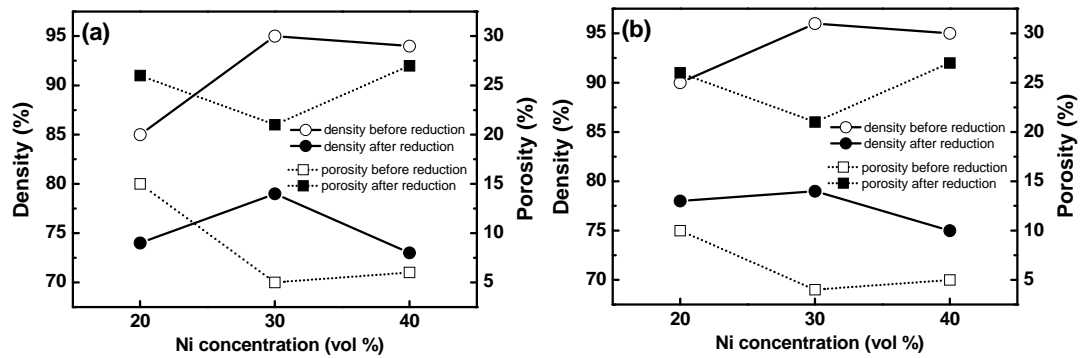
Fig. 5.18: The effect of Ni concentration on density/porosity of (a) chloride and (b) nitrate precursor based constant pH process derived Ni: 8YSZ cermet prepared at sintering condition of 1200 °C.
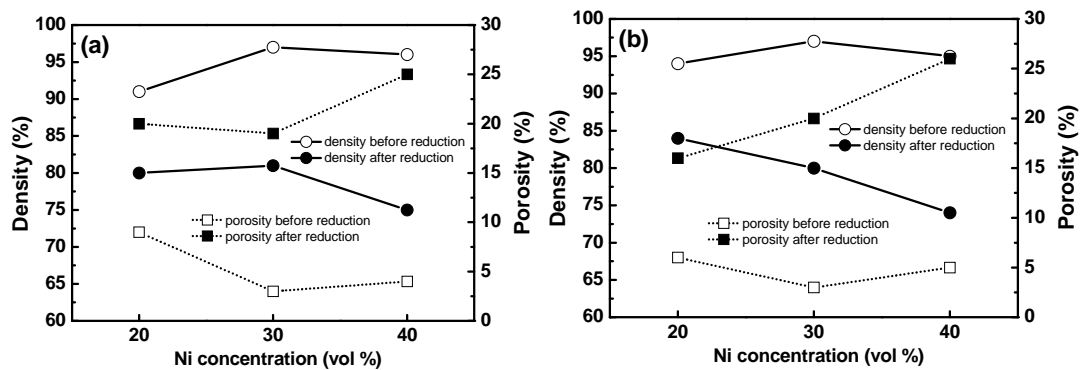
Fig. 5.19: The effect of Ni concentration on density/porosity of (a) chloride and (b) nitrate precursor based constant pH process derived Ni: 8YSZ cermet prepared at sintering condition of 1300 °C.

5.3.3.2: Microstructure

Figure 5.20 shows FE-SEM micrographs of CN20CLS12 R, CN30CLS12 R and CN40CLS12 R and the corresponding EDS mappings are shown in Fig. 5.21. From the three micrographs, it was confirmed that 30 vol % Ni containing cermet shows lower porosity than 20 and 40 vol % Ni containing cermet, which is consistent with density/porosity results shown in Fig. 5.18 (a). Nearly uniform distribution of Ni in 8YSZ matrix was observed in CN30CLS12 R cermet. However, Ni particles are agglomerated and also quite separated for CN20CLS12 R cermet. With

higher Ni concentration for CN40CLS12 R cermet, gradual formation of Ni clusters is observed within YSZ matrix, establishing better connectivity between Ni particles.
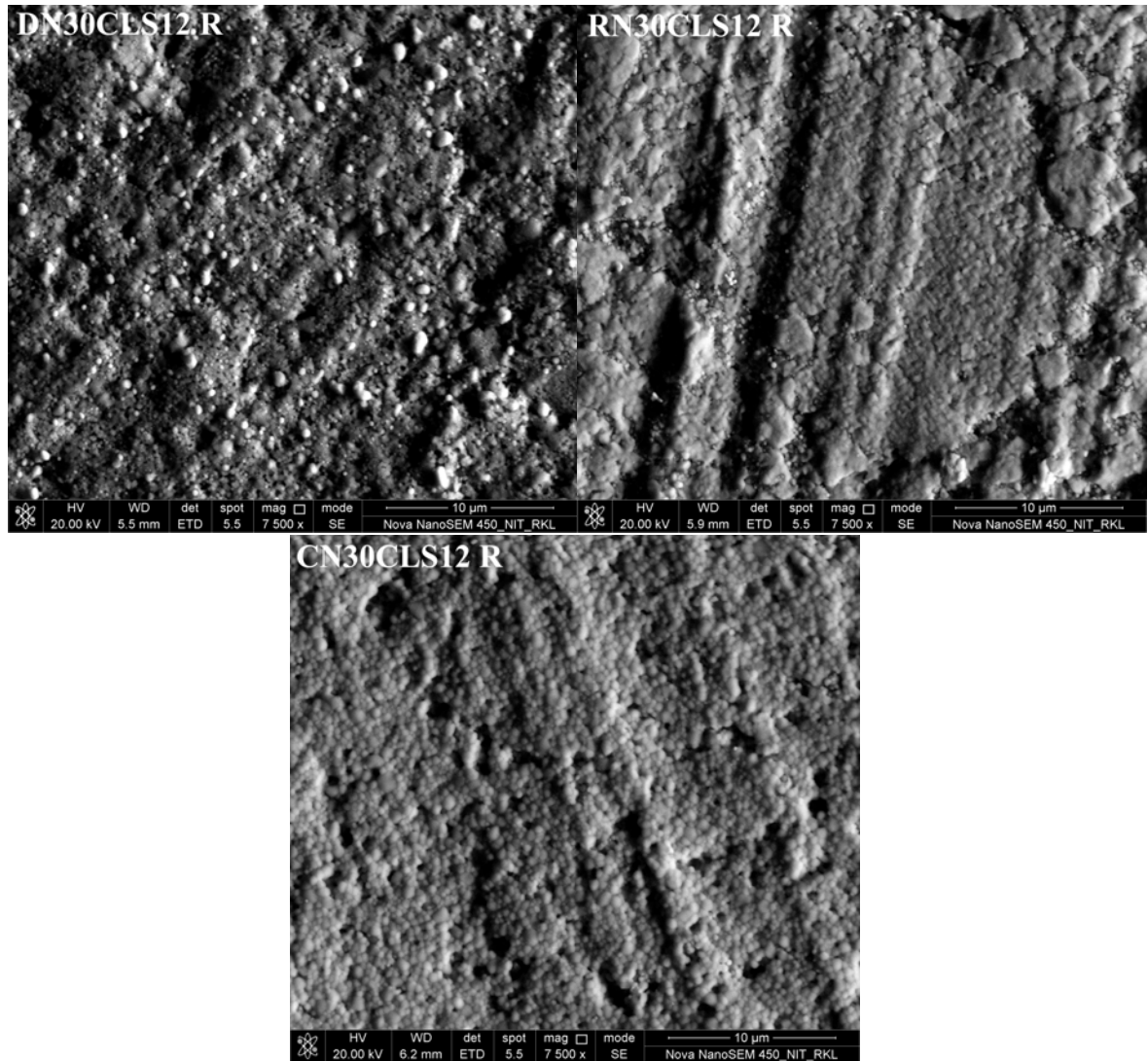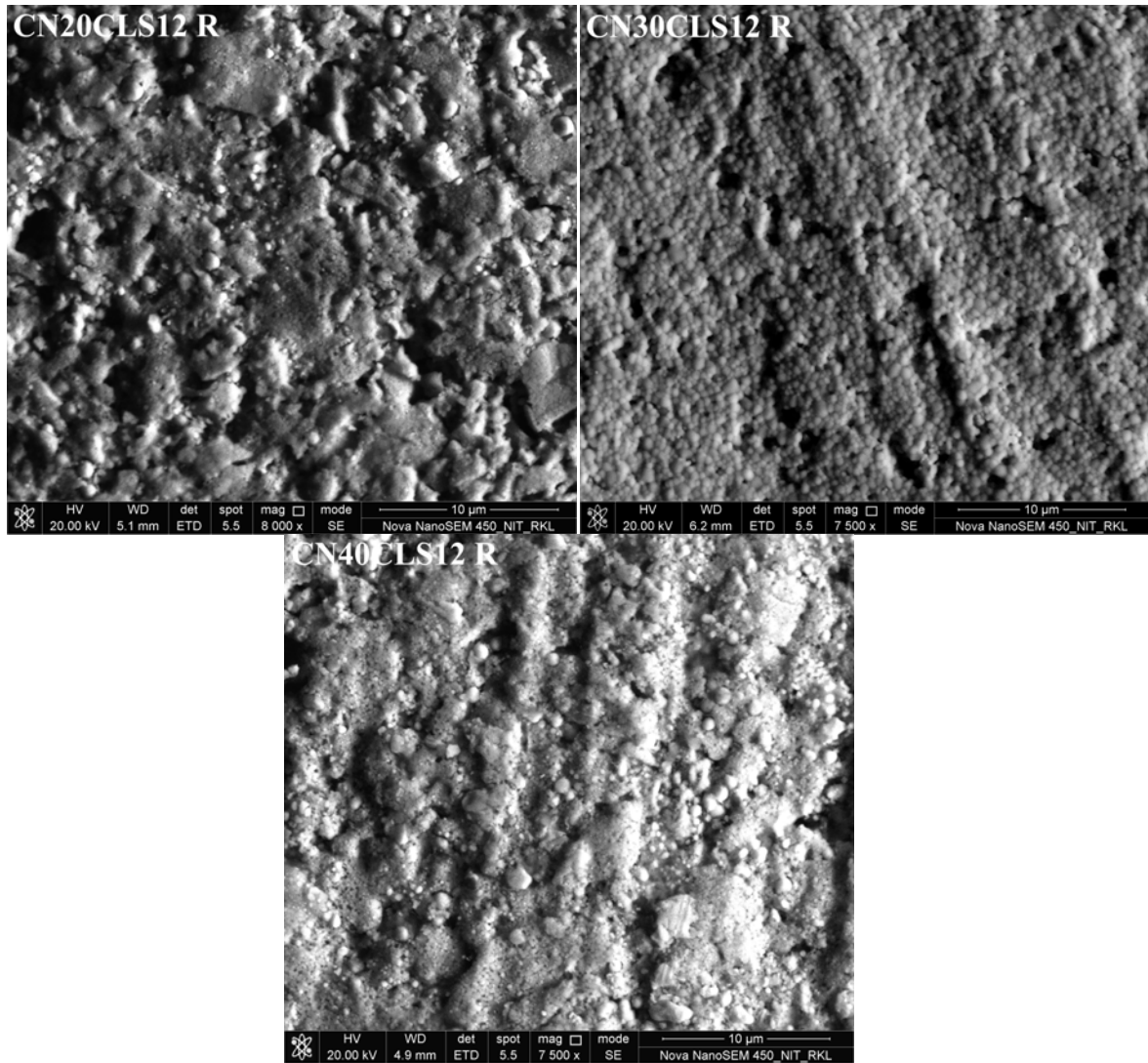

Fig. 5.20: FE-SEM micrographs of CN20CLS12 R, CN30CLS12 R and CN40CLS12 R.
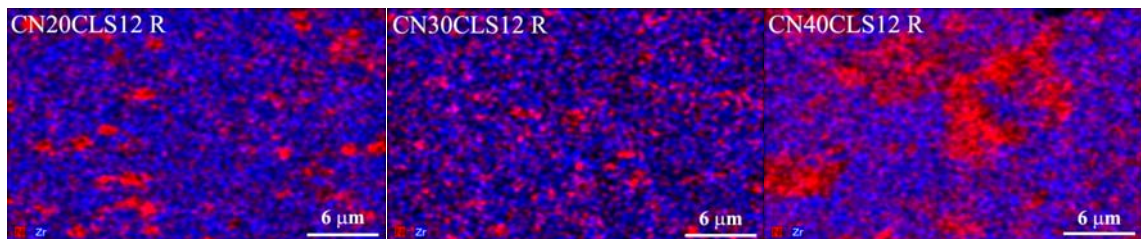
Fig. 5.21: EDS mapping of CN20CLS12 R, CN30CLS12 R and CN40CLS12 R.

In a similar way, microstructure and EDS mapping was performed on nitrate precursor based cermets and are shown in Fig. 5.22 and Fig. 5.23, respectively.
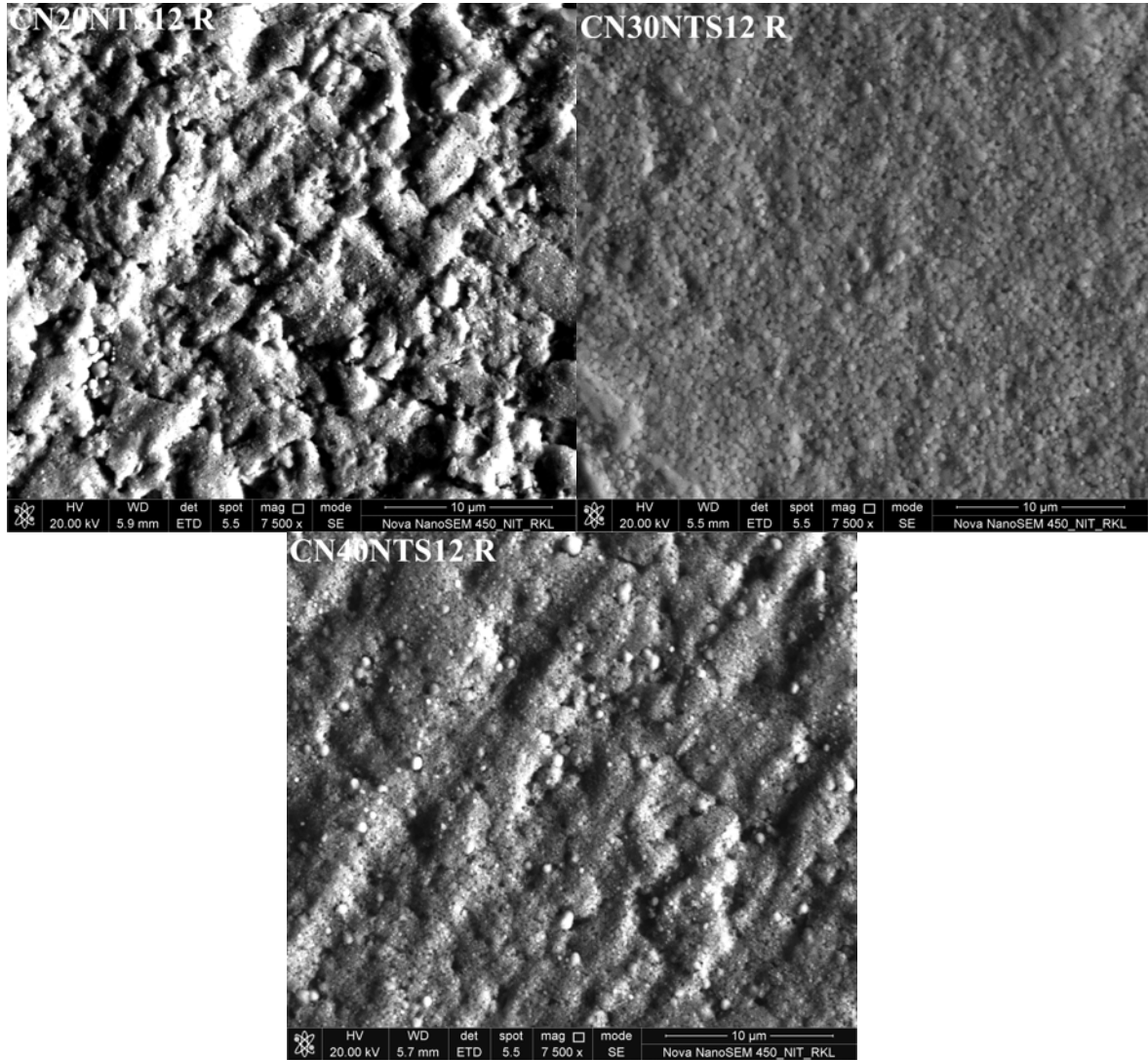
Fig. 5.22: FE-SEM micrographs of CN20NTS12 R, CN30NTS12 R and CN40NTS12 R.
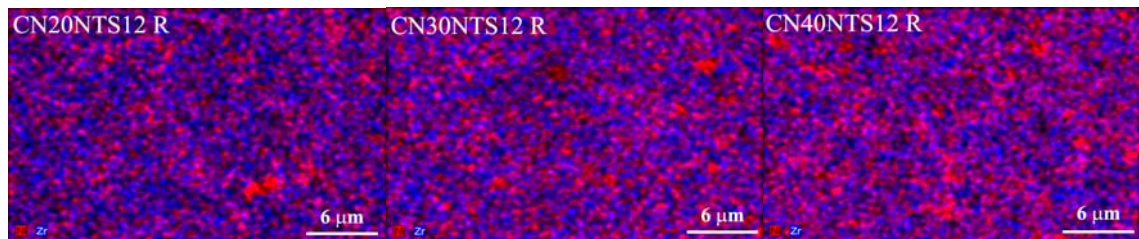
Fig. 5.23: EDS mapping of CN20NTS12 R, CN30NTS12 R and CN40NTS12 R.

From these three micrographs, it was also confirmed that 30 vol% Ni containing cermet (CN30NTS12 R) is less porous as compared to 20 and 40 vol % Ni containing cermets. In all cermets, fine Ni particles are more uniformly distributed in 8YSZ matrix, as confirmed from Fig. 5.23. With increase in Ni concentration, gradual formation of Ni network was also observed.

To further understand the microstructure and distribution of Ni in Ni: 8YSZ cermet prepared at the sintering condition of 1300 °C, FE-SEM with EDS mapping was performed.

Figure 5.24 shows FE-SEM micrographs of CN20CLS13 R, CN30CLS13 R and CN40CLS13 R cermets and corresponding EDS mapping is shown in Fig. 5.25. The particle size was found to increase with increase in sintering temperature from 1200 °C to 1300 °C. However, the particle size in CN30CLS13 R cermet was found to be larger than 20 and 40 vol % Ni contenting cermet. Ni particles are segregated and lie far from each other in 8YSZ matrix, as confirmed from EDS mapping of CN20CLS13 R cermet. However, for CN30CLS13 R cermet, the Ni particles are very fine and seem to be highly dispersed in 8YSZ matrix. With increase in Ni concentration for CN40CLS13 R cermet, gradual establishment of Ni-Ni contact was observed from EDS mapping.

FE-SEM and EDS mapping of CN20NTS13 R, CN30NTS13 R and CN40NTS13 R cermets are shown in Fig. 5.26 and Fig. 5.27, respectively. It was found that the particle size of nitrate precursor based cermet is comparatively larger than the chloride precursor based cermets. In a similar manner, as observed from microstructure (Fig. 5.24) of chloride precursor based cermets, the particle size of nitrate precursor based cermet such as CN30NTS13 R is also found to be quite larger than CN20NTS13 R and CN40NTS13 R cermets. From EDS mapping it was observed that Ni particles are uniformly distributed in both CN20NTS13 R and CN40NTS13 R cermets. However, fine Ni particles seem to be highly dispersed and separated in YSZ matrix for CN30NTS13 R cermet.

For better visualization and understanding of the distribution of Ni particles in 8YSZ matrix particularly for CN30CLS13 R and CN30NTS13 R cermets, secondary image along with EDS mapping was performed. EDS elemental mapping of only Zr, only Ni and both Ni and Zr in combination with SE image are shown in Fig. 5.28 (a), (b) and (c), respectively, for CN30CLS13 R and CN30NTS13 R cermet. From these mappings, it was confirmed that fine Ni particles (500 nm) are not only present at the grain boundary of YSZ (3-5 μm) but are also deposited on surface of YSZ.
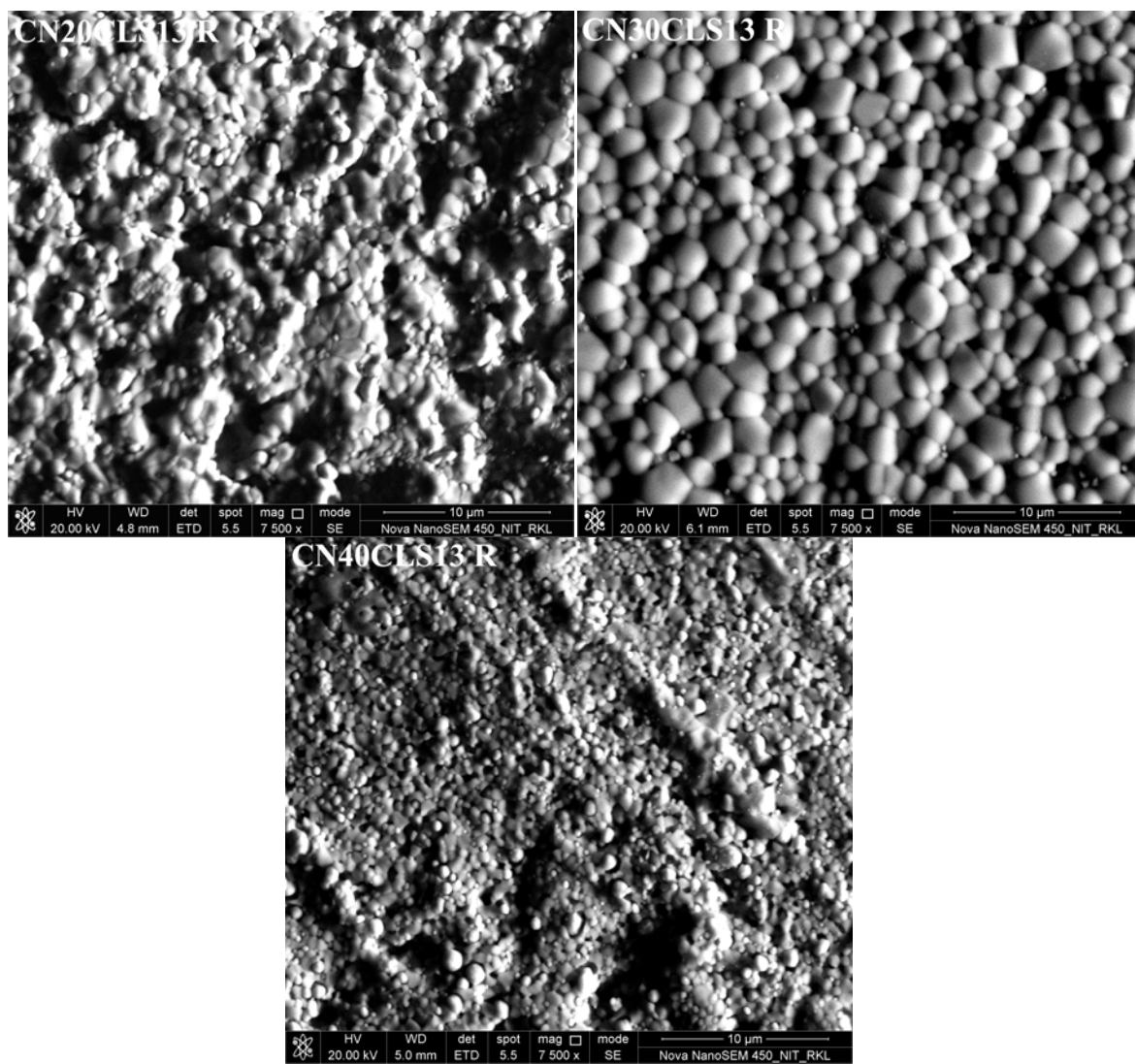
Fig. 5.24: FE-SEM micrographs of CN20CLS13 R, CN30CLS13 R and CN40CLS13 R
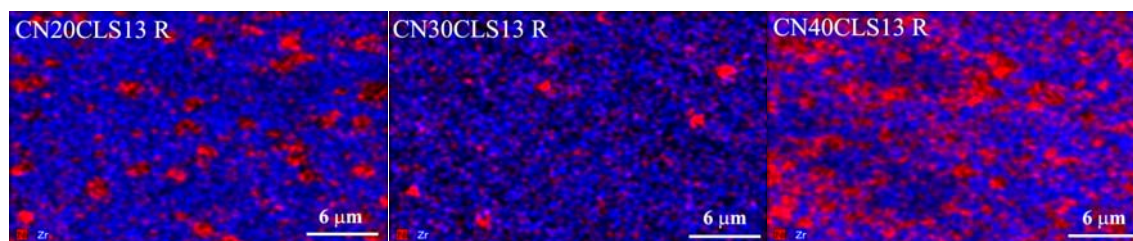
Fig. 5.25: EDS mapping of CN20CLS13 R, CN30CLS13 R and CN40CLS13 R
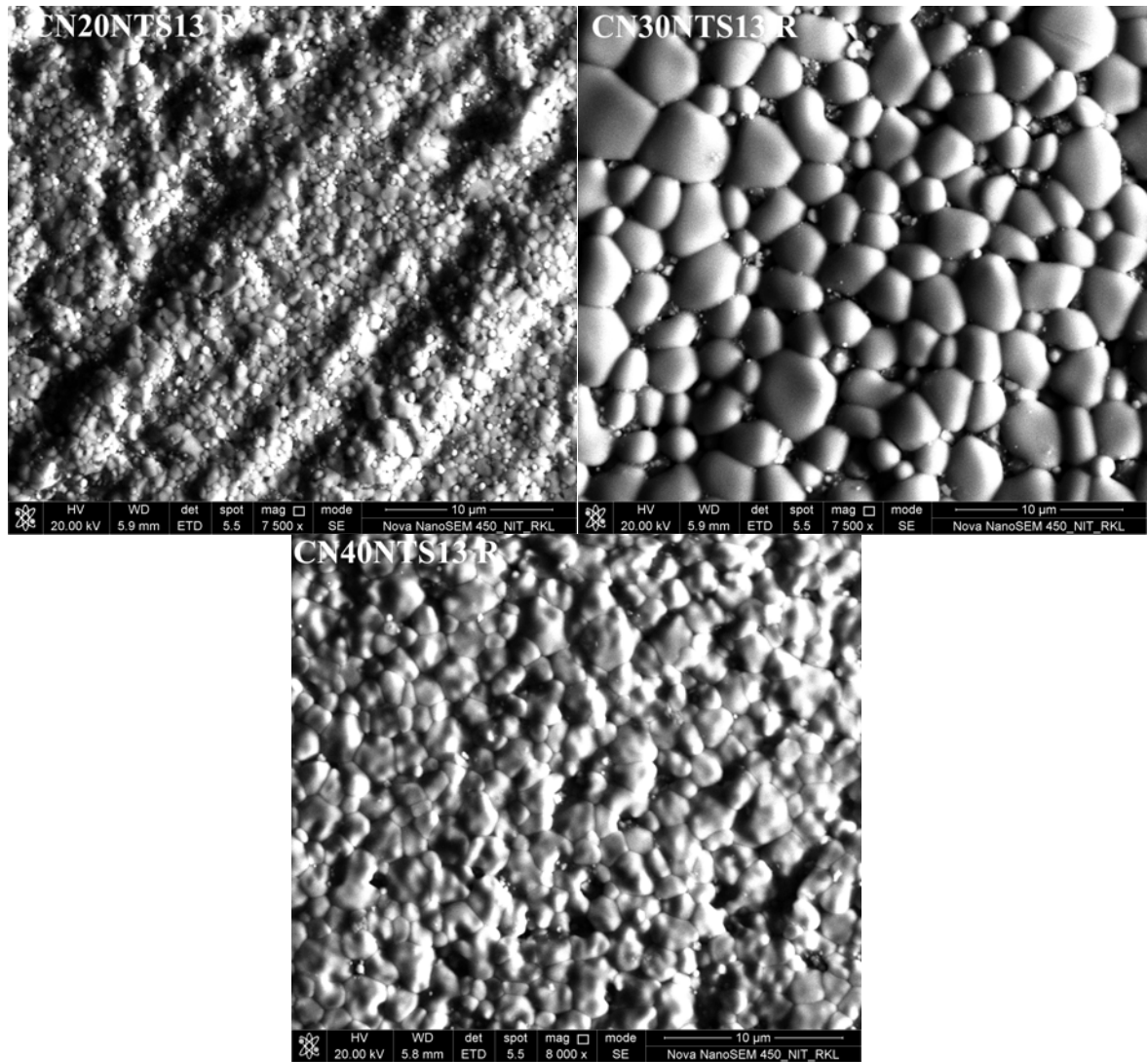
Fig. 5.26: FE-SEM micrographs of CN20NTS13 R, CN30NTS13 R and CN40NTS13 R
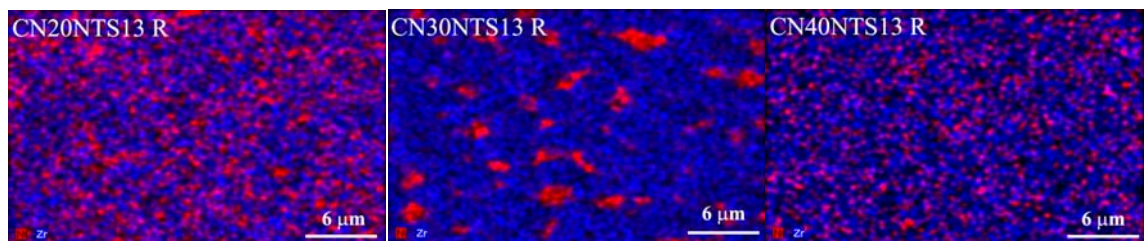
Fig. 5.27: EDS mapping of CN20NTS13 R, CN30NTS13 R and CN40NTS13 R
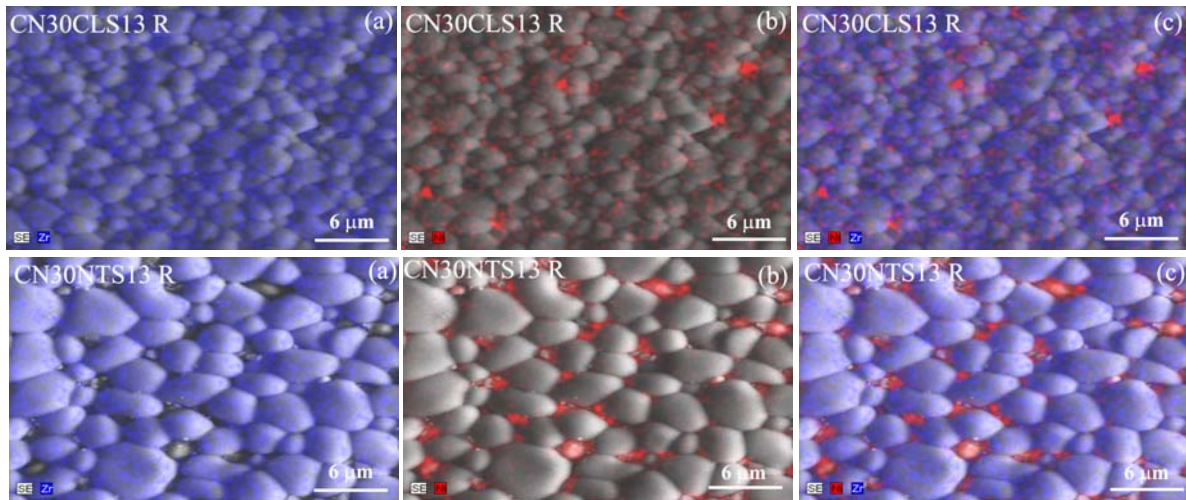
Fig. 5.28: EDS mapping of only Zr (a), only Ni (b), and both Ni and Zr (c) in combination with SE image for the composite CN30CLS13 R and CN30NTS13 R.

The particle size of both Ni and YSZ are found to be smaller in in case of 20 vol % Ni containing cermets (prepared at sintering condition of 1300 °C) such as CN20CLS13 R and CN20NTS13 R due to higher porosity before reduction, which leads to lower contact between the corresponding phases. With increase in Ni concentration, the particle size of YSZ in CN30CLS13 R and CN30NTS13 R was found to increase significantly, which may be due to higher density as well as higher contact between YSZ particles [27]. However, at 40 vol % Ni concentration, the contact between Ni particles in CN40CLS13 R and CN40NTS13 R also increases and the growth of both particles at sintering condition of 1300 °C neutralize each other. Hence the particle size of Ni and YSZ was found to be similar in these cermets.

5.3.3.3: Electrical conductivity

The temperature dependent electrical conductivity of 20, 30 and 40 vol % Ni containing Ni: 8YSZ cermet such as CN20CLS12 R, CN30NTS12 R, CN40CLS12 R, CN20NTS12 R, CN30CLS12 R and CN40NTS12 R are shown in Fig. 5.29 and Fig. 5.30 shows the electrical conductivity behavior with temperature for the cermet such as CN20CLS13 R, CN30NTS13 R, CN40CLS13 R, CN20NTS13 R, CN30CLS13 R and CN40NTS13 R. 20 vol % Ni containing cermets such as CN20CLS12 R, CN20NTS12 R, CN20CLS13 R and CN20NTS13 R show ionic type behavior. However, all other cermets ($\geq$ 30 vol % Ni) show electronic behavior. The ionic behavior is due to better YSZ-YSZ contact, whereas the electronic behavior is due to dominating Ni-Ni contact, as confirmed from EDS mapping. The conductivity value increases with Ni concentration as well as sintering temperature. The typical conductivity value of CN40CLS12 R

and CN40NTS12 R was found to be ~ 650 and ~ 750 S/cm at 300 °C and then decreases to around ~80 and ~100 S/cm at 900 °C, respectively. The typical conductivity value of CN40CLS13 R and CN40NTS13 R was found to be ~1800 S/cm and ~3400 S/cm at 300 °C and then decreases to ~ 150 and ~250 S/cm at 900 °C, respectively.
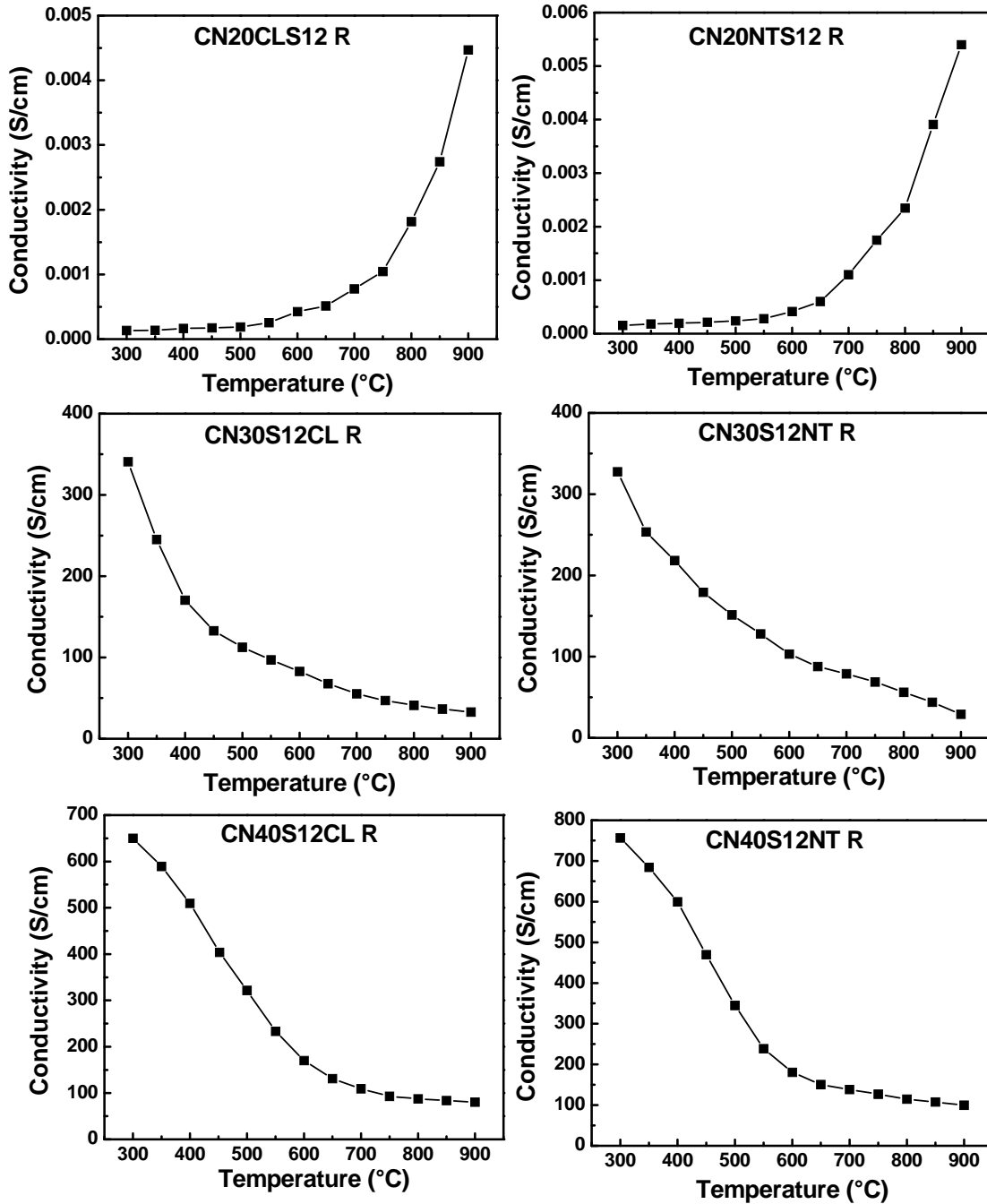
Fig. 5.29: The temperature dependent electrical conductivity of CN20CLS12 R, CN20NTS12 R, CN30CLS12 R, CN30NTS12 R, CN40CLS12 R and CN40NTS12 R.
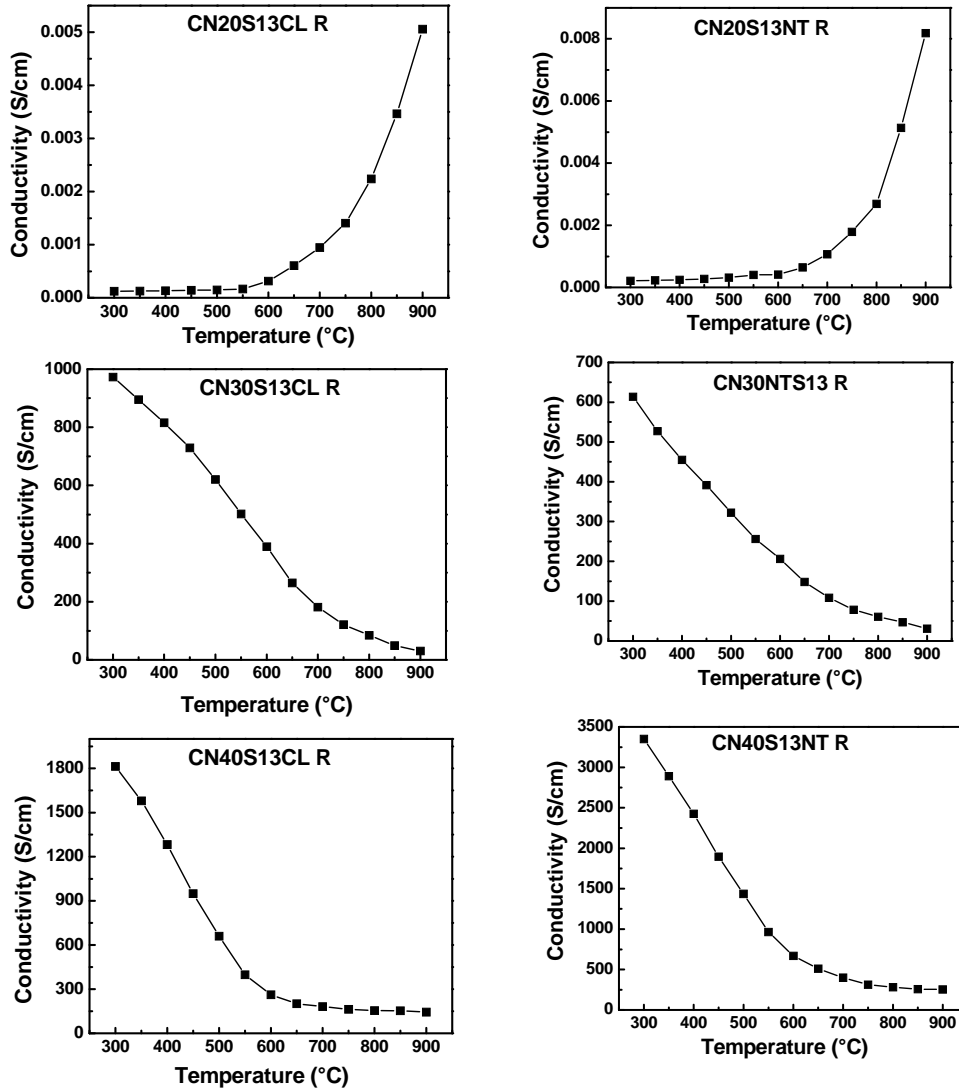
Fig. 5.30: The temperature dependent electrical conductivity of CN20CLS13 R, CN20NTS13 R, CN30CLS13 R, CN30NTS13 R, CN40CLS13 R and CN40NTS13 R.

The ionic behavior of 20 vol % Ni and electronic behavior of $\geq$ 30 vol % Ni containing cermets indicate that the conductivity percolation lies in between 20 to 30 vol% Ni. To further understand this percolation behavior, the temperature dependent electrical conductivity of CN20CLS12 R, CN20NTS12 R, CN20CLS13 R, CN20NTS13 R, CN30CLS12 R, CN30NTS12 R, CN30CLS13 R and CN30NTS13 R was re-plotted and shown in Fig. 5.31. It was confirmed that the conductivity of the cermets prepared with 20 vol% Ni are found to increase with temperature and that with 30 vol% Ni are found to decrease with temperature. These results also confirmed that the conductivity percolation in Ni: 8YSZ cermet was in between 20 to 30 vol % Ni. The graph of log σ versus 1000/T was found to be non-linear in nature for 30 vol % Ni containing cermet, which indicates that there may be some contribution of ionic species to the conductivity [10].
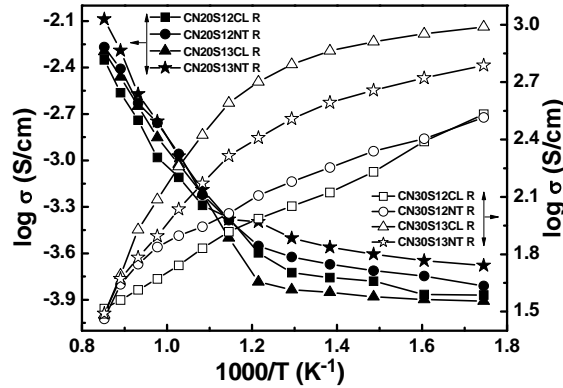
Fig. 5.31: Electrical conductivity as a function of temperature for sample 20 and 30 vol % Ni containing cermets.

The electrical conductivity of Ni: 8YSZ cermet was strongly dependent on the volume concentration of Ni in 8YSZ matrix. The value of electrical conductivity as a function of Ni concentration at different temperatures (400 °C to 800 °C) for chloride based cermet prepared at sintering condition of 1200 °C, nitrate based cermet prepared at sintering condition of 1200 °C, chloride based cermet prepared at sintering condition of 1300 °C and nitrate based cermet prepared at sintering condition of 1300 °C are shown in Fig. 5.32 (a), (b), (c) and (d), respectively.
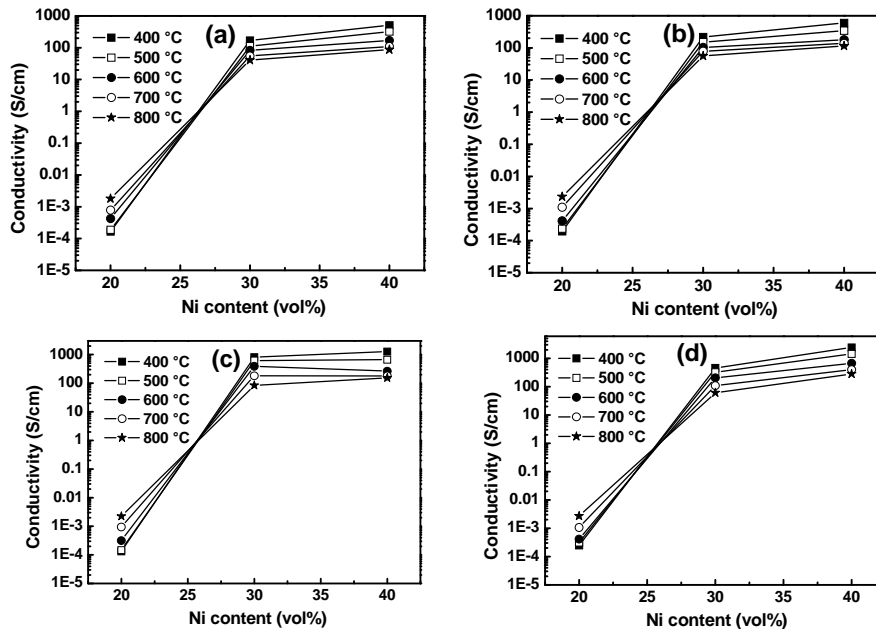
Fig. 5.32: Electrical conductivity as a function of Ni content at different temperatures for (a) chloride based cermet prepared at sintering condition of 1200 °C, (b) nitrate based cermet prepared at sintering condition of 1200 °C, (c) chloride based cermet prepared at sintering condition of 1300 °C and (d) nitrate based cermet prepared at sintering condition of 1300 °C.

In all the above cases, electrical conductivity of Ni: 8YSZ cermet increases with Ni content. However, a sharp change in conductivity is at around 30 vol% nickel, which corresponds to change of conduction mechanism from ionic to electronic. Electrical conductivity of Ni: 8YSZ samples increases with increasing volume concentration of nickel, because the conductivity of metallic nickel was around five orders of magnitude more than YSZ and also better nickel distribution and Ni-Ni contact in YSZ matrix.

Different researchers have developed Ni: 8YSZ cermet via precipitation method at different concentration of Ni, different sintering and reduction temperatures. Li et al. [46] have observed conductivity of 0.08, 88.94 and 709.73 S/cm at 1000 °C using 17, 28 and 43 wt % Ni, respectively, at the sintering condition of 1400 °C and reduction temperature of 1200 °C. Grgicak [48] et al. have obtained conductivity in the range of 400 to 700 S/cm at 1000 °C, using 40 wt % Ni at the sintering condition of 1500 °C and reduction temperature 800 °C. However, Marinšek at al. [45] have observed nearly constant conductivity of ~ 0.4 S/cm at 1000 °C using 42.11 to 99.56 wt % Ni at the sintering condition of 1300 °C and reduction temperature 1000 °C. Similarly, Haberko et al. [56] obtained conductivity of ~ 0.21 S/cm S/cm at 400 °C using 50 wt % Ni at the sintering condition of 1300 °C and reduction temperature 800 °C. The conductivity of Ni: 8YSZ prepared in this present study is comparable with some literature value as well higher than some literature by considering Ni concentration, sintering and reduction condition. It seems that the constant pH co-precipitation method adopted in this present study is highly advantageous for development of better conducting Ni: 8YSZ cermet for SOFC application.

5.3.3.4: Thermal expansion coefficient

Thermal expansion behavior of chloride and nitrate precursor based constant pH process derived cermets prepared at the sintering condition of 1300 °C is shown in Fig. 5.33 (a) and (b), respectively.
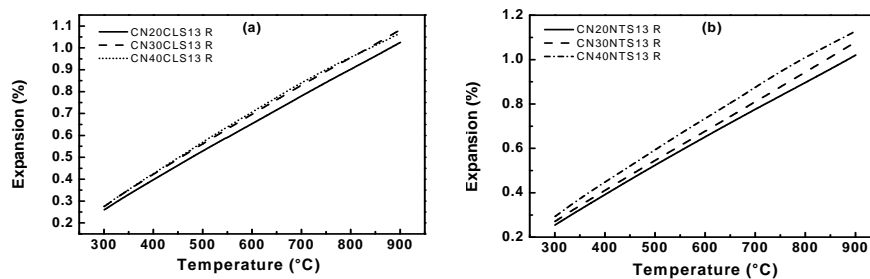
Fig. 5.33: Thermal expansion behavior of Ni: 8YSZ cermet prepared using (a) chloride and (b) nitrate precursors.

The thermal expansion behavior was found to vary linearly with temperature. As expected, the slope of the expansion curve also increases with Ni concentration. TEC of cermet was

calculated from the slope of these linear curves. The TEC as a function of Ni concentration for chloride and nitrate precursor based cermets is shown in Fig. 5.34. In chloride / nitrate based cermet, the TEC value increases with increase in Ni concentration. The TEC of 20 vol % Ni containing cermet prepared from either chloride or nitrate precursors was nearly the same and found to be 12.6×10^{-6} /°C. The 30 vol % Ni containing cermet prepared from either chloride or nitrate was found to be 13.2×10^{-6} /°C 13.3×10^{-6} /°C, respectively. However, TEC of 40 vol % Ni containing cermet CN40NTS13 R was higher of ~ 13.9×10^{-6} /°C as compared to the cermet CN40NTS13 R, which have TEC of ~ 13.4×10^{-6} /°C.
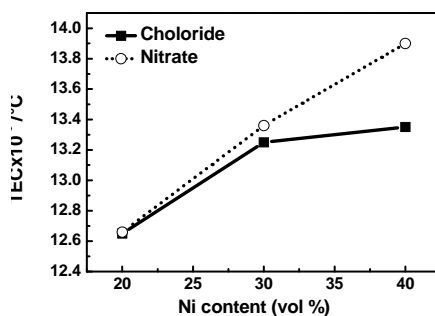
Fig. 5.34: TEC as a function of Ni content for chloride and nitrate precursor based cermets.

5.3.4: Summary

Different concentration of Ni containing Ni: 8YSZ cermets were successfully fabricated using the NiO: 8YSZ powders prepared from chloride and nitrate precursors using constant pH co-precipitation method. Depending on the Ni concentration and sintering temperature, the porosity of Ni: 8YSZ cermets varies in between 20 % to 27 %. The particles of Ni and YSZ were found to be finer and uniform for cermets prepared at sintering condition of 1200 °C and Ni particles are well distributed in YSZ matrix. However, at sintering condition of 1300 °C, the particle size of YSZ increases significantly for 30 vol % Ni containing cermets. In these samples, Ni particles are found to be highly dispersed and deposited at the grain boundary as well on surface of YSZ. The conductivity percolation of Ni: 8YSZ cermet lies between 20 and 30 vol % Ni. The electrical conductivity increases with Ni concentration and sintering condition. The non-linear conductivity behavior of $\geq$ 30 vol % Ni containing cermets may be due to the contribution of ionic species. The TEC of chloride precursor based cermets was found to be lower than the nitrate precursor based cermets.

Constant pH co-precipitation method is suitable for the development of Ni: 8YSZ cermets in terms of porosity, electrical conductivity and TEC and may be apt for use as anode material in IT-SOFC. Further, to confirm the applicability of constant pH co-precipitation derived powders in IT-SOFC, the electrochemical performance of the symmetrical cell was studied and discussed in chapter 7.

CHAPTER 6

Microstructure, electrical conductivity and TEC of Ni: 8YSZ cermet fabricated using heterogeneous precipitation synthesized NiO: 8YSZ powders

This chapter contains three sub-chapters. In Chapter 6.1, the thermal behavior, structure, morphology and shrinkage behavior of 8YSZ powders, prepared by conventional and constant pH precipitation method are described. To obtain dense 8YSZ pellets, different processes were optimized and are discussed in this chapter. The 8YSZ powders, prepared by optimized method, were used in heterogeneous precipitation method to prepare NiO: 8YSZ composites.

In Chapter 6.2, thermal behavior, structure, morphology and shrinkage behavior of 20, 30 and 40 vol % Ni containing NiO: 8YSZ nanopowders, prepared by direct and reverse processes of heterogeneous precipitation method, are studied and analyzed.

In Chapter 6.3, density/porosity, microstructure, electrical conductivity and TEC of 20, 30 and 40 vol % Ni containing Ni: 8YSZ cermet have been studied and analyzed, in order to find the importance of this method of preparation as well as suitability of these anode material for use in IT-SOFC.

CHAPTER 6.1

Synthesis and characterization of 8YSZ powders and fabrication of dense 8YSZ

6.1.1: Introduction

Cubic 8 mol% Y_2O_3 stabilized ZrO_2 (8YSZ) has many potential applications including electrolyte in SOFC [139, 140], thermal barrier coatings [141] and oxygen sensors [142]. In a single cell SOFC, a thin and dense layer of 8YSZ is sandwiched between the cathode and anode, for conduction of oxide ions [143, 144]. Different synthesis and fabrication methods have been proposed to achieve a highly dense 8YSZ for use as electrolyte SOFC. So, in this Chapter, 8YSZ powders have been synthesized via two different ways of precipitation such as conventional and constant pH. Different process parameters were also optimized to obtain a highly dense 8YSZ. Thermal behavior, phase evolution, density and microstructure of the prepared 8YSZ were studied and analyzed.

6.1.2: Experimental

Reactants used for preparation of 8YSZ powders were zirconium oxychloride octahydrate ($ZrOCl_2 \cdot 8H_2O$), yttrium oxide (Y_2O_3) and 20 vol% hydrazine hydrate (N_2H_5OH) [denoted as HH]. Appropriate amount of Y_2O_3 was dissolved in HCl and this solution was mixed with aqueous $ZrOCl_2.8H_2O$ to prepare the precursor solution. 8YSZ nanopowders were prepared by the reaction between the precursor solution and HH via two different ways of precipitation such as conventional and constant pH. In conventional precipitation, HH was added slowly and drop wise to the precursor solution and the pH of the solution was increased up to 10. In constant pH precipitation, the precursor solution was added to HH and the pH of the solution was maintained at ~10 by adding extra amount of HH. After completion of the reaction, the precipitates were collected and thoroughly washed with distilled water and isopropyl alcohol. The washed powders were then dried in an oven. The dried as-prepared powders were finely ground in a mortar pestle and then calcined at 800 °C. Different characterization techniques such as DSC-TG, XRD, TEM and dilatometry were used in order to evaluate the properties of the as synthesized as well as calcined powders. Further, to obtain a highly dense 8YSZ, the calcined powders were milled for 5 h at 350 rpm in a planetary ball mill using zirconia balls. The powders with and without ball milling were compacted into circular pellets and sintered at 1600 °C. Density and microstructure of the sintered 8YSZ pellets were compared and analyzed.

6.1.3 Results and discussion

6.1.3.1: Thermal

Figure 6.1 (a) and (b) show DSC-TG curves of the as synthesized 8YSZ powders prepared by conventional and constant pH precipitation method, respectively.
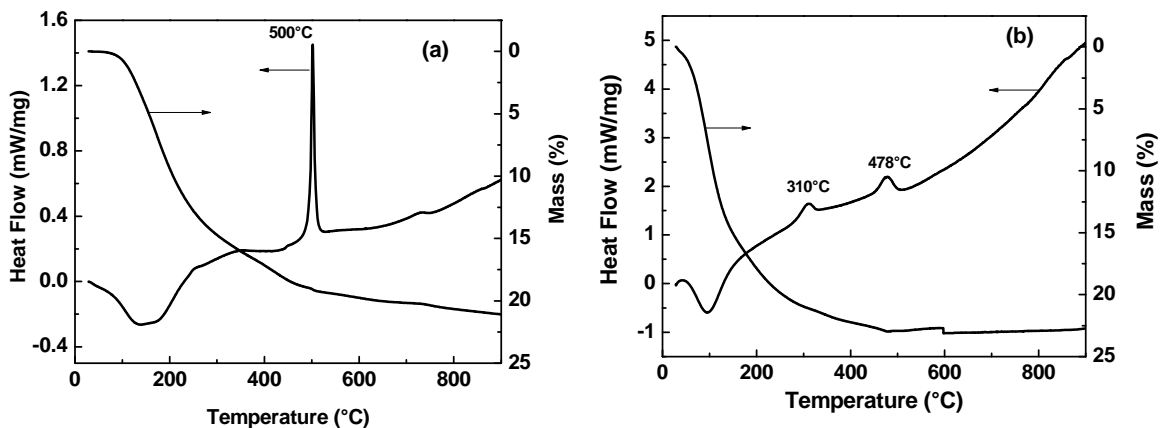
Fig. 6.1: DSC-TG patterns of the as synthesized 8YSZ powders prepared via (a) conventional precipitation and (b) constant pH precipitation.

In both samples, the observed broad endothermic peak at ~150 °C along with a weight loss of ~ 16 %, corresponding to desorption of adsorbed water. A total weight loss of ~ 23% was observed in both samples from room temperature to 900°C. The exothermic peak at ~500°C in Fig. 6.1 (a), corresponds to the crystallization of cubic zirconia. However, a dual-step crystallization process, corresponding to primary crystallization at 310 °C and secondary crystallization at 478°C, was observed for sample prepared through constant pH precipitation. This dual step crystallization may be attributed to the highly ordered structure formed via constant pH precipitation [145]. Further, the weight loss was nearly constant above 500°C for both prepared samples, as confirmed from TG analysis. To study the phase formation behavior, these powders were calcined at higher temperature of 800 °C and 1200 °C and phase analysis was performed using XRD.

6.1.3.2: Structure

Figure 6.2 (a) and (b) show the XRD patterns of 8YSZ powders (synthesized in both methods) calcined at 800 °C and 1200 °C, respectively. The peaks of calcined (800 °C) powders are broad in nature and identified with cubic zirconia, as per the standard JCPDS file number 00-049-1642. It was observed that the constant pH precipitation derived powder possesses better crystallinity at 800°C in comparison to the powder prepared via conventional precipitation method. However, at 1200 °C, sharp peaks are observed which correspond to cubic zirconia.
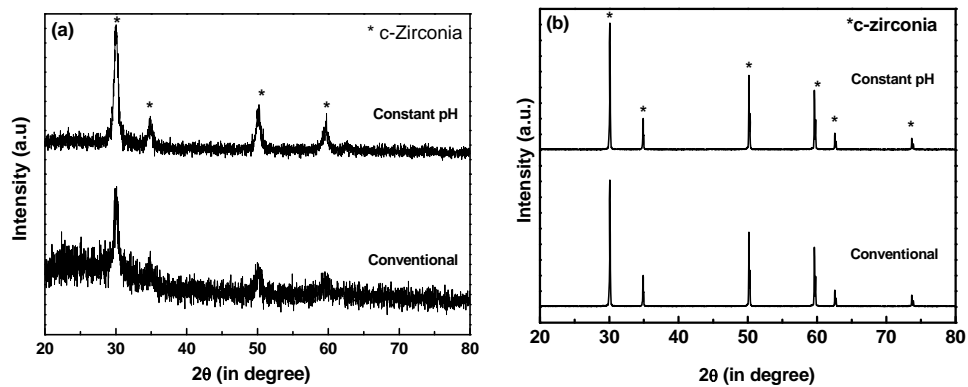
Fig. 6.2: XRD patterns of 8YSZ powders calcined at (a) 800 °C and (b) 1200°C.

6.1.3.3: Powder morphology

In order to study the powder morphology, TEM was performed on calcined (1200°C) 8YSZ powders. Fig. 6.3 (a) and (b) show TEM micrographs of calcined 8YSZ powder, prepared via conventional precipitation and constant pH precipitation, respectively. The particles are agglomerated in nature in both prepared condition, but particle size was smaller (100 to 200 nm) in case of constant pH precipitation.
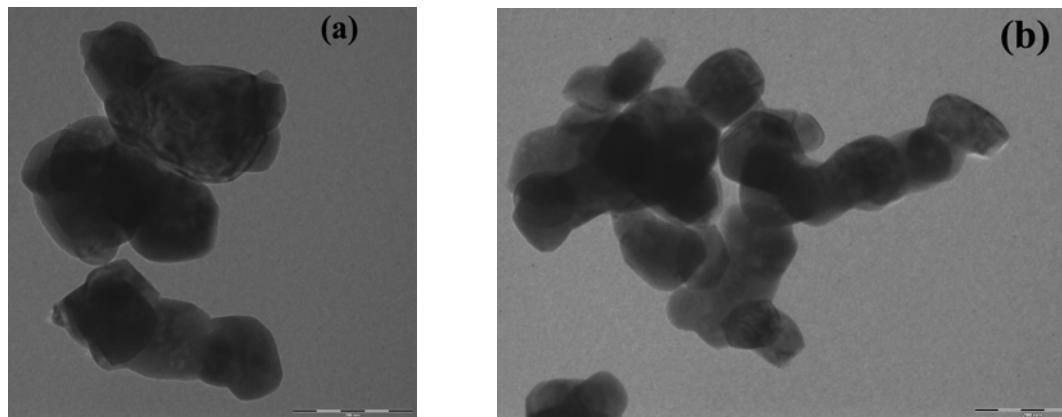
Fig. 6.3: TEM micrographs of calcined (1200°C) 8YSZ powder prepared via (a) conventional precipitation and (b) constant pH method. Scale bar corresponds to 200 nm.

6.1.3.4: Shrinkage

The shrinkage behavior as a function of temperature of 8YSZ pellets is shown in Fig. 6.4. It was confirmed that the powders prepared in constant pH precipitation exhibit lower temperature sinterability as compared to conventional precipitation method. The sinterability at lower temperature may be due to small particle size of the constant pH precipitation derived powders [50, 146, 147].
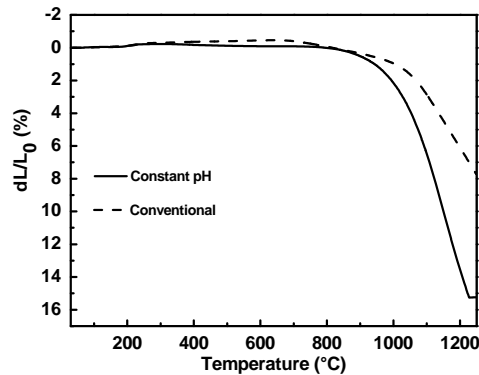
Fig. 6.4: Shrinkage behavior of the 8YSZ pellets prepared via two methods.

6.1.3.5: Microstructure

The minimum temperature to obtain a sintered product was 1200 °C, as confirmed from Fig. 6.4. But, to get a highly dense 8YSZ, the green pellet was sintered at much higher temperature. The higher density 8YSZ strongly depends on the initial particle size of the calcined powders. So, the calcined powders, obtained via conventional precipitation and constant pH precipitation, were further ground in planetary mill using zirconia balls. The 8YSZ powders, without and after ball milling, were sintered at 1600°C. Fig. 6.5 (a) and (b) show two different magnified SEM micrographs of sintered 8YSZ pellets fabricated from calcined powders prepared via conventional precipitation method. The particles were found to be agglomerated in nature and their size varies from 1 μm to 5 μm. The surface of each particle was covered by ultra- small particles, as observed from the higher magnified SEM micrograph [Fig. 6.5 (b)]. The size of the ultra-small particle was found to be in the range of 50 nm to 150 nm. The density of sintered 8YSZ pellets was found to be ~ 82% of theoretical density.
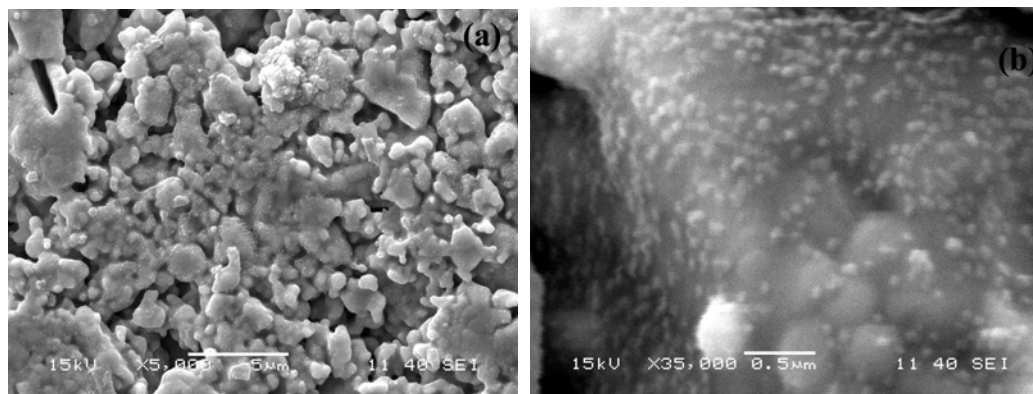
Fig. 6.5: SEM micrographs of sintered 8YSZ pellets prepared via conventional precipitation method

Fig. 6.6 (a) and (b) show two different magnified SEM micrographs of sintered 8YSZ pellets fabricated after ball milling the powders prepared in conventional precipitation method. The porosity of sintered 8YSZ pellets drastically decreased. The grain size was around 2 µm to 5 µm and pores are observed at the grain boundary. The density of this 8YSZ pellet was found to be around 92 % of theoretical density.
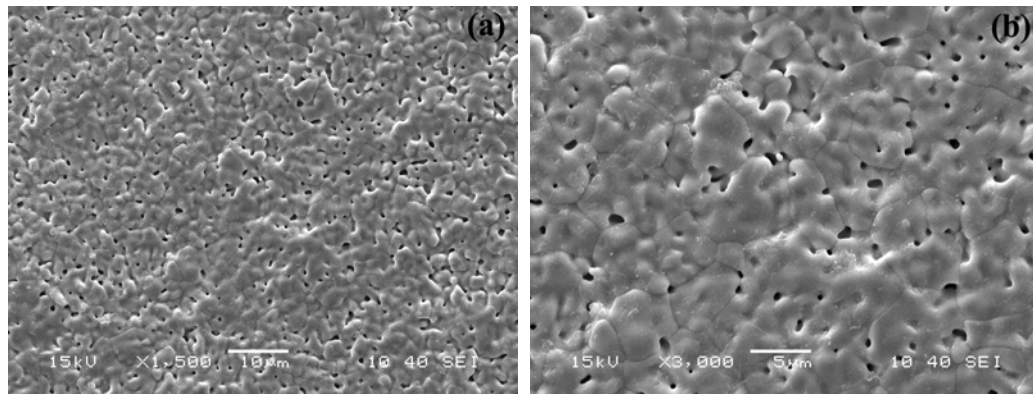
Fig. 6.6: SEM micrographs of sintered 8YSZ pellets prepared via ball mill assisted conventional precipitation method

Fig. 6.7 (a) and (b) show two different magnified SEM micrographs of sintered 8YSZ pellets, fabricated from calcined powders, prepared via constant pH precipitation method. The porosity was found to be nearly same as that of the sintered 8YSZ pellets fabricated via ball mill assisted conventional precipitation method. The density of this sintered 8YSZ pellet was found to be 92 % of theoretical density. The grain size of 8YSZ was smaller than that of conventional precipitation derived sample and found to be 1 µm to 5 µm with pores at grain boundary.
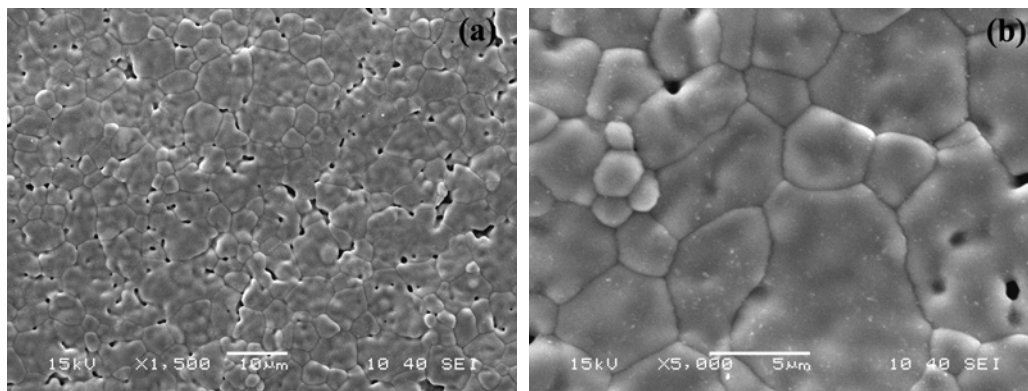
Fig. 6.7: SEM micrographs of sintered 8YSZ pellets prepared via constant pH precipitation.

Fig. 6.8 (a) and (b) show two different magnified SEM micrographs of sintered 8YSZ pellets, fabricated from calcined powders after ball milling, prepared via constant pH precipitation. The porosity of sintered 8YSZ pellet drastically decreased by using constant pH derived ball milled

powders. The grains were larger in size as compared to all other conditions and are in between 10 µm to 40 µm. The density of this sintered 8YSZ pellet increased to 97 % of theoretical density.
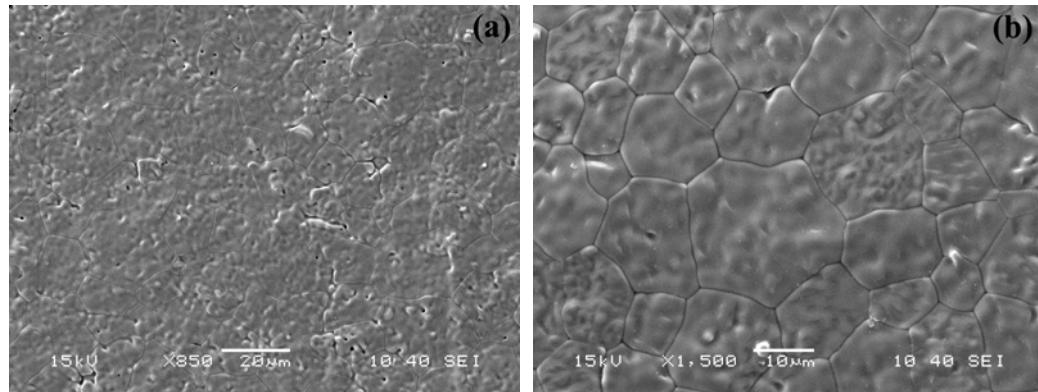
Fig. 6.8: SEM micrographs of sintered 8YSZ pellets prepared via ball mill assisted constant pH precipitation

6.1.4: Summary

Two different ways of synthesis such as conventional precipitation and constant pH precipitation were followed to prepare 8YSZ nanopowders using hydrazine hydrate as a precipitating agent. Cubic zirconia was developed at ~ 800 °C and crystallinity increased after calcination at 1200 °C. The powders are found to be agglomerated and particle size was found to be 100 nm to 200 nm at 1200 °C. By comparing the microstructure of sintered 8YSZ, it was confirmed that the ball mill assisted constant pH precipitation was more advantageous than conventional precipitation or ball milled assisted precipitation method. A highly dense microstructure with well-connected grains was observed in sintered 8YSZ pellets prepared via ball milled assisted constant pH route.

Ball mill assisted constant pH precipitation is more effective in synthesizing 8YSZ powders for fabrication of dense YSZ as electrolyte. These powders may be used as one of the starting material for synthesizing NiO: 8YSZ powders via heterogeneous precipitation method and fabrication of Ni: 8YSZ cermet for use as anode in IT-SOFC.

CHAPTER 6.2

Thermal behavior, structure, morphology and shrinkage behavior of heterogeneous precipitation derived 20, 30 and 40 vol % Ni containing NiO: 8YSZ

6.2.1: Introduction

In this chapter, YSZ powders (prepared via ball mill assisted constant pH precipitation) are used as one of the starting material to prepare 20, 30 and 40 vol % Ni containing NiO: 8YSZ powders via heterogeneous precipitation method using direct and reverse processes. Thermal behavior, structure, morphology and shrinkage behavior of these composites were studied and analyzed.

6.2.2: Experimental

To prepare NiO: 8YSZ powders, the calcined (800 °C) YSZ powders (obtained after ball milled assisted constant pH method) and $NiCl_2 \cdot 8H_2O$ salt solution were ball milled for 30 min to form a dispersed precursor solution. Two different ways of heterogeneous precipitation methods such as direct (D) and reverse (R) processes were followed to synthesize NiO: 8YSZ powders consisting of 20, 30 and 40 vol % Ni, using HH and NaOH. In direct process, mixture solution of HH (20 vol % concentration) and NaOH (1M) was added drop wise to the dispersed precursor solution, whereas, reverse process is the opposite way of direct process. The reaction was carried out in a beaker at a temperature around 70°C – 80°C. After completion of the reaction, the precipitates thus obtained through D and R processes were washed, dried and ground in mortar pestle to obtain as-synthesized powders and then calcined at 650 °C. Samples prepared via D and R processes are designated as HPN*X0* D/R AS, where HP represents heterogeneous precipitation, N*X0'* represents vol % of Ni, D/R represents direct/reverse process and AS represents as-synthesized powders. Different characterization techniques such as DSC-TG, XRD, SEM and dilatometer were performed on these samples and analyzed.

6.2.3: Results and discussion

6.2.3.1: Thermal

DSC-TG curves of 20, 30 and 40 vol% of Ni containing as-synthesized powders, synthesized by direct and reverse process, are shown in Fig. 6.9 (a), (b) and (c), respectively. DSC-TG behavior of HPN20D AS, HPN20R AS and HPN30D AS are similar in nature. The broad endothermic peak at ~ 100 °C and ~ 300 °C for these samples corresponds to evaporation of physically and chemically bonded water, respectively. In addition to this, a sudden decrease in weight loss of ~ 6 % was observed up to 400 °C in TG curves of these samples. However, a slightly

weight gain (~ 2 %) was observed above 500 °C in TG curves of HPN20D AS, HPN20R AS and HPN30D AS. A very weak exothermic peak was also observed at ~ 500 °C and ~ 600 °C for samples HPN20D AS and HPN20R AS, respectively. But, the exothermic peak at ~ 500 °C for HPN30D AS sample was quite broad in nature.
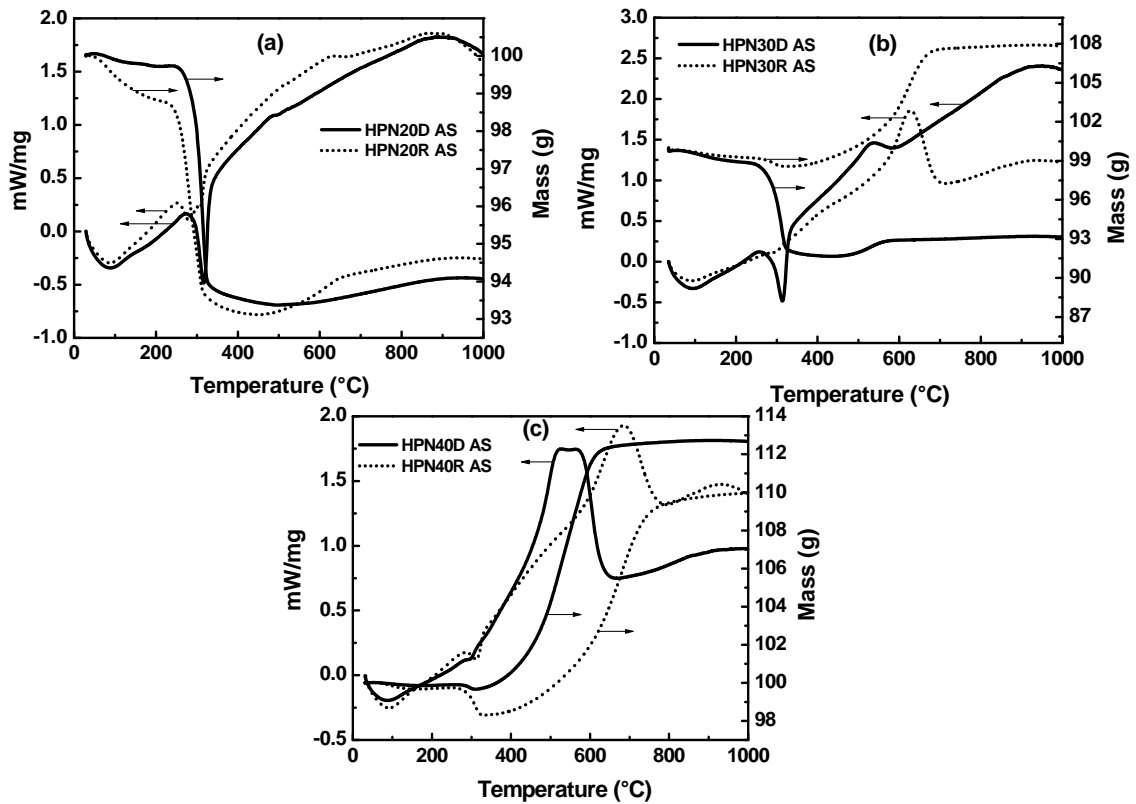
Fig. 6.9: DSC-TG curves (a) 20, (b) 30 and (c) 40 vol% of Ni containing as-synthesized powders prepared using direct and reverse process.

DSC-TG behavior of HPN30R AS, HPN40D AS and HPN40R AS are similar in nature. In these three samples, very broad endothermic peak at ~ 100 °C corresponds to evaporation of physically bonded water. There was a sudden weight loss at ~ 300 °C which corresponds to evaporation of chemically bonded water. In these three samples, there was a sudden weight gain in temperature range in between 350 °C to 700 °C. In this temperature range, the total weight gain of HPN30R AS, HPN40D AS and HPN40R AS are 9 %, 12 % and 12 %, respectively. There was also an intense exothermic peak at ~ 600 °C, 500 °C and 650 °C observed in HPN30R AS, HPN40D AS and HPN40R AS samples, respectively.

To understand the nature of thermal behavior of direct and reverse process derived 20, 30 and 40 vol % Ni containing as-synthesized powders, it is necessary to find out the phases present in

the as-synthesized powders of these samples. So, the phase analysis was performed on these samples using XRD.

6.2.3.2: Structure

Figure 6.10 (a), (b) and (c) show XRD patterns of direct and reverse process derived 20, 30 and 40 vol % Ni containing as-synthesized powders, respectively.
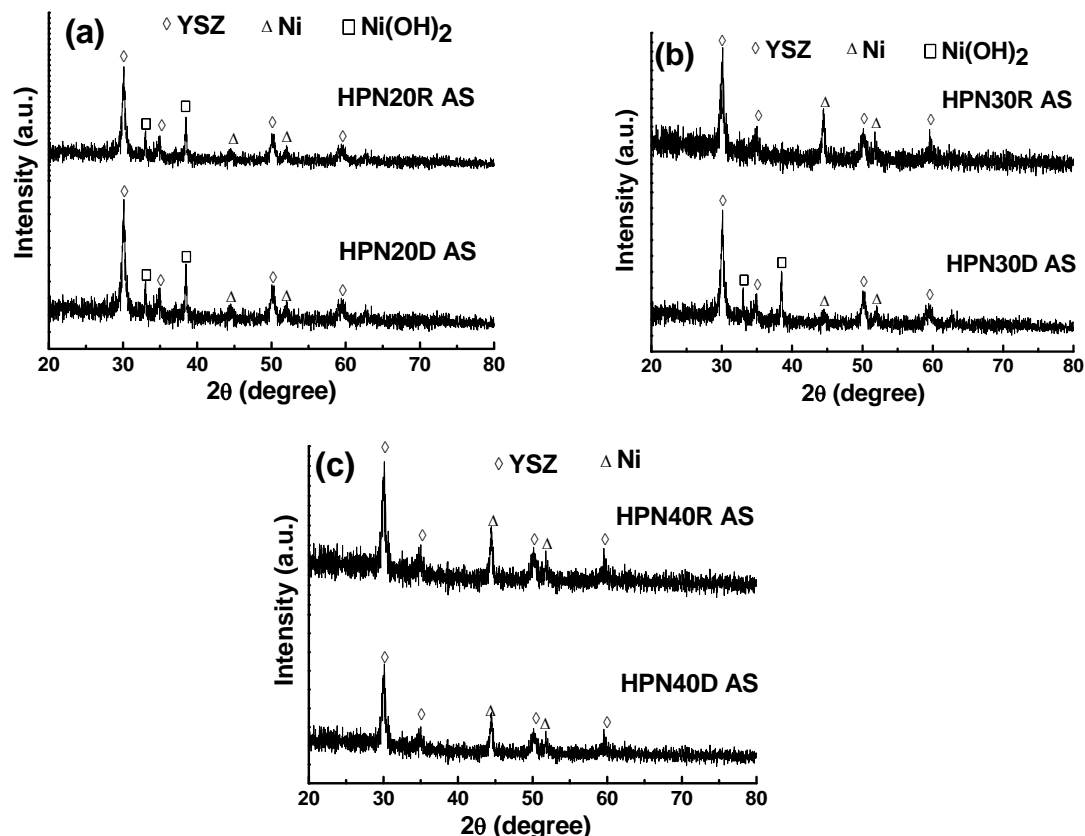
Fig. 6.10: XRD patterns of (a) 20, (b) 30 and (c) 40 vol % Ni containing as-synthesized powders prepared in direct and reverse proceses.

The XRD patterns of as-synthesized samples such as HPN20D AS, HPN20R AS and HPN30D AS look alike. In these three samples, all the peaks are identified with either $Ni(OH)_2$ or Ni along with YSZ. In these three samples, major phases are YSZ and $Ni(OH)_2$ with a minor phase of Ni. However, the XRD patterns of as-synthesized samples such as HPN30R AS, HPN40D AS and HPN40R AS are similar in nature. In these three samples, all the peaks are identified with Ni along with YSZ.

The typical XRD pattern of calcined (650 °C) sample is shown in Fig. 6.11 (a). All the peaks are identified with either YSZ or NiO phase. The crystallite size of YSZ and NiO was found

to be around 15 nm and 20 nm, respectively. To find out the phases after reduction, the NiO: 8YSZ powders were calcined at 1200 °C in air atmosphere and then reduced in H_2 atmosphere at 900 °C. Typical XRD pattern of Ni: 8YSZ powder is shown in Fig. 6.11 (b). All the peaks are assigned to Ni and YSZ, as NiO gets converted to Ni after reduction and forms Ni: 8YSZ.
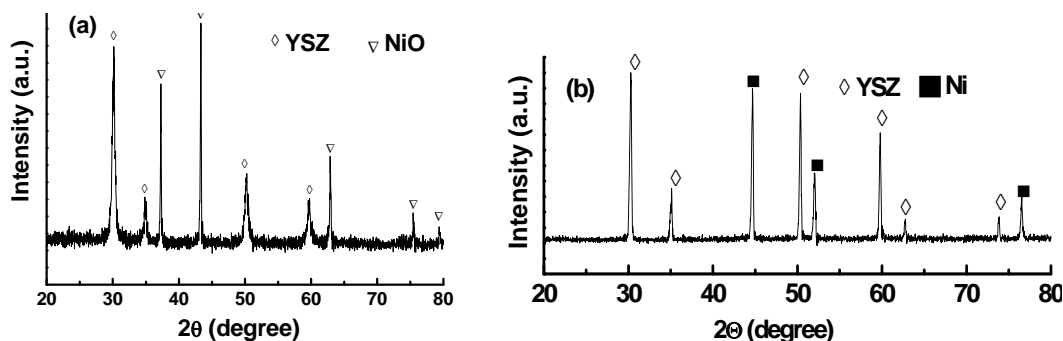
Fig. 6.11: XRD patterns of (a) NiO: 8YSZ and (b) Ni: 8YSZ cermet

From DSC-TG and XRD analysis, it was confirmed that the presence of $Ni(OH)_2$ in the as-synthesized samples of HPN20D AS, HPN20R AS and HPN30D AS, which undergoes decomposition at 300°C, was responsible for the sharp endothermic peak along with the major weight loss at that temperature. The weight gain in Ni containing samples may be attributed to the adsorption of N_2 gas. In addition to this, the observed exothermic peak in DSC curve for all samples either at ~ 500 °C or ~ 600 ° corresponds to the gradual crystallization of NiO.

6.2.3.3: Powder Morphology

Powder morphology of calcined (650°C) HPN30D AS and HPN30R AS was observed using FE-SEM and are shown in Fig. 6.12 (a) and (b), respectively. The particles are nearly spherical in shape and the size lies in between 30 to 50 nm.
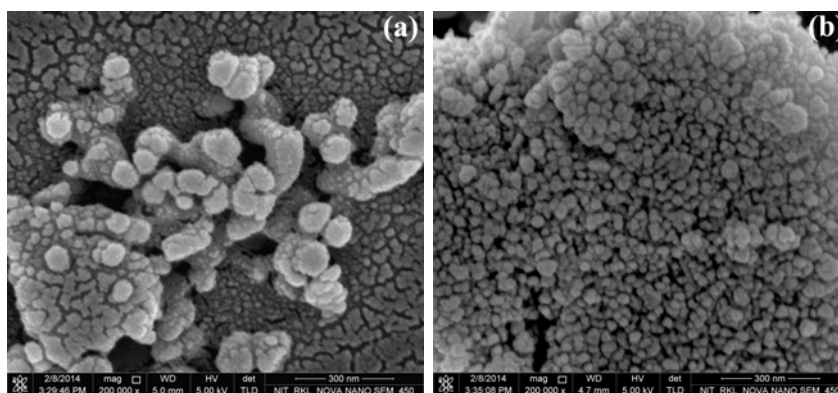
Fig. 6.12: FE-SEM micrograph of calcined (a) HPN30D AS and (b) HPN30R AS.

6.2.3.4: Shrinkage

To further evaluate the shrinkage behavior, dilatometric study was performed on rectangular pellets of two specific samples such as HPN30D 650 and HPN30R 650, as it contains Ni(OH)$_2$ and Ni, respectively, along with YSZ in the as-synthesized condition. The shrinkage behavior of HPN30D 650 and HPN30R 650 are compared and is shown in Fig. 6.13. From this curve, it was confirmed that HPN30D 650 sample shows a better sinterability above 1200 °C as compared to HPN30R 650.
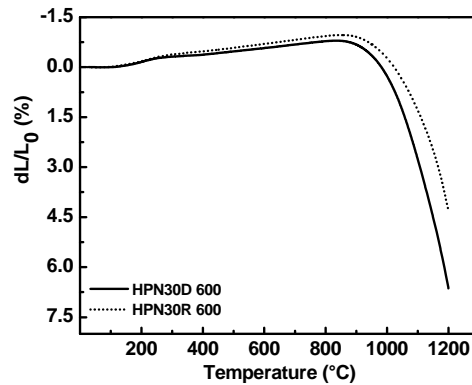
Fig. 6.13: Shrinkage behavior of HPN30D 650 and HPN30R 650.

6.2.4: Summary

NiO: 8YSZ powders consisting of 20, 30 and 40 vol % Ni were successfully prepared by two different ways such as direct and reverse processes using HH and NaOH as precipitating agents. From DSC-TG and XRD analysis, it was confirmed that the presence of Ni(OH)$_2$ in the as-synthesized samples is responsible for weight loss and the presence of Ni helps in weight gain. The particles are nearly spherical in shape and size was found to be in the range of 30 to 50 nm. Shrinkage behavior indicates that the prepared sample may be sintered above 1200 °C to get suitable density and porosity. So, density/porosity, microstructure and electrical conductivity of heterogeneous precipitation derived of Ni: 8YSZ cermet was analyzed.

CHAPTER 6.3

Microstructure, electrical conductivity and TEC of heterogeneous precipitation derived Ni: 8YSZ cermet

6.3.1: Introduction

In Chapter 6.2, 20, 30 and 40 vol% Ni containing NiO: 8YSZ powders were synthesized in heterogeneous precipitation method by direct and reverse processes. From the properties of these powders, it was interesting to study the density/porosity, microstructure, electrical conductivity and TEC of Ni: 8YSZ cermets developed using these powders and hence studied in this Chapter.

6.3.2: Experimental

The as-synthesized powders prepared by direct and reverse process were calcined at 650 °C to obtain 20, 30 and 40 vol % Ni containing NiO: 8YSZ powders. The calcined powders were mixed with 2 wt % PVA and then compacted to rectangular pellets at compaction pressure of 588 MPa. The compact pellets were sintered at 1300°C and then reduced at 900°C in H_2 atmosphere to obtain different concentration (20, 30 and 40 vol %) of Ni containing Ni-8YSZ cermet. The samples prepared are designated as HPNX0D/R S13 UR/R, where HP represents heterogeneous precipitation synthesis, N represent nickel, '*X0*' represents vol % of Ni, and D/R represents direct /reverse process, S13 represents sintering at 1300 °C and UR and R represents before and after reduction of pellets under H_2 atmosphere. Density, microstructure, distribution of Ni, YSZ in the cermet, electrical conductivity and TEC of Ni: 8YSZ cermet was compared and analyzed.

6.3.3: Results and discussion

6.3.3.1: Density and porosity

The effect of Ni concentration on density / porosity of NiO: 8YSZ composites (before reduction) and Ni: 8YSZ cermets (after reduction), prepared via direct and reverse processes are shown in Fig. 6.14 (a) and (b), respectively. NiO/Ni: 8YSZ composites prepared via direct process shows higher density as compared to that prepared via reverse process. In both direct and reverse process, the density of NiO: 8YSZ composite was found to be higher than Ni: 8YSZ cermet due to volume change associated with the conversion of NiO to Ni. Density of NiO/Ni: 8YSZ composites decrease with increase in Ni concentration. The porosity of 20, 30 and 40 vol % Ni containing Ni: 8YSZ cermet prepared via direct process was found to be 15 %, 20 % and 36 %, respectively, whereas, the porosity of 20, 30 and 40 vol % Ni containing Ni: 8YSZ cermet prepared via reverse process was found to be 22 %, 33 % and 39 % respectively.
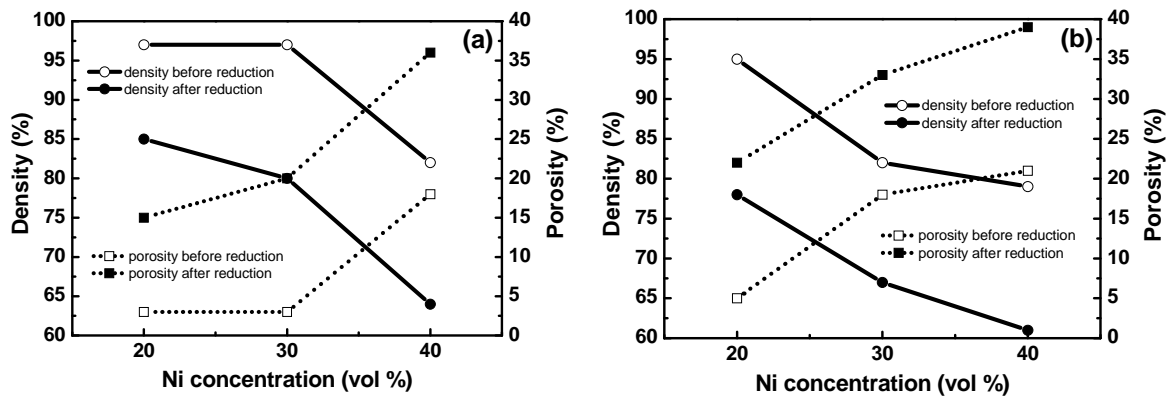
Fig. 6.14: Effect of Ni concentration on density and porosity of NiO/Ni: 8YSZ pellets prepared using (a) direct and (b) reverse technique.

6.3.3.2: Microstructure

Back scattered mode SEM was performed on NiO: 8YSZ composites to understand the microstructure and phase distribution of NiO and YSZ in NiO: 8YSZ composites. Fig. 6.15 shows SEM micrographs of sintered NiO: 8YSZ composites. It was confirmed that smaller size NiO (black portion) particles are uniformly distributed in 8YSZ matrix (gray portion) in both HPN20D S13 UR and HPN20R S13 UR, as compared to other composites. Homogeneous distribution of fine NiO in 8YSZ matrix is due to the fact that the presence of $Ni(OH)_2$ in the as-synthesized powders hinders the mobility of Ni particles in the 8YSZ matrix and hence forms a rigid network [48]. However, with increase in Ni content (30 vol % and 40 vol %) in the composites, the segregation of NiO occurs and agglomerated NiO particles were unevenly distributed in 8YSZ matrix in case of HPN30D S13 UR, HPN30R S13 UR, HPN40D S13 UR and HPN40R S13 UR. Also, the segregation of NiO particles increases with increase in Ni concentration. This is due to the fact that with increase in Ni concentration, the formation of Ni particles in the as-synthesized powders are more accelerated than $Ni(OH)_2$ in 8YSZ matrix. Due to poor wetting property of Ni on YSZ the mobility of Ni particles is higher in YSZ matrix. Porosity was also observed to be higher in the 40 vol % Ni containing NiO: 8YSZ composites prepared by either direct or reverse process.

Fig. 6.16 shows FE-SEM micrographs of Ni: 8YSZ cermet prepared in different processes. After reduction, the samples HPN20D S13 R and HPN20R S13 R show higher density with lower porosity than other samples. Ultra- fine Ni particles are well-distributed in 8YSZ matrix for 20 vol % Ni containing Ni: 8YSZ cermets. The average particle size was found to be in the range of 700 nm to 2 μm. It was also observed that porosity of Ni: 8YSZ cermet increases with Ni concentration prepared either by direct or reverse processes. To further understand the distribution of Ni in 8YSZ matrix in Ni: 8YSZ cermet, EDS mapping was performed.
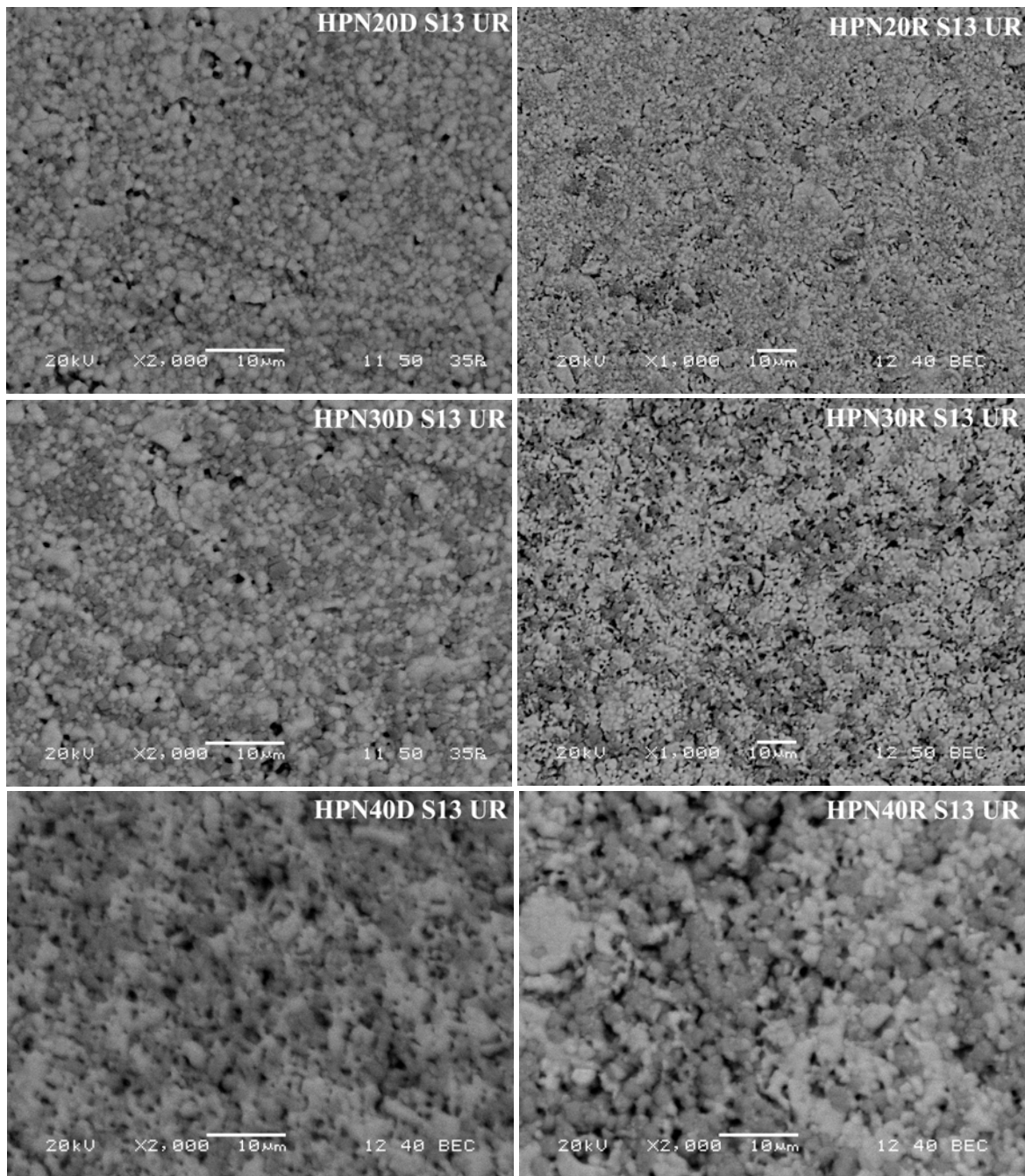
Fig. 6.15: SEM micrographs of direct and reverse process derived NiO: 8YSZ composites.
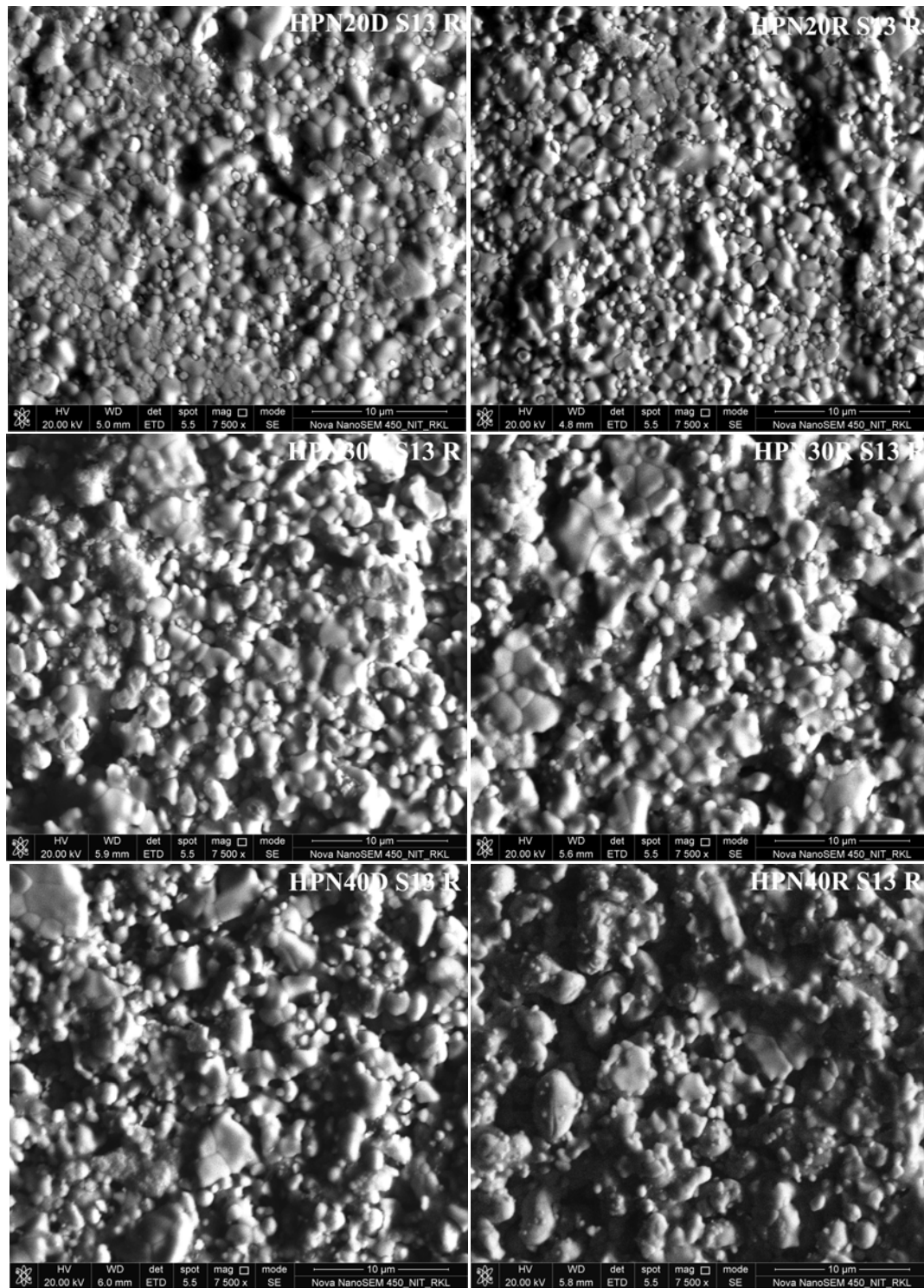
Fig. 6.16: FE-SEM micrographs of direct and reverse process derived Ni: 8YSZ cermet.

EDS elemental mapping of Ni, Zr was performed for all Ni: 8YSZ cermets prepared at direct and reverse process and are shown in Fig. 6.17. EDS mapping of HPN20D S13 R and HPN20R S13 R shows uniform distribution of Ni as compared to other cermets. With increase in Ni concentration, segregation of Ni particles was observed for sample HPN30D S13 R, HPN30R S13 R, HPN40D S13 R and HPN40R S13 R. To confirm the exact distribution of Ni as well as connectivity of Ni in Ni: 8YSZ cermet prepared via direct and reverse process, elemental mapping along with secondary image was performed and are shown in Fig. 6.18.
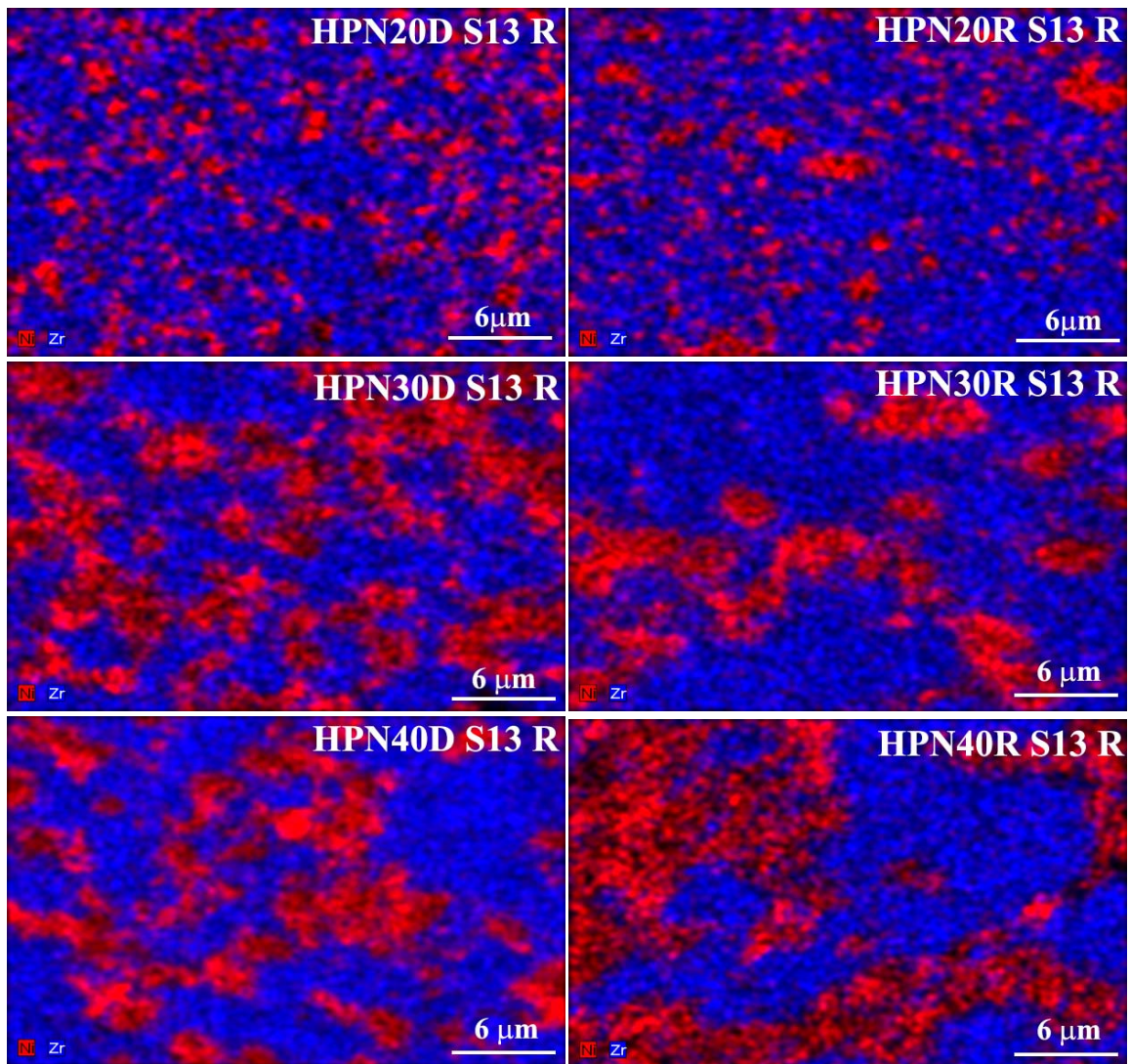
Fig. 6.17: Elemental mapping of Ni, Zr in Ni: 8YSZ cermet prepared via direct and reverse process.
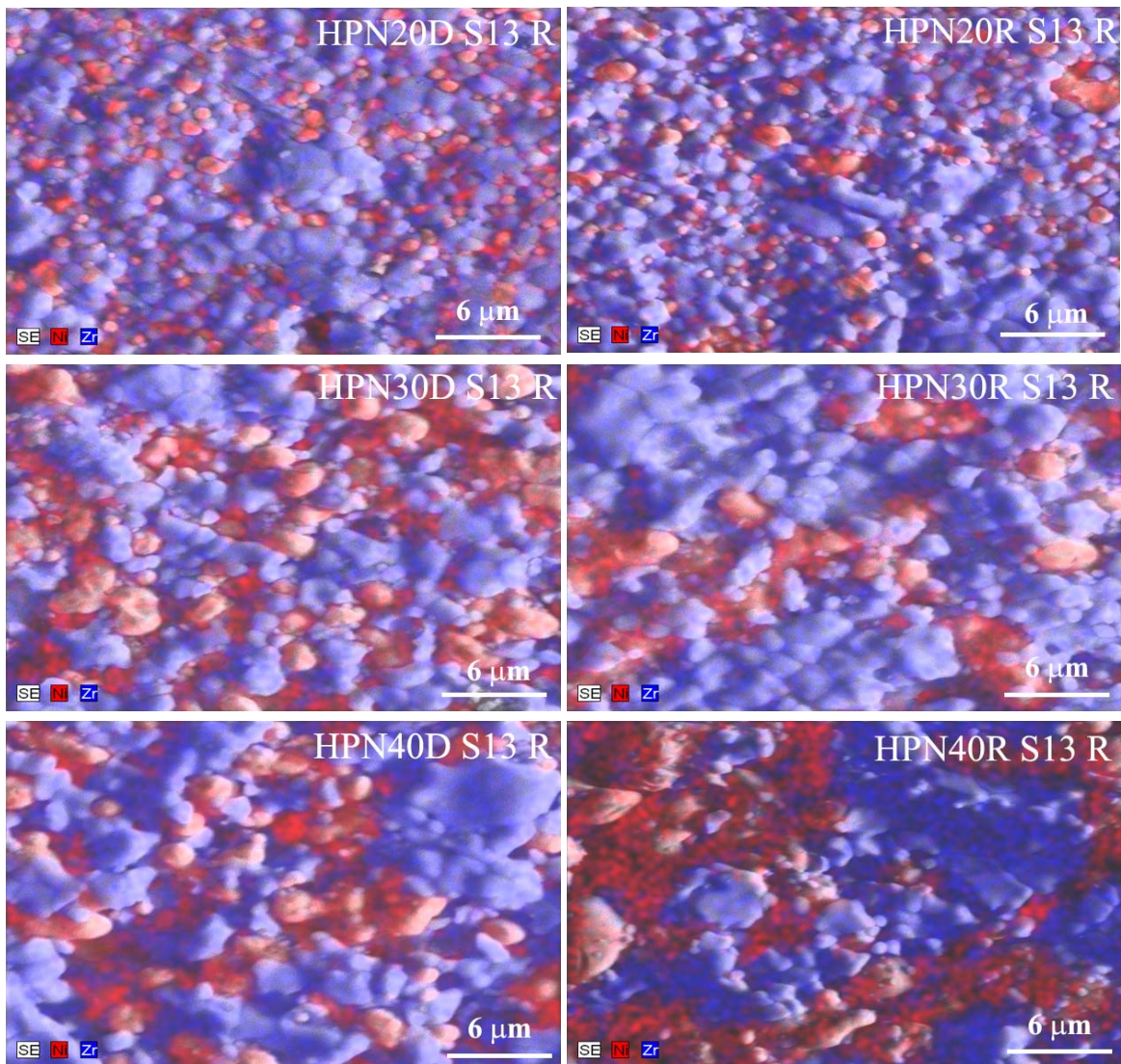
Fig. 6.18: Secondary image with EDS mapping of Ni: 8YSZ cermet prepared via direct and reverse process.

From Fig. 6.18, it was clear that Ni particles are not only present at the grain boundary of YSZ but also deposited on the surface of YSZ particles. With increase in Ni concentration, Ni particles are found to be segregated and separated within YSZ matrix. It was also clear that Ni particles are uniformly distributed in YSZ matrix of the cermet containing 20 vol % Ni, prepared either by direct or reverse process.

6.3.3.3: Electrical conductivity

The temperature dependent electrical conductivity/log(conductivity) versus 1000/T of different concentrations of Ni containing Ni: 8YSZ cermet prepared via direct and reverse process is shown in Fig. 6.19 (a)/(b), respectively.

123
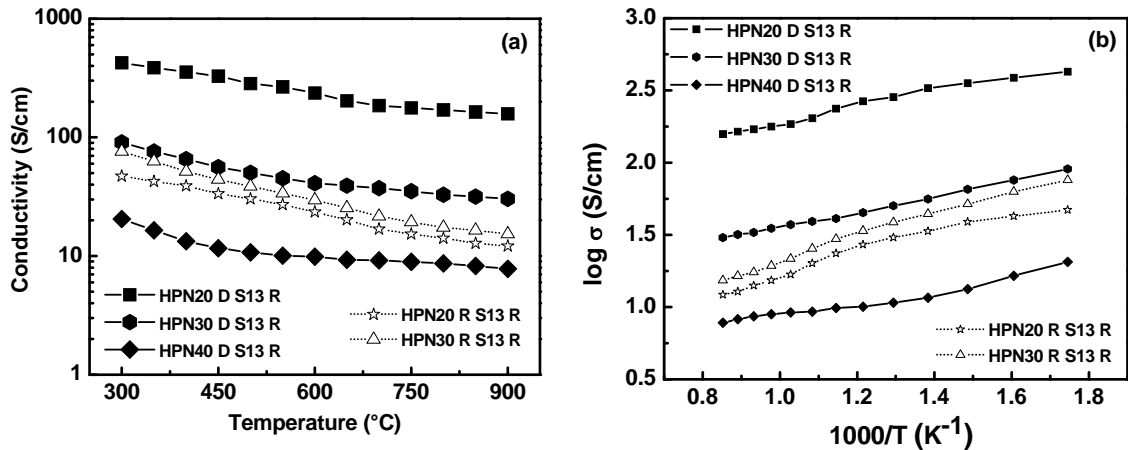
Fig. 6.19: Temperature dependent electrical conductivity (a) and log (conductivity) versus 1000/T (b) of Ni: 8YSZ cermet prepared at different processes.

The conductivity behavior of all cermets [Fig. 6.19 (a)] is electronic in nature, in which conductivity decreases with increase in temperature. The conductivity measurement of the reverse process derived 40 vol% Ni containing cermet (HPN40R S13 R) was not possible due to higher porosity nature as well as very low connectivity between Ni-Ni particles throughout the cermet. The direct process derived 20 vol % Ni containing cermet shows higher conductivity value of around 425 S/cm at 300 °C and decreases to a value of ~ 158 S/cm at 900 °C. With increasing Ni concentration, the conductivity value of cermets (such as HPN30D S13 R and HPN40D S13 R) decreases. It was also observed that direct process derived 20 or 30 vol % Ni containing cermet shows higher conductivity than reverse process derived cermet having same Ni concentration. However, the conductivity value of 30 vol % Ni containing Ni: 8YSZ cermet prepared via reverse process shows slightly better conductivity value (75 S/cm at 300 °C and 15 S/cm at 900 °C) than 20 vol % Ni containing cermet prepared via same process due to its microstructure.

Further, the temperature dependent electrical conductivity of all cermets was re-plotted in the form of log σ versus 1000/T and is shown in Fig. 6.19 (b). In general, the log (conductivity) versus (1000/T) curve of Ni: 8YSZ cermet shows a linear nature, which indicates the contribution of only electronic conduction. From this graph it was confirmed that the main contribution to conduction is due to better contact between electronic species (Ni).

The electrical conductivity in Ni: 8YSZ cermet was strongly dependent on the volume concentration of Ni. To further visualize the electrical conductivity as a function of Ni concentration, conductivity data of direct and reverse process derived Ni: 8YSZ cermet at various temperatures (400 °C, 500 °C, 600 °C, 700 °C and 800 °C) were plotted and are shown in Fig. 6. 20 (a) and (b), respectively. In direct process, the conductivity of 20 vol % Ni containing Ni: 8YSZ

cermet was higher at temperatures and then suddenly decreases with Ni concentration. However, in reverse process, conductivity value increases when Ni concentration increases from 20 vol % to 30 vol %. From this observation, it was confirmed that the conductivity percolation of direct process derived cermet is 20 vol % Ni.
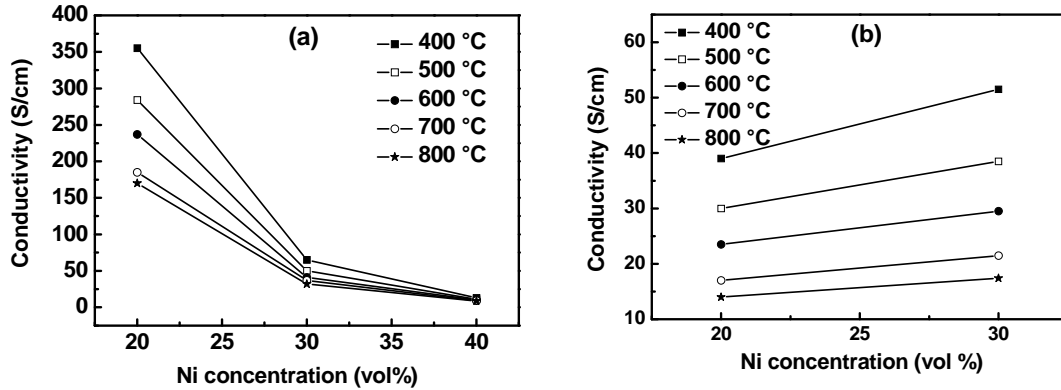
Fig. 6.20: Electrical conductivity as a function of Ni content at different temperatures for Ni: 8YSZ cermet prepared (a) direct process and (b) reverse process.

Generally, heterogeneous precipitation method is used for coating the surface of one material by another material which utilizes the principle of heterogeneous nucleation. Electroless coating as well as deposition methods have been used by different researchers for the development of Ni: 8YSZ cermets using this principle. Hence, the results of electrical conductivity of Ni: 8YSZ cermet prepared via direct process heterogeneous precipitation method is compared with some reported literatures based on coating method. Wang et al. [10] have observed conductivity of 900 S/cm at 600-800 °C using 55 wt % Ni at the sintering condition of 1400 °C and reduction temperature of 800 °C. 40 vol % Ni was used by Kim at al. [16] to develop cermet and the conductivity was found to be of >1400 S/cm at 800 °C at the sintering condition of 1400 °C and reduction temperature of 850 °C. Pratihar et al. [62] have used 20 vol % Ni and obtained a conductivity of 542 S/cm at 1000 °C, at the sintering condition of 1300 °C and reduction temperature of 1000 °C. Mukhopadhyay et al. [66] have used 33 vol % Ni and obtained a conductivity of 500 S/cm at 800 °C, at the sintering condition of 1400 °C and reduction temperature of 1000 °C. However, Rahman et al. [64] have obtained nearly constant conductivity of 150 S/cm at 800 °C using 41, 47 and 51wt % Ni, at the sintering condition of 1300 °C and reduction temperature 900 °C. Similarly, Lin et al. [65] obtained a conductivity of 37.3 S/cm and 61.3 S/cm at 700 °C using 18.9 and 35.7 vol % of Ni, respectively, at the sintering condition of 1400 °C and reduction temperature 1000 °C. The conductivity of Ni: 8YSZ prepared in this present study is comparable with some literature value as well higher than some literature from Ni

concentration, sintering and reduction condition point of view. It seems that the adopted heterogeneous precipitation method is highly advantageous for development of lower Ni containing Ni: 8YSZ cermet for SOFC application.

6.3.3.4: Thermal expansion coefficient

Thermal expansion of direct and reverse process derived 20, 30 and 40 vol % Ni containing cermet is shown in Fig. 6.21 (a) and (b), respectively.
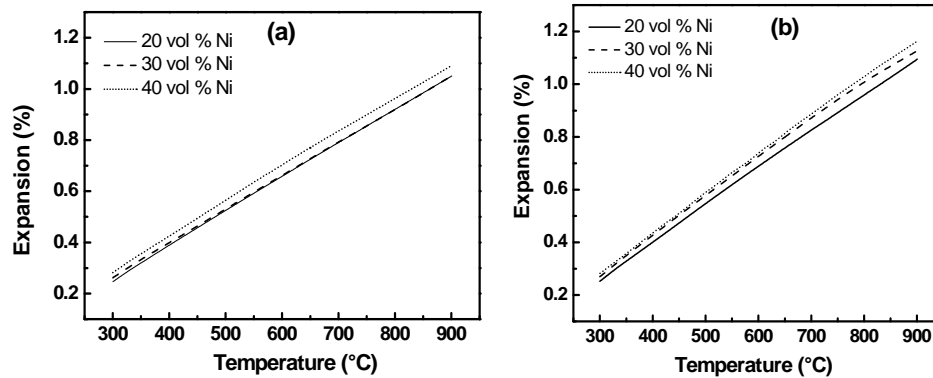
Fig. 6.21: Thermal expansion of Ni: 8YSZ cermet prepared using (a) direct (b) reverse process.

The thermal expansion behavior was found to vary linearly with temperature. As expected the slope of the expansion curve also increases with Ni concentration in the cermet. TEC of these cermets was calculated from the slope of linear curve in Fig. 6.21 and TEC as a function of Ni concentration is shown in Fig. 6.22. The TEC of the cermet prepared via direct process was lower than the TEC value of the cermet prepared via reverse process. TEC of 20 vol % Ni containing cermet prepared by direct and reverse process was found to be 13.05×10^{-6} /°C and 13.8×10^{-6} /°C, respectively. The TEC value was dependent on the Ni concentration in the cermet and the value increases with increase in Ni content. However, TEC value of 20, 30 and 40 vol % Ni containing cermet prepared via direct process was found to be 13.05×10^{-6} /°C, 13.2×10^{-6} /°C and 13.44×10^{-6} /°C, respectively.
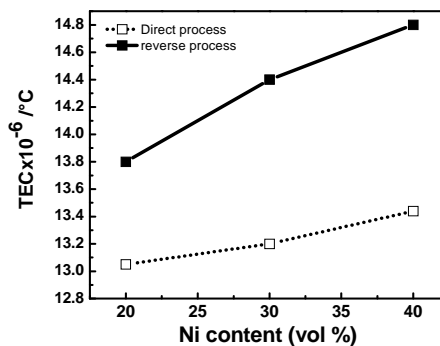
Fig. 6.22: TEC as a function of Ni concentration the Ni: 8YSZ cermet.

6.3.4: Summary

Ni: 8YSZ cermet containing 20, 30 and 40 vol % Ni were successfully fabricated through heterogeneous precipitation method using direct and reverse processes. The porosity of Ni: 8YSZ cermet prepared via direct and reverse process varies from 15 to 39 %, depending on the Ni concentration. Back scattered SEM micrographs of sintered 20 vol % Ni containing NiO: 8YSZ compsoites show uniform distribution of Ni in YSZ matrix, prepared either via direct or reverse processes. With increasing Ni content, NiO particles are agglomerated and segregated in the YSZ matrix. After reduction, Ni particles are deposited at the grain boundary of YSZ in the cermet HPN20D S13 R and HPN20R S13 R. From EDS mapping, it was confirmed that Ni particles are not only deposited on the grain boundary, but also it was present on the surface of YSZ. The cermet prepared through direct process shows better electrical conductivity than that of reverse process cermet with same Ni concentration. Better percolation with higher conductivity was observed in lower Ni (20 vol %) containing Ni: 8YSZ cermet prepared via direct process. The presence of $Ni(OH)_2$ in the as-synthesized powders play a major role for developing a dense Ni: 8YSZ cermet with better electrical conductivity than that containing metallic Ni in the as-synthesized powders. The TEC of HPN20D S13 R cermet is 13.1×10^{-6} /°C and TEC value increases with increase in Ni concentration. So, the potential of this novel heterogeneous precipitation method aids to tailor the microstructure of Ni: 8YSZ cermet having lower content Ni with a comparable TEC in addition to adequate electrical conductivity for use as anode in IT-SOFC. Further, to confirm the applicability of direct process heterogeneous precipitation derived powders in IT-SOFC, the electrochemical performance of symmetrical cell was studied and discussed in chapter 7.

CHAPTER 7

Electrochemical performance of symmetrical SOFC

In this chapter, polarization resistance, electrode conductivity, capacitance and exchange current density of symmetrical cell was determined from impedance spectroscopy using YSZ as electrolyte and prepared Ni: 8YSZ as anode. Four samples such as 40 vol % Ni containing cermet prepared through fuel stoichiometric condition in auto-combustion method, 40 vol % Ni containing cermet prepared using chloride and nitrate precursors in constant pH co-precipitation method and 20 vol % Ni containing cermet prepared through direct process in heterogeneous precipitation method were chosen as anode because of their high electrical conductivity and better microstructure.

7.1: Introduction

In the results and discussion of chapter 4, 5 and 6, it was found that fuel stoichiometric based auto-combustion, constant pH based co-precipitation using chloride and nitrate precursors and direct process based heterogeneous precipitation are the most efficient and suitable ways to develop Ni: 8YSZ cermet having adequate electrical conductivity and proper microstructure. To assess the suitability of the prepared cermet materials for use as anode in IT-SOFC, it is necessary to evaluate one of the important properties such as polarization resistance of symmetrical cell by impedance spectroscopy. Four samples such as 40 vol % Ni containing cermet prepared through fuel stoichiometric condition in auto-combustion method (denoted as CB FS N40), 40 vol % Ni containing cermet prepared using chloride and nitrate precursors in constant pH co-precipitation method (denoted as CP CL/NT N40) and 20 vol % Ni containing cermet prepared through direct process in heterogeneous precipitation method (denoted as HP DP N20) were chosen as anode owing to their high electrical conductivity and better microstructure. Polarization resistance, electrode conductivity, capacitance and exchange current density of symmetrical cell and microstructure of fractured interface have been analyzed.

7.2: Experimental

The anode ink was prepared by mixing NiO-YSZ powders (prepared via different syntheses) in a solution of glycerol (as solvent) and polyethylene glycol (PEG) (as binder). The weight ratio of the glycerol to PEG was kept at 94:6 and the solid loading was 75 wt %. The symmetrical cell such as Ni-YSZ/YSZ/Ni-YSZ was prepared by coating (manually) the anode ink on to both sides of dense YSZ discs. After sintering and reduction (details are described in chapter 3), the performance of symmetrical cell was analyzed by impedance spectroscopy. The impedance of the cells was measured within a frequency range of 42 Hz to 5 M Hz at 1 V, in H_2 atmosphere from 600 °C to 900 °C. The impedance spectra were collected during cooling cycle and extrapolated to low frequency region by Kramers-Kroning relations using ZSimpWin software. The data were fitted with respective equivalent circuits and the polarization resistance, electrode conductivity, capacitance and exchange current density was determined.

7.3: Results and discussion

7.3.1: Impedance spectroscopy

Figure 7.1(a), (b), (c) and (d) show the impedance spectra of symmetrical cells CB FS N40, CP CL N40, CP NT N40 and HP DP N20, respectively, at different temperatures measured within a frequency range of 42 Hz to 5 MHz at 1V.
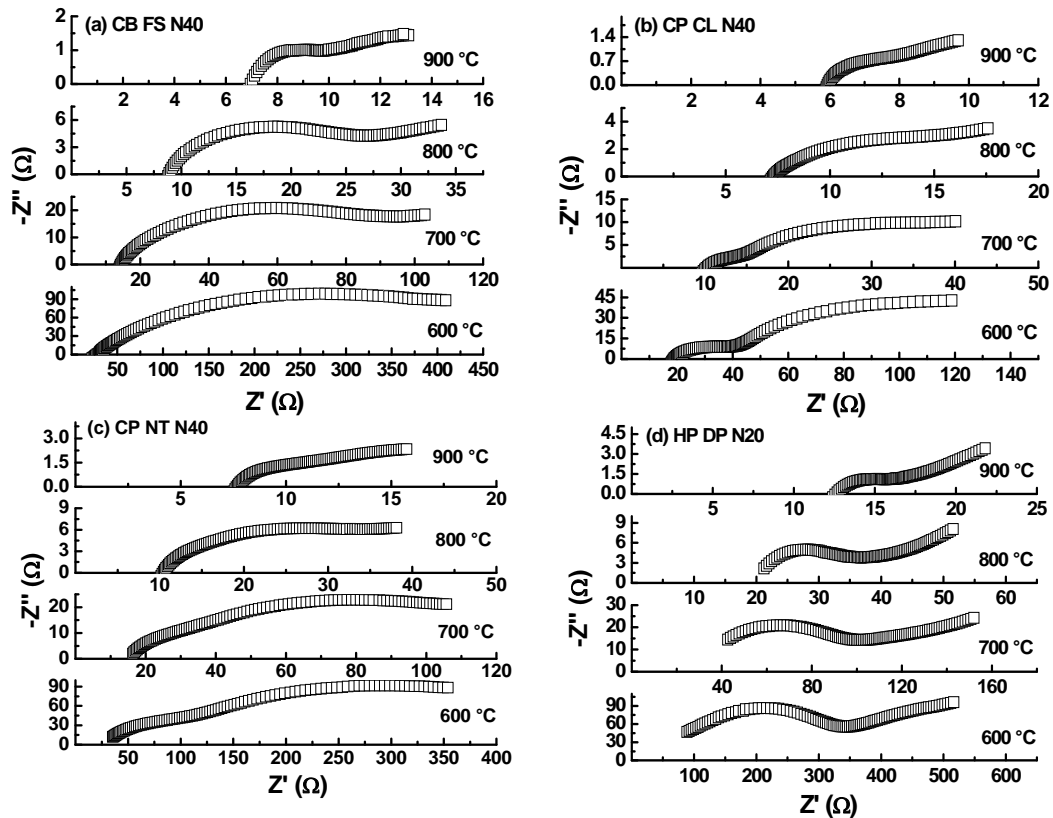
Fig. 7.1: Impedance spectra of CB FS N40 (a), CP CL N40 (b), CP NT N40 (c) and HP DP N40 (d) in the temperature range of 600 °C to 900 °C.

In general, the impedance spectra may consist of one, two or three arcs, depending on the frequency range and also depend on the microstructure of cell also contributes to the impedance spectra. The frequency range such as 1 kHz – 50 kHz, 10 Hz – 1 kHz and 0.1 – 10 Hz correspond to the high, mid and low frequency regions, respectively [115]. As observed from Fig. 7.1, only the high frequency arc and a part of the mid frequency arc was obtained in all cells. Some part of mid and low frequency contribution could not be recorded due to the limitations of frequency range imposed by the instrument. The existence of two arcs, corresponding to high and mid (partly) frequency range can be visualized from impedance spectra at four different temperatures for all cells and was indistinguishable some cases. It is also observed that the intercept of the high frequency arc with the real axis gradually shifted to lower value with increase in temperature. In some cases e.g. HP DP N20, the high frequency arc does not intercept the real axis.

The presence of multiple arcs, correspond to different electrode processes during the oxidation of molecular hydrogen. The high frequency arc corresponds to the polarization arising from the charge transfer reaction at the electrode-electrolyte interface. The polarization arising from the adsorption or desorption of hydrogen on the electrode surface and subsequent diffusion gives

rise to the mid and low frequency arcs [106, 116]. In order to have a better interpretation of the processes, the impedance spectra were extrapolated to the low frequency range, using Kramers-Kroning relation by ZSimpWin software. After appropriate extrapolation, the presence of two arcs in case of CB FS N40 and three arcs in case of CP CL N40, CP NT N40 and HP DP N20 was confirmed. However due to superposition, the mid and low frequency arcs cannot be distinguished. To evaluate the polarization resistance of the symmetrical cells, the arc corresponding to the high frequency region alone was taken into account, because the extrapolated data may or may not give a proper interpretation of the processes in low frequency range. The spectra of CB FS N40 cell was fitted with an equivalent circuit of $LR_S(R_1Q_1)(R_2Q_2)$, whereas $LR_S(R_1Q_1)(R_2Q_2)(R_3Q_3)$ was used to fit the experimental data of CP CL N40, CP NT N40 and HP DP N20 cells. Here, L, R and Q are the inductance, resistance and double layer constant phase element, respectively. The impedance of Q can be expressed as $Z_Q = 1/Y(j\omega)^n$ [115, 148], where, Y is the pseudo-capacitance, j is the imaginary unit, ω is the angular frequency ($\omega=2\pi f$) and n is the frequency power. For ideal capacitors, n=1 and for pure resistors, n=0. The inductance L can be attributed to the inductive processes in the Ni current/voltage leads or the experimental instrument at high temperature. R_S is the electrolyte contribution including its resistance as well as dc resistance of leads and electrode. The deviation from semi-circular nature of the arcs (as observed in impedance spectra) was taken into account and hence, the constant phase element (Q) was chosen instead of capacitance in the equivalent circuit. R-Q element has been considered in the equivalent circuit for fitting the experimental data. The total polarization resistance R_p comprises the charge transfer resistance R_1 and diffusion resistances R_2 and R_3. As the impedance spectra were extrapolated to the low frequency region, the value of R_2 and R_3 may not be predicted with sufficient accuracy. Hence, the contribution of R_1 corresponding to the total polarization resistance is considered. The value of R_1 was determined by fitting the impedance spectra with the equivalent circuits after extrapolation. A typical fitting along with the experimental and calculated spectra for CB FS N40, CP CL N40, CP NT N40 and HP DP N20 cells measured at 800 °C and their equivalent circuits are shown in Figure 7.2. The value of charge transfer resistance corresponding to R_1 was determined from equivalent circuit for all cells. Fig. 7.3 (a) shows the temperature dependent charge transfer resistance of the cells in the form of ln (R_1) versus 1000/T. R_1 is found to decrease with increase in temperature for all symmetrical cells. Lowest resistance was found in all cells at 900 °C. Further, the resistance of CP CL N40 cell was found to be the lowest in comparison to other cells. Irrespective of the lower volume percent of Ni (20 vol %), the sample HP DP N20 shows comparable resistance with CB FS N40, which contains 40 vol% of Ni. The electrode conductivity ($\sigma=1/R$) [103, 116, 149] corresponding to the high frequency arc was calculated and is shown in Fig. 7.3 (b). The electrode

conductivity almost remains the same within a temperature range of 600 °C to 800 °C and sharply increases at 900 °C. Highest conductivity was observed in CP NT N40 at 900 °C. The values of charge transfer resistance and electrode conductivity are summarized in Table 7.1.
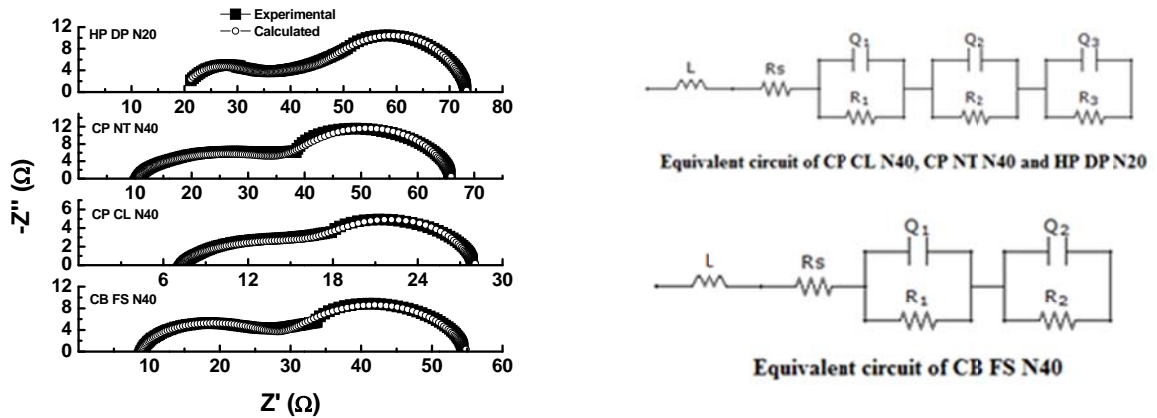
Fig. 7.2: Experimental and calculated impedance spectra of CB FS N40, CP CL N40, CP NT N40 and HP DP N20, measured at 800 °C and their equivalent circuits.
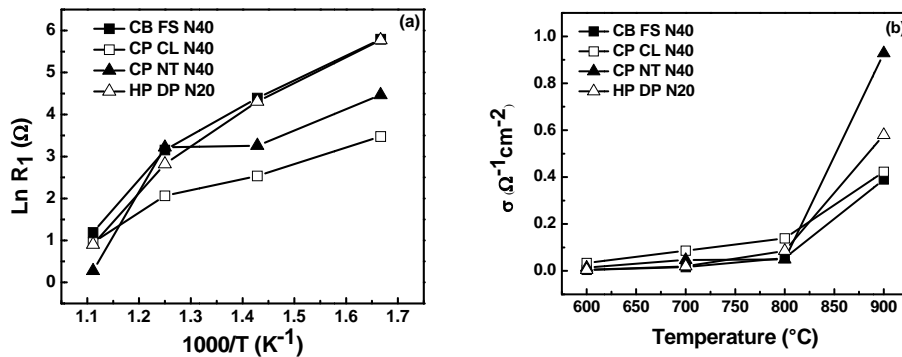
Fig. 7.3: Temperature dependent charge transfer resistance of cells at different temperatures (a) and corresponding electrode conductivity (b).

Table 7.1: Charge transfer resistance (Ω cm^2) and electrode conductivity (Ω^{-1}cm^{-2}) of different cell at various temperatures

Cell	Temperature							
	600 °C		700 °C		800 °C		900 °C	
	R_1 (Ω cm^2)	σ (Ω^{-1}cm^{-2})	R_1 (Ω cm^2)	σ (Ω^{-1}cm^{-2})	R_1 (Ω cm^2)	σ (Ω^{-1}cm^{-2})	R_1 (Ω cm^2)	σ (Ω^{-1} cm^{-2})
CB FS N40	255.46	0.0039	63.17	0.0158	18.30	0.0546	2.56	0.3897
CP CL N40	29.7	0.0337	11.58	0.0864	7.22	0.1384	2.36	0.4227
CP NT N40	71.2	0.014	21.30	0.0469	20.46	0.0488	1.07	0.9283
HP DP N20	224.2	0.0045	51.82	0.0193	11.70	0.0854	1.72	0.5796

The capacitance of the single electrode process corresponding to the high frequency arc was also determined according the equation $C_i = \{(R_iQ_i)^{1/n_i} / R_i\}$ [150, 151]. The value capacitance may correspond to the double layer capacitance at the electrode (Ni: YSZ)/electrolyte (YSZ) interface [152]. Fig. 7.4 shows the temperature dependent capacitance of each symmetrical cell, corresponding to the high frequency arc. It can be observed that the capacitance of CB FS N40, CP NT N40 and HP DP N20 almost remains constant over the entire temperature range. But, the capacitance of CP CL N40 was found to increase sharply above 800 °C.
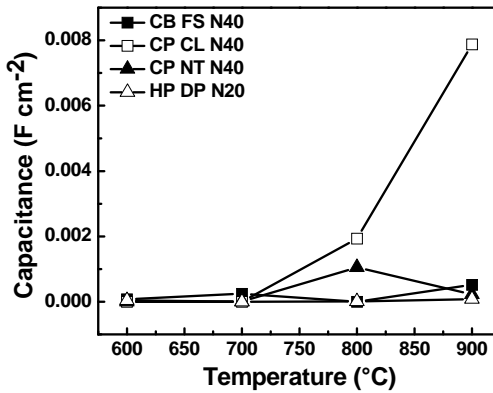
Fig. 7.4: Capacitance of CB FS N40, CP CL N40, CP NT N40 and HP DP N20 cells at different temperatures.

The value of exchange current density per electron, related to the charge transfer polarization, was calculated using the following formula $i_0 = \{RT/zFR_1\}$ [153] and is summarized in Table 7.2. Here, i_0 is the exchange current density, z is the number of electrons participating in the electrode reaction, F is the Faraday constant, R is the universal gas constant and R_1 is the intrinsic charge transfer resistance. The value of exchange current density (in A/cm^2) was found to increase with temperature for all cells.

Table 7.2: Exchange current density i_0 (A/cm^2) of CB FS N40, CP CL N40, CP NT N40 and HP DP N40 at different temperatures.

Temperature Cell	900 °C	800 °C	700 °C	600 °C
CB FS N40	0.039398	0.005052	0.001327	0.000294
CP CL N40	0.042728	0.012802	0.00724	0.002533
CP NT N40	0.093837	0.004518	0.003935	0.001057
HP DP N20	0.058586	0.007901	0.001618	0.000336

7.3.2: Microstructure and EDS mapping

The polarization behavior of the symmetrical cells is strongly dependent on the microstructure of the anode. Figure 7.5 shows the microstructure of the fractured interface of the CB FS N40, CP CL N40, CP NT N40 and HP DP N20.
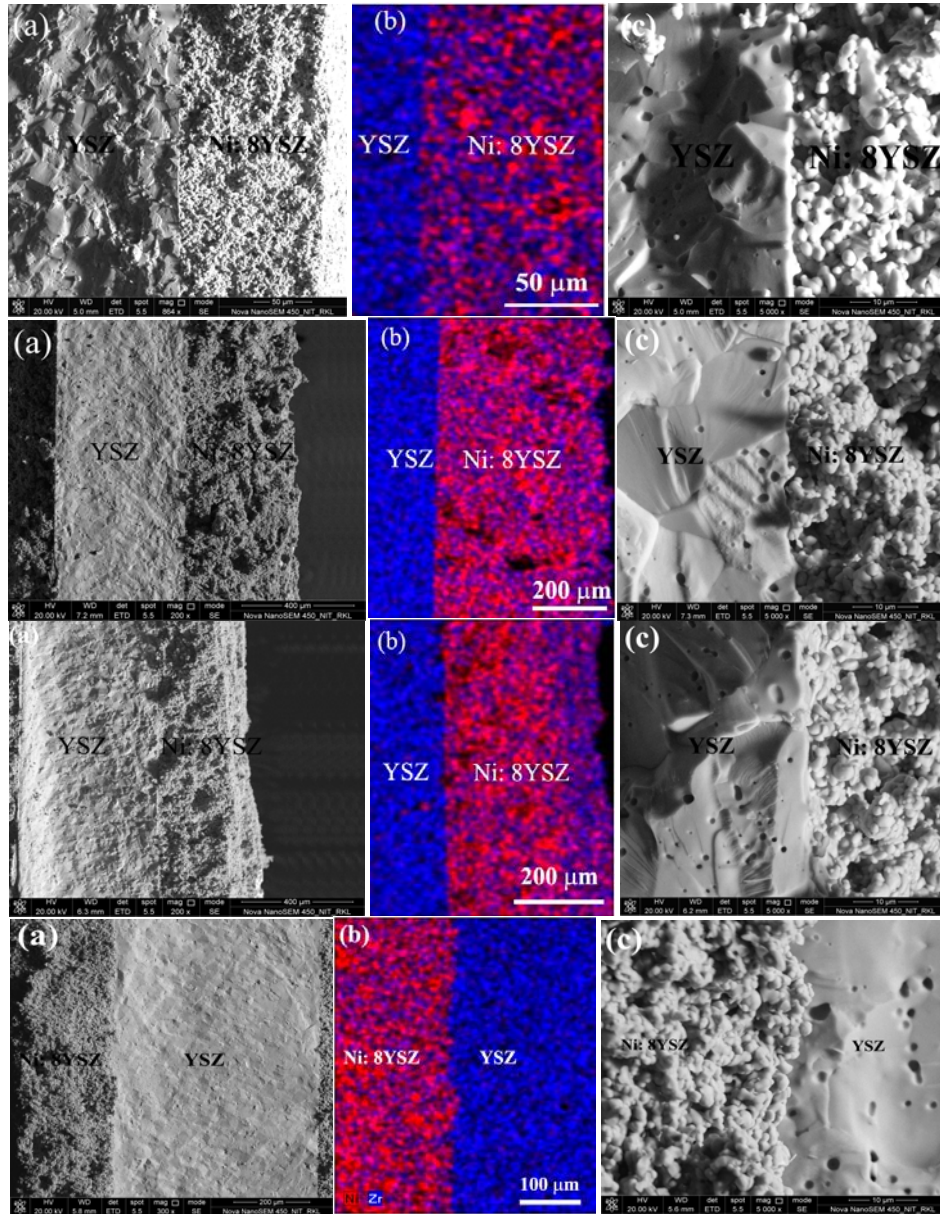
Fig. 7.5: Fracture interface microstructure of CB FS N40, CP CL N40, CP NT N40 and HP DP N40 indicating thickness of anode (a), distribution of Ni (red), YSZ (blue) in cell (b) and interface of electrolyte (YSZ) and anode (Ni: 8YSZ) (c).

It can be observed that the coating thickness of the anode varies from 150 μm to 400 μm for different symmetrical cells. The thickness was found to be highest for CP CL N40 (~ 400 μm) and

lowest for CB FS N40 (~ 150 μm). From the EDS mapping, a very uniform distribution of fine Ni and YSZ particles in the anode layer was confirmed. The porosity of the anode layer seems to be comparable for symmetrical cells. Irrespective of the different syntheses used for preparation of NiO: 8YSZ powders and concentration of Ni, the microstructure shows a strong adherence of the cermet layer to the electrolyte as confirmed from magnified microstructure of the interface. As a consequence, the thermal expansion compatibility of the anode layer with the electrolyte can be contemplated adequately. The thickness of anode layer and microstructure has a direct effect on the electrochemical performance of the symmetrical cells.

The overall lower charge transfer resistance, found for CP CL N40 cell, may be attributed to the higher coating thickness of the anode, as compared to other symmetrical cells. However, at 900 °C, all the four cells show lower and comparable charge transfer resistance. Instead of the lower concentration of Ni (20 vol %) used in HP DP N20 cell, still the charge transfer resistance is comparable to CB FS N40 cell. This is due to a very uniform distribution of fine Ni particles in YSZ matrix, which significantly lowered the percolation threshold and led to higher electrical conductivity (discussed in Chapter 6). These observations further establish the fact that the performance of the symmetrical cells depend upon the coating thickness, vol % of Ni, distribution of Ni in YSZ matrix and overall the microstructure. To further analyze the results obtained from the experiment, polarization resistance or charge transfer resistance reported in various literatures are listed in Table 7.3.

From the reported literatures, it can be deduced that the powder preparation methods, pretreatment effects, concentration of Ni in the cermet, sintering temperature and operation temperature significantly affect the polarization of the cell. Using 40 vol% Ni, the polarization resistance of $0.3 - 9$ Ω cm^2 was obtained at 1000 °C [100] in mixing or ball milling method, but it required additional pre-calcination temperature (1400 °C) and higher sintering temperature (1400 – 1500 °C). In this method, the polarization resistance may also be as high as 104.7 Ω, using 65 vol% Ni [154], but can be minimized either by pre-calcination [154] or by increasing the concentration of Ni [102, 116, 155]. Addition of anode functional layer with higher sintering temperature may also minimize the polarization [106]. But in this study, using 40 vol% of Ni and sintering temperature of 1350 °C, the charge transfer resistance (R$_1$) was found to be as low as 2.56, 2.36 and 1.07 Ω cm^2. Again, an R$_1$ value of 1.72 Ω cm^2 was achieved at a Ni concentration as low as 20 vol%. The polarization resistance can further be minimized at lower temperatures by considering the type of current collector, thickness of anode and electrolyte, concentration of Ni and porosity of the anode

layer, which requires a detailed study. But the potential of these methods to fabricate Ni: 8YSZ anode materials for IT SOFC application can be well understood.

Table 7.3: Polarization resistance (R_p) or charge transfer resistance (R_1) reported in literatures

Powder preparation	Vol % of Ni	Sintering/reduction temperature	Electrode Resistance (R_p/R_1)/measurement temperature	[Ref.]
Mixing or ball milling Precalcination at 1400°C	40	1500 1400 1200	0.3 Ω cm^2 / 1000 °C (R_p) 2.5 Ω cm^2 / 1000 °C 9 Ω cm^2 / 1000 °C	[100]
Mixing method	44 65	1400/1000	99 Ω / 1000 °C (R_1) 104.7 Ω / 1000 °C	[154]
Precalcination (1350 °), Mixing and ball milling	50 86		2.5 Ω / 1000 °C 5.6 Ω / 1000 °C	
Ball milling	80 70	1400	0.60 Ω cm^2 / 1000 °C (R_1) 0.22 Ω cm^2 / 1000 °C	[116]
Mixing method	87 40		340 mΩ cm^2 / 1000 °C 235 mΩ cm^2 / 1000 °C	[102]
Combustion synthesis		1450/800	13 Ω / 681 °C 4.5 Ω / 761 °C	[43]
Mixing and ball milling	Anode substrate and functional layer*	1500/800	0.209 Ω cm^2 / 800 °C (R_1)	[106]
	50**	---/900	0.61 – 0.93 Ω cm^2 / 900 °C	[148]
Co-precipitation	50	1300/800	2.29 Ω cm^2 / 600 °C 0.43 Ω cm^2 / 700 °C 0.15 Ω cm^2 / 800 °C	[51]
Ball milling	65**	1350/800	0.15 – 0.6 Ω cm^2 / 800 °C (R_1)	[155]
High speed mixing	60	1200	0.8 Ω cm^2 / 750 °C 0.2 Ω cm^2 / 800 °C	[156]
Photolithographic process			112.5 Ω cm^2 / 700 °C	[157]
Co-precipitation	50	1350	0.62 Ω cm^2 / 700 °C 0.34 Ω cm^2 / 750 °C 0.23 Ω cm^2 / 800 °C	[53]
Auto-combustion (fuel stoichiometric)	40	1350/900	255.46 Ω cm^2 / 600 °C 63.17 Ω cm^2 / 700 °C 18.30 Ω cm^2 / 800 °C 2.56 Ω cm^2 / 900 °C	[in this study]
Co-precipitation (constant pH, chloride precursor)	40	1350/900	29.7 Ω cm^2 / 600 °C 11.58 Ω cm^2 / 700 °C 7.22 Ω cm^2 / 800 °C 2.36 Ω cm^2 / 900 °C	[in this study]
Co-precipitation (constant pH, nitrate precursor)	40	1350/900	71.2 Ω cm^2 / 600 °C 21.30 Ω cm^2 / 700 °C 20.46 Ω cm^2 / 800 °C 1.07 Ω cm^2 / 900 °C	[in this study]
Heterogeneous precipitation (direct)	20	1350/900	224.2 Ω cm^2 / 600 °C 51.82 Ω cm^2 / 700 °C 11.70 Ω cm^2 / 800 °C 1.72 Ω cm^2 / 900 °C	[in this study]

* 70 wt% NiO (AFL I- 50 wt % NiO) (AFL I- 60 wt % NiO)
** wt % NiO

7.3.3 Summary

Ni-YSZ/YSZ/Ni-YSZ symmetrical cells have successfully been fabricated and their polarization behavior, within the temperature range of 600 °C – 900 °C, was studied by impedance spectroscopy. The impedance spectra of these cells were found to consist of two or three arcs after extrapolation to low frequency range. The charge transfer resistance corresponding to the high frequency arc was calculated by fitting the spectra with plausible equivalent circuits. The charge transfer resistance was found to decrease with increase in temperature and found to be lowest at 900 °C. The cell CP CL N40 was found to have lower resistance in the temperature range of 600 – 800 °C as compared to other cells. The resistance of HP DP N20 was comparable to that of CB FS N40. The values of electrode conductivity, double layer capacitance and exchange current density, were also determined from the charge transfer resistance, using different formula. The microstructure of the fractured interface was observed by FESEM. The coating thickness of different cells was found to vary in between 150 to 400 μm. Uniform distribution of Ni and YSZ particles in the anode layer, with appropriate porosity, was also confirmed from the microstructure. The presence of strong bonding between the anode layer and electrolyte was visualized.

CONCLUSIONS

This Ph.D. work described synthesis of NiO: 8YSZ powders via different solution-based syntheses such as auto-combustion, co-precipitation and heterogeneous precipitation. Using these NiO: 8YSZ powders, different types of microstructure were developed in Ni: 8YSZ anode. Specific anode characteristics such as porosity/density, microstructure, electrical conductivity, thermal expansion coefficient as well as cell performance were studied and the following major points are correlated in this conclusions section.

A. Phase formation in as-synthesized powders

➢ Crystalline NiO, YSZ and minute amount of Ni were formed during fuel stoichiometric based auto-combustion method. The crystallite size of NiO and YSZ was found to be 71 nm and 53 nm, respectively, for the as-synthesized as well as calcined (650 °C) powders and was nearly unaffected up to 850 °C. However, amorphous and semi-crystalline nature was observed in both fuel lean and fuel rich as-synthesized powders.

➢ Crystalline $Ni(OH)_2$ and amorphous hydrous zirconia were formed in the as-synthesized powders, prepared via direct/reverse/constant pH co-precipitation method, using either chloride or nitrate precursor. At 650°C, crystallite size of NiO and YSZ was found to be smaller (12-14 nm and 8 nm, respectively) in constant pH process derived samples.

➢ Crystalline $Ni(OH)_2$, Ni and YSZ were formed in direct/reverse process derived 20 vol % Ni as well as direct process derived 30 vol % Ni containing as-synthesized powders, whereas, Ni and YSZ were formed in reverse process derived 30 vol % Ni as well as direct/reverse process derived 40 vol % Ni containing as-synthesized powders. The crystallite size of NiO and YSZ was found to be 20 nm and 15 nm, respectively at 650 °C in all samples.

B. Density or porosity of NiO/Ni: 8YSZ composites

Density/porosity was optimized during fabrication of NiO: 8YSZ pellets by considering two factors such as binder concentration and compaction pressure. 2 wt % PVA at a compaction pressure ~ 588 MPa was found suitable for obtaining higher dense composite materials.

➢ The density of fuel lean, fuel stoichiometric and fuel rich combustion derived 30 vol % Ni containing sintered (1200 °C) NiO: 8YSZ pellets was found to be 88 %, 87 %and 76 %, respectively. The corresponding porosity of Ni: 8YSZ cermet was found to be 29 %, 28 % and 39 %, respectively. The porosity of fuel stoichiometric combustion derived Ni: 8YSZ cermet lies in between 20 % to 29 %, depending on the sintering condition and Ni concentration.

➢ Density of 30 vol % Ni containing NiO: 8YSZ composite prepared via co-precipitation method using chloride/nitrate precursor, lies in between 85 % to 95 %, depending on the synthesis conditions. The corresponding porosity of Ni: 8YSZ cermet lies in between 20 % to 30 %. The porosity of 1200 °C based constant pH derived (using both precursors) Ni: 8YSZ cermet (20, 30 and 40 vol % Ni) lies in between 20 % to 27 %, whereas, the porosity of 1300 °C based cermets lies within 15 % to 25 %.

➢ Density of sintered (1300 °C) NiO/Ni: 8YSZ pellets, prepared via direct heterogeneous method showed higher density than reverse process. Porosity of direct process derived 20, 30 and 40 vol % Ni containing Ni: 8YSZ cermet was found to be 15 %, 20 % and 36 %, respectively, whereas, porosity of reverse process derived 20, 30 and 40 vol % Ni containing cermet was found to be 22 %, 33 % and 39 %, respectively.

C. Size and distribution of Ni in 8YSZ matrix

The size and distribution of NiO/Ni particles in 8YSZ matrix was found to depend on the initial forms of Ni, concentration of Ni and porosity of the NiO: 8YSZ composites as well as sintering temperature.

➢ Particles of NiO and YSZ are formed at the same time in auto-combustion process and size as well as growth rate depends on the exothermicity of the combustion. Size of Ni was found to be 400 nm to 800 nm and size of YSZ was found to be 700 nm to 1.5 µm for fuel stoichiometric based auto-combustion derived cermets (both 30 and 40 vol % Ni), prepared at a sintering condition of 1200 °C. In this case, Ni and YSZ particles are uniform and well distributed in the matrix. However, at a sintering condition of 1300 °C, the size Ni particles was found to be 600 nm to 900 nm and size of YSZ was found to be ~ 800 nm to ~ 2 µm. At this condition, fine grained Ni particles are forming a continuous chain around YSZ particles in 30 and 40 vol% Ni containing cermets. However, in 20 vol % Ni containing cermet, YSZ particles are bigger in size and Ni particles are at the grain boundary of YSZ.

➢ Particle size of NiO in NiO: 8YSZ powders are further reduced via co-precipitation method using HH and NaOH as precipitating agents. Size of Ni in constant pH co-precipitation derived Ni: 8YSZ cermet (prepared using chloride/nitrate and sintering condition of 1200 °C) was in the range between 200 nm to 700 nm. At this stage, fine Ni and YSZ particles are well distributed. At sintering condition of 1300 °C, 20 and 40 vol % Ni containing cermets showed a uniform grain size of Ni and YSZ. However, particle size of YSZ in 30 vol % Ni containing cermet prepared using chloride and nitrate precursor was 3 and 5 µm, respectively. In these

two samples, fine Ni particles (500 nm) are segregated on grain boundary as well as on the surface.

➢ In case of heterogeneous precipitation method, ultra- fine NiO/Ni particles (~ 700 nm) were well-distributed in 8YSZ matrix for 20 vol % Ni containing NiO/Ni: 8YSZ composites, prepared by either direct or reverse process. However, with increase in Ni content, Ni particles are segregated and separated in YSZ matrix.

D. Electrical conductivity of Ni: 8YSZ cermet

➢ Fuel lean (30 vol % Ni) and fuel stoichiometric (30, 40 vol % Ni) combustion derived Ni: 8YSZ cermets show electronic type behavior, whereas ionic behavior was observed in fuel rich (30 vol % Ni) and fuel stoichiometric (20 vol % Ni) combustion derived cermets. The typical conductivity value of 40 vol % Ni containing cermet (prepared at sintering condition of 1300 °C) is 500 S/cm, at 300 °C and then decreases exponentially to ~ 89 S/cm (at 900°C).

➢ Constant pH co-precipitation derived cermet (using both chloride and nitrate precursor) shows highest conductivity (~ 320 S/cm at 300 °C) than direct/reverse condition. Ionic type behavior was observed in 20 vol % Ni containing cermet at all preparation condition. Conductivity of 30 and 40 vol % Ni containing cermet (both chloride and nitrate precursor based constant pH method and sintered at 1200 °C) was 320 S/cm and 650 S/cm, respectively, at 300 °C. The typical conductivity of chloride and nitrate precursor based 40 vol % Ni containing cermet prepared in constant pH process was 1800 S/cm and 3400 S/cm, respectively at 300 °C and then exponentially decreases to 150 S/cm and 250 S/cm (at 900°C).

➢ Conductivity decreases linearly with temperature for all cermets prepared via heterogeneous precipitation method. The direct process heterogeneous precipitation derived 20 vol % Ni containing cermet showed higher conductivity of ~ 425 S/cm at 300 °C and ~ 158 S/cm at 900 °C.

➢ The percolation threshold of auto-combustion and co-precipitation derived cermet was found to be in between 20 and 30 vol % Ni, whereas, cermet prepared via direct process heterogeneous precipitation method leads to lower percolation threshold of 20 vol % Ni.

➢ The non-linear and linear behavior of conductivity was observed in auto-combustion/co-precipitation and heterogeneous precipitation derived cermets, respectively and the non-linear behavior may be due to the contribution of ionic species in the cermet.

E. Thermal expansion of coefficient

➢ TEC of fuel stoichiometric derived 20, 30 and 40 vol % Ni containing cermet was found to be 12.8×10^{-6} /°C to 12.9×10^{-6} /°C and 13.8×10^{-6} /°C, respectively.

➢ TEC of 20, 30 and 40 vol % Ni containing cermet prepared using chloride precursor in co-precipitation method was found to be 12.6×10^{-6} /°C, 13.2×10^{-6} /°C and 13.4×10^{-6} /°C, respectively. However, TEC of 20, 30 and 40 vol % Ni containing cermet prepared using nitrate precursor in co-precipitation method was found to be 12.6×10^{-6} /°C, 13.3×10^{-6} /°C and 13.9×10^{-6} /°C, respectively.

➢ TEC of the cermet prepared via direct process heterogeneous precipitation method was lower than the TEC of cermet prepared via reverse process heterogeneous precipitation method. TEC of 20, 30 and 40 vol % Ni containing cermet (prepared via direct process) was found to be 13.05×10^{-6} /°C, 13.2×10^{-6} /°C and 13.4×10^{-6} /°C, respectively.

F. Electrochemical performance of symmetrical cell

Based on microstructure, electrical conductivity and TEC results, four different anode inks were prepared using different synthesized NiO: 8YSZ powders such as 40 vol % Ni containing powders prepared via fuel stoichiometric auto-combustion (denoted as CB FS N40), chloride based constant pH co-precipitation (denoted as CP CL N40) as well as nitrate based constant pH co-precipitation (denoted as CP NT N40) and 20 vol % Ni containing powders prepared via direct process heterogeneous precipitation (denoted as HP DP N20). The symmetrical cell such as Ni-YSZ/YSZ/Ni-YSZ was prepared by coating the anode ink on to both sides of dense YSZ discs and electrochemical behavior was studied using impedance spectroscopy.

➢ The spectra of CB FS N40 cell was fitted with an equivalent circuit of $LR_S(R_1Q_1)(R_2Q_2)$, whereas $LR_S(R_1Q_1)(R_2Q_2)(R_3Q_3)$ was used to fit the experimental data of CP CL N40, CP NT N40 and HP DP N20 cells.

➢ The charge transfer resistance of CP CL N40 cell was found to be lowest as compared to other cells. Irrespective of the lower volume percent of Ni (20 vol %), the sample HP DP N20 shows comparable resistance with CB FS N40, which contains 40 vol% of Ni. This is due to a very uniform distribution of fine Ni particles in YSZ matrix, which significantly lowered the percolation threshold and led to higher electrical conductivity.

➢ The electrode conductivity almost remains the same up to 800 °C and then abruptly increases, with the highest conductivity observed for CP NT N40 at 900 °C. The capacitance of all cells almost remains constant over the entire temperature range. But, the capacitance of CP CL N40 was found to increase sharply above 800 °C. The exchange current density was found to increase with temperature for all cells.

➢ The coating thickness of the anode varies from 150 μm to 400 μm for different symmetrical cells. The thickness was found to be the highest for CP CL N40 (~ 400 μm) and lowest for CB FS N40 (~ 150 μm). Irrespective of the different syntheses used for preparation of NiO:

8YSZ powders and concentration of Ni, the microstructure shows a strong adherence of the cermet (Ni: 8YSZ) layer to the electrolyte (8YSZ).

From above results, it was confirmed that the adopted solution-based syntheses such as fuel stoichiometric auto-combustion, constant pH co-precipitation and direct process heterogeneous precipitation are most suitable for developing fine grained NiO: 8YSZ composites. The fabricated Ni: 8YSZ cermet, using these powders, tailors the microstructure of Ni: 8YSZ cermet, having fine Ni particles in 8YSZ matrix with appropriate electrical conductivity, compatible TEC and overall cell performance. Among the solution-based syntheses, constant pH co-precipitation method is more advantageous for developing finer grain size of Ni in the Ni: 8YSZ cermet due to the formation of $Ni(OH)_2$ in the as-synthesized powders and this particular cermet shows better anode properties for IT-SOFC application.

Scope for future work

Based on the results obtained in this Ph.D. work, some of the following points may be taken care and can carry forward as a future work for the development of Ni: 8YSZ cermet anode.

➢ Synthesis of amorphous $Ni(OH)_2$ and amorphous hydrous zirconia via constant pH co-precipitation and heterogeneous precipitation method by varying the concentration of HH and NaOH.

➢ Study the phase development of as-synthesized powders containing amorphous $Ni(OH)_2$ and hydrous zirconia.

➢ Effect of ball milling on particle size and properties of NiO/Ni: 8YSZ composites.

➢ Development of NiO/Ni: 8YSZ composites using the above mentioned calcined NiO: 8YSZ powders.

➢ Effect of Ni concentration (20 vol % to 60 vol %) and sintering temperature on density/porosity, microstructure, electrical conductivity and TEC of Ni: 8YSZ cermet.

➢ Study the electrochemical behavior of symmetrical cell fabricated using above synthesized NiO: 8YSZ powders.

➢ Study the effect of Ni content, effect of coating thickness and effect of thickness of electrolyte on electrochemical behavior symmetrical cell.

APPENDIX 1

Efficient way of precipitation to synthesize Ni^{+2}-ion stabilized tetragonal zirconia nanopowders

_____

A1-1: Introduction

Pure Zirconia (ZrO_2) and stabilized ZrO_2 ceramics modified by the incorporation of transition metal ions receive great attention owing to their potential applications in catalyst and solid oxide fuel cells [158-162]. The transition metal ions especially Ni^{2+} (smaller size and lower valency as compared to Zr^{4+} ions) creates lattice defects which play a major role in stabilizing t / c phase of ZrO_2 [163]. Štefanić et al. [162] have partially stabilized t-ZrO_2 up to 600 °C by increasing pH of the precursor solution up to 10.5. Sato et al. [50] have synthesized homogenous porous structure of NiO/YSZ (yttria stabilized zirconia) nanocomposite particles under highly basic solution (pH 13). Several efforts have been made to stabilize t / c –ZrO_2 with the incorporation of Ni^{2+} using sol-gel or precipitation technique by adding tetramethyl ammonium hydroxide [$(CH_3)_4NOH$] or ammonium hydroxide (NH_4OH) [158, 164]. However, there was no report on the synthesis of Ni^{2+}-stabilized t-ZrO_2 nanopowders using hydrazine hydrate (N_2H_5OH) as precipitating agent. But, Zhu et al. [165] have synthesized mixtures of t- ZrO_2 and monoclinic (m)-ZrO_2 at 150 °C using N_2H_5OH. The stabilization of t-ZrO_2 is strongly dependent on the synthesis methodology [166, 167]. Hence, the main objective of this work is to optimize the way of synthesis using an economically viable process and to investigate the capability of Ni^{2+} ions to stabilize t-ZrO_2 as well as the solubility limit of Ni^{2+} ions in ZrO_2 lattice.

A1-2: Experimental

Stabilized t-ZrO_2 nanopowders were prepared in three different (direct, reverse and constant pH) ways of precipitation from an aqueous salt solutions of (1-x) mol% of 0.2 M $ZrOCl_2.8H_2O$ and (x) mole% of 0.2 M $NiCl_2.6H_2O$ (where x = 0, 10, 20 and 30). In direct process, 10 vol % N_2H_5OH solution was added from a burette slowly to a beaker containing mixture of both salts solution. The reverse process is the reverse way of direct process. In constant pH process, the reverse process was followed with the addition of extra N_2H_5OH solution using a second burette to keep pH value constant at 10. The precipitates obtained were washed, dried and heat-treated at 700 °C and 800 °C for 1h. The Ni^{2+}- added ZrO_2 samples are designated as (D/R/C)NXZT: where 'D', 'R' and 'C' correspond to direct, reverse and constant pH process, respectively; NX stands for Ni^{2+} concentration; 'Z' stands for ZrO_2 and 'T' stands for calcination temperature. Phase analysis and morphology were characterized by X-ray diffraction (XRD) and transmission electron microscopy (TEM), respectively. Debye-Scherrer formula with correction factor was used for determining crystallite size. Lattice parameters and cell volume were calculated using unit cell refinement software. The monoclinic and tetragonal content was calculated using the intensities of several peaks in the XRD patterns, described by Garvie and Nicholson [168]. The strain induced

broadening is given by the Wilson formula as $\beta = 4 \times \varepsilon \times (\tan\theta_B)$: where β is full width at half maxima; ε is lattice strain and θ_B is the Bragg's angle.

A1-3: Results and discussion

The XRD patterns of heat-treated (800 °C) pure (0 mol %) and 10 mol % Ni^{2+}- added ZrO_2, synthesized in three different ways are shown in Fig.A1-1. All samples consist of both t-ZrO_2 and m-ZrO_2 in different volume percentage. But, t-ZrO_2 phase (95 vol %) was the prominent phase for sample CN10Z800 as compared with samples DN10Z800 and RN10Z800. It indicates that the presence of Ni^{2+} ion triggers a partial stabilization of t-ZrO_2 in constant pH process. Usually zirconium hydroxide starts to precipitate prior to nickel hydroxide with the addition of some basic solution in a conventional co-precipitation condition, in which pH of the solution containing constituent metal ions increased step by step [50]. Thus it would be difficult to synthesize Ni^{2+}-added t-ZrO_2 nanopowders either by direct or reverse process due to the inhomogeniety of the precipitation. Hence, to minimize the inhomogeniety, pH of the solution was kept constant. Maintaining higher pH during synthesis leads to decrease in precipitate size as well as the difference of precipitation rate between hydroxides [50]. Hence, the constant pH process is the effective way for synthesizing and stabilizing Ni^{2+} modified t-ZrO_2 nanopowders as compared to direct or reverse processes.
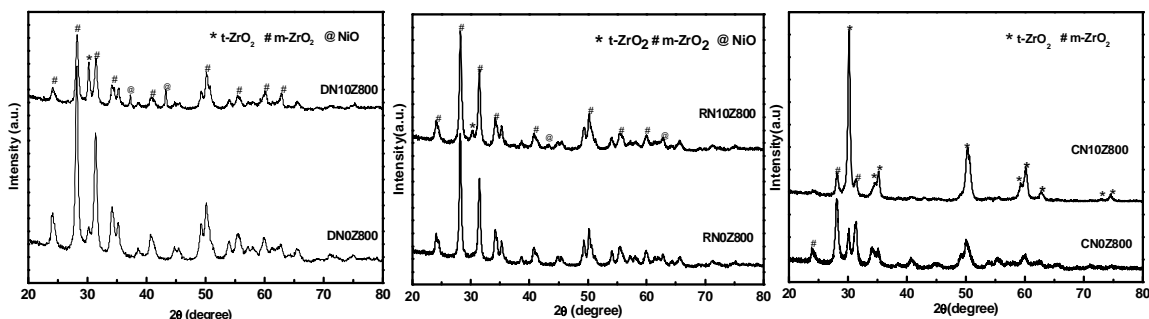
Fig. A1-1: XRD patterns of pure and Ni^{2+} (10 mol %)-added ZrO_2 powders synthesized in three different ways.

To understand the solubility limit of Ni^{2+} ion in ZrO_2 lattice and the capability of Ni^{2+} ions to stabilize t-ZrO_2 using constant pH process, different concentrations of Ni^{2+} ions were incorporated in ZrO_2 matrix. The XRD patterns of heat-treated (700 °C and 800 °C) ZrO_2 nanopowders with varying Ni^{2+} ions concentrations are shown in Fig. A1-2. Nearly equal proportionate of t-ZrO_2 and m-ZrO_2 were present in CN0Z700 and CN0Z800 samples. Tetragonal structure of ZrO_2 was observed at 700 °C and 800 °C only after addition of 10 mol % and 20 mol % Ni^{2+}, respectively. Štefanić et al. [169] reported that the minimum concentration of Ni^{2+} ions is 10 mol % for stabilization of t-ZrO_2 at 600 °C and the maximum solubility of Ni^{2+} ions in ZrO_2 lattice is ~ 5 mol%. Whereas in CuO-ZrO_2 system, the maximum solubility of Cu^{2+} ions in the ZrO_2 lattice is ~ 23 mol % and also stabilizes pure t-ZrO_2 up to 600 °C with addition of only 20 mol % CuO [162]. However in our case, the minimum concentrations of Ni^{2+} for stabilization of t-ZrO_2 at 700

°C and 800 °C are 10 mol % and 20 mol %, respectively. The composition of Ni^{2+} at and above 20 mol % shows distinct NiO reflections and it further confirmed that the maximum solubility limit of Ni^{2+} in ZrO_2 is less than 20 mol %. Phase compositions in volume percentage with crystallite size, lattice parameter, cell volume and lattice strain for different compositions of Ni^{2+}-added ZrO_2 nanopowders calcined at 700 °C and 800 °C are given in Table A1-1. Uniform particle size (~ 15 nm) of t- ZrO_2 was obtained in TEM (Fig. A1-3) and it is a good agreement with the crystallite size calculated from XRD.
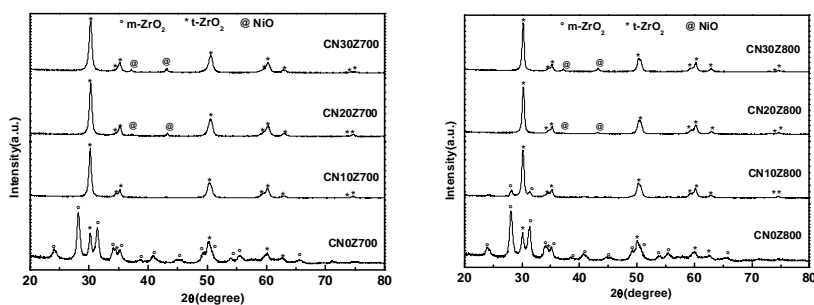
Fig. A1- 2: XRD patterns of calcined t-ZrO_2 nanopowders with addition of different concentration of Ni^{2+} ions.
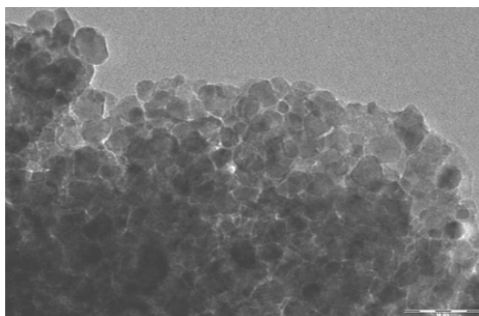
Fig. A1-3: TEM micrograph of 20 mol % Ni^{2+}-added t-ZrO_2 nanopowders. Scale corresponds to 50 nm.

Up to 30 mol % Ni^{2+} ion concentration, a linear decrease in cell volume for samples heat-treated at 700 °C indicates that nickel enters the lattice of ZrO_2 substitutionally. However, for samples heat-treated at 800 °C, the solubility limit of Ni^{2+} ion is 20 mol %. The much smaller extent of decrease in cell volume at this temperature indicates that part of Ni^{2+} ion may enter the ZrO_2 lattice interstitially. This behavior is similar to that reported for Cu^{2+} and Ni^{2+} substitution of Zr^{4+} [158, 170]. The lattice strain increases with increase in Ni concentration for Ni-ZrO_2 systems calcined at 700 °C due to the combined effect of decrease in crystallite size and incorporation of Ni^{2+} ion into the lattice sites of t-ZrO_2. However, for Ni^{2+}-ZrO_2 systems calcined at 800 °C, the increase in lattice strain is disrupted above 20 mol % Ni concentrations due to increase in crystallite size. Xu et al. [171] explained the stabilization behavior of t-ZrO_2 by considering the combined influence of crystallite size and lattice strain.

Table A1-1: Phase composition (in volume percentage) with crystallite size, lattice parameter, cell volume and lattice strain for different compositions of Ni added ZrO_2 nanopowders.

Sample	Phase composition (in volume percentage)	Crystallite size (nm)	Lattice parameter (Å)	Cell volume (Å)³	Lattice strain (%) of t- ZrO_2
CN0Z700	t-ZrO_2 (45) + m-ZrO_2 (55)	20	a = 3.599 c = 5.185	67.19	0.3736
CN10Z700	t-ZrO_2	17	a = 3.598 c = 5.160	66.83	0.4390
CN20Z700	t-ZrO_2 (94) + NiO (6)	16	a = 3.592 c = 5.170	66.70	0.4553
CN30Z700	t-ZrO_2 (93) + NiO (7)	15	a = 3.594 c = 5.159	66.61	0.4995
CN0Z800	t-ZrO_2 (42) + m-ZrO_2 (58)	21	a = 3.604 c = 5.152	66.91	0.3627
CN10Z800	t-ZrO_2 (78) + m-ZrO_2 (12)	19	a = 3.602 c = 5.153	66.88	0.4007
CN20Z800	t-ZrO_2 (93) + NiO (7)	19	a = 3.591 c = 5.171	66.72	0.4113
CN30Z800	t-ZrO_2 (92) + NiO (8)	20	a = 3.594 c = 5.172	66.80	0.3738

A1-4: Conclusions

The constant pH process is more advantageous way of precipitation as compared to the direct or reverse process in synthesizing and stabilizing t-ZrO_2 nanopowders. At 800 °C, the maximum solubility and minimum requirement of Ni^{2+} ions for stabilization of t-ZrO_2 is around 20 mol %. It is well known that the stabilization of t-ZrO_2 strongly depends on the crystallite size or lattice strain or type and amount of stabilizers. However, from our results it was confirmed that the factors which are favorable for stabilization of t-ZrO_2 are strongly dependent on the way of synthesis process. The present synthesis method for synthesizing and stabilizing t-ZrO_2 nanopowders with the incorporation of Ni^{2+} ions using N_2H_5OH is attractive and could be useful in the fabrication of anode or electrolyte material for intermediate temperature solid oxide fuel cell application.

APPENDIX 2

Synthesis, structural and microstructural studies of Ni/NiO: ZrO_2 nanocomposites for intermediate temperature solid oxide fuel cell application

_____

A2-1: Introduction

Solid oxide fuel cells (SOFC) directly and efficiently convert chemical energy to electrical energy and combine the benefits of environmentally benign power generation with fuel flexibility. The use of cubic (c) and tetragonal (t) ZrO_2 in SOFCs, both as electrolyte and in anode material, makes it one of the most studied ceramic materials [1, 172]. Pure ZrO_2 has a monoclinic (m) crystal structure at room temperature and transforms to t-ZrO_2 and c-ZrO_2 on increasing temperature. The higher temperature t / c-ZrO_2 can be stabilized at room temperature by adding suitable aliovalent (Ca^{2+}, Y^{3+}, Sc^{3+}, Mg^{2+}etc) cations [134, 163, 173-177]. Subsequently, transition metal oxides such as, Cr_2O_3, Fe_2O_3, CuO and NiO have been incorporated in ZrO_2 with the possible application in SOFC using different chemical routes [160, 161, 164, 178]. The metal ions, used as dopants, are generally of smaller size and lower valent (compared to Zr^{4+} ions) and creates lattice defect, which plays a major role in stabilizing t / c-ZrO_2 [158]. Generally, Ni or NiO helps to stabilize t-ZrO_2 up to moderate temperature and simultaneously helps in conduction for SOFC application. The lower cost of Ni / NiO, in comparison to other aliovalent oxides, reduces the cost of anode fabrication in SOFC. In this work, an effective way is optimized to synthesize Ni doped t-ZrO_2 nanopowders through precipitation route using hydrazine hydrate as precipitating reagent. Structural and microstructural behavior of Ni / NiO: t-ZrO_2 nanocomposites in presence of air and H_2 atmosphere have been studied for suitability as anode material for SOFC application.

A2-2: Experimental

Three different ways of synthesis procedures (direct, reverse and constant pH) were adopted for preparing Ni (10, 20 and 30 mol %) doped t-ZrO_2 nanopowders through precipitation route. In this work, 0.2 M (M is molarity) hexa-hydrated nickel chloride ($NiCl_2 \cdot 6H_2O$), 0.2 M octa-hydrated zirconium oxychloride ($ZrOCl_2 \cdot 8H_2O$) and 10 vol % hydrazine hydrate ($N_2H_4 \cdot H_2O$) were prepared separately from high-purity chemicals. In direct process, hydrazine hydrate (HH) solution was added from a burette slowly to a beaker containing mixture of $NiCl_2 \cdot 6H_2O$ and $ZrOCl_2 \cdot 8H_2O$ solution. The reverse process is the reverse way of direct process. However, in constant pH process, the reverse process was followed with simultaneous addition of HH using a second burette to maintain the pH of HH solution at ~ 11. The precipitates obtained in these three processes were washed several times with distilled water and dried in an oven for overnight. The as-synthesized powders were further calcined at 700 °C and 800 °C for 1h. The structure and morphology of Ni doped t-ZrO_2 powders were characterized by using X-ray diffraction (XRD) and transmission electron microscope (TEM), respectively. Phase distributions of 50 mol % Ni doped t-ZrO_2 composite pellets, calcined at 700 °C in air and H_2 atmosphere were studied using back scattered

mode scanning electron microscopy (SEM). The porosity of these composite pellets was determined using pycnometer.

A2-3: Results and discussion

Figure A2-1 shows XRD patterns of 10 mol % Ni doped t-ZrO$_2$ nanopowders, synthesized by three different ways and calcined at 800 °C. Major m-ZrO$_2$ along with minute t-ZrO$_2$ phases were observed in both direct and reverse processes. However, nearly 80 vol % of t-ZrO$_2$ phase was found in constant pH process. Denkewicz et al. and Adair et al. also suggested that t-ZrO$_2$ crystallizes from an amorphous zirconium (hydrous) oxide precursor at higher pH in comparison to lower pH [179, 180]. From the above structural analysis, it was confirmed that the constant pH process is the better way to stabilize t-ZrO$_2$ with Ni addition as compared to direct or reverse ways. Hence, the nanopowders of different concentrations of Ni doped t-ZrO$_2$ were synthesized using constant pH process and calcined at 700 °C and 800 °C.
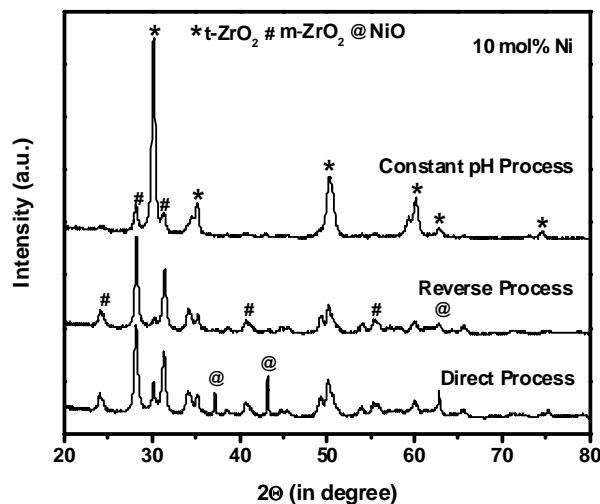
Fig. A2-1: XRD patterns of 10 mol% Ni doped ZrO$_2$ nanopowders prepared by three different ways and calcined at 800°C.

Figure A2-2 shows XRD patterns of pure (without Ni doping) ZrO$_2$ and 10, 20 and 30 mol % Ni doped t-ZrO$_2$ nanopowders, calcined at 700 °C. Pure ZrO$_2$ consists of 80 vol % m-ZrO$_2$ along with 20 vol% t-ZrO$_2$ phase. Addition of nearly 10 mol % Ni stabilizes t-ZrO$_2$ at 700 °C. To understand the high temperature stabilization behavior of Ni doped t-ZrO$_2$, these nanopowders were calcined at 800 °C and the XRD patterns are shown in inset of Fig. A2-2. At this temperature, 10 mol % Ni addition shows small amount of m-ZrO$_2$ along with t-ZrO$_2$ and fully stabilized t-ZrO$_2$ was observed only after 20 mol % Ni addition. Minute amount of NiO phase was also developed only after 20 mol % Ni addition for both calcined powders. From the above XRD results, it was

further confirmed that the minimum concentrations of Ni for stabilization of t-ZrO_2 at 700 °C and 800 °C are 10 mol % and 20 mol %, respectively. Figure A2-3 shows the change in unit cell volume of t-ZrO_2 as a function of Ni concentration.
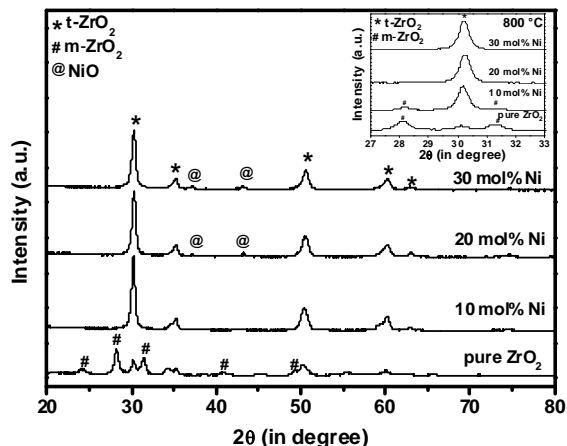
Fig. A2-2: XRD patterns of pure ZrO_2 (0 mol % Ni) and different concentrations of Ni doped t-ZrO_2 nanopowders synthesized using constant pH process and calcined at 700°C. Inset shows XRD patterns of Ni doped t-ZrO_2 nanopowders calcined at 800 °C.
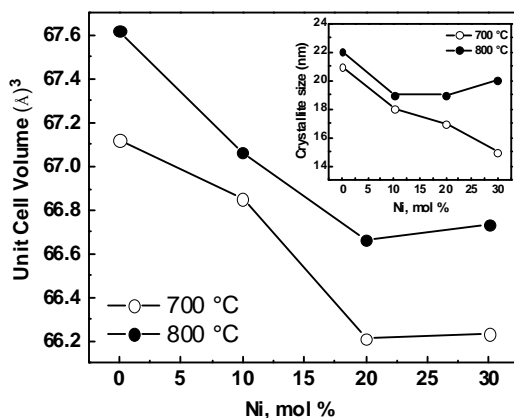
Fig. A2-3: Change in unit cell volume of t-ZrO_2 as a function of Ni concentration. Inset shows crystallite size of t-ZrO_2 as a function of Ni concentration.

The decrease in the unit cell volume of the tetragonal phase with increase in Ni concentration indicates the incorporation of Ni ion into the ZrO_2 lattice. An increase in Ni addition stabilizes t-phase of ZrO_2 with a decrease in crystallite size (see inset of Fig. A2-3). Similar observations are also observed in Fe_2O_3, CuO and NiO addition for stabilization of t-ZrO_2 [158, 161, 169, 181]. Figure A2-4 shows the TEM micrograph of 20 mol% Ni doped ZrO_2 nanopowders, calcined at 800°C. The particles are well dispersed and spherical in shape. The particle size is found to be < 100 nm, in agreement with the grain size determined from X-ray diffraction peaks.
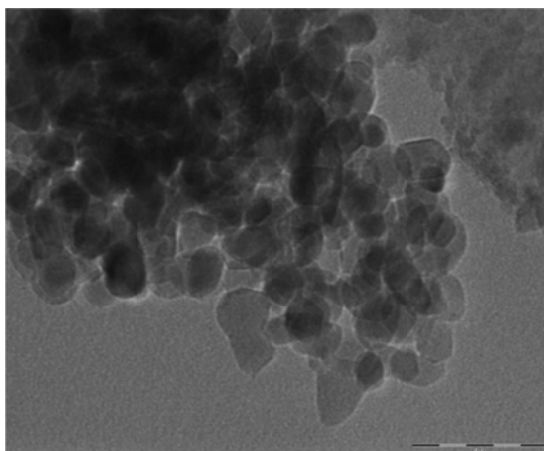
Fig. A2- 4: TEM micrograph of 20 mol % Ni doped t-ZrO$_2$ nanopowders, calcined at 800 °C. Scale corresponds to 50 nm.

To understand the nature of phase evolution and distribution, 50 mol % Ni doped ZrO$_2$ nanopowders were pelletized and calcined at 700 °C in air and H$_2$ atmosphere. An equal proportion of NiO and t-ZrO$_2$ in air atmosphere is seen from XRD pattern of Fig. A2-5.
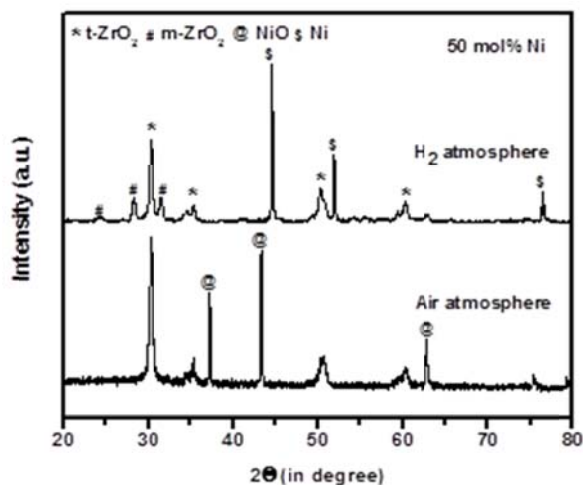
Fig. A2-5: XRD patterns of 50 mol% Ni doped ZrO$_2$ nanocomposite pellets, calcined at 700°C in air and H$_2$ atmosphere.

However, in presence of H$_2$ atmosphere, NiO converts to Ni and evolution of ~ 5 vol % m-ZrO$_2$ along with t- ZrO$_2$ was observed. The development of m-ZrO$_2$ is a consequence of lower solubility of Ni in ZrO$_2$ matrix [158, 169]. When NiO is reduced to metallic Ni, the excess Ni is exsolved from the ZrO$_2$ matrix which makes ZrO$_2$ to approach an equilibrium phase balance with a mixture of monoclinic and tetragonal phases [182]. The development of m-ZrO$_2$ may also be due to the metastable structure of interstitial and substituting Ni in ZrO$_2$ [183]. In order to get a direct and complete picture of the microstructure, back scattered mode SEM was performed for 50 mol % Ni doped ZrO$_2$ pellets. Figure 6 (a) and (b) show the SEM micrographs of these pellets calcined in air

and H_2 atmosphere, respectively. Uniform distribution of Ni or NiO in ZrO_2 matrix with 35-42% porosity was observed in these pellets.
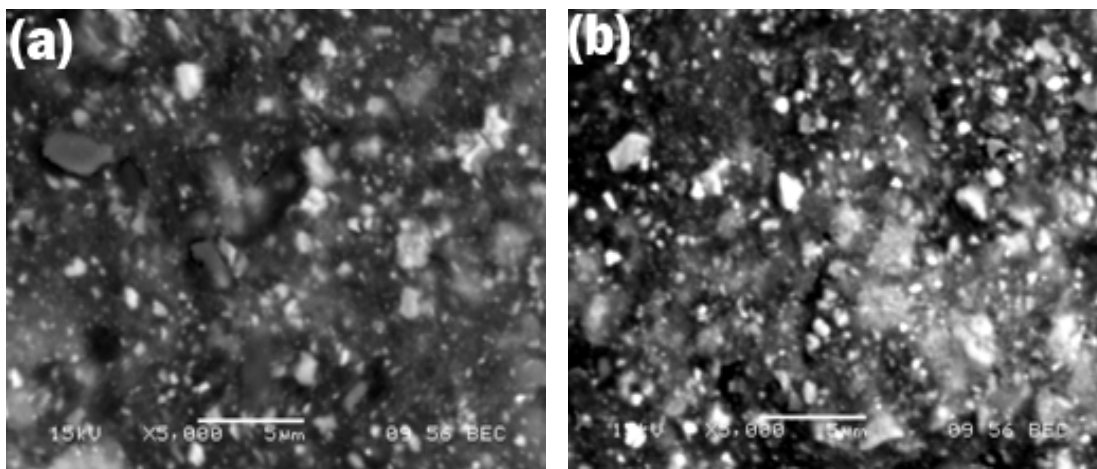
Fig. A2-6: Back scattered mode SEM micrograph of 50 mol % Ni doped t-ZrO_2 pellets calcined in (a) air atmosphere and (b) H_2 atmosphere.

A2-4: Conclusions

Ni doped t-ZrO_2 nanopowders and Ni / NiO: t-ZrO_2 nanocomposites were successfully prepared through precipitation route using HH. The constant pH process is the suitable way for synthesizing Ni / NiO: t-ZrO_2 nanopowders up to moderate temperatures as compared to direct or reverse way. In this work, small amount of Ni goes to interstitial sites of ZrO_2 and try to stabilize t-ZrO_2 up to moderate temperatures. The minimum concentrations of Ni for stabilization of t-ZrO_2 at 700 °C and 800 °C are 10 mol % and 20 mol %, respectively. Phase distributions of Ni or NiO in ZrO_2 matrix were found to be uniform and evolution of NiO and Ni in t-ZrO_2 matrix was observed in air and H_2 atmosphere, respectively. The porosity of these composites was found to be in the range between 35 -42 %. The synthesis method using hydrazine hydrate for preparing Ni / NiO: t-ZrO_2 nanocomposite powder is attractive and could be useful for the fabrication of anode material for intermediate temperature solid oxide fuel cell application.

References

1. S.C. Singhal and K. Kendal, *High Temperature and Solid Oxide Fuel Cells Fundamentals, Design and Applications*, Elsevier (2003).
2. N.Q. Minh and T. Takahashi, *Science and Technology of Ceramic Fuel Cells*, Elsevier (1995).
3. Theo Elmer and S.B. Riffat, State of the art review: Fuel cell technologies in the domestic built environment, *11th International Conference on Sustainable Energy Technologies (SET-2012)*, Vancouver, Canada (2012).
4. M.H. Pihlatie, A. Kaiser, M. Mogensen and M. Chen, *Solid State Ionics* **189** (2011) (1), p. 82.
5. K. Nakao, T. Ogura, T. Ishimoto and M. Koyama, *ECS Trans.* **35** (2011) (1), p. 1661.
6. M.C. Tucker, G.Y. Lau, C.P. Jacobson, S.J. Visco and L.C. De Jonghe, *J. Power Sources* **195** (2010) (10), p. 3119.
7. E.W. Park, H. Moon, M.-s. Park and S.H. Hyun, *Int. J. Hydrogen Energy* **34** (2009) (13), p. 5537.
8. M.J. Escudero, J.T.S. Irvine and L. Daza, *J. Power Sources* **192** (2009) (1), p. 43.
9. D. Marrero-López, J. Peña-Martínez, J.C. Ruiz-Morales, M. Gabás, P. Núñez, M.A.G. Aranda and J.R. Ramos-Barrado, *Solid State Ionics* **180** (2010) (40), p. 1672.
10. F.H. Wang, R.S. Guo, Q.T. Wei, Y. Zhou, H.L. Li and S.L. Li, *Mater. Lett.* **58** (2004) (24), p. 3079.
11. K. Sato, H. Abe, T. Misono, K. Murata, T. Fukui and M. Naito, *J. Eur. Ceram. Soc.* **29** (2009) (6), p. 1119.
12. M. Marinšek and K. Zupan, *Ceram. Int.* **36** (2010) (3), p. 1075.
13. S.-S. Liu, S. Toh, T. Daio, M. Koyama and S. Matsumura, *ECS Trans.* **57** (2013) (1), p. 1401.
14. S.-D. Kim, H. Moon, S.-H. Hyun, J. Moon, J. Kim and H.-W. Lee, *J. Power Sources* **163** (2006) (1), p. 392.
15. J.H. Yu, G.W. Park, S. Lee and S.K. Woo, *J. Power Sources* **163** (2007) (2), p. 926.
16. S.-D. Kim, H. Moon, S.-H. Hyun, J. Moon, J. Kim and H.-W. Lee, *Solid State Ionics* **177** (2006) (9-10), p. 931.
17. J.R. Wilson, W. Kobsiriphat, R. Mendoza, H.-Y. Chen, J.M. Hiller, D.J. Miller, K. Thornton, P.W. Voorhees, S.B. Adler and S.A. Barnett, *Nat Mater* **5** (2006) (7), p. 541.
18. T. Kawashima, S. Miyoshi, Y. Shibuta and S. Yamaguchi, *Journal of Power Sources* **234** (2013) (0), p. 147.
19. H. Iwai, N. Shikazono, T. Matsui, H. Teshima, M. Kishimoto, R. Kishida, D. Hayashi, K. Matsuzaki, D. Kanno, M. Saito, H. Muroyama, K. Eguchi, N. Kasagi and H. Yoshida, *Journal of Power Sources* **195** (2010) (4), p. 955.
20. P.R. Shearing, R.S. Bradley, J. Gelb, F. Tariq, P.J. Withers and N.P. Brandon, *Solid State Ionics* **216** (2012) (0), p. 69.
21. S. De Bondt, L. Froyen and A. Deruyttere, *J. Mater. Sci.* **27** (1992) (7), p. 1983.
22. T. Kawashima and M. Hishinuma, *Mater. Trans. JIM* **37** (1996) (7), p. 1397.
23. Z. Wu and M. Liu, *Solid State Ionics* **93** (1996) (1-2), p. 65.
24. S. Sunde, *J. Electrochem. Soc.* **143** (1996) (3), p. 1123.
25. T. Matsushima, H. Ohrui and T. Hirai, *Solid State Ionics* **111** (1998) (3-4), p. 315.
26. F. Tietz, F.J. Dias, D. Simwonis and D. Stöver, *J. Eur. Ceram. Soc.* **20** (2000) (8), p. 1023.
27. J.H. Lee, H. Moon, H.W. Lee, J. Kim, J.D. Kim and K.H. Yoon, *Solid State Ionics* **148** (2002) (1-2), p. 15.
28. T. Fukui, K. Murata, S. Ohara, H. Abe, M. Naito and K. Nogi, *J. Power Sources* **125** (2004) (1), p. 17.

29.   J.H. Lee, J.W. Heo, D.S. Lee, J. Kim, G.H. Kim, H.W. Lee, H.S. Song and J.H. Moon, *Solid State Ionics* **158** (2003) (3-4), p. 225.
30.   N.K. Singh, P. Singh, M.K. Singh, D. Kumar and O. Parkash, *Solid State Ionics* **192** (2011) (1), p. 431.
31.   O. Parkash, N. Singh, N.K. Singh and D. Kumar, *Solid State Ionics* **212** (2012), p. 100.
32.   D. Kashyap, P.K. Patro, R.K. Lenka, T. Mahata and P.K. Sinha, *Ceram. Int.* **40** (2014) (8, Part A), p. 11869.
33.   R.K. Lenka, T. Mahata, P.K. Patro, A.K. Tyagi and P.K. Sinha, *J. Alloys Compd.* **537** (2012) (0), p. 100.
34.   S.T. Aruna, M. Muthuraman and K.C. Patil, *Solid State Ionics* **111** (1998), p. 45.
35.   F.-Y. Shih, K.-Z. Fung, H.-C. Lin and G.-J. Chen, *J. Power Sources* **160** (2006) (1), p. 148.
36.   M. Marinšek, K. Zupan and J. Maèek, *J. Power Sources* **106** (2002), p. 178.
37.   M.B. Kakade, S. Ramanathan and D. Das, *Ceram. Int.* **37** (2011) (1), p. 195.
38.   M. Liang, B. Yu, M. Wen, J. Chen, J. Xu and Y. Zhai, *Int. J. Hydrogen Energy* **35** (2010) (7), p. 2852.
39.   S.-J. Kim, W. Lee, W.-J. Lee, S.D. Park, J.S. Song and E.G. Lee, *J. Mater. Res.* **16** (2001) (12), p. 3621.
40.   T. Priyatham and R. Bauri, *Mater. Charact.* **61** (2010) (1), p. 54.
41.   H. Mohebbi, T. Ebadzadeh and F.A. Hesari, *J. Power Sources* **178** (2008) (1), p. 64.
42.   H. Mohebbi, T. Ebadzadeh and F.A. Hesari, *Powder Technol.* **188** (2009) (3), p. 183.
43.   A. Ringuedé, D. Bronine and J.R. Frade, *Solid State Ionics* **146** (2002), p. 219.
44.   M. Marinšek and J. Maček, *Key Eng. Mater.* **132-136** (1997).
45.   M. Marinšek, K. Zupan and J. Maček, *J. Power Sources* **86** (2000) (1-2), p. 383.
46.   Y. Li, Y. Xie, J. Gong, Y. Chen and Z. Zhang, *Materials Science and Engineering: B* **86** (2001) (2), p. 119.
47.   S. Li, R. Guo, J. Li, Y. Chen and W. Liu, *Ceram. Int.* **29** (2003) (8), p. 883.
48.   C.M. Grgicak, R.G. Green, W.-F. Du and J.B. Giorgi, *J. Am. Ceram. Soc.* **88** (2005) (11), p. 3081.
49.   C.M. Grgicak, R.G. Green and J.B. Giorgi, *J. Mater. Chem.* **16** (2006) (9), p. 885.
50.   K. Sato, G. Okamoto, M. Naito and H. Abe, *J. Power Sources* **193** (2009) (1), p. 185.
51.   K. Sato, T. Kinoshita and H. Abe, *Fuel Cells* **10** (2010) (2), p. 320.
52.   S. Jung-Hoon, P. Mi-Young and L. Hyung-Tae, *Nano-Micro Letters* **5** (2013) (2), p. 111.
53.   X. Xi, H. Abe, K. Kuruma, R. Harada, A. Shui and M. Naito, *Advanced Powder Technology* **25** (2014) (2), p. 490.
54.   S. Mosch, N. Trofimenko, M. Kusnezoff, T. Betz and M. Kellner, Electrochemical and microstructural characterization of the solid oxide fuel cell anode prepared by co-precipitation, *ECS Trans.* (2007), pp. 1547-1553.
55.   S. Mosch, N. Trofimenko, M. Kusnezoff, T. Betz and M. Kellner, *Solid State Ionics* **179** (2008) (27-32), p. 1606.
56.   K. Haberko, M. Jasinski, P. Pasierb, M. Radecka and M. Rekas, *J. Power Sources* **195** (2010) (17), p. 5527.
57.   J.W. Moon, H.L. Lee, J.D. Kim, G.D. Kim, D.A. Lee and H.W. Lee, *Mater. Lett.* **38** (1999) (3), p. 214.
58.   G. Wen, Z.X. Guo and C.K.L. Davies, *Scr. Mater.* **43** (2000) (4), p. 307.
59.   S.K. Pratihar, A.D. Sharma, R.N. Basu and H.S. Maiti, *J. Power Sources* **129** (2004) (2), p. 138.
60.   S.K. Pratihar, A. Dassharma and H.S. Maiti, *Mater. Res. Bull.* **40** (2005) (11), p. 1936.
61.   S.K. Pratihar, A.D. Sharma and H.S. Maiti, *Mater. Chem. Phys.* **96** (2006) (2-3), p. 388.
62.   S. Pratihar, A. Dassharma and H.S. Maiti, *J. Mater. Sci.* **42** (2007) (17), p. 7220.
63.   S.-D. Kim, H. Moon, S.-H. Hyun, J. Moon, J. Kim and H.-W. Lee, *Solid State Ionics* **178** (2007) (21-22), p. 1304.

64. A.H.M. Esfakur Rahman, J.-H. Kim, K.-H. Lee and B.-T. Lee, *Surf. Coat. Technol.* **202** (2008) (10), p. 2182.
65. J.-D. Lin and Z.-L. Wu, *J. Am. Ceram. Soc.* **92** (2009) (11), p. 2555.
66. M. Mukhopadhyay, J. Mukhopadhyay, A.D. Sharma and R.N. Basu, *Materials Science and Engineering: B* **163** (2009) (2), p. 120.
67. L. Li, P. Zhang, R. Liu and S.M. Guo, *J. Power Sources* **196** (3), p. 1242.
68. R. Bauri, *Journal of Coatings Technology and Research* **9** (2012) (2), p. 229.
69. C. Suciu, A.C. Hoffmann, E. Dorolti and R. Tetean, *Chem. Eng. J. (Lausanne)* **140** (2008) (1-3), p. 586.
70. D.W. Dees, T.D. Claar, T.E. Easler, D.C. Fee and F.C. Mrazek, *J. Electrochem. Soc.* **134** (1987) (9), p. 2141.
71. Y. Min Park and G. Man Choi, *Solid State Ionics* **120** (1999) (1-4), p. 265.
72. Y.M. Park and G.M. Choi, *J. Electrochem. Soc.* **146** (1999) (3), p. 883.
73. Q. Xue, *Eur. Polym. J.* **40** (2004) (2), p. 323.
74. W. Huebner, H.U. Anderson, D.M. Reed, S.R. Sehlin, X. Deng, in:, M. Dokiya, O. Yamamoto, H. Tagawa and S.C. Singhal (Eds.), *Proceedings of the Fourth International Symposium on Solid Oxide Fuel Cells (SOFC-IV)*, Yokohama, Japan (6-9 June 1995), p. 159.
75. R.J. Gorte and J.M. Vohs, *Curr. Opin. Colloid Interface Sci.* **14** (2009) (4), p. 236.
76. H. Itoh, T. Yamamoto, M. Mori, N. Mori, T. Watanabe, in: and B. Thorstensen (Ed.), Proceedings of the Second European Solid Oxide Fuel Cell Forum, Oslo, Norway (6-10 May 1996), p. 453.
77. H. Itoh, T. Yamamoto, M. Mori, T. Horita, N. Sakai, H. Yokokawa and M. Dokiya, *J. Electrochem. Soc.* **144** (1997) (2), p. 641.
78. W.Z. Zhu and S.C. Deevi, *Materials Science and Engineering: A* **362** (2003) (1-2), p. 228.
79. K.R. Han, Y. Jeong, H. Lee and C.-S. Kim, *Mater. Lett.* **61** (2007) (4-5), p. 1242.
80. B.C.H. Steele, in: and U. Bossel (Ed.), Proceedings of the First European Solid Oxide Fuel Cell Forum, Lucerne, Switzerland (3-7 October 1994), p. 375.
81. T. Klemensø and M. Mogensen, *J. Am. Ceram. Soc.* **90** (2007) (11), p. 3582.
82. D. Simwonis, F. Tietz and D. Stöver, *Solid State Ionics* **132** (2000) (3-4), p. 241.
83. A. Davarpanah, A.A. Yaremchenko, D.P. Fagg and J.R. Frade, *Int. J. Hydrogen Energy* (2014) (0).
84. S. Murakami, Y. Akiyama, N. Ishida, T. Yasuo, T. Saito and N. Furukawa, Development of a solid oxide fuel cell with composite anodes, In: F. Grosz, P. Zegers, S.C. Singhal and O. Yamamoto (Eds.), Editors, *Solid Oxide Fuel Cells, Proc. 2nd Int. Symp., Commission of the European Communities*, Athens, Greece (1991), pp. 105-112.
85. T. Shirakawa, S. Matsuda and A. Fukushima, Characterization of NiO/YSZ electrode by temperature-programmed reduction, In: S.C. Singhal and H. Iwahara, Editors, *Solid Oxide Fuel Cells, Proc. 3rd Int. Symp., Electrochemical Society*, Pennington, NJ (1993), pp. 464-472.
86. T. Iwata, *J. Electrochem. Soc.* **143** (1996) (5), p. 1521.
87. A. Tintinelli, C. Rizzo, G. Giunta, A. Selvaggi, in: and U. Bossel (Ed.), Proceedings of the First European Solid Oxide Fuel Cells Forum, Lucerne, Switzerland (3-7 October 1994), p. 455.
88. X. Deng and A. Petric, In: S.C. Singhal and M. Dokiya, Editors, *SOFC - VIII*, Electrochemical Society, Pennington, NJ (2003), pp. 653-661.
89. T. Talebi, M.H. Sarrafi, M. Haji, B. Raissi and A. Maghsoudipour, *Int. J. Hydrogen Energy* **35** (2010) (17), p. 9440.
90. B.A. Horri, C. Selomulya and H. Wang, *Int. J. Hydrogen Energy* **37** (2012) (20), p. 15311.
91. N. Droushiotis, U. Doraswami, K. Kanawka, G.H. Kelsall and K. Li, *Solid State Ionics* **180** (2009) (17-19), p. 1091.

92.   X. Meng, N. Yang, B. Meng, X. Tan, Y. Yin, Z.-F. Ma and J. Sunarso, *Ceram. Int.* **38** (2012) (8), p. 6327.

93.   W. Huebner, D.M. Reed and H.U. Anderson, In: S.C. Singhal and M. Dokiya, Editors, *SOFC-VI*, Electro- chemical Society, Pennington, NJ (1999), pp. 503-512.

94.   L. Jia, Z. Lu, J. Miao, Z. Liu, G. Li and W. Su, *J. Alloys Compd.* **414** (2006) (1-2), p. 152.

95.   S.P. Jiang, J.G. Love and L. Apateanu, *Solid State Ionics* **160** (2003) (1-2), p. 15.

96.   L. Grahl-Madsen, P.H. Larsen, N. Bonanos, J. Engell and S. Linderoth, In: J. Huijsmans, Editor, *5th European SOFC Forum*, European Fuel Cells Forum, Lucerne, Switzerland (2002), p. 82.

97.   L. Grahl-Madsen, P. Larsen, N. Bonanos, J. Engell and S.r. Linderoth, *J. Mater. Sci.* **41** (2006) (4), p. 1097.

98.   M.H. Pihlatie, A. Kaiser and M.B. Mogensen, *Solid State Ionics* **222-223** (2012) (0), p. 38.

99.   T. Kawada, N. Sakai, H. Yokokawa, M. Dokiya, M. Mori and T. Iwata, *Solid State Ionics* **40-41,** Part 1 (1990) (0), p. 402.

100. T. Kawada, N. Sakai, H. Yokokawa, M. Dokiya, M. Mori and T. Iwata, *J. Electrochem. Soc.* **137** (1990) (10), p. 3042.

101. S.P. Jiang, P.J. Callus and S.P.S. Badwal, *Solid State Ionics* **132** (2000) (1-2), p. 1.

102. H. Koide, Y. Someya, T. Yoshida and T. Maruyama, *Solid State Ionics* **132** (2000) (3-4), p. 253.

103. J. Mizusaki, H. Tagawa, T. Saito, T. Yamamura, K. Kamitani, K. Hirano, S. Ehara, T. Takagi, T. Hikita, M. Ippommatsu, S. Nakagawa and K. Hashimoto, *Solid State Ionics* **70-71,** Part 1 (1994) (0), p. 52.

104. S.P. Simner, J.F. Bonnett, N.L. Canfield, K.D. Meinhardt, J.P. Shelton, V.L. Sprenkle and J.W. Stevenson, *J. Power Sources* **113** (2003) (1), p. 1.

105. S.P. Simner, M.D. Anderson, L.R. Pederson and J.W. Stevenson, *J. Electrochem. Soc.* **152** (2005) (9), p. A1851.

106. J. Kong, K. Sun, D. Zhou, N. Zhang, J. Mu and J. Qiao, *J. Power Sources* **166** (2007) (2), p. 337.

107. D. Prakash, R.K. Lenka, A.K. Sahu, P.K. Patro, P.K. Sinha and A.K. Suri, Effect of cathode functional layer on the electrical performance of tubular solid oxide fuel cell, *ASME 2010 8th International Conference on Fuel Cell Science, Engineering and Technology, FUELCELL 2010* (2010), pp. 439-444.

108. X. Xi, H. Abe and M. Naito, *Ceram. Int.* In press, Accepted manuscript (2014) (0).

109. M. Chen, B.H. Kim, Q. Xu and B.G. Ahn, *J. Membr. Sci.* **334** (2009) (1-2), p. 138.

110. F.P.F. van Berkel, F.H. van Heuveln and J.P.P. Huijsmana, In: S.C. Singhal and H. Iwahara, Editors, *SOFC-III*, The Electrochemical Society, Pennington, NJ (1993), pp. 744-751.

111. J. van Herle, R. Ihringer and A.J. McEvoy, Development of a standard Ni-YSZ cermet anode for intermediate temperatures, In: U. Stimming, S.C. Singhal, H. Tagawa and W. Lehnert, Editors, *SOFC-V*, The Electrochemical Society, Pennington, NJ (1997), pp. 565-574.

112. S. Primdahl, B.F. Sørensen and M. Mogensen, *J. Am. Ceram. Soc.* **83** (2000) (3), p. 489.

113. T.S. Li, W.G. Wang, H. Miao, T. Chen and C. Xu, *J. Alloys Compd.* **495** (2010) (1), p. 138.

114. F.P.F. van Berkel, F.H. van Heuveln and J.P.P. Huijsmans, *Solid State Ionics* **72, Part 2** (1994) (0), p. 240.

115. S. Primdahl and M. Mogensen, *J. Electrochem. Soc.* **144** (1997) (10), p. 3409.

116. S.P. Jiang and S.P.S. Badwal, *Solid State Ionics* **123** (1999) (1-4), p. 209.

117. N. Nakagawa, H. Sakurai, K. Kondo, T. Morimoto, K. Hatanaka and K. Kato, *J. Electrochem. Soc.* **142** (1995) (10), p. 3474.

118. C. Wen, R. Kato, H. Fukunaga, H. Ishitani and K. Yamada, *J. Electrochem. Soc.* **147** (2000) (6), p. 2076.

119. C.W. Tanner, K.Z. Fung and A.V. Virkar, *J. Electrochem. Soc.* **144** (1997) (1), p. 21.

120. F. Zhao and A.V. Virkar, *J. Power Sources* **141** (2005) (1), p. 79.

121. T. Suzuki, Z. Hasan, Y. Funahashi, T. Yamaguchi, Y. Fujishiro and M. Awano, *Science* **325** (2009) (5942), p. 852.

122. C.M. An, J.-H. Song, I. Kang and N. Sammes, *J. Power Sources* **195** (2010) (3), p. 821.

123. A. Singh and V. Krishnan, *ECS Trans.* **6** (2008) (21), p. 25.

124. T. Fukui, K. Murata, S. Ohara, H. Abe, M. Naito and K. Nogi, *J. Power Sources* **125** (2004) (1), p. 17.

125. Z.-C. Chen, Y. Sakane, T. Tsurumaki, Y. Ayame and F. Fujita, Microstructure and electrical conductivity of Ni/YSZ cermets for SOFC, *16ᵗʰ International Conference on Composite Materials* (2007), pp. 1-6.

126. J.-Y. Choi, Y.-K. Lee, S.-M. Yoon, H.C. Lee, B.-K. Kim, J.M. Kim, K.-M. Kim and J.-H. Lee, *J. Am. Ceram. Soc.* **88** (2005) (11), p. 3020.

127. S.R. Jain, K.C. Adiga and V.R. Pai Verneker, *Combust. Flame* **40** (1981) (0), p. 71.

128. J.W. Park, E.H. Chae, S.H. Kim, J.H. Lee, J.W. Kim, S.M. Yoon and J.-Y. Choi, *Mater. Chem. Phys.* **97** (2006) (2-3), p. 371.

129. K.-M. Kim, J.-H. Lee, S.-M. Yoon, H.-C. Lee, Y.-K. Lee and J.-Y. Choi, *Journal of Electroceramics* **17** (2006) (2-4), p. 339.

130. G.-y. Huang, S.-m. Xu, G. Xu, L.-y. Li and L.-f. Zhang, *Transactions of Nonferrous Metals Society of China* **19** (2009) (2), p. 389.

131. P. Kumar, A.N. Tiwari and P. Bhargava, *Trans. Indian Ceram. Soc.* **72** (2013) (2), p. 130.

132. K. Sasaki, J.-P. Wurth, R. Gschwend, M. Gödickemeier and L.J. Gauckler, *Journal of the Electrochemical Society* **143** (1996) (2), p. 530.

133. B.D. Cullity, *Elements of X-ray diffraction*, addition-Wesley publishing company, INC. reading massachusetts, United States of America (1956).

134. A. Mondal and S. Ram, *Solid State Ionics* **160** (2003) (1-2), p. 169.

135. B.A. Moisă, A. Chiran, I. Priceputu and Z. Bacinschi, The controlled atmosphere influence over the aspect of the stainless steel strip, *The Scientific Bulletin of VALAHIA University – Materials and Mechanics* (2011), pp. 63 - 69.

136. M. Marinšek, S. Pejovnik and J. Mač ek, *J. Eur. Ceram. Soc.* **27** (2007) (2-3), p. 959.

137. U. Anselmi-Tamburini, G. Chiodelli, M. Arimondi, F. Maglia, G. Spinolo and Z.A. Munir, *Solid State Ionics* **110** (1998) (1-2), p. 35.

138. D.A. Osinkin, D.I. Bronin, S.M. Beresnev, N.M. Bogdanovich, V.D. Zhuravlev, G.K. Vdovin and T.A. Demyanenko, *J. Solid State Electrochem.* **18** (2013) (1), p. 149.

139. R. Nédélec, S. Uhlenbruck, D. Sebold, V.A.C. Haanappel, H.P. Buchkremer and D. Stöver, *J. Power Sources* **205** (2012) (0), p. 157.

140. C.-W. Kuo, Y.-H. Lee, I.M. Hung, M.-C. Wang, S.-B. Wen, K.-Z. Fung and C.-J. Shih, *J. Alloys Compd.* **453** (2008) (1-2), p. 470.

141. L. Wang, Y. Wang, X.G. Sun, J.Q. He, Z.Y. Pan and C.H. Wang, *Ceram. Int.* **38** (2012) (5), p. 3595.

142. E. Caproni, D. Gouvêa and R. Muccillo, *Ceram. Int.* **37** (2011) (1), p. 273.

143. R.A. De Souza, M.J. Pietrowski, U. Anselmi-Tamburini, S. Kim, Z.A. Munir and M. Martin, *Phys. Chem. Chem. Phys.* **10** (2008) (15), p. 2067.

144. K. Rajeswari, M.B. Suresh, D. Chakravarty, D. Das and R. Johnson, *Int. J. Hydrogen Energy* **37** (2012) (1), p. 511.

145. J. Wang, L.S. Ee, S.C. Ng, C.H. Chew and L.M. Gan, *Mater. Lett.* **30** (1997) (1), p. 119.

146. S. K. Mohanty, B. B. Nayak, G. Purohit, A. Mondal, R.D. Purohit and P.K. Sinha, *Mater. Lett.* **65** (2011) (6), p. 959.

147. S. K. Mohanty, G. Purohit, R. D. Purohit, P. K. Sinha, A. Mondal and B. B. Nayak, *Int. J. Nanosci.* **10** (2011) (04-05), p. 727.

148. M. Zhi, X. Chen, H. Finklea, I. Celik and N.Q. Wu, *J. Power Sources* **183** (2008) (2), p. 485.

149. H. Fukunaga, M. Koyama, N. Takahashi, C. Wen and K. Yamada, *Solid State Ionics* **132** (2000) (3-4), p. 279.

150. X. Ding, X. Kong, J. Jiang, C. Cui and X. Guo, *Mater. Res. Bull.* **45** (2010) (9), p. 1271.
151. H. Patra, S.K. Rout, S.K. Pratihar and S. Bhattacharya, *Int. J. Hydrogen Energy* **36** (2011) (18), p. 11904.
152. P. Holtappels, I.C. Vinke, L.G.J. de Haart and U. Stimming, *J. Electrochem. Soc.* **146** (1999) (8), p. 2976.
153. A.V. Virkar, J. Chen, C.W. Tanner and J.-W. Kim, *Solid State Ionics* **131** (2000) (1-2), p. 189.
154. C.-H. Lee, C.-H. Lee, H.-Y. Lee and S.M. Oh, *Solid State Ionics* **98** (1997) (1-2), p. 39.
155. L. Zhang, S.P. Jiang, H.Q. He, X. Chen, J. Ma and X.C. Song, *Int. J. Hydrogen Energy* **35** (2010) (22), p. 12359.
156. Y.-T. An, B.-H. Choi, M.-J. Ji, K.-J. Lee and H.J. Hwang, *Solid State Ionics* **207** (2012) (0), p. 64.
157. W. Yao and E. Croiset, *J. Power Sources* **226** (2013) (0), p. 162.
158. M.K. Dongare, K. Malshe, C.S. Gopinath, I.K. Murwani and E. Kemnitz, *J. Catal.* **222** (2004) (1), p. 80.
159. A. Mondal, A. Zachariah, P. Nayak and B.B. Nayak, *J. Am. Ceram. Soc.* **93** (2), p. 387.
160. G. Štefanić, S. Popović and S. Musić, *Mater. Lett.* **36** (1998) (5-6), p. 240.
161. G. Štefanić, B. Grźeta, K. Nomura, R. Trojko and S. Musić, *J. Alloys Compd.* **327** (2001) (1-2), p. 151.
162. G. Štefanić, S. Musić and M. Ivanda, *J. Alloys Compd.* **491** (2010) (1-2), p. 536.
163. S. Fabris, A.T. Paxton and M.W. Finnis, *Acta Mater.* **50** (2002) (20), p. 5171.
164. A. Chandra Bose, R. Ramamoorthy and S. Ramasamy, *Mater. Lett.* **44** (2000) (3-4), p. 203.
165. H. Zhu, D. Yang, Z. Xi and L. Zhu, *J. Am. Ceram. Soc.* **90** (2007) (4), p. 1334.
166. A. Mondal and S. Ram, *J. Am. Ceram. Soc.* **87** (2004) (12), p. 2187.
167. B.B. Nayak, S.K. Mohanty, M.Q.B. Takmeel, D. Pradhan and A. Mondal, *Mater. Lett.* **64** (2010) (17), p. 1909.
168. R.C. Garvie and P.S. Nicholson, *J. Am. Ceram. Soc.* **55** (1972) (6), p. 303.
169. G. Štefanić, M. Didović and S. Musić, *J. Mol. Struct.* **834-836** (2007) (0), p. 435.
170. M.K. Dongare, V. Ramaswamy, C.S. Gopinath, A.V. Ramaswamy, S. Scheurell, M. Brueckner and E. Kemnitz, *J. Catal.* **199** (2001) (2), p. 209.
171. G. Xu, Y.W. Zhang, C.S. Liao and C.H. Yan, *J. Am. Ceram. Soc.* **87** (2004) (12), p. 2275.
172. S.B. Patil, A.K. Jena and P. Bhargava, *Int. J. Appl. Ceram. Technol.* **10** (2012), p. E247.
173. A.H. Heuer and L.W. Hobbs, *Science and Technology of Zirconia*, American Ceramic Society, Inc, Columbus, Ohio (1981).
174. R. Muccillo, R.C. Buissa Netto and E.N.S. Muccillo, *Mater. Lett.* **49** (2001) (3-4), p. 197.
175. D. Lee, I. Lee, Y. Jeon and R. Song, *Solid State Ionics* **176** (2005) (11-12), p. 1021.
176. H. Gocmez and H. Fujimori, *Materials Science and Engineering: B* **148** (2008) (1-3), p. 226.
177. J.C. Ray, P. Pramanik and S. Ram, *Mater. Lett.* **48** (2001) (5), p. 281.
178. Y. Wang and R.A. Caruso, *J. Mater. Chem.* **12** (2002) (5), p. 1442.
179. R.P. Denkewicz, K.S. TenHuisen and J.H. Adair, *J. Mater. Res.* **5** (1990) (11), p. 2698.
180. J. Adair and R. Denkewicz, *Ceramic powder science 3* (1990).
181. M. Bhagwat, A.V. Ramaswamy, A.K. Tyagi and V. Ramaswamy, *Mater. Res. Bull.* **38** (2003) (13), p. 1713.
182. S. Linderoth, N. Bonanos, K.V. Jensen and J.B. Bilde-Sørensen, *J. Am. Ceram. Soc.* **84** (2001) (11), p. 2652.
183. S. Yang, S.M. Guo, G.-L. Zhao and E. Khosravi, Highly infrared reflective nickel doped ZrO2 from first principles simulation, *Proc. Int. Conf. Computational Science — ICCS 2009 "Compute. Discover Innovate"* (2009).

Curriculum Vitae

Subrat Kumar Mohanty

Department of Ceramic Engineering
National Institute of Technology
Rourkela – 769008
Odisha, INDIA
E-mail: kumarsubrat08@gmail.com
Mobile No.: +91 9438790234

Research Area: Solid Oxide Fuel Cell (SOFC), Nano-composites.

Awards/Honours:

- Appointed as Junior Research Fellow (JRF)/Senior Research Fellow (SRF) in the BRNS (BARC) sponsored project *"Microstructural evolution of nanograin nickel-zirconia cermet anode materials for solid oxide fuel cell (SOFC) application"*, during 2009-2012.
- Awarded Senior Research Fellowship (SRF) in the project ``*Microstructural tuning and electrical characterization of Ni-YSZ anode for intermediate temperature SOFC*´´ by Council of Scientific and Industrial Research (CSIR), Govt. of India during 2012-2014.
- Sanctioned full air fare from CSIR, New Delhi, for ICMAT 2013, Singapore in 2013.
- Selected for the post of Inspector of Weights and Measures under Odisha Staff Selection Commission (OSSC) in 2009.
- Awarded Senior Merits Scholarship from 1997-1999.

Educational Qualification

Education	Institute/University/Council/Board	Year of Passing	Division/Grade
Ph.D.	Department of Ceramic Engineering NIT Rourkela	Jan 2015	-
M. Sc. (Physics)	Ravenshaw Autonomous College Cuttack, Odisha	2004	First
+3 Sc. (Phy. Hons)	Utkal Universiy, Bhubaneswar Odisha	2002	First (Hons)/ Distinction
+2 Sc.	Council of Higher Secondary Education, Bhubaneswar, Odisha	1999	First
10th	Board of Seconday Education, Cuttack, Odisha	1997	First

Publications

1. S. K. Mohanty, B. B. Nayak, "Crystallization and microstructure of 8YSZ nanopowders synthesized by ball-mill assisted constant pH route", American Institute of Physics Conference Proceeding, 1536, 227 (2013).
2. S. K. Mohanty, G. Purohit, R. D. Purohit, P. K. Sinha, A. Mondal, B. B. Nayak, "*Synthesis, structural and microstructural studies of Ni/NiO: ZrO_2 nanocomposites for intermediate temperature solid oxide fuel cell application*" International Journal of Nanoscience, 10, 727 (2011).
3. S. K. Mohanty, B. B. Nayak, G. Purohit, A. Mondal, R. D. Purohit, P. K. Sinha, "*Efficient way of precipitation to synthesize Ni^{2+}-ion stabilized tetragonal zirconia nanopowders*", Materials Letters, 65, 959 (2011).

4. B. B. Nayak, S. K. Mohanty, Md Q. B. Takmeel, D. Pradhan, A. Mondal, "*Borohydride synthesis and stabilization of flake-like tetragonal zirconia nanocrystallites*", Materials Letters, 64, 1909 (2010).

5. S. K. Mohanty, B. B. Nayak "Porosity controlled transition from ionic to electronic conductivity in auto-combustion derived Ni: 8YSZ cermet" (submitted).

6. S. K. Mohanty, B. B. Nayak "Microstructure, electrical conductivity and cell performance of fuel stoichiometric derived Ni: 8YSZ anode" (submitted).

7. S. K. Mohanty, B. B. Nayak "Microstructural development and electrical characterization of co-precipitation derived Ni: 8YSZ anode" (submitted).

8. S. K. Mohanty, B. B. Nayak "A novel heterogeneous precipitation method for the synthesis of highly percolated fine NiO/Ni particles in 8YSZ matrix and its electrical behavior" (submitted).

Papers presented in international/national conference

1. S. K. Mohanty, B. B. Nayak, "Densification, microstructure and electrical properties of auto-combustion derived nanostructured NiO/Ni-8YSZ composites for IT-SOFC application" - 7th International conference on Materials for Advanced Technologies (ICMAT-2013) Suntec, Singapore.

2. S. K. Mohanty, B. B. Nayak, R. D. Purohit, P. K. Sinha "A novel heterogeneous precipitation method for the synthesis of highly percolated fine NiO/Ni particles in 8YSZ matrix for IT-SOFC application" - 7th International conference on Materials for Advanced Technologies (ICMAT-2013) Suntec, Singapore.

3. B. B. Nayak, N. B. Nayak, S.K. Mohanty, A. Mondal, "Morphology controllable synthesis of nickel nanostructures through solution route using hydrazine hydrate as a precipitating agent" - 7th International conference on Materials for Advanced Technologies (ICMAT-2013) Suntec, Singapore.

4. S. K. Mohanty, B. B. Nayak "Crystallization and microstructure of 8YSZ nanopowders synthesized by ball-milled assisted constant pH route" - International Conference on Recent trends in applied physics and materials science (RAM 2013), 1st- 2nd February 2013,Govt. Engineering College, Bikaner, India.

5. S. K. Mohanty, G. Purohit, R. D. Purohit, P. K. Sinha, A. Mondal, B. B. Nayak, Phase evolution and morphological studies of NiO/Ni-ZrO$_2$ nanocomposites for IT-SOFC applications"- 3rd EICOON school science and technology renewable and clean energy sources (EICOON 2012), 30th April - 1st May 2012, p.103, Hotel ITC Sonar,Kolkata, India.

6. S. K. Mohanty, G. Purohit, R. D. Purohit, P. K. Sinha, A. Mondal, B. B. Nayak, "Synthesis, structural and microstructural studies of Ni/NiO: ZrO$_2$ nanocomposites for intermediate temperature solid oxide fuel cell application" - International conference on Nano Science and Technology (ICONSAT-2010), 17th - 20th Feb 2010, IIT Bombay, Mumbai.

7. S. K. Mohanty, G. Purohit, R. D. Purohit, P. K. Sinha, B. B. Nayak, "*Synthesis and characterization of Ni/NiO stabilized zirconia nanopowders for solid oxide fuel cell application*" - International Conference on Advanced Functional Materials (ICAFM 2009), 09th - 10th Dec 2009, Thiruvananthapuram, India.

Personal Information

Father's Name:	Mr. Laksmidhar Mohanty
Mother's Name:	Mrs. Manjubala Mohanty
Date of Birth:	27th June 1982
Sex:	Male
Marital Status:	Married
Religion:	Hindu
Nationality:	Indian
Languages Known:	Odia, Hindi and English
Hobbies & Interests:	Playing guitar (Hawaiin), Travelling, Playing, Movies and Music

Permanent Address: At: Sasansima, P.O: Dhanmandal, Dist: Jajpur, PIN: 754024, ODISHA